DISSERTATION

FLUOROALKYL AND FLUOROARYL FULLERENES, POLYCYCLIC AROMATIC

HYDROCARBONS, AND COPPER(I) COMPLEXES: SYNTHESIS, STRUCTURE,

ELECTROCHEMICAL, PHOTOPHYSICAL, AND DEVICE PROPERTIES

Submitted by

Brian J. Reeves

Department of Chemistry

In partial fulfillment of the requirements

For the Degree of Doctor of Philosophy

Colorado State University

Fort Collins, Colorado

Summer 2020

Doctoral Committee:

    Advisor: Steven H. Strauss

    Matthew P. Shores
    Anthony K. Rappé
    Andrew McNally
    John Ridley

ABSTRACT

FLUOROALKYL AND FLUOROARYL FULLERENES, POLYCYCLIC AROMATIC

HYDROCARBONS, AND COPPER(I) COMPLEXES: SYNTHESIS, STRUCTURE,

ELECTROCHEMICAL, PHOTOPHYSICAL, AND DEVICE PROPERTIES

In many fields of research, ranging from materials chemistry to medicinal chemistry, understanding the structural, electrochemical, and photophysical properties of materials is essential to establishing trends and predicting usefulness and future performance. This work has focused on the impact of strongly electron withdrawing perfluoroaryl and perfluoroalkyl substituents on the properties of fullerenes, polycyclic aromatic hydrocarbons (PAHs), hetero-PAHs, and copper(I) complexes with the goal of establishing and understanding the fundamental reasons for any observed trends.

In Chapter 1, the first successful example of vacuum-deposited organic photovoltaic cells (OPVs) based on a fullerene derivative and a small-molecule donor is reported. A series of thermally robust fluorous fullerene acceptors with experimental gas-phase electron affinities ranging from 2.8 to 3.3 eV are paired with new dicyanovinyl thiophene-based molecular donors to enable direct comparison of their performance in planar and bulk heterojunction architectures in cells fabricated by vacuum deposition. Unprecedented insights into the role of the acceptor intrinsic molecular and electronic structures are obtained, which are not obscured by solvent and additive effects as in the typical solution-processed fullerene-based OPVs. Additionally, the fullerene derivative, $C_{60}CF_2$, was utilized in vacuum-deposited organic field effect transistors (OFETs), and it was shown to have superior device lifetime compared to C_{60} based OFETs.

In Chapter 2, a new synthesis of 9,10-bis(perfluorobenzyl)anthracene, a promising blue organic light emitting diode (OLED) material is reported. The yield was improved from 7% to 17%, while the separations conditions were improved to only require one stage of HPLC.

In Chapters 3 and 4, the trifluoromethylation of two hetero-PAHs, phenanthroline and phenanthridine, is discussed. The structure, solid-state packing, and electronic properties of the products are examined. Previously unknown structure-property relationships were established between the electronic properties and the position of CF_3 groups. Additionally, the synthesis and excited-state dynamics for a series of homoleptic copper(I) phenanthroline complexes with 2, 3, and 4 trifluoromethyl groups are reported. Surprisingly, the observed time-resolved dynamics and emission trend is that addition of trifluoromethyl groups past two decreases the excited state lifetime and increases excited-state distortion.

ACKNOWLEDGMENTS

iv

TABLE OF CONTENTS

LIST OF TABLES

LIST OF FIGURES

LIST OF SCHEMES

LIST OF ACRONYMS AND ABBREVIATIONS

ANTH	anthracene; $C_{14}H_{10}$ (see drawing on page 3 of introduction)
BHJ	bulk heterojunction
BnF	perflurobenzyl; $CF_2C_6F_6$
$C_{60}FHF$	C_{60} fauxhawk fullerene; $C_{60}(cyclo\text{-}CF_2(2\text{-}C_6F_4))$
CV	cyclic voltammetry
DCE	1,2-dichloroethane; $1,2\text{-}C_2H_4Cl_2$
DCM	dichloromethane, CH_2Cl_2
DMSO	dimethylsulfoxide
DFT	density functional theory
EA	gas-phase electron affinity
ETL	electron transport layer
equiv	equivalent or equivalents
FF	fill factor
FHF	C_{60} fauxhawk fullerene; $C_{60}(cyclo\text{-}CF_2(2\text{-}C_6F_4))$
GSB	ground state bleach
HOMO	highest occupied molecular orbital
HPLC	high-performance liquid chromatography
HTL	hole transport layer
IC	internal conversion
IE	gas-phase ionization energy
IPES	inverse photoelectron spectroscopy

ISC	intersystem crossing
ITO	indium tin oxide
J_{SC}	short circuit current
LMCT	ligand-to-metal charge transfer
LUMO	lowest unoccupied molecular orbital
MeCN	acetonitrile
MLCT	metal-to-ligand charge transfer
ESI-MS	electrospray ionization mass spectrometry (or spectrum)
NMP	N-methylpyrrolidone
NMR	nuclear magnetic resonance
OFET	organic field-effect transistor
OLED	organic light-emitting diode
OPV	organic photovoltaic
PAH	polycyclic aromatic hydrocarbon
PCE	power conversion efficiency
PES	photoelectron spectroscopy
PFAF	perfluoroalkylfullerene
phen	1,10-phenanthroline (see drawing on page 3 of introduction)
PHNZ	phenazine
PHRD	phenanthridine (see drawing on page 3 of introduction)
PHJ	planar heterojunction
RF	perfluoroalkyl
RT	room temperature

SC-XRD	single crystal X-ray diffraction
TDDFT	time-dependent density functional theory
TMF	trifluoromethylfullerene; $(C_{60}CF_3)_n$
TRMC	time-resolved microwave conductivity
UV-vis	ultraviolet-visible (spectroscopy)
V_{OC}	open circuit voltage
QY	quantum yield

INTRODUCTION: AUTHOR'S CONTRIBUTIONS AND MOTIVATION

The main focus of the author's dissertation research was a class of organic molecules with electron-withdrawing CF_3, CF_2, $CF_2C_6F_5$, and cyclo-CF_2(2-C_6F_4) groups. The research discussed in the dissertation includes the synthesis and purification and/or physicochemical characterization and/or use in organic electronic devices of polycyclic aromatic hydrocarbons (PAHs), hetero-PAHs, and fullerenes with one or more of these substituents. The overarching goal throughout this work is to determine structural, electrochemical, and photophysical properties of the materials. Understanding these structure-property relationships is essential to establishing trends and predicting usefulness and future performance for materials applications. Bond-line drawings of the PAHs, hetero-PAHs and fullerene substrates that were studied are shown in the figure on page 3. The abbreviations and acronyms used throughout this dissertation are listed on page xvi.

Chapter 1 describes the modified syntheses of multiple fluorinated fullerene acceptors as well as the fabrication and testing of vacuum deposited organic photovoltaic (OPV) and organic field effect transistors (OFETs). The fullerenes derivatives that were studied included multiple CF_3 substituents, a CF_2 substituent, or a cyclo-CF_2(2-C_6F_4) group. With the exception of $C_{60}CF_2$, the aforementioned fullerene derivatives have not been reported in OPV devices. OFET devices were made with $C_{60}CF_2$ and stability studies were conducted. In addition to fabricating OPV devices, correlations are made between gas-phase, solution-phase, and solid state electronic properties for perfluoroalkylfullerenes (PFAF) acceptors. The OPV work has been published in a paper with the author of this dissertation as the first of two graduate student co-authors.[1] The OFET research has been submitted for publication with the author of this dissertation as the second of two graduate student co-authors.

Chapter 2 describes optimization of the synthesis and isolation of 9,10-bis(perfluorobenzyl)anthracene via the direct perfluorobenzylation of 9,10-dibromoanthracene. This compound was originally synthesized and characterized by former Strauss Boltalina group member, Long K. San. The synthesis was improved by the author of this dissertation. A manuscript describing this work is in preparation.

Chapter 3 describes new phenanthroline (phen) compounds with three, four, or five CF_3 substituents. The initial reaction to produce $phen(CF_3)_n$ derivatives was performed by former graduate student Dr. Igor Kuvychko, while all of the compounds were isolated and characterized by the author. A new method, developed by the author, to target specific isomers of phen with three or four CF_3 substituents is also described. The $phen(CF_3)_n$ compounds were then studied by single crystal x-ray diffraction (SC-XRD) and cyclic voltammetry (CV). A manuscript describing this work with the author of this dissertation as the first author is in preparation. Finally, the synthesis of homoleptic copper(I) complexes with $phen(CF_3)_n$ is described. The resulting complexes were then studied via pump-probe transient absorption spectroscopy and density functional theory (DFT) by Dr. Maksim Livshits at the University of New Mexico. The results of this work were published with the author of this dissertation as the second author.[2]

Chapter 4 describes new phenanthridine (PHRD) compounds with three and four CF_3 substituents. The $PHRD(CF_3)_n$ derivatives were isolated and characterized by the author from the product mixtures from a high-temperature sealed ampoule reaction performed by former graduate student Dr. Igor V. Kuvychko. The compounds were then studied by SC-XRD and CV. A manuscript with the author of this dissertation as the first author is in preparation.

The PAHs and hetero-PAHs used in the research reported in this dissertation

anthracene (ANTH)

phenanthridine (PHRD)

1,10-phenanthroline (phen)
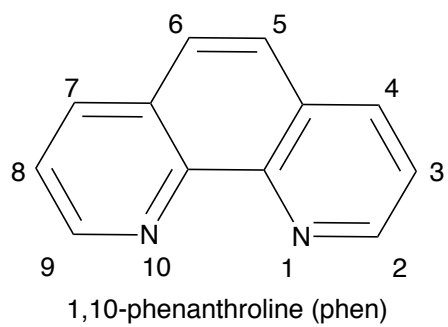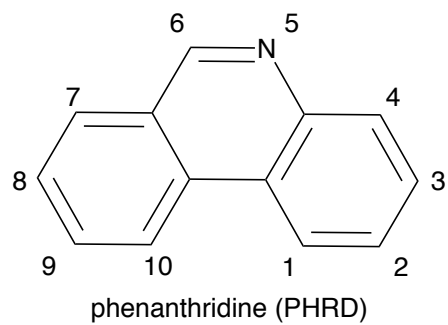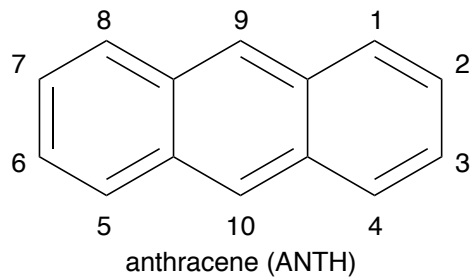
REFERENCES FOR INTRODUCTION

1.   Reeves, B. J.; Brook, C. P.; Gerdes, O.; Deng, S. H. M.; Yuan, Q.; Wang, X.-B.; Strauss, S. H.; Boltalina, O. V.; Walzer, K. Fluorous Fullerene Acceptors in Vacuum-Deposited Photovoltaic Cells. *Solar RRL* **2019**, *3*, 1900070.

2.   Livshits, M. Y.; Reeves, B. J.; DeWeerd, N. J.; Strauss, S. H.; Boltalina, O. V.; Rack, J. J. Trifluoromethylated Phenanthroline Ligands Reduce Excited-State Distortion in Homoleptic Copper(I) Complexes. *Inorg. Chem.* **2020**, *59*, 2781-2790.

CHAPTER 1. FLUOROUS FULLERENE ACCEPTORS IN VACUUM-DEPOSITED PHOTOVOLTAIC CELLS AND ORGANIC FIELD EFFECT TRANSISTORS

In this section, a series of fluorinated fullerenes acceptors are tested in organic photovoltaic (OPV) cells and organic field effect transistors (OFET). The structures and abbreviations of the fullerene acceptors are shown in **Figure 1.1**. Synthetic improvements and/or modifications are described for several fullerene acceptors. The OPV devices were prepared by the author of this dissertation at Heliatek, GmbH in Dresden, DE under the supervision of Dr. Karsten Walzer. The donor molecules were prepared by Dr. Olga Gerdes at Heliatek, GmbH. All fullerene acceptors were prepared by the author of this dissertation with the exception of 60-2-1. 60-2-1 was prepared by Strauss Boltalina lab group member Colin Brook. The OFET devices were prepared by graduate student Raj Krishnan in the laboratory of Prof. Björn Lüssem at Kent State University.

1.1   Introduction

OPV research has reached impressive milestones in the past decade, including improved performance of 10-13% power conversion efficiency (PCE) of vacuum processed multijunction OPV devices[1] and a remarkable 17.3% PCE tandem device produced recently by Meng et al.,[2] with the theoretically predicted limits of 25-33% yet to be achieved.[3] Continuous effort in fundamental understanding of the photophysics, material science, device physics, and engineering of OPVs has resulted in formulation of new research directions including the search for alternative donor and acceptor molecular and polymeric materials, morphology control, exploration of ternary compositions for active layers and others.

The first OPV cells were made using a double-layer architecture, frequently called planar heterojunctions (PHJ), or flat heterojunctions (FHJ), or bilayer architecture in which a thin layer of the acceptor material (e.g., perylene tetracarboxylic derivative in Tang's 1986 report) and a light-absorbing donor material (e.g., copper phthalocyanine) were deposited consecutively on the

In$_2$O$_3$-covered glass substrate via vacuum sublimation.[4] Later, fullerene C$_{60}$ was used as an acceptor in such PHJ-type devices, prompting the boost of OPV research in the early 1990s that resulted in the development of the now-dominating in research solution-processed bulk heterojunction (BHJ) OPVs.[5-7]

The relative simplicity of the PHJ-type cells, in which an active layer consists of three distinct phases (a bulk layer of donor, D, a bulk layer of acceptor, A, and D/A interface provides an outstanding platform for studying photoinduced charge generation in the D/A systems and effects on photovoltaic figures of merit. It is particularly invaluable when the comparisons between different active materials are desired, under strictly controlled conditions. Despite continuous efforts to understand, control, measure, and quantify morphology in solution-processed bulk heterojunction OPV devices, it remains challenging to de-convolute molecular structural and energetic effects on the macroscopic characteristics of the photovoltaic devices.[8-9] The lack of the protocol universally accepted in the OPV field makes such comparisons and analysis of the meta-data ever more difficult.[10]

In principle, one can prepare PHJ cells using solution-processing, but it proved difficult to create uniform D/A interfaces due to poor control of the surface of the spin-cast films, solubility issues, D/A intermixing and low stability of such devices.[11-12]

Fabrication of photovoltaic devices via vacuum deposition, on the other hand, can be done under strictly controlled anaerobic conditions, where the main processing variables include the rate of material deposition and the temperature of the substrate. It requires that both D and A materials possess high thermal stability and can be sublimed without degradation. A large number of thermally stable donor compounds, such as phthalocyanines, porphyrins and oligothiophenes have been reported as components of high-performing vacuum-deposited OPVs.[12] In contrast, only

a handful of acceptor materials have been employed, including parent fullerenes C_{60} and C_{70}, perfluorinated porphyrins, phthalocyanines and perylene tetracarboxylic derivatives.[12] The most common fullerene derivative acceptor, [6,6]-phenyl-C_{61}-butyric acid methyl acid (PC$_{60}$BM), as shown by us and others,[13-14] partially decomposes and isomerizes upon sublimation and thus is not suitable for vacuum deposition processing. When fluorinated functional groups are added to a fullerene, either via direct fluorination, as in fluorofullerenes, or via attachment of R_F groups in perfluoroalkylfullerenes, PFAFs, (where R_F is CF_3, C_nF_{2n+1} (*n*=2-12), or CF_2X), such derivatives possess high air, light, and thermal stability and can be sublimed without decomposition, and typically at much lower temperatures than parent fullerenes.[15]

Besides an outstanding thermal stability, several other distinct features of PFAFs make them particularly suitable for studies of fundamental aspects of OPV science. For many synthetically readily accessible PFAFs, molecular structures and solid-state packing are well-characterized by X-ray crystallography to allow for molecular-level insights into intermolecular interactions in the solid state and hence electronic coupling between acceptor molecules in polycrystalline films.[16] Members of PFAF families exhibit one of the widest ranges of electron acceptor strengths (whether quantified in electrochemical reduction potentials ($E_{1/2}$), in the gas-phase electron affinity (EA) or DFT-calculated lowest unoccupied molecular orbital (LUMO) energy (E_{LUMO}). In the case of fluorofullerenes, the electron affinity can vary from 2.7 eV ($C_{60}F_2$) to 4.3 eV ($C_{60}F_{48}$) and was found to correlate with degree of fluorination.[16] In the case of PFAFs, electronic properties are determined mainly by the addition patterns, i.e., positions of R_F groups on the cage, and to a lesser extent, by the number of R_F groups. Within the same composition, different isomers can span $E_{1/2}$ values over a wide range, e. g., 500 mV for $C_{60}(CF_3)_{10}$ isomers.[15,17]

Such variability in molecular energetics was utilized in the series of studies of the driving force in photoinduced charge carrier generation in the BHJ OPV active layers with selected PFAFs and polymeric donors or with single-wall carbon nanotubes by time-resolved microwave conductivity (TRMC) and ultra-fast transient absorption spectroscopy (fs-TAS) and time-resolved photoluminescence spectroscopy (TRPL) methods.[18-20] These studies indicated that PFAFs with 58- or 56-electron π-systems (i.e., bis- or tetrakis- PFAF derivatives) could be good candidates for high-performing OPVs due to efficient inter-fullerene electronic coupling and better frontier orbital overlaps with the typical donor materials. Local electron mobilities were estimated to be comparable to that of $PC_{60}BM$.

A recent comparative study of photostability of OPV active layers demonstrated that PFAF acceptors with higher electron-affinity values (i.e., above 2.8 eV) significantly slow down donor photooxidation rates in the active layers compared to $PC_{60}BM$ and other common acceptors.[21-22] In fact, it was shown that acceptors possessing a higher LUMO energy may accelerate photodegradation when compared to neat polymer films.[23] Finally, the presence of hydrophobic perfluoroalkyl groups R_F in PFAFs may result in improved resistance to humidity as was shown for perfluoroalkylated polycyclic aromatic hydrocarbons. These properties of PFAFs can be instrumental for improving the life-time of devices.

All these data inspired the current study that involves the use of the selected PFAFs in vacuum-deposited OPV cells. Here, several goals were set: (i) determine optimal conditions for vacuum sublimation of PFAFs and demonstrate the possibility of the preparation of working fullerene-derivative-based thin-film OPV cells via vacuum deposition; (ii) compare solid-state energetics in the series of PFAFs with varying gas-phase EA (and $E_{1/2}$) with that of C_{60}; (iii) using a prototypical model molecular donor counterpart, determine optimal OPV fabrication conditions

such as substrate temperature and active layer thickness within the cell architecture developed for C_{60}. In this study, there was not an intention to fully optimize these cells with respect to achieving highest possible OPV figures of merit but rather to explore, for the first time, how this rare class of sublimable fullerene derivatives with chemically similar fluorous substituents and widely tunable electronic properties behave in OPV cells prepared under strictly controlled vapor-deposition conditions. Of particular fundamental interest are the questions concerning correlations of gas-phase and solution-phase electronic properties of the PFAF acceptors with those in the solid-state; direct effects of variable acceptor molecular energetics on open circuit voltage (V_{OC}); effects of the device type (PHJ vs BHJ) on the V_{OC} values for the same active layer compositions and, finally, identify factors that influence fill factor (FF) in such devices and hence assess the feasibility of mitigating absorbance/FF trade-offs in these systems[3] and building thicker devices and multijunction cells in the future.

1.2   Molecular Donor Properties

Dicyanovinyl oligothiophenes have been successfully used as donors paired with C_{60} in OPV devices.[24-27] More specifically, dicyanovinyl quaterthiophene derivatives yield higher V_{OC} compared to the pentamers and hexamers.[27] It has been shown that substituting hydrogens on the 1st and 4th thiophenes with ethyl substituents (**Figure 1.2**, left) on dicyanovinyl quaterthiophene derivatives leads to molecules aligning themselves in a nearly flat orientation with reference to the substrate. This allows for very strong light absorption which should lead to high short circuit current (J_{SC}) values.[28] Furthermore, isostructural methyl substituted quaterthiophenes have been shown to have higher current and FF compared to ethyl and non-substituted quaterthiophenes in the C_{60}-based OPVs .[24]

A comparative X-ray structure analysis of those compounds showed that the methyl substituents allow for a very high degree of intermolecular connectivity through weak hydrogen bond interactions as well as excellent π-π interaction in comparison to ethyl and non-substituted derivatives.[24] Fitzner et al. hypothesized that these structural features allowed for better electronic coupling between molecules and improved charge transport.[24]

The donor used in this study, DCV4T-Me[14], is a dicyanovinyl capped quaterthiophene with methyl substituents on the 1st and 4th thiophene units (**Figure 1.2**, right). The DFT-calculated HOMO and LUMO levels for DCV4T- Me[14] are −5.31 eV and −4.09 eV, respectively. As reported previously, one of the widely accepted guidelines in fullerene OPV material design to provide an optimal driving force for charge separation states that the matching acceptor and donor should have LUMO energy offset at approximately 300 meV. This condition is satisfied by nearly all PFAF acceptors used in this study.

1.3   Synthetic Modifications and Improvements for Fluorous Fullerene Acceptors

Before devices were fabricated, it was necessary to modify the syntheses and purification methods for some of the fullerene derivatives. To make a series of devices, 50 to 100 mg of a material is desirable. In some cases, modifications were made in an effort to improve the yield or purification process. In other cases, synthetic modifications were made to improve safety.

1.3.1   Investigation and Improvement of 1,9-C_{60}(*cyclo*-CF_2(2-C_6F_4)) (C_{60}FHF) Synthesis

1,9-C_{60}(*cyclo*-CF_2(2-C_6F_4)) (C_{60}FHF) was originally reported by our group.[29] The original synthesis utilizes a two-step reaction, as shown in **Scheme 1.1**. In this synthesis, a hydrofullerene precursor, is synthesized by a reaction of perfluorobenzyl iodide (Bn_FI) (8 equiv), tributyltin hydride (4 equiv), and C_{60}, followed by isolation via HPLC. A reaction of the hydrofullerene precursor and the organic base, proton sponge, leads to the final product C_{60}FHF, after a second

stage of HPLC separation. It was also reported that can be synthesized in a single step reaction, albeit with a low yield of 7%. These conditions lead to difficulty in producing large amounts of $C_{60}FHF$ for using in devices.

It was later determined that excess pyridine could be used as the organic base and that this reaction could be completed in a one-pot reaction with only 1.1 equivalents of Bn_FI and tributyltin hydride. The use of 1.1 equivalents of Bn_FI and tributyltin hydride significantly improves selectivity, which in turn improves purification. The addition of pyridine to the reaction mixture leads to the deprotonation of the hydrofullerene precursor *in situ*. This allowed for one stage HPLC purification and led to a significantly improved 22% isolated yield.[30] In this reaction by DeWeerd, C_{60}, tributyltin hydride, Bn_FI, and pyridine were heated together in a sealed Kontes flask for 16 h. It was hypothesized by the author of this dissertation that the organic base should be added after the hydrofullerene was allowed to form, rather than adding it with the rest of the reagents as described in **Scheme 1.2**. To do this, a Schlenk flask with a rubber septum was utilized instead of a Kontes flask, so that anhydrous, deoxygenated pyridine could be added via syringe while the reaction mixture was still being heated.

The first reaction (**Figure 1.3**, red trace), in which pyridine was added after 2 h, followed by heating for 1 h, led to a 29% isolated yield. In the second reaction (**Figure 1.3**, black trace), it was determined that increasing the C_{60} concentration from 2.8 mM to 5.6 mM leads to improved conversion of C_{60} to $C_{60}FHF$, with a similar amount of multiple addition products. This allowed for an isolated yield of 37%. Finally, in a third reaction (**Figure 1.3**, green trace), it was hypothesized that adding the Bn_FI and tributyltin hydride to the solution after the C_{60} had been heated would essentially prime the C_{60} to react with the Bn_FI and tributyltin hydride to prevent multiple addition compounds. This did not prove to be the case, as a similar amount of C_{60} was

converted and a similar amount of multiple addition compounds were produced. Additionally, it was found that injecting Bn_FI and tributyltin hydride into a hot solution of C_{60} did not impact the yield. The yield of 37% allows for approximately 100 mg of $C_{60}FHF$ to be produced in a single reaction from 200 mg of C_{60}.

1.3.2   Investigation and Improvement of $C_{60}CF_2$ Synthesis

Sidorov et al. initially reported the synthesis of $C_{60}CF_2$.[31] In this reaction, sodium chlorodifluoroacetate is heated to reflux with C_{60} in o-DCB in the presence of a phase transfer catalyst. The chlorodifluoroacetate undergoes thermal decomposition to produce a CF_2 carbene, sodium chloride, and carbon dioxide. The CF_2 carbene then undergoes insertion into the C_{60} cage to produce the fullerene derivative $C_{60}CF_2$. The best reaction reported by Sidorov et al. resulted in a 18% isolated yield of $C_{60}CF_2$ after reflux for 1 h.

Previous Strauss-Boltalina group member, Dr. Bryon Larson, found that using the phase transfer catalyst 15-crown-5 instead of 18-crown-6 lead to a higher conversion of C_{60} and a higher yield based on the HPLC chromatogram.[32] This result was expected since 15-crown-5 is more selective for the Na^+ ion (resulting from sodium chlorodifluoroacetate), while 18-crown-5 would be selective for K^+ ions.

The reaction was studied by the author of this dissertation using fullerene extract in a sealed Schlenk tube, while changing the reaction times. 15-crown-5 was used as the phase transfer catalyst since Larson had showed higher conversion of C_{60} compared to reactions in which 18-crown-6 was used. It was determined that increasing reaction time from 1 h to 3 h improves conversion of C_{60} to $C_{60}CF_2$ (measured by HPLC), as shown in **Figure 1.4**. A 3 h reaction performed using C_{60} instead of fullerene extract led to a 29% isolated yield of $C_{60}CF_2$.

1.3.3 Improvement of $S6$-$C_{60}(CF_3)_{12}$ (60-12-1) Synthesis

The synthesis of 60-12-1 was reported by Troyanov et al. and later by Sidorov et al.[33-34] In the reported syntheses, a three-section, sealed glass ampoule is utilized. The first section, containing C_{60}, is placed in the reaction zone (T=693 K). The second section, the condensation zone (T=573K to 523K), allowed for collection of the volatile trifluoromethylated products. The third section (room temperature) contained liquid CF_3I (at a pressure of ca. 506.6 kPa or 5 atm). This high pressure is generally considered unsafe for sealed glass ampoules, which are typically used at pressures of less than 2 atm.

To make this synthesis safer, a stainless-steel reactor was designed (**Figure 1.5**). The design was based on the reactor designed by Strauss Boltalina Research Group members Dr. Eric Bukovsky and Dr. Nicholas Deweerd.[35] The reactor was modified by the author of this dissertation to include a cold finger for condensing CF_3I gas and a glass liner for collection of volatile trifluoromethylated products. The steel in this reactor is able to withstand extreme pressures of 680 atm, although that is not necessary for this synthesis. When this reactor was used, 60-12-1 was synthesized in yields up to 43%. While this is not as high as the yield reported by Sidorov et al. (78%), it is significantly safer while still producing enough material to test devices.

1.4 Fluorous Fullerene Acceptor Properties

Figure 1.1 shows a gallery of PFAF acceptors selected for this study. They can be divided in two groups by the type of functionalization. The first group consists of monocycloadducts: $C_{60}FHF$ has a five-membered carbocycle attached to the 6,6 junction on the core, and the second compound $C_{60}CF_2$ has a three-membered cycle attached to the 6,6 junction, as shown in **Figure 1.1**. Significantly, such simple cycloaddition patterns along 6,6 junctions result in the least distortion of the conjugated π-system of the fullerene (albeit reduced from 60- to 58- π-electron system),

which is manifested in the similarity of their absorption spectra with that of underivatized C_{60} (Appendix 1 Figures A1.12, A1.13, and A1.14). For both compounds, good-yield selective synthetic procedures were developed, and their electrochemical properties are known. $C_{60}FHF$ has the same $E_{1/2}$ value as C_{60}, whereas the $E_{1/2}$ of $C_{60}CF_2$ is 150 mV more positive than that of C_{60}.

The second group of acceptors consists of trifluoromethylfullerenes (TMFs), $C_{60}(CF_3)_{2n}$, which are formed by additions of pairs of CF_3 groups in *para*-positions of the same hexagon on the core. This type of addition introduces a double bond in a pentagon in the case of $C_{60}(CF_3)_2$. Upon further CF_3 additions, ribbons of edge-sharing hexagons $C_{60}(CF_3)_2$ are typically formed, as shown on the Schlegel diagrams for the selected TMFs in **Figure 1.1**. These compounds were chosen so that a wide compositional range (from 2 to 12 CF_3 groups), and a wide range of acceptor strength ($E_{1/2}$ spanning nearly 500 mV, from -160 to $+330$ mV vs $C_{60}^{-/0}$)[17,29,36-37] could be studied in OPV cells.

1.4.1   Thermal Properties

Fluorine-fluorine intermolecular interactions are known to be weaker than hydrogen bonding or π-π interactions in solids.[38] This is manifested in the higher volatility of fluorinated compounds compared to hydrocarbon counterparts. For example, highly fluorinated fullerenes have lower sublimation enthalpies and sublimation temperatures than C_{60}.[39] Vapor deposition study of fluorous fullerene acceptors in this work (Appendix 1 Table A1.1) has demonstrated a similar trend in the sublimation temperatures, with one exception. As the number of CF_3 groups per cage increases, the TMFs become more volatile and sublime at lower temperatures. In particular, for the evaporation rate at 0.2 Å/s (under ultra-vacuum at a base pressure of 10^{-7} mbar) the sublimation temperature of 450 °C is measured for un-derivatized C_{60}, it is 360 °C for 60-2-1, while for 60-8-1 it is only 200 °C.

Interestingly, this tendency, i.e., correlation between number of fluorine atoms per cage and sublimation temperature is not universal. For example, the anomalously high sublimation temperature of 635 °C for $C_{60}CF_2$ (even higher than that of C_{60}) was not anticipated and needs further investigation, including determination of molecular packing via X-ray crystallography.

1.4.2 Electronic properties

Electrochemical properties of all selected TMFs were studied previously (**Figure 1.1** for $E_{1/2}$ values vs. $C_{60}^{-/0}$), whereas gas-phase electron affinity values were known only for three TMFs. In this work, electron affinities of $C_{60}CF_2$ and 60-8-1 measured by low-temperature photoelectron spectroscopy, are reported. The TMF 60-8-1 is the strongest acceptor in the series, according to the cyclic voltammetry data (**Figure 1.1**), and the newly measured EA value of 3.27 (0.02) eV confirms it to be true in the gas phase as well.

The EA value of 2.88(0.05) eV for $C_{60}CF_2$ (**Figure 1.6**) is higher than the EAs of C_{60} and $C_{60}FHF$ acceptors. **Figure 1.7** presents plots of $E_{1/2}$ values and DFT-derived E_{LUMO} vs gas-phase EA data obtained in this work and taken from the literature.[40-42] Linear correlations are observed on both graphs, however, the slope for the $E_{1/2}$ vs EA plot deviates from 1 significantly. This implies that electron acceptor strength in the condensed phase (i.e., when molecules are surrounded by solvent molecules) is considerably attenuated in this series, with the slope of 0.56, in accord with decreasing solvation energies in the series from C_{60} to 60-12-1.[17]

Previously, the Strauss Boltalina Research Group reported a similar, but weaker, attenuation effect was observed for the series of $C_{60}(R_F)_2$ (where $R_F = C_nF_{2n-1}$, $n = 1$-8) and it was explained by the opposite trends in the solvation energies and gas-phase electron affinities with the increasing size of the perfluoroalkyl chains. The solid-state EAs (e.g., by inverse photoelectron spectroscopy (IPES) or photoelectron spectroscopy (PES) methods) are not known for TMFs, and

it is difficult to predict whether attenuation of acceptor strength in the solid films made of the pure acceptors will be weaker or stronger than in solution.

While measuring solid-state EA values (e.g., using IPES method) for these compounds would be desirable, (but not accessible currently) their usefulness for detailed quantitative analysis of OPV figures of merit will still be limited. It has been demonstrated (both experimentally and theoretically)[3,43] that it is the molecular energetics at the heterojunctions that is relevant to V_{OC} (it determines energy of "charge transfer" state, E_{ct}), and not molecular energetics of the bulk pristine D and A films. Therefore, solid-state energetics of the fluorous acceptors is first probed experimentally in the thin films in the reference OPV devices as described below.

1.5 Reference Photovoltaic Cells

The reference cell architecture was adopted from the C_{60}-based planar heterojunction OPV cell structure (choice of electrodes, hole transport layer (HTL) material and p-doped HTL layer), in which a colored donor layer was absent (**Figure 1.8**, cell type R), such that the HTL/C_{60} interface defines the donor-acceptor interface. A layer of the fullerene derivative (10 nm) was deposited onto glass coated with indium tin oxide (ITO). The HTL material 9,9-bis[4-(N,N-bis-biphenyl-4-yl-amino)phenyl]-9H-fluorene (BPAPF) (10 nm) was then deposited. A 50 nm layer of p-doped BPAPF (NDP9 as p-dopant) was then deposited. A 1-nm layer of NDP9 was deposited to facilitate charge extraction. Finally, aluminum (100 nm) was deposited as the top electrode. This type of stack architecture is shown in **Figure 1.8**, left, along with a representative *J-V* curve. In the absence of a strongly absorbing donor, excitons are predominantly generated by absorption at the fullerene acceptor layer (the absorbance from transparent HTL, BPAPF, is negligible and can be ignored). Exciton diffusion to the interface of the acceptor and BPAPF results in the charge separation and charge transport. **Table 1.1** shows the J_{SC}, FF, V_{OC} and the difference in V_{OC} versus C_{60} (ΔV_{OC})

measured in cells R1 through R8 for each of the fullerene derivatives. Absence of the strongly absorbing donor in such cells allows for direct comparison of the acceptor thin film properties. In particular, the measured V_{OC} has been used to estimate the energetic shift (or shift in LUMO) for each derivative versus C_{60}, denoted as ΔV_{OC} in **Table 1.1**. Unexpectedly, a stronger linear correlation (with the slope of 0.8) between ΔV_{OC} and gas-phase EA_g was found than between $E_{1/2}$ and ΔV_{OC} for TMFs (**Figure 1.9**). So, it appears that gas-phase EA is a more accurate estimate for solid-state EA of fluorous acceptors than the cyclic voltammetry-derived $E_{1/2}$.

The ΔV_{OC} value measured for the monoadduct $C_{60}CF_2$ does not follow the observed linear trend, and the total outlier is 60-12-1, which showed V_{OC} much lower than expected according to its $E_{1/2}$ value, i.e., 160 mV less positive than that of C_{60} (**Table 1.1** and Appendix 1 Table A1.3). Neither of the highly trifluoromethylated fullerenes, 60-8-1 or 60-12-1 yielded any measurable current. This suggests that either their LUMO levels are too deep for the given device architecture and charge extraction was not possible, or presence of multiple CF_3 groups on the cage has an insulating effect and results in poor charge transport.

The latter is in agreement with the earlier findings on the decreased electron mobilities of several isomers of $C_{60}(CF_3)_{8,10}$ as estimated from TRMC study of BHJ films with P3HT.[20] Four other acceptors yielded J_{SC} values of 0.7-1.0 mA/cm^2, which is only half of that of the C_{60} cell, and the range of FF values from 48 to 65%, slightly lower than that of C_{60}. In further studies, acceptors 60-8-1 and 60-12-1 were not used because of the inferior characteristics, whereas 60-2-1, 60-4-1 and $C_{60}CF_2$ were used to fabricate PHJ and BHJ cells as described below.

1.6   OPV Device Optimization with $C_{60}CF_2$ Acceptor

Once solid-state energetics of the fluorous acceptors had been established via the reference devices, the donor 1,4-dimethyl(dicyanovinylquaterthiophene) DCV4T-Me[14] was chosen for OPV

studies. Initial optimization was performed using $C_{60}CF_2$. $C_{60}CF_2$ can be prepared in gram quantities using a highly selective reaction and inexpensive reagents, and can be easily purified. It has a prominent CV-derived LUMO shift of 150 mV vs C_{60} (and even larger V_{OC} shift of 330 mV in R type cell vs C_{60}) allowing for observable energetic effects. Finally, $C_{60}CF_2$ also has the smallest fluorous substituent attached to the core, so that intermolecular contacts are not impeded by the bulky functional groups as in other acceptors, in line with its high sublimation temperature.

First, PHJ devices P3 and P4 were made with DCV4T-Me[14] as a donor and $C_{60}CF_2$ as an acceptor (**Figure 1.8**, middle and **Table 1.2**). In the cell P4, a thicker donor layer (10 nm) was used compared to the cell P3, in which a 6 nm donor layer was used. Analogous cells (**Table 1.2**, P1 and P2), were made with C_{60} for comparison purposes.

Comparison of the OPV figures of merit in cells P1-P4 shows that the difference in V_{OC} of 0.23-0.25 V between C_{60} and $C_{60}CF_2$ cells reflects the difference in the LUMO levels of these acceptors (**Table 1.2**), however, it is smaller than the difference in V_{OC} observed in R type cells with these acceptors (cf. R1 and R5, **Table 1.1**). Lower J_{SC} and FF values for $C_{60}CF_2$ cells than for C_{60} cells are in qualitative agreement with the results obtained for R type cells. BHJ devices were made to determine if changes in the device structure and morphology would improve the performance of devices with $C_{60}CF_2$ (**Figure 1.8**, right, and **Table 1.3**). In the initial device testing, the BHJ layer was deposited onto a room temperature substrate (B1 and B2 cells). This resulted in a low V_{OC} of 0.81 V and very low FF values. Increase of the active layer thickness was accompanied by a decrease in J_{SC}, which is regarded as a sign of poor exciton or charge transport, or fast recombination. In some cases, this issue is associated with film morphology and can be improved by changing the substrate temperature during BHJ deposition.

Deposition of active layers at the substrate temperature 50 °C in cells B7 and B8 yielded significant improvements in all figures of merit. In particular, J_{SC} values doubled compared to the cells fabricated at room temperature. Noteworthy, cell B8 with a thicker active layer showed a higher J_{SC} than that in cell B7, as one will expect for increasing absorber layer thickness. Introducing a thin layer of C_{60} between ITO and active layer had some positive effects on FF and J_{SC} values in a thinner cell B3 compared to cell B7 (where $C_{60}CF_2$ was used as electron transport layer), but not in a thicker cell B4 compared to B8. To further probe the temperature effect, cells B5 and B6 were fabricated using substrate temperature of 70 °C, while keeping the same cell structure as in cells B3 and B4. This resulted in a decrease in J_{SC} and V_{OC} compared to cells B3 and B4, while FF remained almost identical. The decrease in J_{SC} and V_{OC} can be attributed to the observed crystallization due to the higher substrate temperature.

The best device for $C_{60}CF_2$ was cell B8, with PCE of 2.3 %. In this device, the fullerene layer between BHJ layer and ITO was $C_{60}CF_2$ (instead of C_{60}) and the BHJ layer was deposited at 50 °C. The V_{OC} was 0.92 V and J_{SC} increased to 6.1 mA/cm^2 from 4.7 in cell B4. This improvement in J_{SC} can be tentatively attributed to the lack of energetic barrier for transport at the C_{60}/ $C_{60}CF_2$ interface. Notably, a thicker device (cell B8) had higher current than the thinner cell with the same architecture (cell B7). The only OPV data in the literature involving $C_{60}CF_2$ as an acceptor (in a blend with P3HT fabricated using solution processing) reported a PCE of 0.1% (J_{SC} of 1.56 mA cm^{-2}, V_{OC} of 0.25 V and FF of 37.4 %).[37]

Figure 1.10 illustrates dramatic changes in the $\Delta V_{OC} = V_{OC}(C_{60}\text{-cell}) - V_{OC}(C_{60}CF_2\text{-cell})$ for different types of $C_{60}CF_2$-based cells studied in this work. Identical reference devices, PHJ, and BHJ were also made with C_{60} allowing direct comparisons of their figures of merit. The largest ΔV_{OC} value is obtained in the reference cells. It is larger than the molecular energetics differences

(E_{LUMO} or $E_{1/2}$) between the two acceptors. In the PHJ devices ΔV_{OC} is lower by 100 mV, and the drastic decrease is observed in the BHJ cells: ΔV_{OC} value is close to zero, which means that the $C_{60}CF_2$-based BHJ cell has as high V_{OC} as C_{60} (0.93 V). Thus, direct comparison of the PHJ and BHJ devices with the same components provides a striking example of modulation of OPV characteristics by changing the active layer from bilayer to the D/A blend. We also observe a significant impact of substrate temperature on V_{OC} in BHJ devices: in going from RT to 50 °C, a 100-mV increase was noted for $C_{60}CF_2$ cells (cells B1 and B7), which points to considerable morphological changes upon thermal treatment. The family of DCVnT donors was shown to be prone to considerable morphological changes in the blends with C_{60} when substrate temperature varies, and these changes can be either beneficial to the device performance or detrimental by causing too large phase segregation.[44] A detailed study of PHJ and BHJ devices based on C_{60} and donor rubrene showed the strong impact of the crystallinity of the donor phase on V_{OC}, which was correlated with the existence of different CT state energetics.[45]

1.7 BHJ Devices with TMFs

Once optimization using $C_{60}CF_2$ had been completed, BHJ devices based on the B8 cell were made with 60-2-1, 60-4-1, and C_{60} for comparison. **Table 1.4** contains OPV characteristics of the BHJ devices with TMFs. The lowest voltage was observed in the 60-4-1 cells as might be expected because of the deeper LUMO compared to 60-2-1. It also has the lowest FF and J_{SC} of all BHJ devices. In a thicker cell, B14, no significant improvement in J_{SC} was observed, while FF decreased significantly.

The device with 60-2-1 had a high J_{SC} value comparable to the equivalent C_{60} and $C_{60}CF_2$ devices. FF was improved significantly compared to the $C_{60}CF_2$ device, but V_{OC} was lower than

both the C_{60} and the $C_{60}CF_2$ devices. In the reference devices (**Table 1.1**), 60-2-1 had V_{OC} value between C_{60} and $C_{60}CF_2$ and followed the acceptor strength trend.

Noteworthy, in the thicker (20-nm BHJ) 60-2-1 cell, B12, the FF value maintained at 96% of FF in the thinner cell (10-nm BHJ), B11. In contrast, in the analogous C_{60} cells, only 83 % FF was maintained in the thicker cell. This may open an opportunity to improve the performance of the 60-2-1 cells in the future studies by gradually increasing the thickness of the active layer to increase the current, while maintaining high FF value. The absorbance/FF trade-off has been identified among one of the major limiting factors for OPV performance.[3] When the thickness of the active layer is increased in an attempt to improve absorbance and J_{SC}, a drastic drop in FF value leads to inferior device performance, as documented in numerous studies.[46-49]

1.8   Devices with 60-2-1 and Fluorinated Donor

Finally, BHJ devices with 60-2-1 and DCV5T-F_2(3,3)-Me_4(2,2,4,4) (**Figure 1.11**) as the active layer were made (cells B17-B20). The device architecture is shown in **Figure 1.12**. DCV5T-F_2(3,3)-Me_4(2,2,4,4) and 60-2-1 have a larger ΔLUMO when compared to DCV4T-Me[14] (0.6 eV vs 0.5 eV) (Appendix 1 Tables A1.2 and A1.3). Based on the previous devices, it was predicted that this higher driving force for charge separation would lead to large FF and a very minimal decrease when making thicker devices. In fact, when comparing cells B19 and B20 in **Table 1.5**, there was not a drop in FF. Interestingly, both devices have significantly higher V_{OC} than predicted by the difference in HOMO and LUMO of the donor and acceptor, respectively. This allowed for PCEs of 3.5 and 3.8 % in cells B17 and B18. These devices are especially good when considering that these are largely unoptimized devices; however, these devices do not outperform the voltage and resulting PCE of the C_{60} devices (B19 and B20). The only optimization condition tested was

21

the temperature of the substrate during deposition of the BHJ layer, where it was found that deposition at 50 °C leads to better FF, V_{OC}, and J_{SC} than deposition at 70 °C.

Interestingly, PHJ devices with 60-2-1:DCV5T-F$_2$(3,3)-Me$_4$(2,2,4,4) (**Table 1.6**) do not follow the same trend as PHJ devices with $C_{60}CF_2$: DCV4T-Me[14] in regard to the attenuation of ΔV_{OC} compared to reference devices and BHJ devices. This effect is not well understood, but it implies that this donor simply is not matched well for 60-2-1 morphologically or that more optimization must be done to make a device with improved morphology.

1.9   Organic Field Effect Transistors (OFETs)

In addition to OPVs, fullerenes and fullerene derivatives have been used extensively as n-type materials in OFETs. With the discovery of new organic semiconductors, OFETs have seen significant improvement in switching speed and overall performance. However, this progress has largely been limited to p-type OFETs, while the development of n-type OFETs has been stagnant. In order to make desirable complimentary circuits with p-type and n-type transistors, it is necessary to improve the reliability and performance of n-type transistors.[50]

Fullerenes and fullerene derivatives have been explored extensively as n-type materials in OFETs, with C_{60} being the most commonly used material.[51] In C_{60} based devices, charge carrier mobilities ranging from 0.1–1 cm^2 V^{-1} s^{-1} are achieved regularly.[51] In addition, mobility up to 5 cm^2 V^{-1} s^{-1} was achieved with aligned C_{60} single crystal needles and ribbons.[52] The success of C_{60} devices have inspired the synthesis and testing of a large number of C_{60} derivatives.[53] Of the 88 fullerene derivatives discussed in the review by Zhang et al.,[53] none of the fullerene derivatives that were tested had a maximum mobility higher than 0.5   cm^2 V^{-1} s^{-1} and only one fullerene derivative had a maximum mobility higher than 0.3 cm^2 V^{-1} s^{-1}.

Additionally, many fullerene derivatives cannot be sublimed to make pristine solvent-free devices, which limits the device processing techniques that can be used. In some cases, such as PCBM, the fullerene derivative decomposes during the deposition process.[13] The Strauss Boltalina Group in collaboration with the Lüssem Group at Kent State University, recently reported n-type OFET devices with average electron mobility of 0.34 $cm^2 V^{-1} s^{-1}$ based on $C_{60}FHF$.

While fullerene derivatives do not exhibit mobilities as high as pristine C_{60} in n-type OFET devices, C_{60} based OFETs tend to degrade quickly when exposed to air and moisture. Trap states are generated in the C_{60} lattice when oxygen is present, which prevent efficient electron transport. As oxygen penetrates the lattice of nanostructured C_{60}, the conductivity decreases significantly.[54]

It is necessary to develop high performance n-type materials that are also stable to air and moisture. When developing new n-type electron transport materials, the following considerations must be taken into account for high performance and stability: 1) The electron transport material should have a large number of π-bonds and short inter-fullerene cage to cage distances to improve π-π contact and mobility.[53] Addition of functional groups to a fullerene will disrupt the π-system, and larger substituents typically increase the inter-fullerene cage distances, which can have an insulating effect. Thus, it is desirable to have a small number of substituents that have minimal steric bulk; 2) A lower-lying LUMO is necessary to alleviate the likelihood of reaction between the electron carrier and water or oxygen; 3) The LUMO must align with the Fermi level of the electrode; 4) The adiabatic electron affinity should be large; 5) Thermal stability is desirable so that the molecule can be deposited via sublimation without degradation.

$C_{60}CF_2$ is a fullerene derivative that meets all of these requirements. It was shown above that $C_{60}CF_2$ can be substituted for C_{60} as the fullerene acceptor in organic photovoltaic (OPV) devices to achieve a power conversion efficiency (PCE) of 2.27 %. $C_{60}CF_2$ has a CV-derived

LUMO shift of 150 mV vs C_{60}[15] and a gas phase electron affinity (EA_g) of 2.88 eV. In the bilayer

OPV reference devices, in which an absorbing donor layer was absent, there was an even larger

330 mV shift in V_{OC}. This suggests that there is a larger difference in LUMO between C_{60} and

$C_{60}CF_2$ in the solid state, which will be accounted for in OFET devices. Additionally, the slight

distortion from the C_{60} shape allows for the formation of a dipole moment, which could lead to

improved electron transport.[36] It exhibits high thermal stability and can be sublimed without

decomposition. N-type OFET devices are reported with $C_{60}CF_2$ as the electron transport material

with an average mobility of $\mu = 0.83 \pm 0.52 \text{ cm}^2\text{V}^{-1}\text{s}^{-1}$ and significantly enhanced air and

moisture stability compared to equivalent C_{60} based devices. Although the mobility is lower than

that of optimized C_{60} transistors ($\mu = 2.26 \pm 0.81 \text{ cm}^2\text{V}^{-1}\text{s}^{-1}$) right after processing, $C_{60}CF_2$

OFETs outperform C_{60} OFETs by an order of magnitude after prolonged exposure to ambient air.

Overall, a mobility of $\mu = 0.14 \pm 0.13 \text{ cm}^2\text{V}^{-1}\text{s}^{-1}$ is observed after 36h of exposure.

1.9.1 $C_{60}CF_2$ vs C_{60} based OFET Devices

The general device architecture for the OFET devices is shown in **Figure 1.13**. The average

mobility of the devices for different dopant layer thickness is shown in **Figure 1.14.** In general,

C_{60} devices have a higher mobility compared to $C_{60}CF_2$ devices. Among the $C_{60}CF_2$ devices, the

ones with gold injection layer show the best mobility. The average mobility of C_{60} OFETs with

gold contacts and without dopant layer is $\mu = 2.26 \pm 0.81 \text{ cm}^2\text{V}^{-1}\text{s}^{-1}$. The average mobility for

$C_{60}CF_2$ OFETs with gold contacts and without dopant layer is $\mu = 0.83 \pm 0.52 \text{ cm}^2\text{V}^{-1}\text{s}^{-1}$,

which is still amongst the best performance for functionalized fullerenes.[13] Some devices even

have mobility as high as $\mu = 2.02 \text{ cm}^2\text{V}^{-1}\text{s}^{-1}$, however this result has to be seen as a statistical

outlier. Similar $C_{60}CF_2$ OFETs with doped n-type injection layer have average mobilities of $\mu =$

$0.38 \pm 0.13 \text{ cm}^2\text{V}^{-1}\text{s}^{-1}$ and $\mu = 0.27 \pm 0.06 \text{ cm}^2\text{V}^{-1}\text{s}^{-1}$ for doped n-type contacts with

doping concentrations of 4 weight % and 8 weight % respectively. Based on the mobility data, it appears that gold is best suited for optimal performance in $C_{60}CF_2$ OFETs.

1.9.2 $C_{60}CF_2$ OFET Device Stability

$C_{60}CF_2$ should exhibit enhanced air stability compared to C_{60}. To study the relative air-stability of C_{60} and $C_{60}CF_2$ OFETs, devices with gold injection layer and without dopant layer were chosen to focus on effects that occur due to the organic semiconductor layer or at the OSC/dielectric interface. C_{60} and $C_{60}CF_2$ samples with gold contacts (12 OFETs each) were taken out of the glovebox and exposed to air for a specific amount of time. The samples were then measured in the glovebox and the process is repeated for a total of 60 h. The C_{60} OFETs degrade at a much faster rate compared to the $C_{60}CF_2$ OFETs as shown in **Figure 1.15** and **Figure 1.16**. When comparing the transfer characteristics, the C_{60} devices noticeably degrade after 8 h indicated by the large hysteresis (**Figure 1.15** C), while the $C_{60}CF_2$ devices show minimal degradation after 36 h (**Figure 1.15** D). C_{60} OFETs show a mobility drop from $\mu = 2.26 \pm 0.81\ cm^2V^{-1}s^{-1}$ to $\mu = 0.016 \pm 0.013\ cm^2V^{-1}s^{-1}$. Meanwhile, the $C_{60}CF_2$ devices mobility drops from $\mu = 0.83 \pm 0.52\ cm^2V^{-1}s^{-1}$ to $\mu = 0.14 \pm 0.13\ cm^2V^{-1}s^{-1}$, which confirms the hypothesis of greater air stability for $C_{60}CF_2$ devices.

1.10 Conclusions and Outlook

Presented here are the first results of OPV cells prepared by high-vacuum deposition composed of fluorous fullerene acceptors and the molecular donors DCV4T-Me[14] and DCV5T-F$_2$(3,3)-Me$_4$(2,2,4,4). It is demonstrated that these acceptors possess remarkable thermal stability and can be safely sublimed as thin films. This finding is important not only for further studies of these materials in organic photovoltaics, but also because it opens the opportunity to apply vacuum sublimation as highly efficient re-purification technique. While HPLC methods have been

successfully applied for isolation and purification of these materials, and purity of 98+% is readily achievable, the organic solvent entrapment in the solid samples is quite possible, especially if the high-boiling point solvents (*o*-dichlorobenzene, chlorobenzene) are used for HPLC processing.

As shown previously for parent fullerenes C_{60} and C_{70}, residual solvent can lead to partial degradation of fullerenes (up to 20% of the sample) upon thermal heating, whereas fullerenes purified via vacuum sublimation do not exhibit degradation when heated. Furthermore, presence of the solvent molecules (which is difficult to quantify) in the solid samples of fullerenes affect their morphology in unpredictable ways, and thus charge transport properties can be diminished. For example, thin films of C_{60} grown via vacuum deposition have higher electron mobility than thin films made via solution processing. Some of the compounds studied in this work show good transport properties, comparable to C_{60} (in reference devices) and it is therefore of interest to study more of these fullerene derivatives, for example, in OFETs fabricated via vacuum sublimation. Another important advantage is that their sublimation temperatures are generally much lower than that of parent fullerenes making the fabrication process energy-efficient.

Comparison of electronic properties in gas-phase, solution and solid-state (via V_{oc} in reference cells) revealed that within the series of homologue trifluoromethyl derivatives excellent linear correlations were observed. Unusually, the strongest linear correlation is found between gas-phase electron affinity and V_{oc}, whereas the correlation of V_{oc} with $E_{1/2}$ was weaker. Future IPES measurements of EAs of solid films of these materials will help validate the approach used here to probe the acceptor energetics in the reference cells.

From a practical point of view, the most promising acceptor is 60-2-1 which showed the best performing device with PCE of 3.3%. Full optimization would include investigations of alternative donors with varying energetics and structural motifs that improve interfacial

morphology and fabrication of thicker devices and multijunction architectures, since this work shows that the FF does not drastically drop with increasing thickness.

Overall, introducing these fluorinated acceptors in the field of organic electronics opens new opportunities (not possible with any other fullerene derivative acceptors) for various case studies that address strict morphological control and molecular level understanding of the photoinduced charge generation, separation, and transport. Aside from OPVs and OFETs, perovskite based solar cells may benefit from new options for sublimable, fullerene based electron transport layers other than C_{60}.[55] In addition to vacuum-deposition, solution processed OPVs can be made with these materials (which have good solubility in organic solvents) so that the effects of fabrication method can be directly and accurately compared.

1.11 Experimental

1.11.1 Reagents and Materials:

The following reagents and solvents were obtained from the indicated sources and were used as received or were purified/treated/stored as indicated. Heptafluorobenzyl iodide, 98% (SynQuest). Trifluoromethyl iodide, 98% (SynQuest). C_{60}, 99.5% (MTR Ltd.). Toluene, ACS (Sigma Aldrich). Heptane, HPLC Grade (Sigma Aldrich). *O*-dichlorobenzene, ACS grade (Sigma Aldrich). Sodium chlorodifluoroacetate, (Oakwood Chemical). 15-crown-5 ether, 98% (Sigma Aldrich).

1.11.2 High Performance Liquid Chromatography:

HPLC was conducted using a Shimadzu liquid chromatography instrument (CBM-20A control module, SPD-20A UV-vis detector set to 300 nm, LC-6AD pump, manual injector valve.) The HPLC columns utilized were 25 mm I.D. x 250 nm COSMOSIL Buckyprep column and 10

mm I.D. x 250 nm COSMOSIL Bucky-M prep column (Nacalai Tesque, Inc.). The eluent was ACS grade toluene, HPLC grade heptane at a flow rate of 14 mL min^{-1} or 7 ml min^{-1}.

1.11.3 ^{1}H and ^{19}F NMR Analysis:

^{1}H and ^{19}F NMR spectra were recorded on a Varian INOVA instrument. ^{1}H NMR spectra were acquired at 400 MHz. ^{19}F NMR spectra were acquired at 376 MHz. ^{19}F NMR spectra were referenced to hexafluorobenzene ($-\delta = -164.9$).

1.11.4 UV-Visible Spectroscopy:

UV-vis absorption spectra were recorded on a Perkin Elmer Lambda 19 spectrometer.

1.11.5 Device Preparation:

Thin films and heterojunction solar cell devices were prepared by thermal vapor deposition in ultra-high vacuum at a base pressure of 10^{-7} mbar. Thin films for absorption and emission measurements were prepared on quartz substrates at room temperature. Solar cells were made on tin-doped indium oxide (ITO) coated glass (Thin Film Devices, USA, sheet resistance of 30 Ω sq^{-1}). Layer thickness is measured by quartz microbalances, which are tooled against a reference quartz, and by "optical tooling", i.e. evaluation of the OD of the film of a reference substance. The thin films prepared for absorption and emission measurements were 30 nm thick. Thin film absorption spectra were recorded on a Shimadzu UV-2101/3101 UV-vis spectrometer (Appendix 1 Figures A1.12-17). Bulk-heterojunction solar cells were prepared layer by layer without breaking the vacuum.

9,9-bis[4-(N,N-bis-biphenyl-4-yl-amino)phenyl]-9H-fluorene (BPAPF) was used as a hole transport layer. NDP9 (purchased from Novaled AG Germany) was used as a p-dopant (10 wt%) for BPAPF and as a p-dopant layer. Organic materials were deposited at a rate between 0.1-0.4 Å/s. Order of deposition was dependent on device architecture described below or in the main text.

Each set of BHJ devices (B1-B14) contained two devices of 10 nm and two devices of 20 nm absorber thickness. Each set of BHJ devices (B15-B20) contained two devices of 20 nm and two devices of 30 nm absorber thickness. Reproducibility studies in very similar vacuum deposited devices can be viewed in work by Fitzner et al.[25] BHJ layers were produced by co-evaporation of donor and acceptor in 1:1 ratios by mass and deposited onto the substrate.

1.11.6 Photovoltaic Characterization:

J–V and EQE measurements were carried out in a glove box with nitrogen atmosphere. J–V characteristics were measured using a source-measure unit (Keithley SMU 2400) and an AM 1.5G sun simulator (KHS Technical Lighting SC1200). The intensity was monitored with a silicon photodiode (Hamamatsu S1337), which was calibrated at Fraunhofer ISE. The mismatch between the spectrum of the sun simulator and the solar AM 1.5G spectrum was taken into account for the calculation of current density. For well-defined active solar cell areas, aperture masks (2.76 mm^2) were used. Simple EQE measurements were carried out using the sun simulator in combination with color filters for monochromatic illumination. The illumination intensities were measured with a silicon reference diode (Hamamatsu S1337).

1.11.7 Synthesis of Acceptors:

60-2-1 synthesis: A modified literature procedure was used to selectively synthesize 60-2-1.[56] To the GTGS reactor, which was preloaded with C_{60} (55.1 mg, 0.076 mmol) and kept under dynamic vacuum overnight, was added CF_3I (15 torr). The base of the reactor was then heated using a hot plate to give an internal temperature of 480 °C (600 °C external temperature). After 10 hours, the heat source was removed, and the reactor was opened to vacuum to removed unreacted CF_3I as well as iodine that forms during the reaction. The remaining crude material was then purified by HPLC using a Bucky-M column in 1:1 toluene:heptane. Resulting in 18.4 mg isolated yield (28%)

of $C_{60}(CF_3)_2$. The ^{19}F NMR spectrum of pure sample shown in Appendix 1 Figure A1.1. The HPLC chromatogram of the purified sample is shown in Appendix 1 Figure A1.2.

$C_{60}CF_2$ synthesis: $C_{60}CF_2$ was prepared with slight adaptation of two different literature procedures with purity greater than 95%.[32,31] A 1000 mL 2 neck flask was charged with C_{60} (250 mg, 0.347 mmol), sodium chlorodifluoroacetate (160 mg, 1.05 mmol, 3 equiv.), O-DCB (500 mL), and the phase transfer catalyst 15-crown-5 (20.5 μL, 0.103 mmol, 0.3 equiv.). The flask was then fitted with a reflux condenser under N_2 flush. The solution was refluxed for 3 hrs at which point the heating mantle was switched off and the solution was allowed to cool naturally while continuing to stir. The o-DCB was removed *in vacuo*. Finally, the product was dissolved in 50 mL of toluene, filtered and purified twice via HPLC using 100% toluene as the eluent on a Buckyprep preparative stationary phase with a flow rate of 14 mL min^{-1} to obtain a of a black/brown powdered solid in 29 % isolated yield (78.5 mg). The ^{19}F NMR spectrum of the purified sample is shown in Appendix 1 Figures A1.3 and A1.4. The HPLC chromatogram of the purified sample is shown in Appendix 1 Figure A1.5.

$C_{60}FHF$ synthesis: A 100 mL Schlenk flask was charged with C_{60} (200 mg, 0.278 mmol). 50 mL of *o*-dichlorobenzene and 0.082 mL of tributyltin hydride (1.1 equiv) were added to the flask via syringe in a glove box. 0.048 mL of heptafluorobenzyl iodide (1.1 equiv) was added via syringe and the flask was submerged into an oil bath at 145 °C. The reaction was allowed to stir for 2 hrs. Excess pyridine (5 mL) was then added via syringe. After one hour, the flask was allowed to cool to room temperature. The solvent was removed *in vacuo* and the crude product was washed with heptane (3 x 5 mL). Finally, the product was dissolved in 50 mL of toluene, filtered and purified via HPLC using 100% toluene as the eluent on a Buckyprep stationary phase with a flow rate of 14 mL min^{-1} to obtain a of a brown powdered solid in 37 % isolated yield (0.094 grams).

Chromatogram of HPLC separation is shown in Appendix 1 Figure A1.6. The ^{19}F NMR spectrum is shown in Appendix 1 Figure A1.7 and the HPLC chromatogram of the pure sample is shown in Apppendix 1 Figure A1.8.

60-12-1 synthesis: 60-12-1 was prepared via a modified literature procedure.[33] Rather than using a glass ampoule, a stainless steel reactor was used to allow for high pressures without risk of explosion (Figure 1.5). A glass liner (glass tube with one open end and one sealed end) was filled with C_{60} (30 mg). The C_{60} was spread out over 2 ¼" from the sealed end of the tube. The tube was placed in the metal reactor so that the sealed end faced toward the hot zone. The reactor was completely assembled and placed under vacuum to remove residual moisture and air for 12 hours. CF_3I (12 atm) was then condensed into the reactor and the reactor was sealed at the valve. The reactor was then placed into a furnace (450 ºC) so that the hot zone shown below (6 inches) was in the furnace and the rest of the reactor was outside of the furnace. After 24 hours, the reactor was removed from the furnace and allowed to cool to room temperature. After cooling, the reactor was placed under vacuum to remove excess CF_3I and iodine. The reactor was then disassembled and the glass liner was removed. All material in glass liner was then sonicated and washed repeatedly with toluene, heptane and *ortho*-dichlorobenzene until washings were colorless. Once washings were colorless, the remaining red/orange crystals were isolated (28 mg, 43% yield). These crystals were dissolved in boiling *ortho*-dichlorobenzene to obtain an ^{19}F NMR spectrum (Appendix 1 Figure A1.9).

1.11.8 Synthesis of Donors:

Multi-Step Synthesis of Donor, DCV4T-Me14 (Scheme 1.3):

Synthesis of 5,5'-Bis-trimethylstannanyl-[2,2']bithiophenyl (2): 831 mg (5 mmol) of 2,2'-Bithiophene **1** were dissolved in 10 ml of anhydrous THF under argon and the mixture was cooled

down to -78°C. 6.25 ml (10 mmol) of 1.6-M-BuLi were slowly added via syringe and reaction mixture was stirred for 2 h at -78°C. 10 ml (10 mmol) of 1-M-Me$_3$SnCl was added in one portion and the mixture was allowed to reach room temperature overnight. Reaction mixture was given into 100 ml of petroleum ether and resulting mixture was washed three times with demineralized water. Organic layer was dried over sodium sulphate and solvents were removed on rotary evaporator to afford 1.85 g (75% yield) of desired crude product **2**, which was used without further purification. GC-MS, m/z: 492 [M, 50%], 477 [M-15, 100%].

Synthesis of 2-(5-Bromo-4-methyl-thiophen-2-ylmethylene)-malononitrile (**3**): 5 g (24.4 mmol) of 2-Brom-3-methyl-5-formylthiophen, 4.84 g (73.2 mmol) of Malononitrile and 133 mg (1.5 mmol) of ß-Alanine were dissolved in the mixture of 134 ml anhydrous Ethanol and 134 ml Dichloroethane under argon. The mixture was heated to reflux temperature and stirred for 16 h. Then, the reaction mixture was allowed to reach room temperature, concentrated in vacuum (rotary evaporator) to a residual volume of 90 mL, stored in the fridge for 2 h and the formed precipitate was collected by means of vacuum filtration. The crude product was then washed with anhydrous EtOH (3 x 15 mL) and dried in high vacuum to afford 5.35 g (87% yield) of anticipated product **3** as a yellow solid (4.00 g). ^{1}H-NMR (CDCl$_3$), δ, ppm: 7.68 (1H, s), 7.43 (1H, s), 2.26 (3H, s).

Synthesis of DCV4T-Me[14] (**4**): 500 mg (1.01 mmol) of **2** and 531 mg (2.10 mmol) of **3** were dissolved in 10 ml of anhydrous DMF. This mixture was degassed and 119 mg (0.10 mmol) of Pd[PPh$_3$]$_4$ were added. Reaction mixture was heated to 80°C for 24 h. After the reaction mixture was cooled down to room temperature, formed precipitate was filtered off and washed with methanol. Crude product was purified by recrystallization from chlorobenzene to afford 237 mg (46% yield) of desired product **4** as dark green shining solid. UV/Vis (DCM), nm: 506 nm. ^{1}H-

NMR (d2-TCE, 80°C) δ, ppm: 7.72 (1H, s), 7.62 (1H, s), 7.41 (1H, d), 7.36 (1H, d), 2.57 (3H, s). MALDI-MS, m/z: 510 [M].

Multi-step Synthesis of Donor, DCV5T-F2(3,3)-Me4(2,2,4,4) (Scheme 1.4):

Synthesis of (3,4-Dimethyl-thiophen-2-yl)-trimethyl-stannane (2): 1.0 g (8.9 mmol) of 3,4-Dimethylthiophene **1** were dissolved in 10 ml of dry THF under argon and this solution was cooled down to -78°C. 3.56 ml (8.9 mmol) of 2.5-M-BuLi was slowly added to reaction mixture via syringe and the mixture was stirred for 1 h at -78°C. 8.9 ml (8.9 mmol) of 1-M-Me₃SnCl solution were added and the reaction mixture was stirred for 1 h at -78°C and then overnight at room temperature. Reaction mixture was given into 100 ml petroleum ether and organic layer was three times extracted with 50 ml demineralized water. Organic layer was dried over Na_2SO_4 and then all solvents were removed on rotary evaporator to afford 2.0 g (81% yield) of desired crude product **2**, which was used without further purification. GC-MS, m/z: 276 [M], 261 [M-15, 100%]. ^{1}H-NMR (CDCl₃) δ, ppm: 7.17 (1H, s), 2.21 (3H, s), 2.20 (3H, s), 0.36 (9H, s).

Synthesis of 2,5-Dibromo-3,4-difluoro-thiophene (3): 2,5-Dibromo-3,4-difluoro-thiophene was prepared as described in the literature.[57]

Synthesis of 3',4'-Difluoro-3,4,3'',4''-tetramethyl-[2,2';5',2'']terthiophene (4): 667 mg (2.40 mmol) of **3**, 1.98 g (7.20 mmol) of **2** and 33 mg (0.57 mmol) of dry KF were dissolved in 15 ml of dry toluene and this mixture was degassed under argon. 597 mg (0.52 mmol) of Pd(PPh₃)₄ were added and the reaction mixture was heated to reflux for 24 h. After reaction mixture was cooled down to room temperature, the mixture was given into 100 ml DCM and extracted three times with demineralized water. Organic layer was dried over Na_2SO_4 and all solvents were removed on rotary evaporator. The residue was further purified by column chromatography on silica gel in

petroleum ether/DCM 4/1 to afford 305 mg (37% yield) of desired product **4** as yellow solid. GC-MS, m/z: 340 [M, 100%]. ^{1}H-NMR (CDCl$_3$) δ, ppm: 7.00 (1H, s), 2.28 (3H, s), 2.20 (3H, s).

Synthesis of 3',4'-Difluoro-3,4,3'',4''-tetramethyl-5,5''-bis-trimethylstannanyl-[2,2';5',2'']terthiophene (5): 305 mg (0.90 mmol) of **4** were dissolved in 10 ml of dry THF under argon and this solution was cooled down to -78°C. 1.40 ml (2.24 mmol) of 1.6-M-BuLi was slowly added to reaction mixture via syringe and the mixture was stirred for 1 h at -78°C and 1 h at room temperature. The mixture was cooled down again to -78°C and 2.5 ml (2.5 mmol) of 1-M-Me$_3$SnCl solution were added. The reaction mixture was stirred for 1 h at -78°C and then overnight at room temperature. Reaction mixture was given into 100 ml dichloromethane and it was three times extracted with 50 ml demineralized water. Organic layer was dried over Na$_2$SO$_4$ and then all solvents were removed on rotary evaporator to afford 529 mg (89% yield) of desired crude product **5**, which was used without further purification. ^{1}H-NMR (CDCl$_3$) δ, ppm: 2.12 (6H, s), 0.27 (9H, s).

Synthesis of 2-(5-Bromo-thiophen-2-ylmethylene)-malononitrile (6): 2-(5-Bromo-thiophen-2-ylmethylene)-malononitrile was prepared according to the literature.[58]

Synthesis of DCV5T-F2(3,3)-Me4(2,2,4,4) (7): 529 mg (0.79 mmol) of **5** and 570 mg (2.38 mmol) of **6** were dissolved in the mixture of 5 ml THF and 5 ml toluene. This mixture was degassed and 119 mg (0.10 mmol) of Pd[PPh$_3$]$_4$ were added. Reaction mixture was heated to reflux for 24 h. After the reaction mixture was cooled down to room temperature, formed precipitate was filtered off and washed with methanol. Crude product was purified by recrystallisation from chlorobenzene to afford 234 mg (45% yield) of desired product **7** as dark green shining solid. Mp (DSC) 314 °C. UV/Vis (DCM), nm: 477 nm. ^{1}H-NMR (d2-TCE, 100°C) δ, ppm: 7.82 (1H, d), 7.81 (1H, s), 7.39 (1H, d), 2.49 (3H, s), 2.39 (3H, s). MALDI-MS, m/z: 656 [M].

1.11.9 Low-Temperature Negative Ion Photoelectron Spectroscopy (LT-NIPES)

The LT-NIPES experiments were performed with a low temperature apparatus that couples an electrospray ionization source and a temperature-controlled cryogenic ion trap to a magnetic-bottle time-of-flight photoelectron spectrometer. [59]

Fresh spray solutions were prepared by adding an aliquot of an acetonitrile solution of an electron-donor compound, tetrakis(dimethyamino)ethylene (TDAE), and 1,8-Diazabicyclo[5.4.0]undec-7-ene (DBU) to 0.1 mM toluene/acetonitrile solution of $C_{60}CF_2$, and $C_{60}(CF_3)_8$ isomer 1, respectively. The desired anions produced were guided by two RF-only quadrupoles and directed by a 90° ion bender into the 3-D ion trap, where they were accumulated and thermalized via collisions with a background buffer gas (ca. 0.1 mTorr 20/80 H_2/He) for a period of 20 to 100 ms before being pulsed out into the extraction zone of a time-of-flight mass spectrometer at a repetition rate of 10 Hz. The trap was operated at 10 K in the current experiments in order to achieve the best instrument resolution, as well as to eliminate vibrational hot bands. For each NIPES experiment, the anions were mass selected and decelerated before being intercepted by a 266 nm (4.661 eV) laser beam from a Nd:YAG laser in the photodetachment zone. The laser was operated at a 20 Hz repetition rate with the ion beam off at alternating laser shots to enable shot-by-shot background subtraction. Photoelectrons were collected at nearly 100% efficiency by the magnetic bottle, analyzed in a 5.2 m long calibrated flight tube, and converted to kinetic energy spectra. The electron binding energy (EBE) spectra were obtained by subtracting the kinetic energy spectra from the detachment photon energy used. The energy resolution ($\Delta E/E$) was ca. 2% (i.e., ca. 20 meV for 1 eV kinetic energy electrons).[59]

Table 1.1. Summary of photovoltaic figures of merit for cell types R (reference devices).[a]

cell	acceptor	J_{SC}, mA/cm^2	FF, %	V_{OC}, V	ΔV_{OC}, V
R1	C_{60}	1.7	70.8	0.93	0.0
R2	$C_{60}FHF$	1	64.9	0.91	0.02
R3	60-2-1	1	61.4	0.72	0.21
R4	60-4-1	0.7	65.4	0.61	0.31
R5	$C_{60}CF_2$	0.7	47.9	0.60	0.33
R6	60-8-1	0	41.9	0.48	0.45
R7	60-12-1	0.1	36.3	0.36	0.57

[a] Device architecture is shown in **Figure 1.8**, left. [b] ΔV_{OC} represents the V_{OC} relative to C_{60}. R (reference device) = glass/ITO/fullerene/HTL/Al, where HTL = BPAPF/p-BPAPF/NDP9.

Table 1.2. Summary of photovoltaic figures of merit for PHJ OPV cells with $C_{60}CF_2$ and C_{60}.[a]

Cell	J_{SC}, mA/cm^2	FF, %	V_{OC}, V	ΔV_{OC},[b] V
P1	5.6	61.2	1.07	
P2	6.1	55.5	1.08	
P3	4	41.3	0.84	0.23 (vs P1)
P4	3.9	37.4	0.83	0.25 (vs P2)

[a] Device architecture is shown in **Figure 1.8**, middle. [b] ΔV_{OC} is V_{OC} versus V_{OC} in the identical C_{60} device. P (planar heterojunction device) = glass/ITO/fullerene/donor/HTL/Al, where HTL = BPAPF/p-BPAPF/NDP9. Devices P1 and P2 contained C_{60} as the fullerene. Devices P3 and P4 contained $C_{60}CF_2$ as the fullerene acceptor. Devices P1 and P3 had a donor layer thickness of 6 nm. Devices P2 and P4 had a donor layer thickness of 10 nm.

Table 1.3. Summary of photovoltaic figures of merit for BHJ cells with 1:1 $C_{60}CF_2$:DCV4T-Me[14] active layer.[a]

Cell	ETL on ITO	BHJ layer thickness (nm)	substrate temperature (°C)	J_{SC} (mA/cm^2)	FF (%)	V_{OC} (V)	PCE (%)
B1	$C_{60}CF_2$	10	RT	2.8	32.6	0.81	0.74
B2	$C_{60}CF_2$	20	RT	2.5	28.7	0.81	0.58
B3	C_{60}	10	50	4.9	46.7	0.92	2.11
B4	C_{60}	20	50	4.7	41.7	0.9	1.76
B5	C_{60}	10	70	4.4	46	0.85	1.72
B6	C_{60}	20	70	4.5	41.2	0.87	1.61
B7	$C_{60}CF_2$	10	50	4.7	44.3	0.93	1.94
B8	$C_{60}CF_2$	20	50	6.1	40.5	0.92	2.27

[a] B (bulk heterojunction device) = glass/ITO/ETL/ $C_{60}CF_2$:DCV4T-Me[14] (1:1)/HTL/Al, where HTL = BPAPF/p-BPAPF/NDP9 and ETL is C_{60} or $C_{60}CF_2$.

Table 1.4. Summary of photovoltaic figures of merit for BHJ devices with C_{60}, $C_{60}CF_2$, 60-2-1 and 60-4-1.[a]

Cell	fullerene on ITO	BHJ layer thickness (nm)	J_{SC} (mA/cm^2)	FF (%)	V_{OC}(V)	PCE (%)
B9	C_{60}	10	6.7	60.1	0.97	3.9
B10	C_{60}	20	8.1	49.9	0.96	3.88
B7	$C_{60}CF_2$	10	4.7	44.3	0.93	1.94
B8	$C_{60}CF_2$	20	6.1	40.5	0.92	2.27
B11	60-2-1	10	4.4	61	0.87	2.34
B12	60-2-1	20	6.4	58.4	0.89	3.33
B13	60-4-1	10	3.0	51.1	0.74	1.13
B14	60-4-1	20	3.5	42.3	0.75	1.11

[a] B (bulk heterojunction device) = glass/ITO/ETL/acceptor:donor (1:1)/HTL/Al, where HTL = BPAPF/p-BPAPF/NDP9 and ETL is the fullerene acceptor used in the BHJ layer.

Table 1.5. Summary of photovoltaic figures of merit for BHJ devices with DCV5T-F$_2$(3,3)-Me$_4$(2,2,4,4).

Cell	fullerene on ITO	BHJ Layer Thickness (nm)	Substrate temperature	J$_{SC}$ (mA/cm^2)	FF (%)	V$_{OC}$ (V)	PCE (%)
B15	C$_{60}$ (10 nm)	20	70 °C	6.9	68.2	0.97	4.6
B16	C$_{60}$ (10 nm)	30	70 °C	8	65.2	0.98	5.1
B17	60-2-1 (10 nm)	20	70 °C	6	53.2	0.73	2.3
B18	60-2-1 (10 nm)	30	70 °C	6	51.2	0.55	1.7
B19	60-2-1 (10 nm)	20	50 °C	6.6	62.5	0.85	3.5
B20	60-2-1 (10 nm)	30	50 °C	7	62.7	0.86	3.8

[a] In each case, the fullerene on ITO was also the fullerene used in a BHJ layer with DCV5T-F$_2$(3,3)-Me$_4$(2,2,4,4).
[b] Devices made in accordance with Figure 1.12.

Table 1.6. Summary of photovoltaic figures of merit for PHJ devices with DCV5T-F$_2$(3,3)-Me$_4$(2,2,4,4) as donor.

Cell	Acceptor	Donor	J$_{SC}$ (mA/cm^2)	FF (%)	V$_{OC}$ (V)	PCE (%)
P5	C$_{60}$	6	5.5	53.5	1.06	3.1
P6	C$_{60}$	10	5.2	49	1.05	2.7
P7	60-2-1	6	4.5	58.5	0.97	2.6
P8	60-2-1	10	4.8	51.2	0.97	2.4
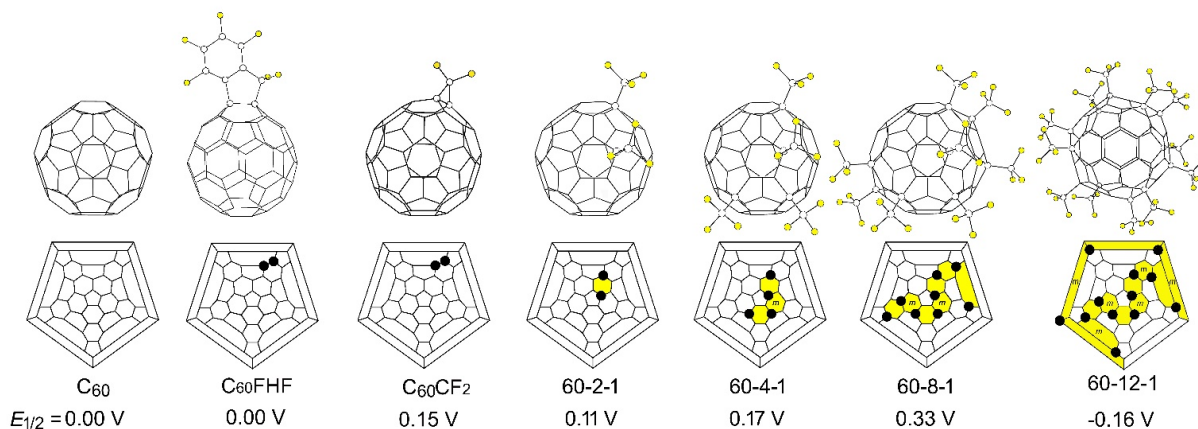
Figure 1.1. Top: Drawings of molecular structures of fluorous fullerene acceptors used in this work. Middle: Schlegel diagrams with addition patterns (black circles are located at the sp^3 carbon atoms, yellow field shows edge-sharing hexagons on C_{60} core with *para-* or *meta-* CF_3 groups). Bottom: $E_{1/2}$ values vs C_{60} from the literature.[17,29] Notations for the $C_{60}(CF_3)_{2n}$ compounds are abbreviated as follows: 60-A-B, where "60"- is a type of fullerene core, "A" is number of CF_3 groups, "B" is a number of the isomer, adopted in the literature.[15] C_{60}FHF is an abbreviation for $C_{60}(CF_2C_6F_4)$, also known as fauxhawk fullerene.[29]
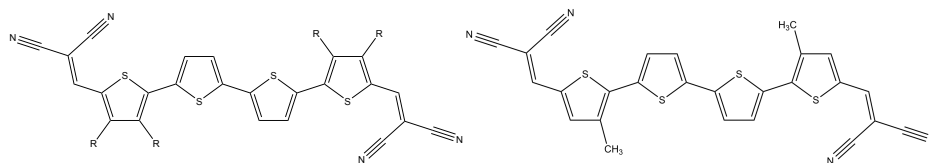
Figure 1.2. A drawing of molecular structure of DCV4T-R[1144] where R = Me or Et (left) and DCV4T-Me[14] donor (right) used in this work.
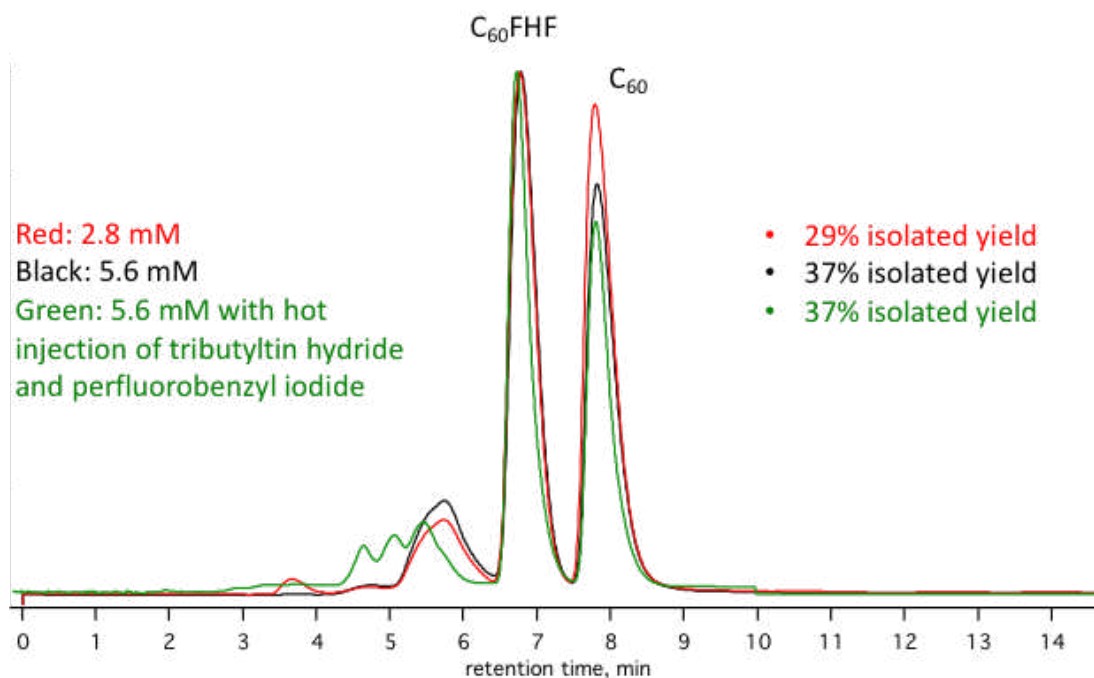
Figure 1.3. HPLC chromatograms of crude $C_{60}FHF$ reactions. Higher concentration leads to improved conversion of C_{60} to $C_{60}FHF$, with a similar amount of multiple addition products. Injecting into hot solution does not impact yield. Eluent is toluene at 14 mL/min on a Buckyprep stationary phase measured at 300 nm.

Figure 1.4. HPLC chromatograms of crude $C_{60}CF_2$ reactions. Increasing reaction time from 1 h to 3 h improves conversion of C_{60} to $C_{60}CF_2$. Eluent is toluene at 14 mL/min on a Buckyprep stationary phase measured at 300 nm.
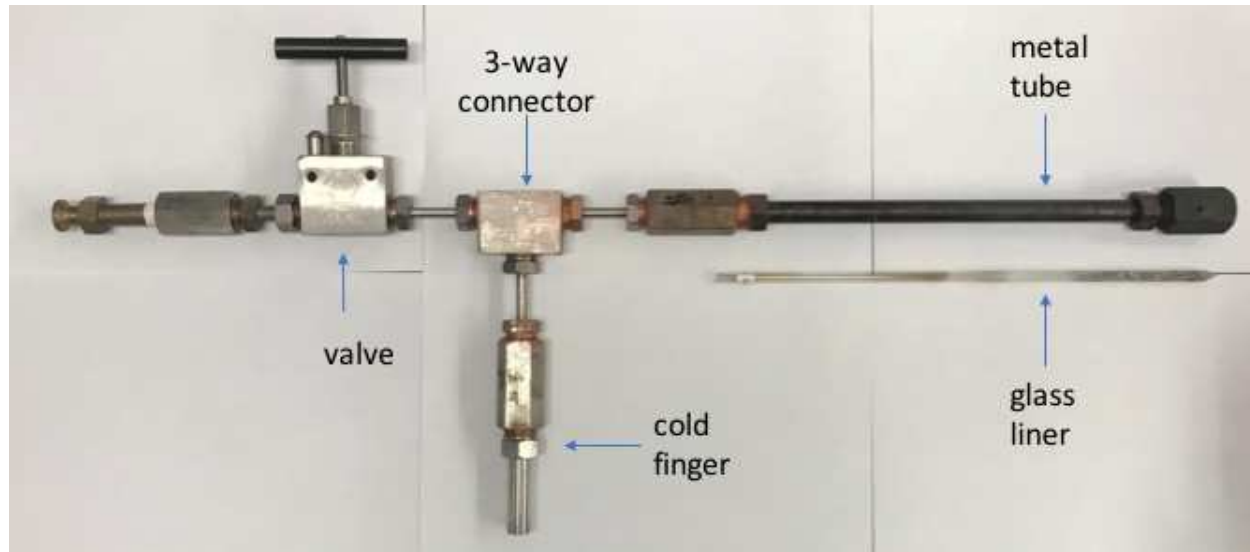
Figure 1.5. Metal reactor used for 60-12-1 synthesis. The cold finger is used to condense CF_3I into the reactor and to act as a reservoir of CF_3I during the reaction. C_{60} is placed in the glass liner, which is inserted into the metal tube. The metal tube portion is placed halfway into the furnace during the reaction.
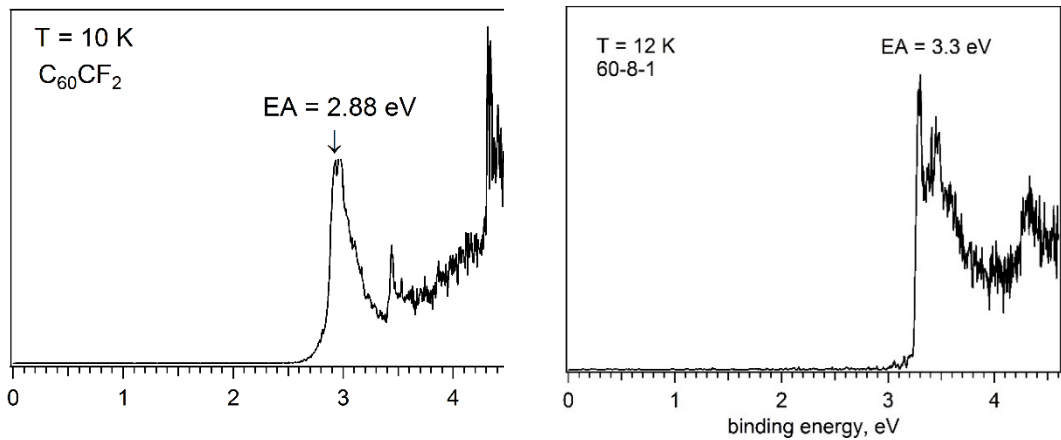
Figure 1.6. Low-temperature photoelectron spectrum of $C_{60}CF_2{}^-$ ((T = 10 K, left) and (60-8-1)$^-$ (T = 12 K, right).
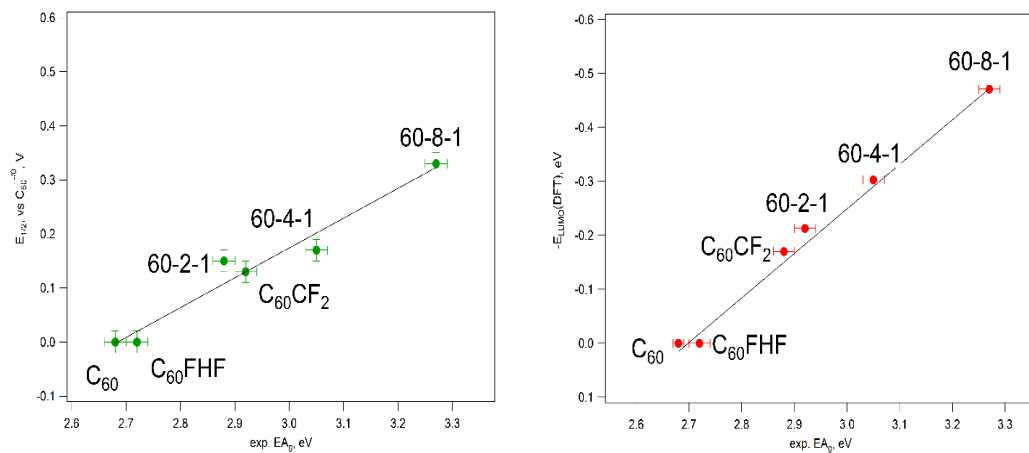
Figure 1.7. Right: Gas-phase electron affinity vs DFT-calculated LUMO energy of fluorous acceptors. Left: Gas-phase electron affinity vs $E_{1/2}$ values measured by cyclic voltammetry.
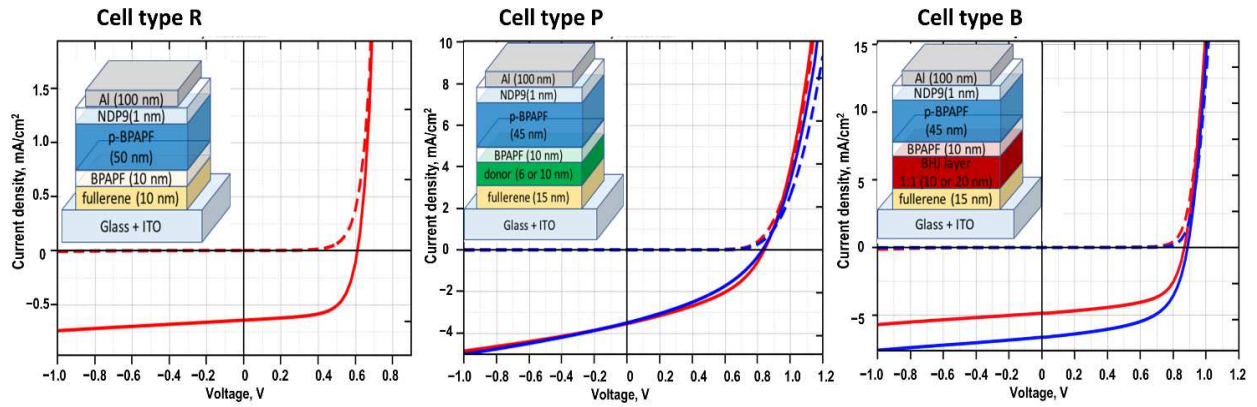
Figure 1.8. *Left:* J-V curves for reference cell R4, inset shows reference cell stack architecture. *Middle*: J-V curves for cells P3 (red) and P4 (blue); inset shows stack architecture used for PHJ cells. *Right*: J-V curves for cells B11 (red) and B12 (blue); inset shows stack architecture used for BHJ cells. For well-defined active solar cell areas, aperture masks (2.76 mm^2) were used.
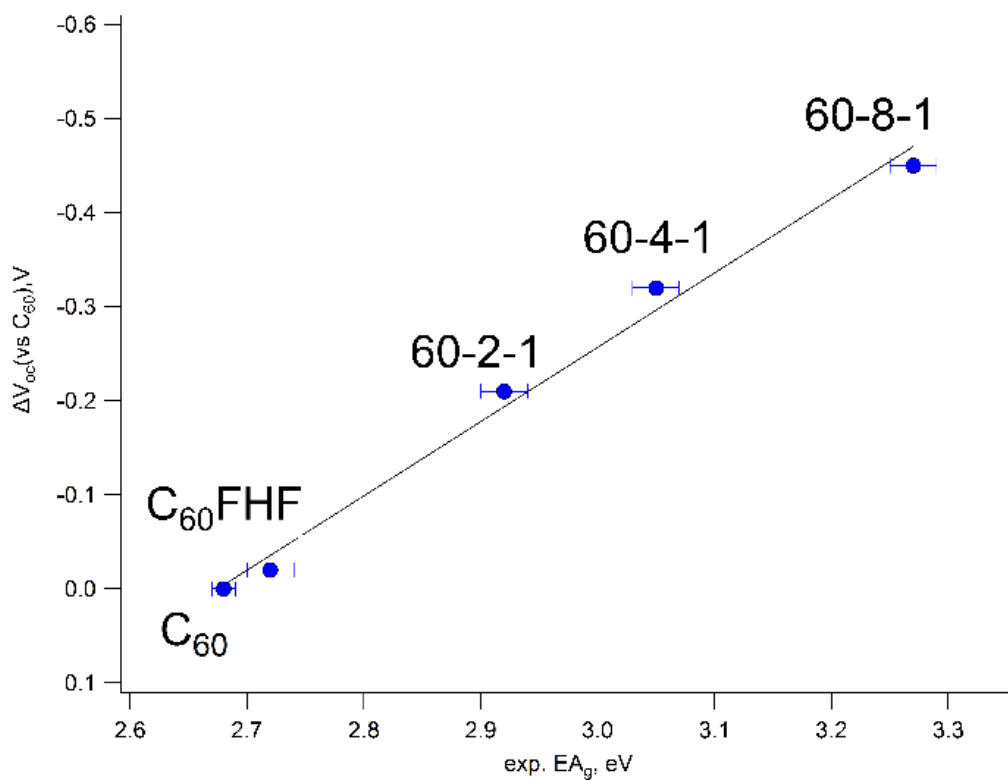
Figure 1.9. Gas-phase electron affinity vs ΔV_{OC} measured in reference cells with fluorous acceptors (see Table 1.1).
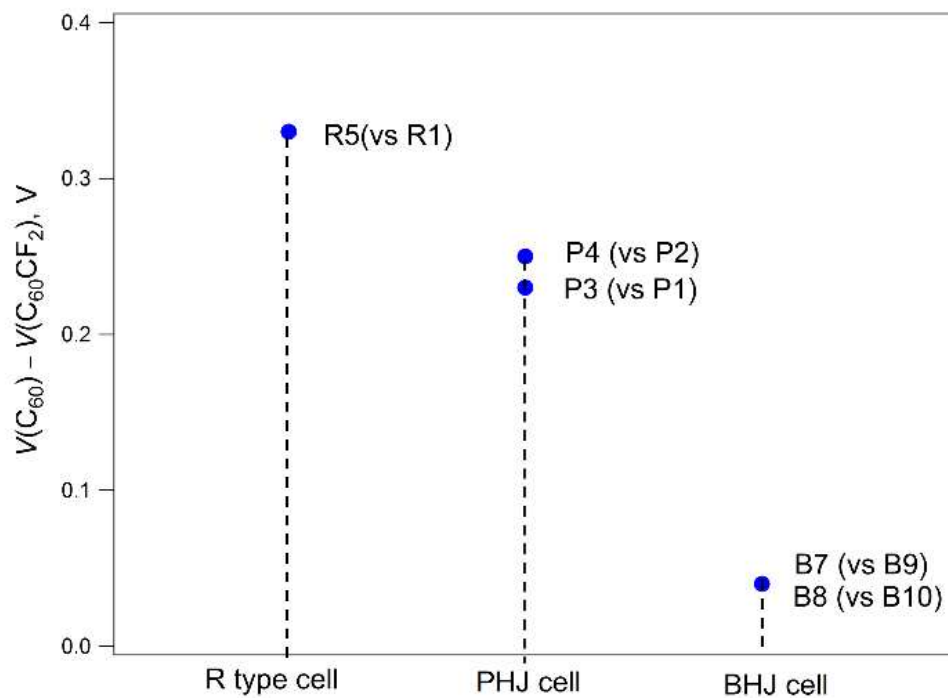
Figure 1.10. Changes in the $\Delta V_{OC} = V_{OC}(C_{60}\text{-cell}) - V_{OC}(C_{60}CF_2\text{-cell})$ for different OPV cell types. Dashed lines are for eye guide only.
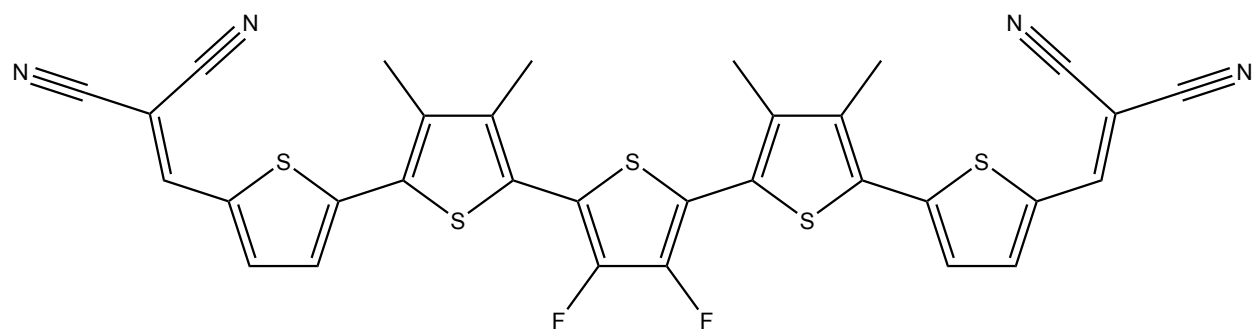
Figure 1.11. Structure of the fluorinated donor, DCV5T-F$_2$(3,3)-Me$_4$(2,2,4,4).
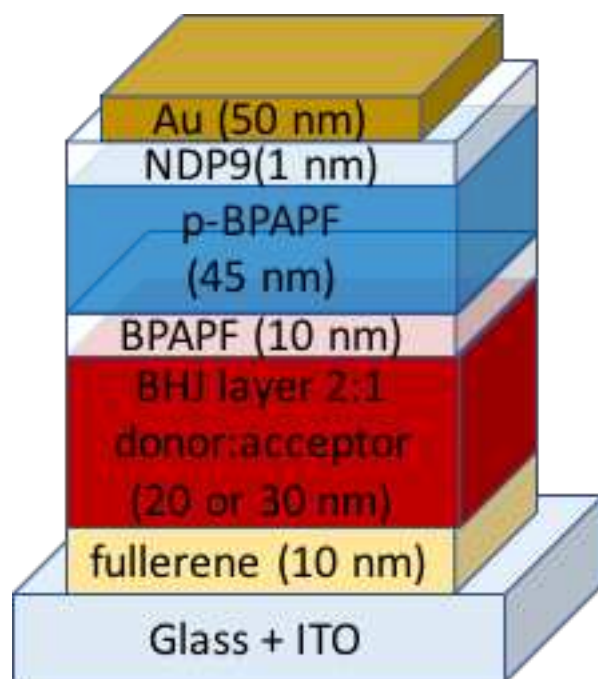
Figure 1.12. Device architecture for BHJ devices with 60-2-1 (acceptor) and DCV5T-F$_2$(3,3)-Me$_4$(2,2,4,4) (donor).
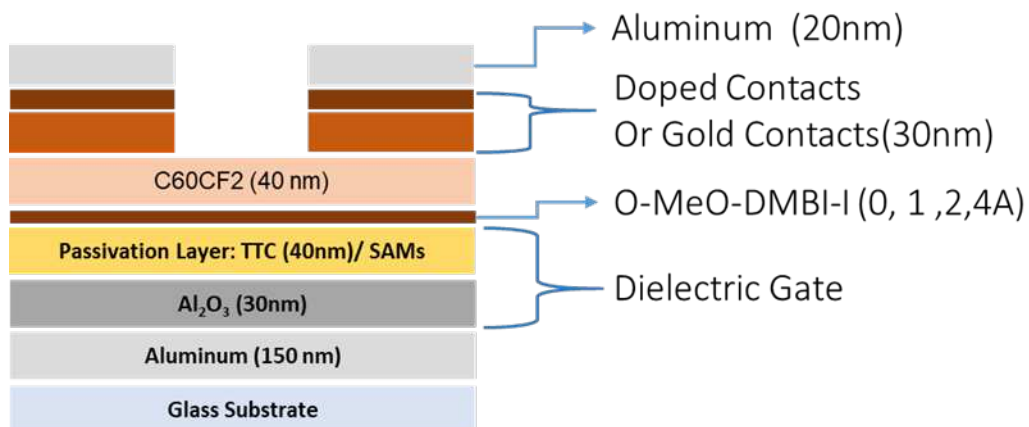
Figure 1.13. OFET device architecture (C_{60}/O-MeO-DMBI-I 4 wt% and 8 wt%, Au) and varying thickness of dopant at the Gate dielectric/OSC interface.
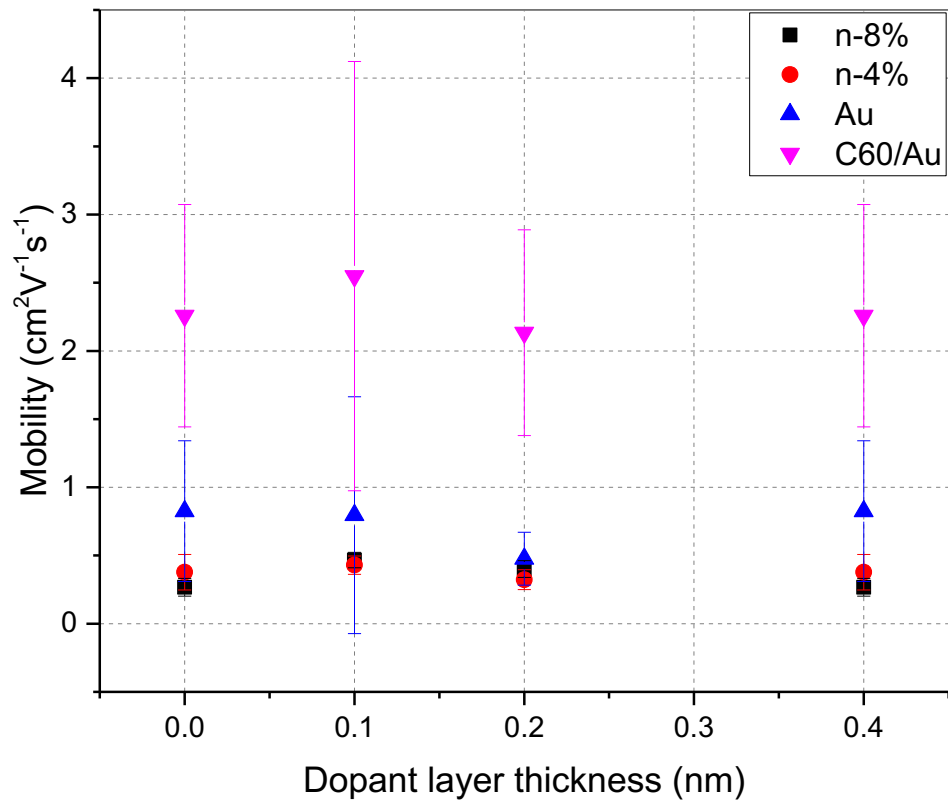
Figure 1.14. Average mobility of C_{60} and $C_{60}CF_2$ OFETS with varying dopant layer thickness.
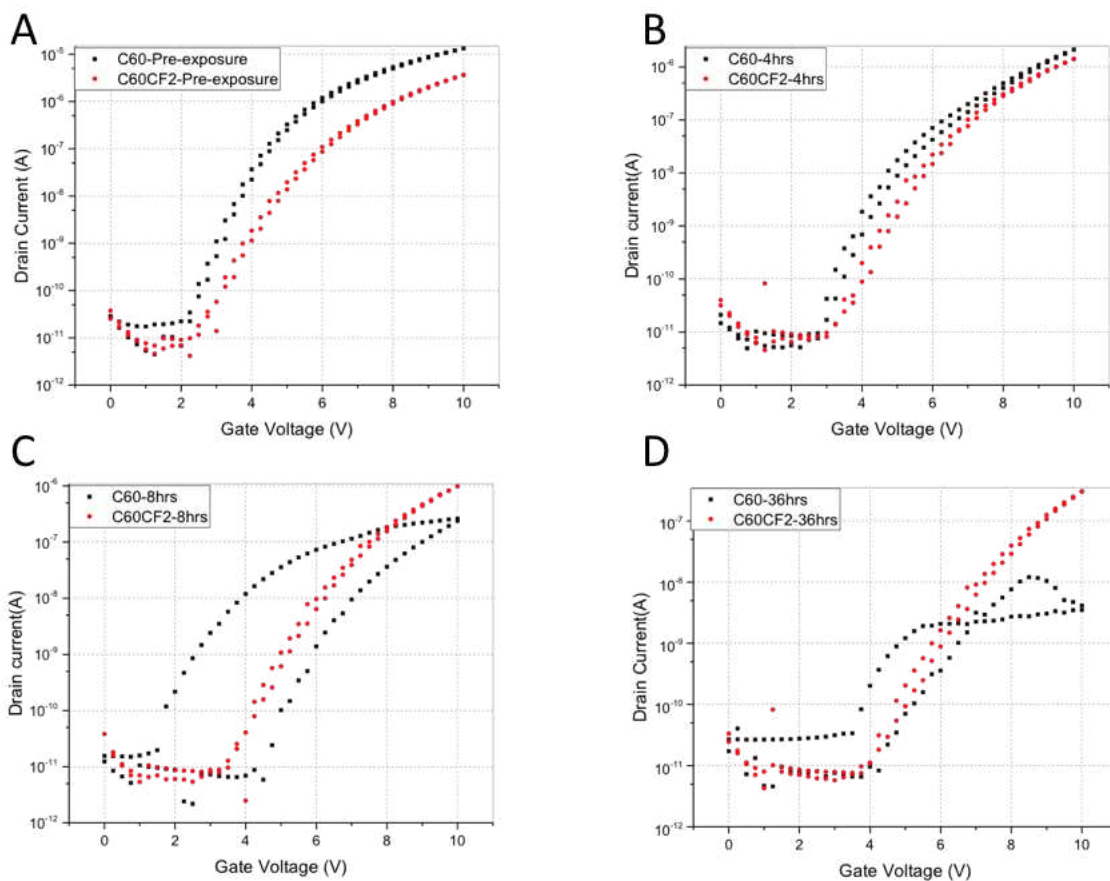
Figure 1.15. (A) Transfer characteristics of a C_{60} and a $C_{60}CF_2$ OFET before exposure to air; (B) after 4 h; (C) after 8 h; (D) after 36 h of exposure.
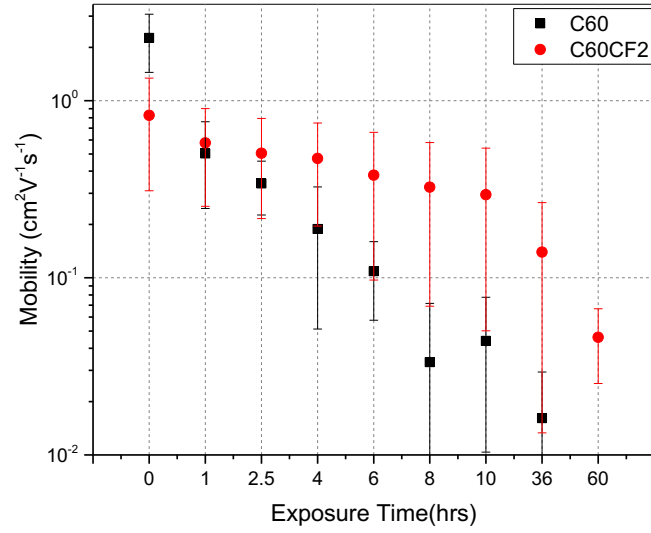
Figure 1.16. Average mobility of C_{60} and $C_{60}CF_2$ OFETs versus air exposure time.
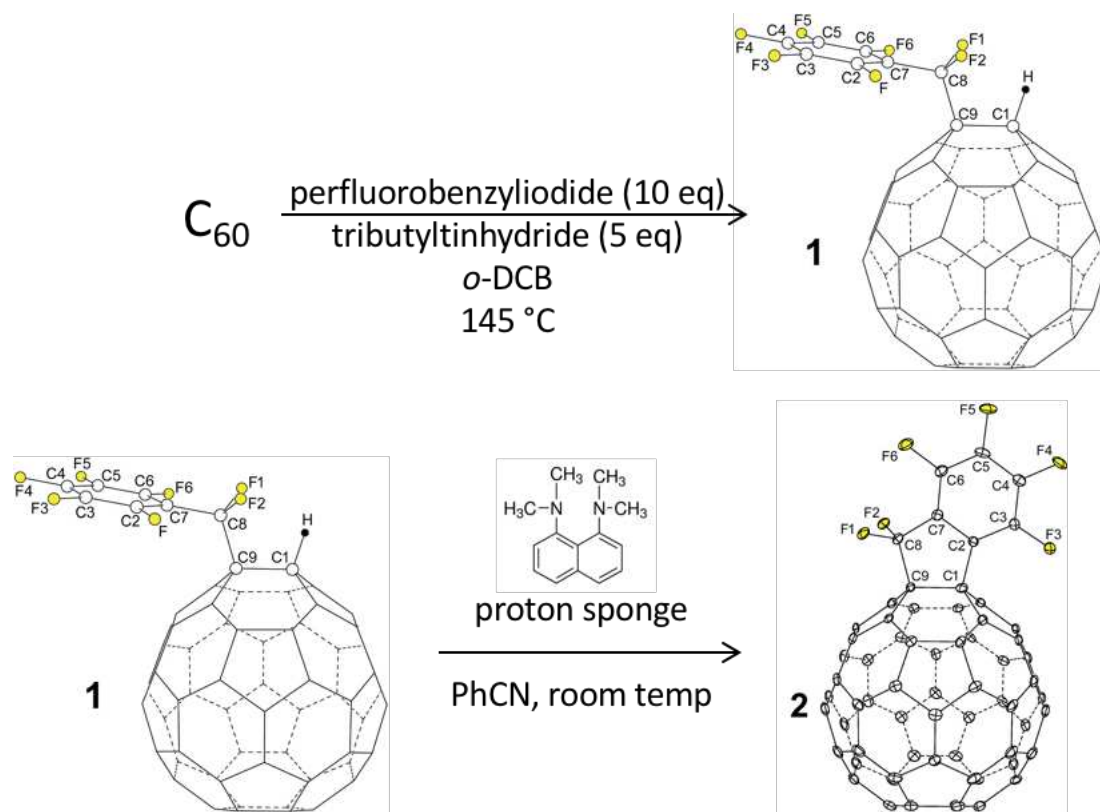
Scheme 1.1. Literature prep for $C_{60}FHF$. Requires two stages of HPLC for 27% yield.[29]
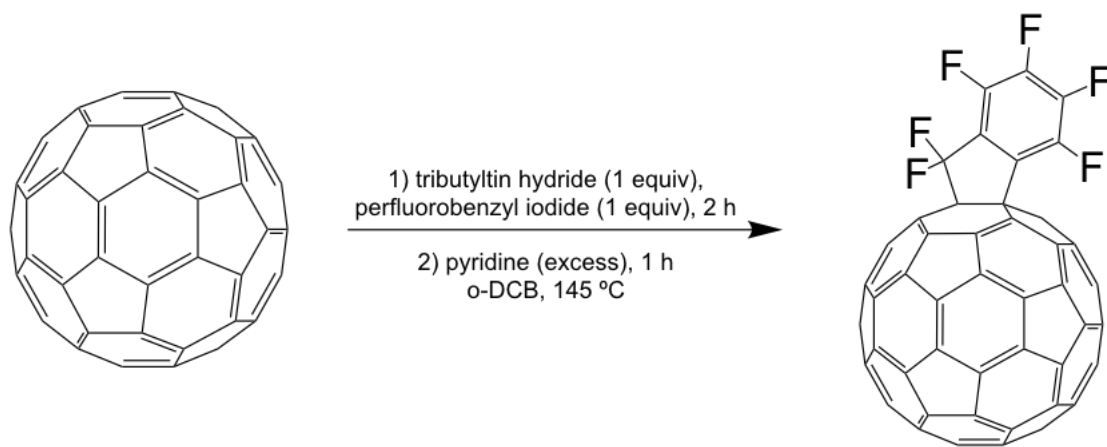
Scheme 1.2. Optimized synthesis of $C_{60}FHF$. Only one stage of HPLC is required for a 37% yield.
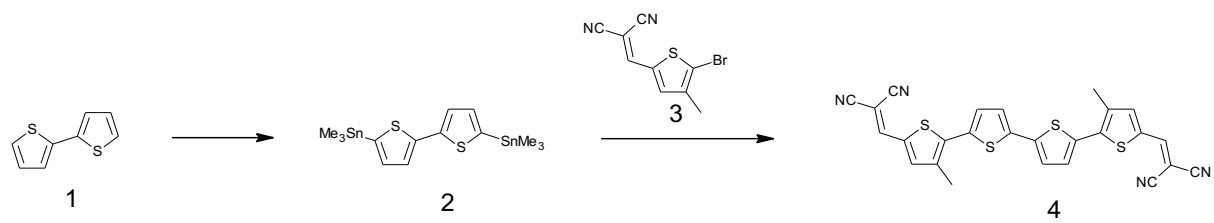
Scheme 1.3. Synthesis of the donor, DCV4T-Me[14].
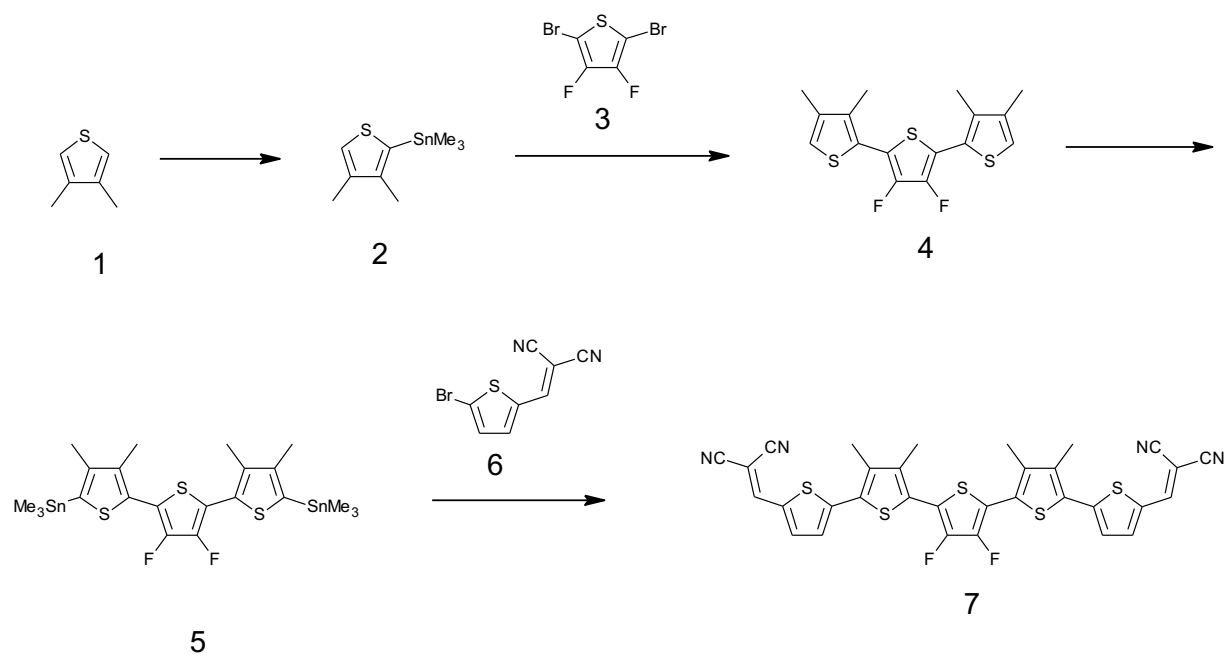
Scheme 1.4. Synthesis of the donor, DCV5T-F2(3,3)-Me4(2,2,4,4)

CHAPTER 1 REFERENCES

1.   Heliatek, Heliatek sets new Organic Photovoltaic world record efficiency of 13.2%. Heliatek.com, 2016.

2.   Meng, L.; Zhang, Y.; Wan, X.; Li, C.; Zhang, X.; Wang, Y.; Ke, X.; Xiao, Z.; Ding, L.; Xia, R.; Yip, H.-L.; Cao, Y.; Chen, Y. Organic and solution-processed tandem solar cells with 17.3% efficiency. *Science* **2018**, *361*, 1094-1098.

3.   Ramirez, I.; Causa, M.; Zhong, Y.; Banerji, N.; Riede, M. Key Tradeoffs Limiting the Performance of Organic Photovoltaics. *Adv. Energy Mater.* **2018**, *8*, 1703551.

4.   Tang, C. W. Two-layer organic photovoltaic cell. *Appl. Phys. Lett.* **1986**, *48*, 183-185.

5.   Schulze, K.; Uhrich, C.; Schüppel, R.; Leo, K.; Pfeiffer, M.; Brier, E.; Reinold, E.; Bäuerle, P. Efficient Vacuum-Deposited Organic Solar Cells Based on a New Low-Bandgap Oligothiophene and Fullerene C60. *Adv. Mater.* **2006**, *18*, 2872-2875.

6.   Sariciftci, N. S.; Smilowitz, L.; Heeger, A. J.; Wudl, F. Photoinduced Electron Transfer from a Conducting Polymer to Buckminsterfullerene. *Science* **1992**, *258*, 1474-1476.

7.   Yu, G.; Gao, J.; Hummelen, J. C.; Wudl, F.; Heeger, A. J. Polymer Photovoltaic Cells: Enhanced Efficiencies via a Network of Internal Donor-Acceptor Heterojunctions. *Science* **1995**, *270*, 1789-1791.

8.   Moulé, A. J.; Meerholz, K. Morphology Control in Solution-Processed Bulk-Heterojunction Solar Cell Mixtures. *Adv. Funct. Mater.* **2009**, *19*, 3028-3036.

9.   Diao, Y.; Shaw, L.; Bao, Z.; Mannsfeld, S. C. B. Morphology control strategies for solution-processed organic semiconductor thin films. *Energ. Environ. Sci.* **2014**, *7*, 2145-2159.

10.   Jackson, N. E.; Savoie, B. M.; Marks, T. J.; Chen, L. X.; Ratner, M. A. The Next Breakthrough for Organic Photovoltaics? *J. Phys. Chem. Lett.* **2015**, *6*, 77-84.

11.   Ayzner, A. L.; Tassone, C. J.; Tolbert, S. H.; Schwartz, B. J. Reappraising the Need for Bulk Heterojunctions in Polymer−Fullerene Photovoltaics: The Role of Carrier Transport in All-Solution-Processed P3HT/PCBM Bilayer Solar Cells. *J. Phys. Chem. C* **2009**, *113*, 20050-20060.

12.   Nakano, K.; Tajima, K. Organic Planar Heterojunctions: From Models for Interfaces in Bulk Heterojunctions to High-Performance Solar Cells. *Adv. Mater.* **2017**, *29*, 1603269.

13.   Larson, B. W.; Whitaker, J. B.; Popov, A. A.; Kopidakis, N.; Rumbles, G.; Boltalina, O. V.; Strauss, S. H. Thermal [6,6] → [6,6] Isomerization and Decomposition of PCBM (Phenyl-C61-butyric Acid Methyl Ester). *Chem. Mater.* **2014**, *26*, 2361-2367.

14.   Maibach, J.; Adermann, T.; Glaser, T.; Eckstein, R.; Mankel, E.; Pucci, A.; Müllen, K.; Lemmer, U.; Hamburger, M.; Mayer, T.; Jaegermann, W. Impact of processing on the chemical and electronic properties of phenyl-C61-butyric acid methyl ester. *J. Mater. Chem. C.* **2014**, *2*, 7934-7942.

15.   Boltalina, O. V.; Popov, A. A.; Kuvychko, I. V.; Shustova, N. B.; Strauss, S. H. Perfluoroalkylfullerenes. *Chem. Rev.* **2015**, *115*, 1051-1105.

16.   Bukovsky, E. V.; Larson, B.; Clikeman, T.; Chen, Y.-S.; Popov, A.; Boltalina, O.; Strauss, S. H., Thirteen Decakis(trifluoromethyl)decahydro(C60-Ih)[5,6]fullerenes (C60(CF3)10). 2017; pp 59-89.

17.   Popov, A. A.; Kareev, I. E.; Shustova, N. B.; Stukalin, E. B.; Lebedkin, S. F.; Seppelt, K.; Strauss, S. H.; Boltalina, O. V.; Dunsch, L. Electrochemical, Spectroscopic, and DFT Study of C60(CF3)n Frontier Orbitals (n = 2−18): The Link between Double Bonds in Pentagons and Reduction Potentials. *J. Am. Chem. Soc.* **2007**, *129*, 11551-11568.

18.	Coffey, D. C.; Larson, B. W.; Hains, A. W.; Whitaker, J. B.; Kopidakis, N.; Boltalina, O. V.; Strauss, S. H.; Rumbles, G. An Optimal Driving Force for Converting Excitons into Free Carriers in Excitonic Solar Cells. *J. Phys. Chem. C* **2012**, *116*, 8916-8923.

19.	Ihly, R.; Mistry, K. S.; Ferguson, A. J.; Clikeman, T. T.; Larson, B. W.; Reid, O.; Boltalina, O. V.; Strauss, S. H.; Rumbles, G.; Blackburn, J. L. Tuning the driving force for exciton dissociation in single-walled carbon nanotube heterojunctions. *Nat. Chem.* **2016**, *8*, 603-609.

20.	Larson, B. W.; Reid, O. G.; Coffey, D. C.; Avdoshenko, S. M.; Popov, A. A.; Boltalina, O. V.; Strauss, S. H.; Kopidakis, N.; Rumbles, G. Polymer Solar Cells: Inter-Fullerene Electronic Coupling Controls the Efficiency of Photoinduced Charge Generation in Organic Bulk Heterojunctions (Adv. Energy Mater. 24/2016). *Adv. Energy Mater.* **2016**, *6*.

21.	Nellissery Viswanathan, V.; Ferguson, A. J.; Pfeilsticker, J. R.; Larson, B. W.; Garner, L. E.; Brook, C. P.; Strauss, S. H.; Boltalina, O. V.; Ramamurthy, P. C.; Braunecker, W. A. Strategic fluorination of polymers and fullerenes improves photostability of organic photovoltaic blends. *Org. Electron.* **2018**, *62*, 685-694.

22.	Garner, L. E.; Nellissery Viswanathan, V.; Arias, D. H.; Brook, C. P.; Christensen, S. T.; Ferguson, A. J.; Kopidakis, N.; Larson, B. W.; Owczarczyk, Z. R.; Pfeilsticker, J. R.; Ramamurthy, P. C.; Strauss, S. H.; Boltalina, O. V.; Braunecker, W. A. Photobleaching dynamics in small molecule vs. polymer organic photovoltaic blends with 1,7-bis-trifluoromethylfullerene. *J. Mater. Chem. A* **2018**, *6*, 4623-4628.

23.	Hoke, E. T.; Sachs-Quintana, I. T.; Lloyd, M. T.; Kauvar, I.; Mateker, W. R.; Nardes, A. M.; Peters, C. H.; Kopidakis, N.; McGehee, M. D. The Role of Electron Affinity in Determining

Whether Fullerenes Catalyze or Inhibit Photooxidation of Polymers for Solar Cells. *Adv. Energy Mater.* **2012**, *2*, 1351-1357.

24.   Fitzner, R.; Elschner, C.; Weil, M.; Uhrich, C.; Körner, C.; Riede, M.; Leo, K.; Pfeiffer, M.; Reinold, E.; Mena-Osteritz, E.; Bäuerle, P. Interrelation between Crystal Packing and Small-Molecule Organic Solar Cell Performance. *Adv. Mater.* **2012**, *24*, 675-680.

25.   Fitzner, R.; Mena-Osteritz, E.; Mishra, A.; Schulz, G.; Reinold, E.; Weil, M.; Körner, C.; Ziehlke, H.; Elschner, C.; Leo, K.; Riede, M.; Pfeiffer, M.; Uhrich, C.; Bäuerle, P. Correlation of π-Conjugated Oligomer Structure with Film Morphology and Organic Solar Cell Performance. *J. Am. Chem. Soc.* **2012**, *134*, 11064-11067.

26.   Fitzner, R.; Mena-Osteritz, E.; Walzer, K.; Pfeiffer, M.; Bäuerle, P. A–D–A-Type Oligothiophenes for Small Molecule Organic Solar Cells: Extending the π-System by Introduction of Ring-Locked Double Bonds. *Adv. Funct. Mater.* **2015**, *25*, 1845-1856.

27.   Mishra, A.; Bäuerle, P. Small Molecule Organic Semiconductors on the Move: Promises for Future Solar Energy Technology. *Angew. Chem. Int. Ed.* **2012**, *51*, 2020-2067.

28.   Guskova, O.; Schünemann, C.; Eichhorn, K.-J.; Walzer, K.; Levichkova, M.; Grundmann, S.; Sommer, J.-U. Light Absorption in Organic Thin Films: The Importance of Oriented Molecules. *J. Phys. Chem. C* **2013**, *117*, 17285-17293.

29.   San, L. K.; Bukovsky, E. V.; Larson, B. W.; Whitaker, J. B.; Deng, S. H. M.; Kopidakis, N.; Rumbles, G.; Popov, A. A.; Chen, Y.-S.; Wang, X.-B.; Boltalina, O. V.; Strauss, S. H. A faux hawk fullerene with PCBM-like properties. *Chem. Sci.* **2015**, *6*, 1801-1815.

30.   Liu, S. Y.; DeWeerd, N. J.; Reeves, B. J.; San, L. K.; Dahal, D.; Krishnan, R. K. R.; Strauss, S. H.; Boltalina, O. V.; Lussem, B. Doped N-Type Organic Field-Effect Transistors Based on Faux-Hawk Fullerene. *Advanced Electronic Materials* **2019**, *5*.

31.   Pimenova, A. S.; Kozlov, A. A.; Goryunkov, A. A.; Markov, V. Y.; Khavrel, P. A.; Avdoshenko, S. M.; Vorobiev, V. A.; Ioffe, I. N.; Sakharov, S. G.; Troyanov, S. I.; Sidorov, L. N. Preparation and structures of [6,6]-open difluoromethylene[60]fullerenes: C60(CF2) and C60(CF2)2. *Dalton Trans.* **2007**, 5322-5328.

32.   Larson, B. W. Synthesis and characterization of Fluorine-Containing C60 Derivatives and Their Charge Carrier Photophysics in Organic Photovoltaics. Ph. D. Dissertation, Colorado State University, 2013.

33.   Troyanov, S. I.; Dimitrov, A.; Kemnitz, E. Selective Synthesis of a Trifluoromethylated Fullerene and the Crystal Structure of C60(CF3)12. *Angew. Chem. Int. Ed.* **2006**, *45*, 1971-1974.

34.   Romanova, N. A.; Papina, T. y. S.; Luk'yanova, V. A.; Buyanovskaya, A. G.; Varuschenko, R. M.; Druzhinina, A. I.; Goryunkov, A. A.; Markov, V. Y.; Panin, R. A.; Sidorov, L. N. S6 Isomer of C60(CF3)12: Synthesis, properties and thermodynamic functions. *The Journal of Chemical Thermodynamics* **2013**, *66*, 59-64.

35.   Bukovsky, E. V.; DeWeerd, N. J.; Strauss, S. H.; Boltalina, O. V. Versatile metal reactor for high-temperature and high-pressure trifluoromethylation of carbon-rich substrates. *J. Fluorine Chem.* **2018**, *210*, 56-64.

36.   Tokunaga, K.; Ohmori, S.; Kawabata, H. Theoretical study on possible usage of difluoromethylene fullerenes as electron-transport materials. *Thin Solid Films* **2009**, *518*, 477-480.

37.   Brotsman, V. A.; Ioutsi, V. A.; Rybalchenko, A. V.; Bogdanov, V. P.; Sokolov, S. A.; Belov, N. M.; Lukonina, N. S.; Markov, V. Y.; Ioffe, I. N.; Troyanov, S. I.; Magdesieva, T. V.; Trukhanov, V. A.; Paraschuk, D. Y.; Goryunkov, A. A. Alkylated [6,6]-open

difluoromethanofullerenes C60(CF2)R2: Facile synthesis, electrochemical behavior and photovoltaic applications. *Electrochim. Acta* **2016**, *219*, 130-142.

38.   Baker, R. J.; Colavita, P. E.; Murphy, D. M.; Platts, J. A.; Wallis, J. D. Fluorine–Fluorine Interactions in the Solid State: An Experimental and Theoretical Study. *J. Phys. Chem. A* **2012**, *116*, 1435-1444.

39.   Boltalina, O. V., 1 - Electronic Properties and Applications of Fluorofullerenes. In *New Fluorinated Carbons: Fundamentals and Applications*, Boltalina, O. V.; Nakajima, T., Eds. Elsevier: Boston, 2017; pp 1-34.

40.   Kuvychko, I. V.; Whitaker, J. B.; Larson, B. W.; Folsom, T. C.; Shustova, N. B.; Avdoshenko, S. M.; Chen, Y.-S.; Wen, H.; Wang, X.-B.; Dunsch, L.; Popov, A. A.; Boltalina, O. V.; Strauss, S. H. Substituent effects in a series of 1,7-C60(RF)2 compounds (RF = CF3, C2F5, n-C3F7, i-C3F7, n-C4F9, s-C4F9, n-C8F17): electron affinities, reduction potentials and E(LUMO) values are not always correlated. *Chem. Sci.* **2012**, *3*, 1399-1407.

41.   Clikeman, T. T.; Deng, S. H. M.; Avdoshenko, S.; Wang, X.-B.; Popov , A. A.; Strauss, S. H.; Boltalina, O. V. Fullerene "Superhalogen" Radicals: the Substituent Effect on Electronic Properties of 1,7,11,24,27-C60X5. *Chem. Eur. J.* **2013**, *19*, 15404-15409.

42.   Huang, D.-L.; Dau, P. D.; Liu, H.-T.; Wang, L.-S. High-resolution photoelectron imaging of cold C60− anions and accurate determination of the electron affinity of C60. *J. Chem. Phys.* **2014**, *140*, 224315.

43.   Burke, T. M.; Sweetnam, S.; Vandewal, K.; McGehee, M. D. Beyond Langevin Recombination: How Equilibrium Between Free Carriers and Charge Transfer States Determines the Open-Circuit Voltage of Organic Solar Cells. *Adv. Energy Mater.* **2015**, *5*, 1500123.

44.   Koerner, C.; Ziehlke, H.; Fitzner, R.; Riede, M.; Mishra, A.; Bäuerle, P.; Leo, K., Dicyanovinylene-substituted oligothiophenes for organic solar cells. In *Elementary Processes in Organic Photovoltaics*, Springer: 2017; pp 51-75.

45.   Ndjawa, G. O. N.; Graham, K. R.; Mollinger, S.; Wu, D. M.; Hanifi, D.; Prasanna, R.; Rose, B. D.; Dey, S.; Yu, L.; Brédas, J.-L.; McGehee, M. D.; Salleo, A.; Amassian, A. Open-Circuit Voltage in Organic Solar Cells: The Impacts of Donor Semicrystallinity and Coexistence of Multiple Interfacial Charge-Transfer Bands. *Adv. Energy Mater.* **2017**, *7*, 1601995.

46.   Gasparini, N.; Lucera, L.; Salvador, M.; Prosa, M.; Spyropoulos, G. D.; Kubis, P.; Egelhaaf, H.-J.; Brabec, C. J.; Ameri, T. High-performance ternary organic solar cells with thick active layer exceeding 11% efficiency. *Energ. Environ. Sci.* **2017**, *10*, 885-892.

47.   Zang, Y.; Xin, Q.; Zhao, J.; Lin, J. Effect of Active Layer Thickness on the Performance of Polymer Solar Cells Based on a Highly Efficient Donor Material of PTB7-Th. *J. Phys. Chem. C* **2018**, *122*, 16532-16539.

48.   Moulé, A. J.; Bonekamp, J. B.; Meerholz, K. The effect of active layer thickness and composition on the performance of bulk-heterojunction solar cells. *J. Appl. Phys.* **2006**, *100*, 094503.

49.   Nam, S.; Song, M.; Kim, H.; Bradley, D. D. C.; Kim, Y. Thickness Effect of Bulk Heterojunction Layers on the Performance and Stability of Polymer:Fullerene Solar Cells with Alkylthiothiophene-Containing Polymer. *ACS Sustain. Chem. Eng.* **2017**, *5*, 9263-9270.

50.   Zaumseil, J.; Sirringhaus, H. Electron and Ambipolar Transport in Organic Field-Effect Transistors. *Chem. Rev.* **2007**, *107*, 1296-1323.

51.   Haddon, R. C.; Perel, A. S.; Morris, R. C.; Palstra, T. T. M.; Hebard, A. F.; Fleming, R. M. C-60 Thin-Film Transistors. *Appl. Phys. Lett.* **1995**, *67*, 121-123.

52.   Li, H.; Tee, B. C. K.; Cha, J. J.; Cui, Y.; Chung, J. W.; Lee, S. Y.; Bao, Z. High-Mobility Field-Effect Transistors from Large-Area Solution-Grown Aligned C-60 Single Crystals. *J. Am. Chem. Soc.* **2012**, *134*, 2760-2765.

53.   Zhang, Y.; Murtaza, I.; Meng, H. Development of fullerenes and their derivatives as semiconductors in field-effect transistors: exploring the molecular design. *J. Mater. Chem. C.* **2018**, *6*, 3514-3537.

54.   Ahmed, R.; Simbrunner, C.; Schwabegger, G.; Baig, M. A.; Sitter, H. Air stability of C60 based n-type OFETs. *Synth. Met.* **2014**, *188*, 136-139.

55.   Gatti, T.; Menna, E.; Meneghetti, M.; Maggini, M.; Petrozza, A.; Lamberti, F. The Renaissance of fullerenes with perovskite solar cells. *Nano Energy* **2017**, *41*, 84-100.

56.   Kuvychko, I. V.; Whitaker, J. B.; Larson, B. W.; Raguindin, R. S.; Suhr, K. J.; Strauss, S. H.; Boltalina, O. V. Pressure effect on heterogeneous trifluoromethylation of fullerenes and its application. *J. Fluorine Chem.* **2011**, *132*, 679-685.

57.   Sakamoto, Y.; Komatsu, S.; Suzuki, T. Tetradecafluorosexithiophene: The First Perfluorinated Oligothiophene. *J. Am. Chem. Soc.* **2001**, *123*, 4643-4644.

58.   Raposo, M. M. M.; Fonseca, A. M. c. C.; Kirsch, G. Synthesis of donor–acceptor substituted oligothiophenes by Stille coupling. *Tetrahedron* **2004**, *60*, 4071-4078.

59.   Wang, X.-B.; Wang, L.-S. Development of a low-temperature photoelectron spectroscopy instrument using an electrospray ion source and a cryogenically controlled ion trap. *Rev. Sci. Instrum.* **2008**, *79*, 073108.

CHAPTER 2. IMPROVED SYNTHESIS OF
9,10-BIS(PERFLUOROBENZYL)ANTHRACENE

2.1 Introduction

Indoor and display lighting accounted for 10% of commercial sector electricity consumed in the U.S. in 2018.[1] Higher light-production efficiency would lower energy costs, decrease dependence on fossil fuels, and profoundly benefit the environment by reducing greenhouse-gas emissions. A viable step in that direction is to develop a more efficient light-production technology while maintaining cost effectiveness.

Low cost is necessary to make lighting technology available to a majority of residential and commercial users. Light-emitting diodes (LEDs) are currently the most efficient form of lighting, but they are also the most expensive form because they contain rare semi-metals such as gallium, indium, and selenium.[2] Organic light-emitting diodes (OLEDs) are the best alternative to high-cost LEDs because they can use molecular metal-complex phosphors with earth-abundant organic ligands or polycyclic aromatic hydrocarbons (PAHs). OLEDs can be solution processed, avoiding costly vapor-deposition processing. Additionally, OLEDs have potential for widespread use in solid state lighting as well as display technology. For OLED displays to be successful, highly soluble, efficient, and stable red, green and blue emitters are necessary.[3] Within these three colors, stable blue emitters are the most difficult to achieve. The high energy levels of blue emitters often lead to an increased likelihood of degradation.[4] Unfortunately, OLEDs are often made with organic ligands requiring multi-step syntheses, which are often susceptible to rapid degradation over time.[3,5-6]

Anthracene and its derivatives have previously been identified as potential molecules for blue emitting OLEDs due to their high thermal stability and high quantum yields.[7-11] In fact,

9,10-diphenylanthracene (9,10-ANTH(Ph)$_2$) has a quantum yield (Φ_f) of near unity (0.84 to 1.00)[12] and has been used as a reference material for quantum yield measurements.[13] It has been shown that anthracene derivatives containing aromatic groups at the 9 and 10-positions lead to improved electroluminescent performance.[8,14-16]

Previous Strauss Boltalina group member, Dr. Long San, identified 9,10-bis(perfluorobenzyl)anthracene (9,10-ANTH(Bn$_F$)$_2$) as a strong blue emitter and determined that it has excellent air and photo-stability as well as having a higher fluorescence quantum yield compared to other fluorinated anthracene derivatives.[17] Additionally, the perfluorobenzyl groups at the 9,10-positions cause the molecule to pack in way such that there is virtually no π-π overlap as shown in **Figure 2.1** and **Figure 2.2**. A lack of close packing has been hypothesized to limit intermolecular emission quenching.[3] Furthermore, it has been predicted through DFT calculations that fluorinated substituents can improve air stability of arenes including anthracene derivatives.[18]

These characteristics make 9,10-ANTH(Bn$_F$)$_2$ an interesting candidate for use in OLEDs. Unfortunately, the current synthetic yield of the compound prevents it from being a viable contender. In the original syntheses performed by San, the yield of 9,10-ANTH(Bn$_F$)$_2$ was was 7%.[17] This was achieved by reacting 5 equivalents of perfluorobenzyl iodide (Bn$_F$I) with anthracene in DMSO with a copper promoter. It is also worth noting that four stages of HPLC were required to isolate 9,10-ANTH(Bn$_F$)$_2$ due to difficulty in separating 9-ANTH(Bn$_F$) from 9,10-ANTH(Bn$_F$)$_2$. In order to perform further studies on 9,10-ANTH(Bn$_F$)$_2$, it was of interest to improve the synthesis and the separation conditions. This has led to an investigation into the optimization of the synthesis of 9,10-ANTH(Bn$_F$)$_2$.

The strategies employed for improving the yield of 9,10-ANTH(Bn$_F$)$_2$ included the following: 1) changing the starting substrate from anthracene to 9,10-dibromoanthracene (9,10-

ANTH(Br)$_2$); 2) changing the solvent; 3) changing parameters within each set of reactions (i.e. reaction time, concentration, equivalents and method of addition of reagents). Additionally, the use of perfluorotertbutyl and perfluoroisopropyl substituents were investigated.

It was hypothesized that the synthesis could be improved by using 9,10-ANTH(Br)$_2$ as the starting material instead of anthracene. Literature suggested this type of reaction would take place at a lower temperature (i.e. 120 °C vs 145 °C) and result in higher selectivity due to the bromine substituents.[19] The weaker carbon–bromine bond is easier to cleave than a carbon–hydrogen bond, resulting in a higher likelihood of radical substitution at those positions. To the best of the author's knowledge, there have not been any examples of perfluorobenzyl substitution of a PAH from research groups other than the Strauss-Boltalina Research Group and perfluorobenzyl substitution of a bromo-substituted PAH has not been achieved prior to this work.[17,20-21]

2.2   Synthesis of 9,10-ANTH(Bn$_F$)$_2$ in dimethyl sulfoxide (DMSO)

In a series of reactions (DMSO 1-7), reaction temperature, the reagent addition method, concentration and equivalents were varied as described in **Table 2.1**. The first attempted reaction (DMSO 1) was performed in DMSO based on literature reaction of perfluoroalkyl groups with bromo-substituted PAHs.[19] The reaction was performed at 120 °C and 9,10-ANTH(Br)$_2$ (1 equiv) was added after Bn$_F$I (5 eq.) had been heated in the presence of copper (5 equiv). This reaction resulted in a mixture of compounds, which included unidentified compounds and a small amount of unreacted 9,10-ANTH(Br)$_2$, as shown in the ^{1}H NMR spectrum (**Figure 2.3**). Additionally, a large amount of biperfluorobenzyl was formed as indicated by the ^{19}F NMR spectrum. This suggests that the perfluorobenzyl radicals reacted with each other before the 9,10-ANTH(Br)$_2$ was added.

In the next reaction (DMSO 2), 9,10-ANTH(Br)$_2$ and Bn$_F$I were heated together at 120 °C. Heating the reagents at the same time resulted in a number of unidentified products, as indicated by ^{1}H NMR spectrum (**Figure 2.3**) that could not be separated via HPLC. In addition, biperfluorobenzyl was again the major compound in the ^{19}F NMR spectrum and 9,10-ANTH(Bn$_F$)$_2$ was not identified in the product mixture.

In reaction DMSO 3, the reaction temperature was increased to 145 °C and the reactants were heated together as in reaction DMSO 2. Reaction DMSO 3 produced 9,10-ANTH(Bn$_F$)$_2$ in observable quantities among other unidentified compounds. This suggests that the higher temperature is necessary to form 9,10-ANTH(Bn$_F$)$_2$.

In reaction DMSO 4, the reaction temperature was kept at 145 °C, but perfluorobenzyl iodide was added to a hot solution of 9,10-ANTH(Br)$_2$. This reaction converted the 9,10-ANTH(Br)$_2$, but it produced a number of unidentified compounds as evidenced by the ^{1}H NMR spectrum (**Figure 2.3**).

The reaction DMSO 5 was performed in the same manner as reaction DMSO 3, except that 10 equivalents of Bn$_F$I were used instead of 5 equivalents. It was hypothesized that more equivalents of Bn$_F$I would lead to an increased yield of 9,10-ANTH(Bn$_F$)$_2$. Interestingly, this did not lead to the formation of more 9,10-ANTH(Bn$_F$)$_2$. Instead, reaction DMSO 5 produced a product mixture that appears similar to reaction DMSO 1 based on their ^{1}H NMR spectra (**Figure 2.3**).

In the reaction DMSO 6, a shorter reaction time of 4 h was tested while otherwise being comparable to reaction DMSO 4. The product mixture of the reaction DMSO 6 appeared to be quite similar to the reaction DMSO 3 as these reactions both produced 9,10-ANTH(Bn$_F$)$_2$ as the

major product among other unidentified products as evidenced by their ^{1}H NMR spectra (**Figure 2.3**).

In the reaction DMSO 7, the concentration of 9,10-ANTH(Br)$_2$ was increased 5-fold compared to reaction DMSO 6. The product mixture of reaction DMSO 7 was quite similar to that of reaction DMSO 4 as evidenced by the ^{1}H NMR spectra (**Figure 2.3**). This similarity was surprising considering the differences in the reaction concentration and the reaction time of DMSO 4 and 7, shown in **Table 2.1**.

2.3   Perfluorotertbutylation and perfluoroisopropylation of 9,10-ANTH(Br)$_2$.

In addition to perfluorobenzyl substitution, perfluorotertbutyl and perfluoroisopropyl substitutions were investigated. In these reactions, analogous conditions from reaction DMSO 3 were used, while substituting perfluoroisopropyl iodide (DMSO iPr) and perfluorotertbutyl iodide (DMSO tBut) for Bn$_F$I.

Both of these reactions appeared to be quite selective. The ^{1}H NMR spectra of the product mixtures each contained one major product. The reaction DMSO iPr was less selective than reaction DMSO tBut as shown in **Figure 2.4** and **Figure 2.5**, respectively. There were two other main products in the DMSO iPr reaction mixture.

The ^{1}H NMR spectrum indicates that the major compound in DMSO tBut was a 9,10-substituted compound based on the proton splitting, but there were not any signals in the ^{19}F NMR spectrum. When single crystals of the compound in DMSO tBut were grown, it was discovered that 9,10-bis(methylsulfanyl)anthracene was the major product (**Figure 2.6**). This was surprising as the only source of sulfur in these reactions is the solvent DMSO. By comparing the ^{1}H NMR spectrum of DMSO iPr F3 (**Figure 2.4**) to the ^{1}H NMR spectrum of the product of the reaction DMSO tBut (**Figure 2.5**), it can be determined that both reactions produced 9,10-

bis(methylsulfanyl)anthracene. It is likely that the steric bulk of the perfluoroisopropyl and perfluorotertbutyl radicals is too large for the substitution reaction to occur. Instead, these radicals reacted with DMSO, which then reacted with the 9,10-ANTH(Br)$_2$. The ^{1}H NMR spectrum of DMSO iPr F1 (**Figure 2.4**) shows that a single substitution also occurred to produce 9-thiomethylanthracene.[22] The major compound in DMSO iPr F2 can be identified by the ^{1}H NMR spectrum as 9-bromoanthracene.

When comparing reactions DMSO 1-7, it was noticed that NMR resonances for the compound 9,10-bis(methylsulfanyl)anthracene were also present in the ^{1}H NMR spectra of reactions DMSO 4-6 (**Figure 2.3**). The reactions DMSO 4 and 6 were different from reactions DMSO 1-3 in that the Bn$_F$I was added after the solution containing 9,10-ANTH(Br)$_2$ and copper was heated. This suggests that in perfluorobenzyl substitution reactions which are heated to a high temperature before a perfluorobenzyl radical is introduced, the DMSO is more susceptible to reaction. The reaction DMSO 7 was the only reaction in which the Bn$_F$I was added after the solution was heated, but the compound 9,10-bis(methylsulfanyl)anthracene was not observed in the product mixture. It is possible that the higher concentration of reaction DMSO 7 led to most of the perfluorobenzyl radicals reacting with the substrate before they could react with the solvent. Unfortunately, reaction DMSO 7 did not lead to the formation of 9,10-ANTH(Bn$_F$)$_2$. Reaction DMSO 5 was different from reactions DMSO 1-3 in that 10 equivalents of Bn$_F$I were used instead of 5 equivalents. This would suggest that such an excess of perfluorobenzyl radicals leads to a higher probability that some perfluorobenzyl radicals will react with the solvent before they react with the substrate.

2.4   Synthesis of 9,10-ANTH(Bn$_F$)$_2$ in chlorobenzene

Chlorobenzene was selected as a new solvent for this synthesis mainly due to its boiling point near 140 °C, since it was shown in the reactions using DMSO that high temperatures are necessary for this reaction to proceed. It was hypothesized that the substrate would be more reactive than the solvent, considering the relative bond dissociation energies of C-Br (285 kJ/mol) vs C-Cl (339 kJ/mol).[23] Four reactions in chlorobenzene are reported (PhCl 1-4) as described in **Table 2.2**.

In reactions PhCl 1 and PhCl 2, both reactions were performed with 5 equivalents of Bn$_F$I, while the mixture was heated at once in reaction PhCl 1, and the Bn$_F$I was added after the other reagents had been heated to reflux in reaction PhCl 2. As shown in **Figure 2.7**, there was a slight increase in the yield of 9,10-ANTH(Bn$_F$)$_2$ in reaction PhCl 2 compared to reaction PhCl 1, relative to the starting material, 9,10-ANTH(Br)$_2$. Reaction PhCl 3 used the same reaction conditions as reaction PhCl 2, but this reaction was allowed to proceed for 48 hours. This allowed for complete conversion of the 9,10-ANTH(Br)$_2$, however the isolated yield of 9,10-ANTH(Bn$_F$)$_2$ was only 5%.

A 5:1 ratio of Bn$_F$I to 9,10-ANTH(Br)$_2$ was used for the reactions PhCl 1-3. Increasing to a 10:1 ratio of Bn$_F$I to 9,10-ANTH(Br)$_2$ while also decreasing the reaction time from 48 h to 5 h for reaction PhCl 4 resulted in the highest yield of either the DMSO or the PhCl reactions (14%). In this reaction, it was determined that a shorter reaction time could be used after TLC conditions had been developed to monitor the reaction. TLC showed that 9,10-ANTH(Br)$_2$ had been consumed after 5 hours when 10 equivalents of Bn$_F$I were used. Interestingly, the ^{1}H NMR spectra of reactions PhCl 3 and PhCl 4 appear to be quite similar (**Figure 2.7**), but there is almost a 3-fold difference in yield of 9,10-ANTH(Bn$_F$)$_2$. This difference can partially be explained in the HPLC chromatograms (**Figure 2.8**). The peak shape of F1 in the chromatogram of reaction PhCl 3

appears to contain more than one major compound. There is also a set of major peaks in the ^{1}H NMR spectrum of PhCl 3 that cannot be assigned. This could be a side product that causes the yield to be lower. These peaks are also present in the ^{1}H NMR spectrum of PhCl 2, which had similar reaction conditions to PhCl 3.

The increased yield of reaction PhCl 4 is likely related to the increase in radical concentration at any one time in the reaction. It should be noted that 3 stages of separation were required to isolate the desired compound 9,10-ANTH(Bn$_F$)$_2$. This is possibly due to reaction between chlorobenzene and perfluorobenzyl radicals. As can be seen in **Figure 2.9**, the HPLC chromatograms at 300 nm and 370 nm are strikingly different. The HPLC trace at 300 nm contains significantly more peaks. While anthracene derivatives absorb at 370 nm, many smaller aromatic compounds only absorb at shorter wavelengths. This difference in the two chromatograms indicates that the solvent, chlorobenzene, reacted to form products that absorb at smaller wavelengths. It is likely that these products caused the difficulty in isolation of 9,10-ANTH(Bn$_F$)$_2$ and consumed a significant amount of Bn$_F$I during the reaction. This could be a reason why 10 equivalents of Bn$_F$I were necessary to obtain a 14% yield of 9,10-ANTH(Bn$_F$)$_2$ in chlorobenzene.

2.5   Synthesis of 9,10-ANTH(Bn$_F$)$_2$ in N-methylpyrrolidone (NMP)

Due to the reactivity of DMSO and chlorobenzene, NMP was chosen as a solvent for its radical stability. Initially, four reactions were studied to understand how variation in reaction time, equivalents of Bn$_F$I, or concentration of 9,10-ANTH(Br)$_2$ affect the yield of 9,10-ANTH(Bn$_F$)$_2$. The reaction conditions are described in further detail in **Table 2.3**. Analysis of crude NMP reactions via NMR spectroscopy proved difficult due to residual NMP, even after extensive washing. HPLC chromatograms were used to analyze the crude reactions as an alternative.

The reaction NMP 1 used 5 equivalents of Bn_FI, a reaction time of 6.5 hours, and a 0.008 mM concentration of 9,10-ANTH(Br)$_2$. As can be seen in **Figure 2.10**, 9,10-ANTH(Bn_F)$_2$ was not the major product. It was hypothesized that the reaction time could have been too short to convert to 9,10-ANTH(Bn_F)$_2$ since there was evidence in the HPLC chromatogram of 9,10-ANTH(Br)$_2$ eluting at 15 minutes. From reaction NMP 1 to reaction NMP 2, the reaction length was increased from 6.5 hours to 20.5 hours, while concentration and equivalents were held constant. This reaction did not noticeably improve the yield of 9,10-ANTH(Bn_F)$_2$ based on the HPLC chromatograms (**Figure 2.10**). The fraction that contains 9,10-ANTH(Bn_F)$_2$ (F1) is not the major fraction in either reaction. Since a longer reaction time did not improve the synthesis of 9,10-ANTH(Bn_F)$_2$, the reaction time of reaction NMP 3 was returned to 6.5 hours and the Bn_FI equivalents were increased from 5 to 10. While this did produce more of the desired compound, it was still a low-yielding reaction based on the HPLC chromatogram (**Figure 2.10**). In the reaction NMP 4, the concentration of 9,10-ANTH(Br)$_2$ was increased from 0.008 mM to 0.02 mM. In this reaction, 9,10-ANTH(Bn_F)$_2$ was the major compound based on HPLC analysis. These four reactions suggest that increasing reaction concentration and decreasing reaction time are beneficial to forming 9,10-ANTH(Bn_F)$_2$.

Based on this, a higher concentration reaction in NMP was carried out. This higher concentration reaction, NMP 5, contained 5 equivalents of Bn_FI and the concentration of 9,10-ANTH(Br)$_2$ was 0.04 mM. NMP 5 was the best reaction to date. After one stage of HPLC separation, shown in **Figure 2.10**, pure 9,10-ANTH(Bn_F)$_2$ was obtained in a 17% yield. This is considerably improved from the initial reactions which required four stages of separation to achieve a 7% yield.

It should be noted that 9,10-ANTH(Br)$_2$ has a significantly longer retention time than 9,10-ANTH(Bn$_F$)$_2$ on a Buckyprep stationary phase. Therefore, it is likely that that a single bromo substituent allows enough interaction with the HPLC stationary phase to aid in the separation, which allows for fewer stages of HPLC to isolate 9,10-ANTH(Bn$_F$)$_2$.

2.6   Summary and Conclusions

From the three sets of reactions, it was found that DMSO was unstable under some reaction conditions with Bn$_F$ radicals present. In chlorobenzene, it was observed that increased Bn$_F$I equivalents, addition of Bn$_F$I after the solution was hot and decreased reaction time were beneficial. It was also determined that in NMP, increased reaction concentration and decreased reaction time were beneficial to forming ANTH(Bn$_F$)$_2$.

It was determined that DMSO and chlorobenzene are not desirable solvents for perfluorobenzyl substitution of 9,10-ANTH(Br)$_2$ as they both have undesirable interactions with the perfluorobenzyl radical. NMP seems to be a good solvent choice for this reaction. The yield of 9,10-ANTH(Bn$_F$)$_2$ achieved in NMP was higher than in DMSO or chlorobenzene. Although the yield was not significantly higher than in chlorobenzene (17% vs 14%), the compound 9,10-ANTH(Bn$_F$)$_2$, could be isolated via a single stage of HPLC separation compared to three or four stages for reactions performed with chlorobenzene or DMSO as the solvent. Overall, 9,10-ANTH(Br)$_2$ appears to be a better starting material compared to anthracene when synthesizing and isolating 9,10-ANTH(Bn$_F$)$_2$.

2.7   Experimental

2.7.1   Reagents and Materials

The following reagents and solvents were obtained from the indicated sources and were used as received or were purified/treated/stored as indicated. Heptafluorobenzyl iodide, 98% (SynQuest),

iodononafluoro-t-butane, 97% (SynQuest), 2-iodoheptafluoropropane, 97% (SynQuest), dibromoanthracene, 98% (Alfa Aesar), copper powder 99% Lot number A1141129 (Strem Chemical), chlorobenenzene, ACS (Sigma, dried on 3Å molecular sieves), dimethyl sulfoxide, ACS (Sigma, dried on 3Å molecular sieves), N-methylpyrrolidone, ACS (Sigma, dried on 3Å molecular sieves).

2.7.2   High Performance Liquid Chromatography

HPLC was conducted using a Shimadzu liquid chromatography instrument (CBM-20A control module, SPD-20A UV-vis detector set to 300 nm, LC-6AD pump, manual injector valve.) The HPLC columns utilized were 25 mm I.D. x 250 nm COSMOSIL Buckyprep column and 10 mm I.D. x 250 nm COSMOSIL Buckyprep column (Nacalai Tesque, Inc.). The eluent was ACS grade acetonitrile, HPLC grade methanol, or a mixture of HPLC grade toluene:heptane (75:25) at a flow rate of 12 mL min^{-1}, 5 mL min^{-1} or 3 mL min^{-1}.

2.7.3 ^{1}H and ^{19}F NMR Analysis:

^{1}H and ^{19}F NMR analyses were acquired on a Varian INOVA instrument. ^{1}H NMR spectra were acquired at 400 MHz. ^{19}F NMR spectra were acquired at 376 MHz. ^{19}F NMR spectra were referenced to hexafluorobenzene ($-\delta = -164.9$).

2.7.4   Synthesis of 9,10-ANTH(Bn$_F$)$_2$ in chlorobenzene

Typically, 9,10-ANTH(Br)$_2$ (0.0134 g, 0.04 mmol, 1 eq.) was mixed with copper powder (100 mg) in a 10 mL round bottom flask, in a glove box. Chlorobenzene (5 mL) was added to the round bottom and a reflux condenser was affixed. The mixture was freeze pump thawed and subsequently heated to reflux. Once reflux was achieved, heptafluorobenzyl iodide (68 uL, 10 eq.) was added via syringe. After 5 hrs, the reaction was removed from the oil bath, covered in aluminum foil, and allowed to cool to room temperature. The reaction mixture was filtered to remove copper. Solvents

were removed *in vacuo* producing an orange oil. 9,10-ANTH(Bn$_F$)$_2$ was isolated via two stages of HPLC separation. Changes were made to each reaction performed in chlorobenzene. These changes can be found in **Table 2.2**. In reactions which required all reagents to be heated together, the perfluorobenzyl iodide was added and the mixture was freeze pump thawed three times before being placed in the oil bath.

2.7.5   Synthesis of 9,10-ANTH(Bn$_F$)$_2$ in DMSO or NMP

Typically, 9,10-ANTH(Br)$_2$ (0.0132 g, 0.04 mmol, 1 eq.) was mixed with copper powder (100 mg) in a 10 mL rotavis reaction tube fitted with a wired septa in the glovebox. NMP (5 mL) was added to the reaction tube and the mixture was degassed with N$_2$. The mixture was subsequently heated to 145 °C. Once reflux was achieved, heptafluorobenzyl iodide (34 μL, 5 eq.) was added dropwise via syringe. After 4 hrs, the reaction was removed from oil bath, covered in aluminum foil, and allowed to cool to room temperature. The reaction mixture was filtered to remove copper. Solvents were removed *in vacuo* producing an orange oil. 9,10-ANTH(Bn$_F$)$_2$ was isolated via one stage of HPLC separation in methanol for reactions in NMP, while reactions in DMSO required multiple stages of separation. Changes were made to each reaction performed in NMP and DMSO. These changes can be found in **Table 2.1** and **Table 2.3**. In reactions which required all reagents to be heated together, the perfluorobenzyl iodide was added and the mixture was freeze pump thawed three times before being placed in the oil bath.

Table 2.1. DMSO reactions 1-7.

Reaction	Bn$_F$I Equiv	Method of Addition of Bn$_F$I	Temperature (°C)	[9,10-ANTH(Br)$_2$] (mM)	time (h)
DMSO 1	5	added before Br$_2$ANTH	120	0.02	12
DMSO 2	5	all heated together	120	0.02	11
DMSO 3	5	all heated together	145	0.007	15
DMSO 4	5	dropwise after hot	145	0.007	12
DMSO 5	10	all heated together	145	0.008	16
DMSO 6	5	dropwise after hot	145	0.008	4
DMSO 7	5	dropwise after hot	145	0.04	4

[a] Reaction method of addition for Bn$_F$I or equivalents of Bn$_F$I are varied.

Table 2.2. Chlorobenzene reactions 1-4.

Reaction	Bn$_F$I Equiv	Time (h)	Method of Addition of Bn$_F$I	Isolated Yield of 9,10-ANTH(Bn$_F$)$_2$
PhCl 1	5	16	all heated together	n/a
PhCl 2	5	16	dropwise after hot	n/a
PhCl 3	5	48	dropwise after hot	5%
PhCl 4	10	5	dropwise after hot	14%

[a]Reaction time, method of Bn$_F$I addition, and equivalents are varied to determine how the reaction is affected by these variables.
[b]Yields are reported for PhCl 3 and 4 since they were separated completely.
[c]The concentration of 9,10-ANTH(Br)$_2$ in PhCl 1-3 is 0.004 mM. In PhCl 4, the concentration was 0.008 mM.
[d]Reactions were all performed at 135 °C (reflux).

Table 2.3. NMP reactions 1-5.

Reaction	BnₐI Equiv	Time (h)	[9,10-ANTH(Br)$_2$] (mM)	Method of Addition of Bn$_F$I	Temperature (°C)
NMP 1	5	7	0.008	all heated together	135
NMP 2	5	20.5	0.008	all heated together	135
NMP 3	10	6.5	0.008	all heated together	135
NMP 4	10	6.5	0.02	all heated together	135
NMP 5	5	4	0.04	dropwise after hot	145

[a]Reaction time, equivalents of Bn$_F$I or concentration of 9,10-ANTH(Br)$_2$ are varied to determine how the reaction is affected by these variables.
[b]Reactions were all performed at 135 °C and all reagents were heated together.
[c]HPLC traces for these reactions are shown in **Figure 2.10**.
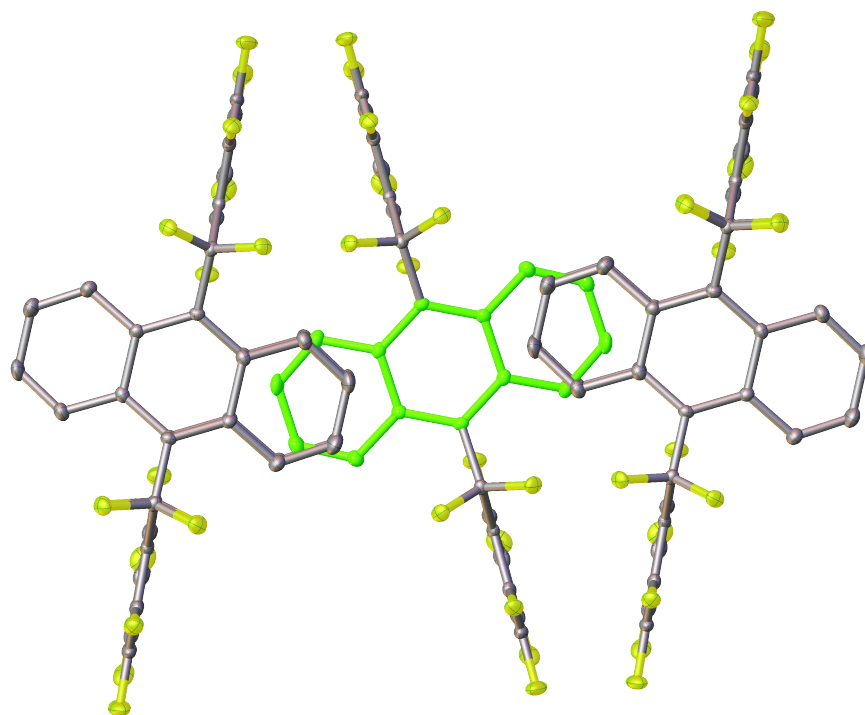
Figure 2.1. Top view of the solid-state packing of 9,10-ANTH(Bn$_F$)$_2$. Two different stacked columns are colored in green and grey, and the fluorine atoms are colored in yellow. Hydrogen atoms are omitted for clarity.
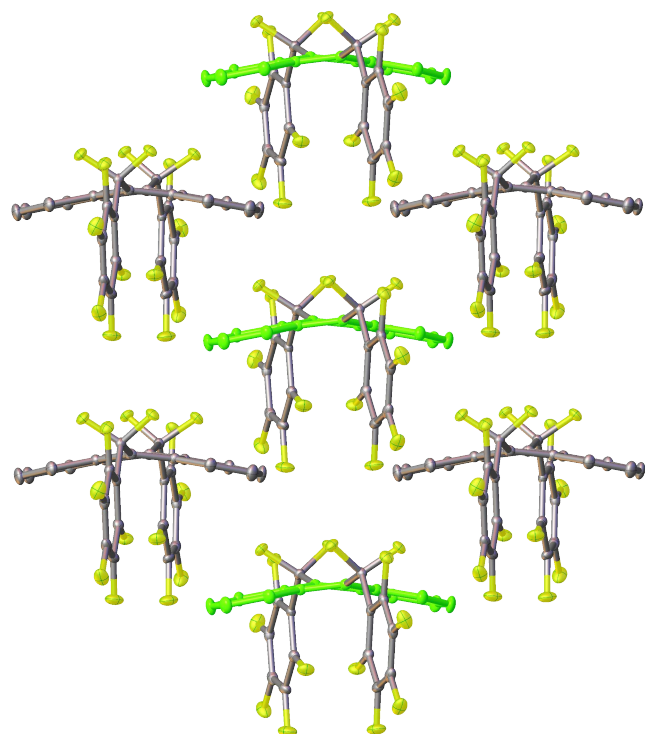
Figure 2.2. Side view of the solid-state packing of 9,10-ANTH(Bn$_F$)$_2$. Two different stacked columns are colored in green and grey, and the fluorine atoms are colored in yellow. Hydrogen atoms are omitted for clarity.
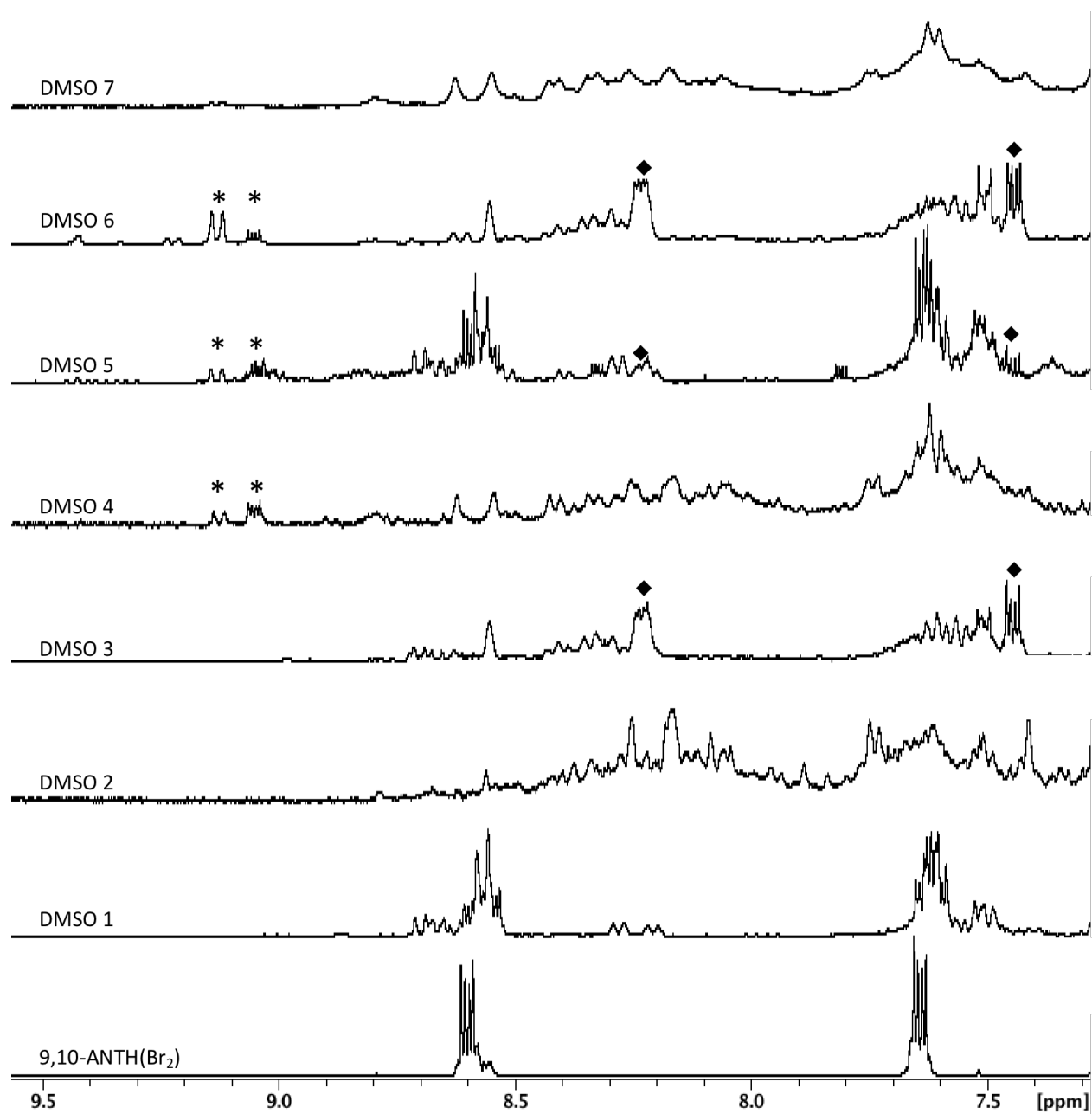
Figure 2.3. ^{1}H NMR spectra of 9,10-ANTH(Br$_2$) and crude DMSO reactions 1-7 recorded in CDCl$_3$. The conditions for these reactions are described in Table **2.1**. The signals for 9,10-ANTH(Bn$_F$)$_2$ are indicated by the diamonds on the spectra.
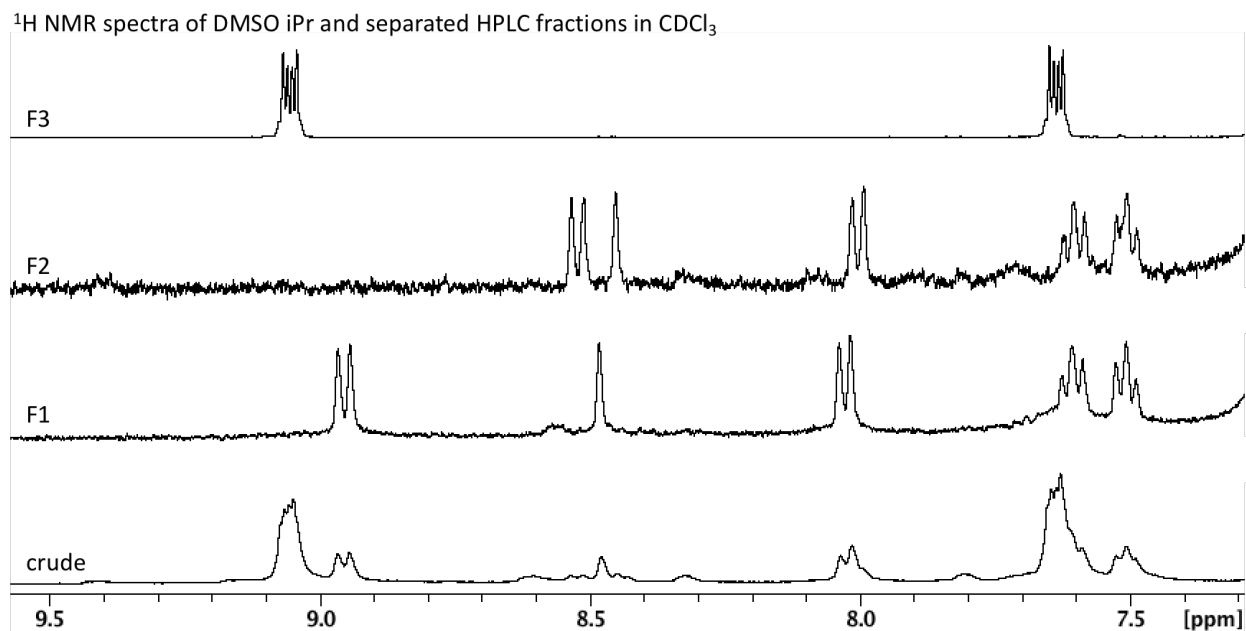
Figure 2.4. ¹H NMR spectra of crude DMSO iPr (perfluoroisopropyl) and the fractions separated from HPLC. This reaction was fairly selective as NMR spectra of the fractions appears to show only 3 major compounds. The ¹⁹F NMR spectra of these fractions did not contain any signals. F1 appears to be 9-thiomethylanthracene.[22] F2 appears to be 9-bromoanthracene.
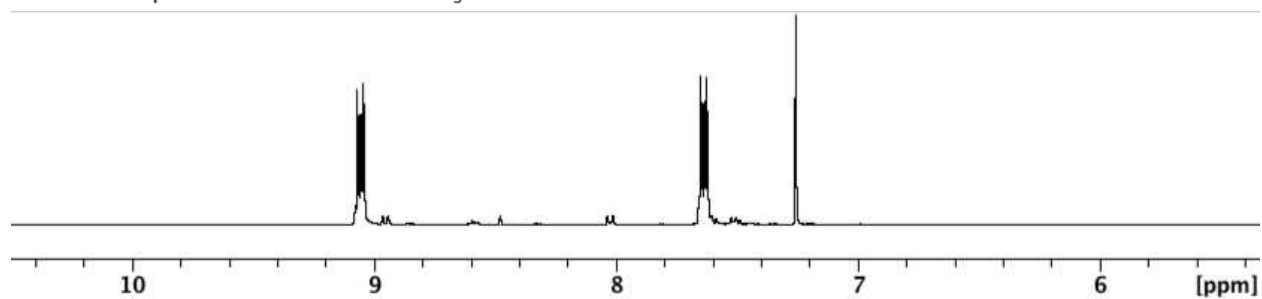
Figure 2.5. ^{1}H NMR spectrum of crude DMSO tBut (perfluorotertbutyl) in CDCl$_3$. Only one major compound is present. Based on the NMR spectrum, it is a compound substituted at the 9,10-positions of anthracene. Single crystals of this compound were grown and it was found to be 9,10-bis(methylsulfanyl)anthracene.
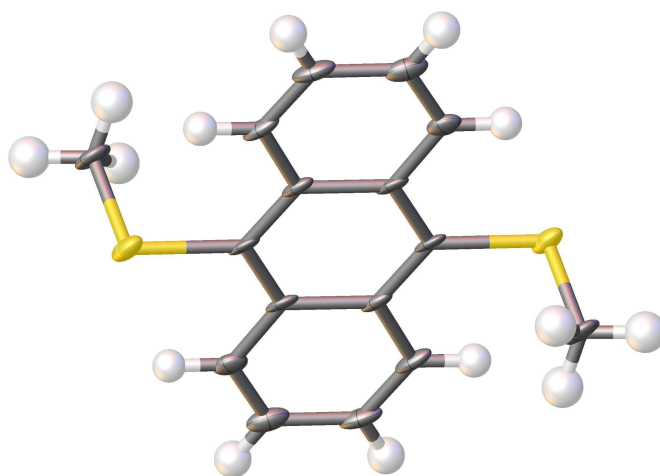
Figure 2.6. Single crystal X-ray structure of 9,10-bis(methylsulfanyl)anthracene. This compound was crystallized from the crude mixture via slow evaporation of dichloromethane. This compound shows that rather than a perfluorotertbutyl radical reacting with 9,10-ANTH(Br)$_2$, the solvent (DMSO) reacted instead. This suggests that the steric bulk of the perfluorotertbutyl and perfluoroisopropyl radicals is too large to react with the substrate, and instead reacts with the solvent first.
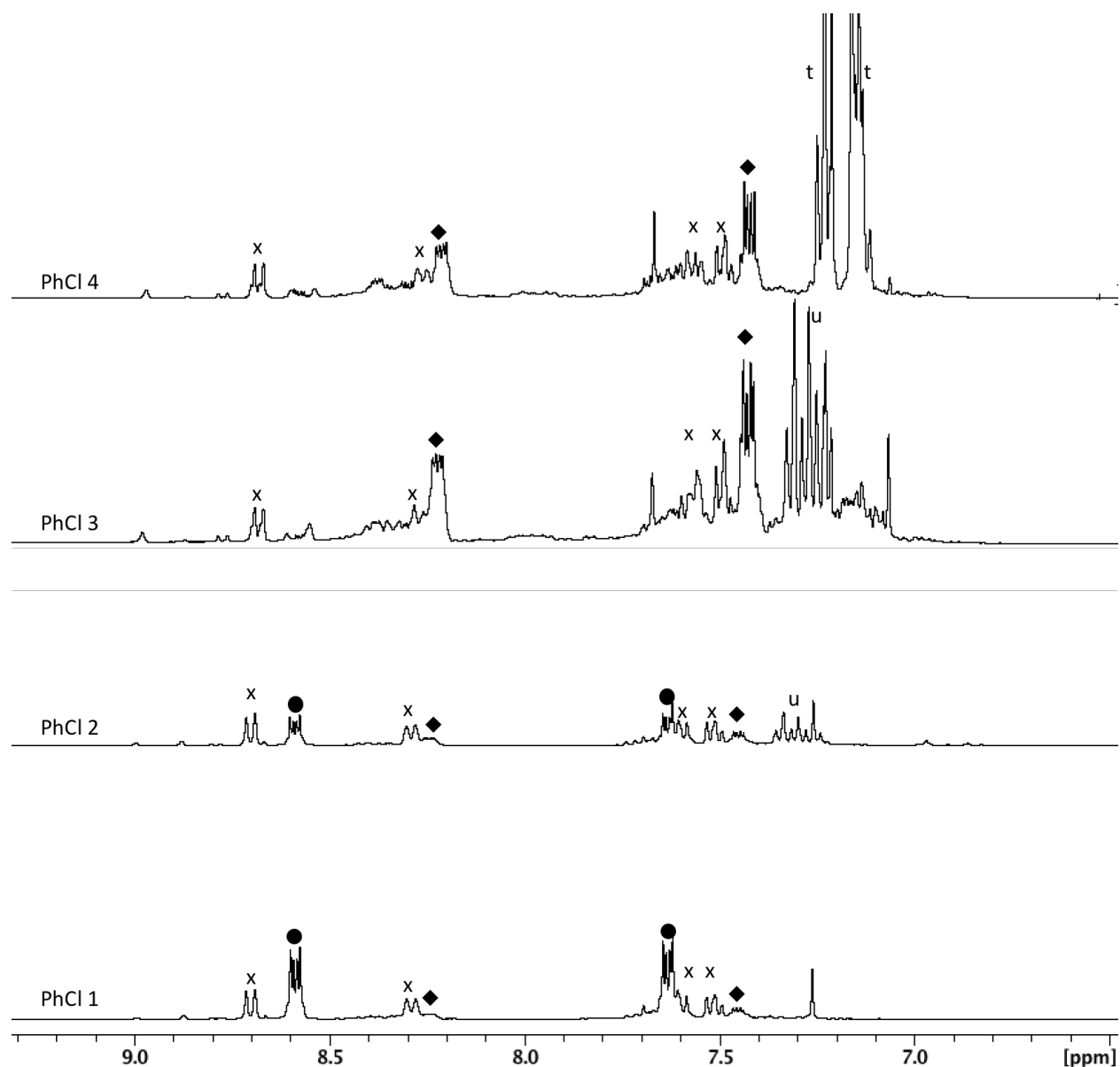
Figure 2.7. ^{1}H NMR spectra of chlorobenzene reactions 1-4. The reaction conditions are described in Table **2.2**. Diamonds indicate 9,10-ANTH(Bn$_F$)$_2$, dots indicate starting material, x symbols indicate the peaks for 9-bromo-10-perfluorobenzylanthracene, t symbols indicate residual toluene, and u symbols indicate an unknown major compound that is produced in PhCl 2 and PhCl 3.
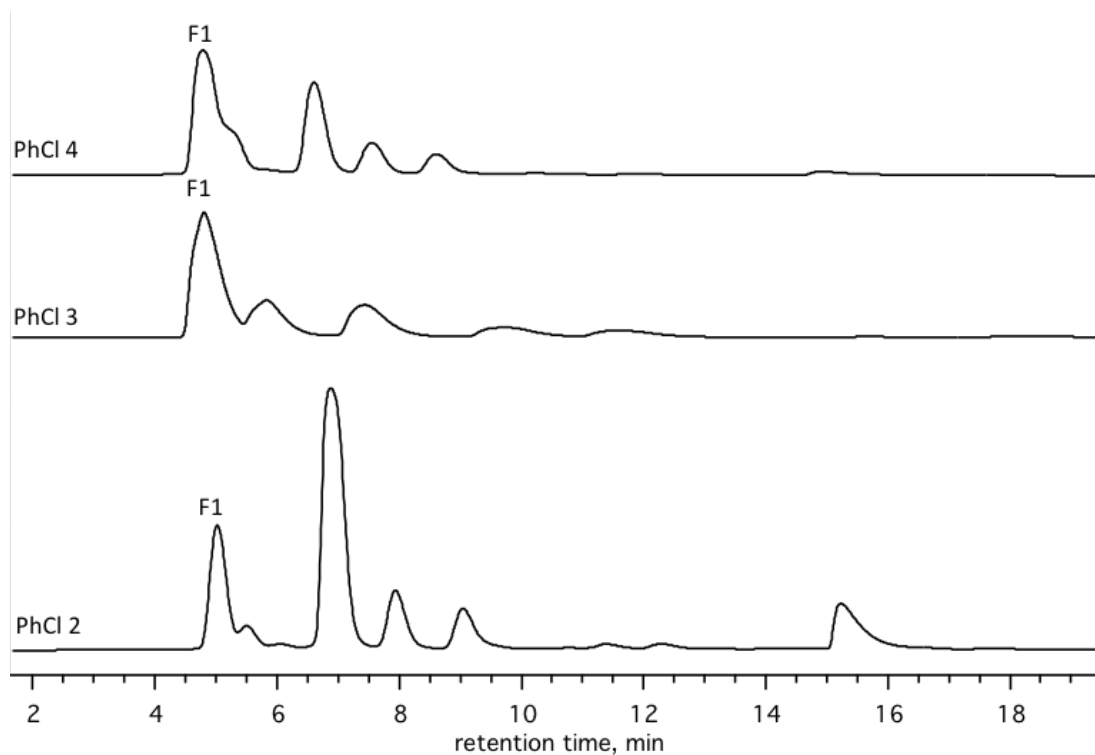
Figure 2.8. HPLC chromatograms of PhCl reactions 2-4. Eluent is 100% acetonitrile on a Buckyprep stationary phase. Reaction conditions for PhCl 2-4 are described in Table 2. The peaks labeled F1 in the chromatograms contain the compound 9,10-ANTH(Bn$_F$)$_2$. PhCl 1 was not analyzed with HPLC, but the crude ^{1}H NMR spectrum showed that there was very little conversion of starting material.
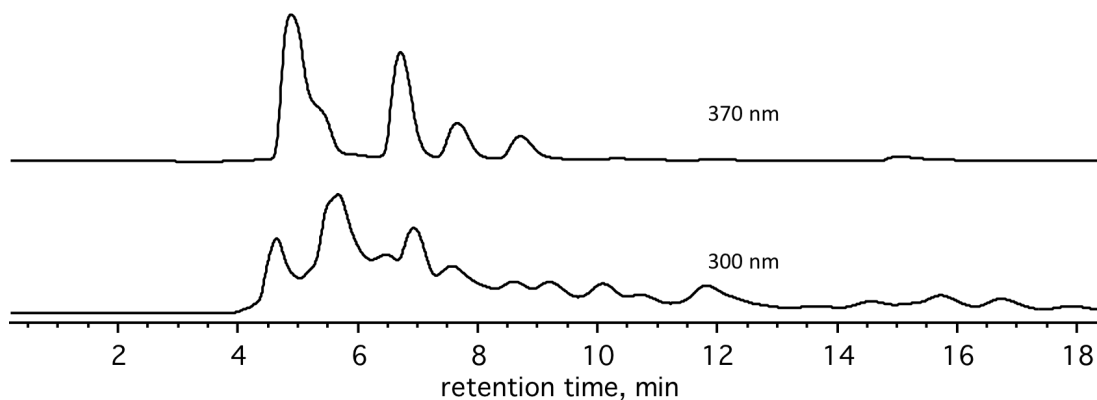
Figure 2.9. HPLC chromatogram of PhCl 4. Eluent is acetonitrile at 5 mL/min. The top chromatogram is recorded at 370 nm, while the bottom chromatogram is recorded at 300 nm. While anthracene derivatives absorb at 370 nm, many smaller aromatic compounds only absorb at shorter wavelengths. This dichotomy between the two wavelengths suggests that the solvent, chlorobenzene, is reacting to form products that absorb at smaller wavelengths.
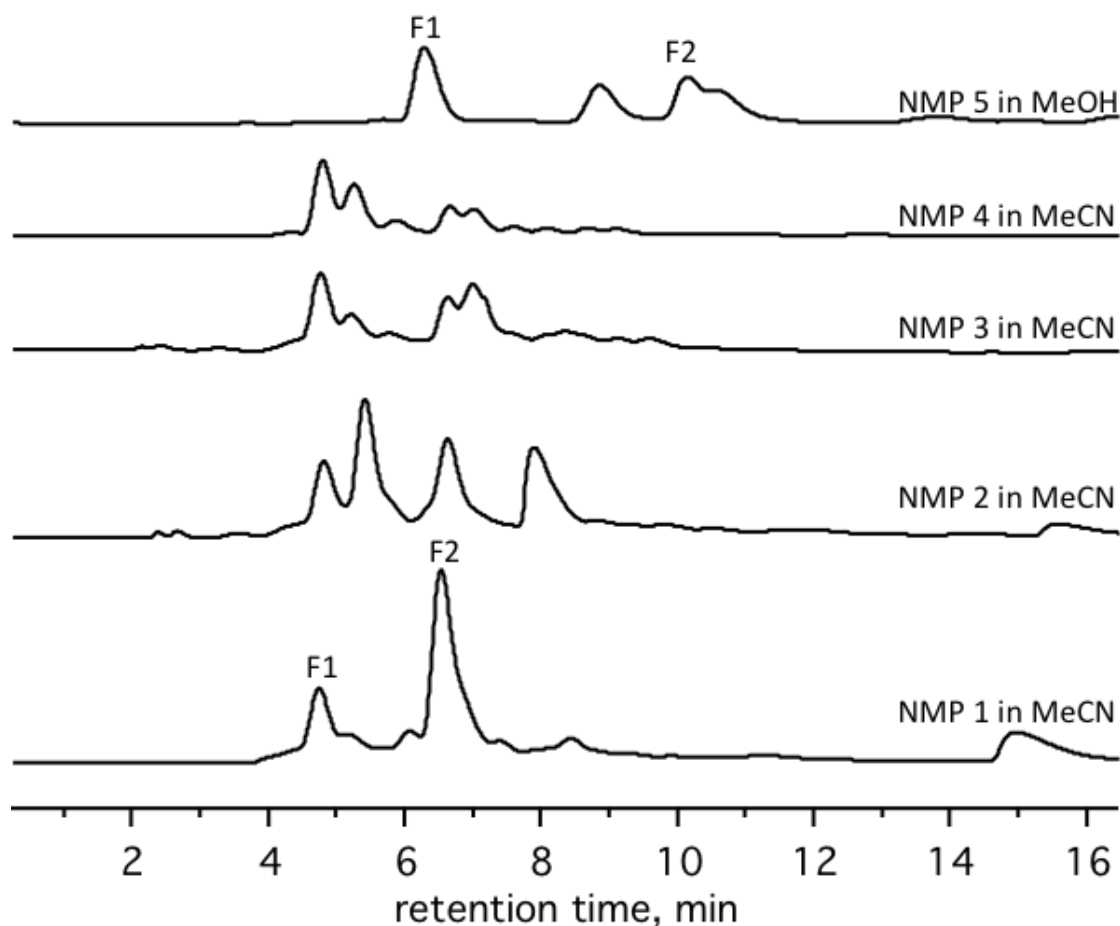
Figure 2.10. HPLC chromatograms of NMP reactions 1-5. Eluent is 100% acetonitrile on a Buckyprep stationary phase for reactions NMP 1-4 and 100% MeOH for reaction NMP 5. Reaction conditions for NMP 1-5 are described in Table 2. The peaks labeled F1 in the chromatograms contain the compound 9,10-ANTH(Bn$_F$)$_2$. The peaks labeled F2 in MeCN and in MeOH chromatograms contain the compound 9-bromo-10-ANTH(Bn$_F$). The intensity of peak F1 relative to the other peaks in a given chromatogram was used to determine whether the changed variable had a positive or negative impact on the reaction. In these plots, it can be observed that increasing reaction concentration and decreasing reaction time are beneficial to forming ANTH(Bn$_F$)$_2$.

CHAPTER 2 REFERENCES

1.   U.S. Energy Information Administration. How much electricity is used for lighting in the United States? https://www.eia.gov/tools/faqs/faq.php?id=99&t=3 (accessed January 20, 2020).

2.   Zhong, C.; Duan, C.; Huang, F.; Wu, H.; Cao, Y. Materials and Devices toward Fully Solution Processable Organic Light-Emitting Diodes. *Chem. Mater.* **2011**, *23*, 326-340.

3.   Zhu, X.-H.; Peng, J.; Cao, Y.; Roncali, J. Solution-processable single-material molecular emitters for organic light-emitting devices. *Chem. Soc. Rev.* **2011**, *40*, 3509-3524.

4.   Yang, X.; Xu, X.; Zhou, G. Recent advances of the emitters for high performance deep-blue organic light-emitting diodes. *J. Mater. Chem. C.* **2015**, *3*, 913-944.

5.   Huang, C.; Zhen, C.-G.; Su, S. P.; Chen, Z.-K.; Liu, X.; Zou, D.-C.; Shi, Y.-R.; Loh, K. P. High-efficiency solution processable electrophosphorescent iridium complexes bearing polyphenylphenyl dendron ligands. *J. Organomet. Chem.* **2009**, *694*, 1317-1324.

6.   Schmidbauer, S.; Hohenleutner, A.; König, B. Chemical Degradation in Organic Light-Emitting Devices: Mechanisms and Implications for the Design of New Materials. *Adv. Mater.* **2013**, *25*, 2114-2129.

7.   Slodek, A.; Filapek, M.; Schab-Balcerzak, E.; Grucela, M.; Kotowicz, S.; Janeczek, H.; Smolarek, K.; Mackowski, S.; Malecki, J. G.; Jedrzejowska, A.; Szafraniec-Gorol, G.; Chrobok, A.; Marcol, B.; Krompiec, S.; Matussek, M. Highly Luminescence Anthracene Derivatives as Promising Materials for OLED Applications. *Eur. J. Org. Chem.* **2016**, *2016*, 4020-4031.

8.   Lee, H. W.; Kim, H. J.; Kim, Y. S.; Kim, J.; Lee, S. E.; Lee, H. W.; Kim, Y. K.; Yoon, S. S. Blue electroluminescent materials based on phenylanthracene-substituted fluorene derivatives for organic light-emitting diodes. *Displays* **2015**, *39*, 1-5.

9.   Garay, R. O.; Naarmann, H.; Muellen, K. Synthesis and characterization of poly(1,4-anthrylenevinylene). *Macromolecules* **1994**, *27*, 1922-1927.

10.   Park, J. K.; Lee, K. H.; Park, J. S.; Seo, J. H.; Kim, Y. K.; Yoon, S. S. Highly Efficient Blue Light-Emitting Diodes Based on Diarylanthracene/Triphenylsilane Compounds. *J. Nanosci. Nanotechnol.* **2011**, *11*, 4357-4362.

11.   Zhang, P.; Dou, W.; Ju, Z.; Yang, L.; Tang, X.; Liu, W.; Wu, Y. A 9,9′-bianthracene-cored molecule enjoying twisted intramolecular charge transfer to enhance radiative-excitons generation for highly efficient deep-blue OLEDs. *Org. Electron.* **2013**, *14*, 915-925.

12.   Hamai, S.; Hirayama, F. Actinometric determination of absolute fluorescence quantum yields. *J. Phys. Chem.* **1983**, *87*, 83-89.

13.   Morris, J. V.; Mahaney, M. A.; Huber, J. R. Fluorescence quantum yield determinations. 9,10-Diphenylanthracene as a reference standard in different solvents. *J. Phys. Chem.* **1976**, *80*, 969-974.

14.   Fukagawa, H.; Shimizu, T.; Ohbe, N.; Tokito, S.; Tokumaru, K.; Fujikake, H. Anthracene derivatives as efficient emitting hosts for blue organic light-emitting diodes utilizing triplet–triplet annihilation. *Org. Electron.* **2012**, *13*, 1197-1203.

15.   Marsitzky, D.; Scott, J. C.; Chen, J. P.; Lee, V. Y.; Miller, R. D.; Setayesh, S.; Müllen, K. Poly-2,8-(indenofluorene-co-anthracene)—A Colorfast Blue-Light-Emitting Random Copolymer. *Adv. Mater.* **2001**, *13*, 1096-1099.

16.   Shi, J.; Tang, C. W. Anthracene derivatives for stable blue-emitting organic electroluminescence devices. *Appl. Phys. Lett.* **2002**, *80*, 3201-3203.

17.   San, L. K. Strong Fullerene and Polycyclic Aromatic Hydrocarbon Electron Acceptors with Perfluorinated Substituents. Ph. D. Dissertation, Colorado State University, 2015.

18.   Sun, H.; Putta, A.; Billion, M. Arene Trifluoromethylation: An Effective Strategy to Obtain Air-Stable n-Type Organic Semiconductors with Tunable Optoelectronic and Electron Transfer Properties. *J. Phys. Chem. A* **2012**, *116*, 8015-8022.

19.   Li, Y.; Tan, L.; Wang, Z.; Qian, H.; Shi, Y.; Hu, W. Air-Stable n-Type Semiconductor: Core-Perfluoroalkylated Perylene Bisimides. *Org. Lett.* **2008**, *10*, 529-532.

20.   San, L. K.; Clikeman, T. T.; Dubceac, C.; Popov, A. A.; Chen, Y.-S.; Petrukhina, M. A.; Strauss, S. H.; Boltalina, O. V. Corannulene Molecular Rotor with Flexible Perfluorobenzyl Blades: Synthesis, Structure and Properties. *Chem. Eur. J.* **2015**, *21*, 9488-9492.

21.   Brook, C. P.; DeWeerd, N.; Strauss, S. H.; Boltalina, O. V. Structural and Electronic Effects in Perfluorobenzylated Perylenes. *J. Fluorine Chem.* **2020**, *231*, 109465.

22.   Saeva, F. D.; Breslin, D. T. Intramolecular photochemical rearrangement via an in-cage cation-radical/radical pair of an anthrylsulfonium salt derivative. *J. Org. Chem.* **1989**, *54*, 712-714.

23.   Klein, D., *Organic Chemistry*. 1st ed.; John Wiley & Sons: Hoboken, NJ, 2012.

CHAPTER 3. POLYTRILFUORMETHYL 1,10-PHENANTHROLINE LIGANDS AND COPPER(I) COMPLEXES: SYNTHESIS, ISOLATION, STRUCTURAL STUDIES, ELECTROCHEMICAL PROPERTIES, AND PHOTOPHYSICAL CHARACTERIZATION

Seven new trifluoromethyl (CF_3) 1,10-phenanthroline (phen) compounds, of which one is a phen derivative with five CF_3 substitutions, four are phen derivatives with four CF_3 substitutions, and two are phen derivatives with three CF_3 substitutions have been isolated and structurally characterized. The compounds and their abbreviations are shown in **Figure 3.1**. The phen compounds have been characterized and examined by single crystal X-ray diffraction (SC-XRD), nuclear magnetic resonance (NMR) spectroscopy, and cyclic voltammetry (CV).

Homoleptic copper(I) phen complexes have been synthesized, in which the phen ligands have 2, 3, and 4 CF_3 groups. The complexes were structurally characterized by NMR spectroscopy, mass spectrometry, and SC-XRD. Additionally, these compounds have been studied via electronic absorption and emission spectroscopy as well as pump-probe transient absorption spectroscopy. Density functional theory (DFT), emission spectroscopy, and pump-probe transient absorption measurements were performed by Dr. Maksim Livshits in Prof. Jeffrey Rack's laboratory at the University of New Mexico.

3.1 Introduction

Polypyridyl Cu(I) complexes featuring low lying metal-to-ligand charge transfer excited-states have drawn much attention due to their similarity to well-studied Ru(II) counterparts.[1-7] Recent reports highlight the use of Cu(I) complexes in photoredox,[8] OLEDs[2] and dye-sensitized solar cells.[1,3] Moreover, unlike many photoactive 1st-row transition metals (Cr^9, Fe^{10-11}, and Co^{12}), these Cu(I) complexes do not suffer from lower-lying metal centered or d–d states, which act to quench the charge-transfer excited state on a sub-picosecond to picosecond time scale. However, initial experiments by McMillin and co-workers demonstrated that the room-temperature emission

lifetime and quantum yield (QY) for Cu(I) polypyridine MLCT excitedstates are smaller than related ruthenium complexes, as well as extremely sensitive to the solvent Lewis basicity.[6,13-14] As bis(diimine) copper(I) complexes are excited, they undergo a metal to ligand charge transfer in which the copper atom is formally oxidized to copper(II). This leads to a structural change in which the pseudo-tetrahedral, D_{2d} complex adopts a flattened square planar conformation. This distortion results in an exposed metal center enabling solvent coordination to shorten the excited-state lifetime. More recent experiments and calculations have demonstrated that the pseudo-Jahn-Teller distortion originating from the Cu(I) d^{10} to Cu(II) d^{9} oxidation occurs on a sub-picosecond timescale lowering the inter-ligand dihedral angle which in turn relaxes the symmetry of the complexes creating more non-radiative excited-state deactivation pathways.[15-19]

A number of attempts have been made to lessen the degree of pseudo-Jahn-Teller distortion in the excited state by adding steric hindrance to the phen ligand. One strategy was to derivatize phen in the 2,9 or 3,8 positions with bulkier functional groups. This strategy has been pursued by a number of researchers and has yielded much success in extending the MLCT lifetime from ns to μs.[20-26] In aggregate, all reports demonstrated that inhibition of the pseudo-Jahn-Teller distortion yields a shift to higher energy of the emission maxima, an increase in the emission QY, and an elongation of the excited-state lifetime measured by time-resolved emission and transient absorption spectroscopy. It should be noted that the largest changes in the inhibition of the pseudo-Jahn-Teller distortion came from increasing the steric bulk of the 2,9 positions from methyl to 2,9-diyl(bis(methanylylidene))bis(2-methylaniline) or 2,9-di(sec-butyl)-3,4,7,8-tetramethyl.[22,25]

An alternative strategy for the inhibition of pseudo-Jahn-Teller distortion is by substitution of the 2,9-methyl groups with 2,9 CF_3 groups.[27] While inhibition of the pseudo-Jahn-Teller distortion was not the original goal for the trifluoromethylation of phen, it was noticed that the

inter-ligand dihedral angle (θ) in the ground state is 87° (close to idealized 90°) compared to the

72 – 83° of the 2,9-dimethyl-1,10-phenanthroline (dmp).[28-29] Further crystal structure comparison

of the Cu(I) 2,9-trifluoromethyl-1,10-phenanthroline (bfp or phen-2-1) complex with different

anions calculated a ground state θ spread from 86 – 90°.[30] The anion dependence of the $[Cu(NN)_2]^+$

single crystal structure has been observed for many Cu(I) complexes and is ascribed to crystal

stress. To complement the ground state change in θ, the $[Cu(phen-2-1)_2]^+$ complex also exhibits a

blue shift in the emission maxima, enhanced QY (almost 10 times) and elongated emission lifetime

relative to the $[Cu(dmp)_2]^+$ similar to the other $[Cu(NN)_2]^+$ complexes with sterically bulkier phen.

These results of the $[Cu(phen-2-1)_2]^+$ are expected as CF_3 groups are bulkier than CH_3 groups,

although it would be expected that CF_3 groups would also lower the ligand LUMO energy resulting

in a slightly lower energy MLCT maxima as observed in trifluoromethylated polypyridyl

ruthenium(II) complexes.[31]

In 2015, Housecroft et al. reported that adding CF_3 groups to bipyridine ligands in copper(I)

dyes has led to improved photocurrents and photoconversion efficiencies in dye sensitized solar

cells.[27] The higher photocurrents are attributed to the increased oxidation potential of the copper(I)

complexes, as well as the increased resistance to the pseudo-Jahn Teller distortion and flattening

that occurs when the complexes are excited. Considering that $[Cu(phen-2-1)_2]^+$ has been reported

to have the highest Cu(II/I) oxidation potential of any bis(phen)copper(I) complex,[32] it is believed

that adding more electron-withdrawing CF_3 substituents, while maintaining steric bulk at the 2,9-

positions, will further increase the oxidation potential of a copper(I) complex.

Unfortunately, little excited state investigation has been performed on the $[Cu(phen-2-1)_2]^+$

beyond ground-state electronic absorption, emission spectra, and emission lifetimes. In addition

$[Cu(NN)_2]^+$complexes with more than two CF_3 groups have not been synthesized or studied prior

to this work. While CF_3 substitutions at the 2,9-position of phen represent an interesting opportunity to increase steric bulk, the use of this steric bulk with more electron withdrawing ligands has not been studied.

Although phen is a versatile ligand with uses ranging from organic, inorganic, and materials chemistry,[33-35] few examples of direct trifluoromethylation of phen have been reported. Macmillan, Baran, and Sanford have all demonstrated radical-based methods for the trifluoromethylation of heterocycles, but these examples do not include phen derivatives as substrates.[36-39] In 2015, Xu et al. demonstrated a first example of copper catalyzed direct trifluoromethylation of phen.[40] In the proposed mechanism, phen binds to a copper(II) catalyst, promoting nucleophilic attack at the C=N bond of phen, which is already prone to nucleophilic addition. Based on their reported results and the proposed mechanism, it is likely that this reactivity is limited to the 2-position of phen. In addition to direct methods, indirect methods have been employed by Beer et al. to trifluoromethylate phen.[41] This method involves converting dmp into 2,9-bis(trichloromethyl)-1,10-phenanthroline, followed by conversion to phen-2-1.

Herein, two methods for the synthesis of trifluoromethylated phen derivatives are reported, including the direct radical trifluoromethylation of phen-2-1 to target specific isomers of trifluoromethylated phen with 3 and 4 substitutions in moderate to good yields. Additionally, the synthesis and excited-state dynamics are reported for a series of trifluoromethylated copper(I) phen complexes with 2, 3, and 4 CF_3 groups, in which all phen ligands are substituted at the 2,9-positions with CF_3 groups. The excited-state evolution for all complexes is reported, examining the effect of the number and position of CF_3 groups on the phen core on the excited state pseudo-Jahn-Teller distortion using ultrafast pump-probe and nanosecond flash photolysis transient absorption. Preliminary restricted and unrestricted DFT and time-dependent density functional theory

(TDDFT) electronic structure calculations were performed to optimize the ground state (S_0), lowest energy triplet (T_1), and singlet (S_1) excited states as well as the singlet state with the largest transition oscillator strength from the ground state (S_n). All of the trifluoromethylated ligands have identical steric bulk at the 2,9-positions, making it possible to make correlations between the number of electron withdrawing groups and excited-state lifetimes and quantum yields.

3.1.1 Synthesis of phen(CF$_3$)$_n$ Method 1

Trifluoromethylated phen derivatives were synthesized via a hot radical method utilized by the Strauss Boltalina Research Group (**Scheme 3.1**).[42] This ampoule reaction was performed by former Strauss Boltalina Research Group postdoctoral researcher, Dr. Igor Kuvychko. All isolation and characterization was performed by the author or this dissertation. This method allows for the substitution of aromatic hydrogens with $CF_3 \bullet$ radicals that are generated from CF_3I gas. It is well known to produce a large number of compounds with a different number of substitutions and substitution patterns. Compounds with 3, 4, and 5 CF_3 substitutions were isolated from the reaction of 10 equivalents of $CF_3I(g)$ and one equivalent of phenanthroline monohydrate in a sealed ampoule that was heated at 330 ºC for 10 h. It should be noted that these were not optimized conditions as Dr. Kuvychko was screening the reactivity of different polycyclic aromatic hydrocarbons (PAH) with this method. Isolation of the phen(CF$_3$)$_x$ compounds was achieved through multiple steps of HPLC described below. The yields for isolated compounds were low ranging from 0.1-2.4%. The highest yielding compounds were substituted with four CF_3 groups.

3.1.2 HPLC purification of phen(CF$_3$)$_n$ compounds from Method 1

Primary separation of the phen(CF$_3$)$_n$ derivatives was performed on a semi-preparative Cosmosil Buckyprep HPLC column with acetonitrile as the eluent (**Figure 3.2**). This separation

afforded five major fractions, of which four required secondary separation to yield pure isomers of tris, tetra and penta-substituted trifluoromethylated phen derivatives.

The compound 2-hydroxyl-3,5,7,9-tetrakis(trifluoromethyl)-1,10-phenanthroline (2-OH-phen-4-1) was isolated from Fraction 5 at 12.7-14.5 min as the only pure compound produced from the primary separation (11 mg, 0.024 mmol, 1.9 % yield).

Secondary separation of Fraction 1 (3.0-3.9 min) in MeOH at 5 mL/min led to the isolation of 2,4,6,7,9-pentakis(trifluoromethyl)-1,10-phenanthroline (phen-5-1) at 6.8-7.7 min (0.4 mg, 0.0008 mmol, 0.06 % yield).

Secondary separation of Fraction 2 (4.0-4.8 min) in MeOH at 5 mL/min led to the isolation of 2,5,9-tris(trifluoromethyl)-1,10-phenanthroline (phen-3-1) at 16.5-17.5 min (0.7 mg, 0.002 mmol, 0.16 % yield).

Fraction 3 was sonicated in heptane, and insoluble materials were filtered off (approximately 2 mg, which did not show observable NMR signals when dissolved in $CDCl_3$). The heptane-soluble material (F3H) was then separated in a 25:75 toluene:heptane mixture. This significantly improved the separation and yielded two major compounds. The compound 2,4,7,9-tetra(trifluoromethyl)-1,10-phenanthroline (phen-4-2) was isolated at 6.5-7.5 min (2.7 mg, 0.006 mmol, 0.5 % yield). The compound 2,4,6,9-tetrakis(trifluoromethyl)-1,10-phenanthroline (phen-4-1) was isolated at 7.5-8.2 min (14.1 mg, 0.031 mmol, 2.4 % yield). The highest yielding isolable compound from the reaction mixture was phen-4-1.

Secondary separation of Fraction 4 (6.0-6.8 min) in MeOH at 5 mL/min allowed for the collection of a fraction at 18.5 min (F4b). F4b was sonicated in a mixture of 75:25 heptane:toluene and filtered. Soluble material was dried and recrystallized from DCM. High quality single crystals

were isolated from this mixture allowing for the identification of 2,4,6,8-tetrakis(trifluoromethyl)-1,10-phenanthroline (phen-4-3).

3.1.3   Synthesis Method 2: Selective Trifluoromethylation of phen

In Method 1, 1,10-phenanthroline monohydrate was used as the starting material. This reaction resulted in phen derivatives with 3-5 CF_3 groups with poor selectivity and poor yields for each isomer. Initial attempts to improve selectivity included lowering the equivalents of CF_3I gas in ampoule reactions. This always resulted in significant amounts of carbonaceous char in addition to poor selectivity. In previous work on the trifluoromethylation of phenazine, it was shown that longer reaction times led to a higher number of additions.[43] It has also been shown through DFT calculations on corannulene derivatives that there is a relative energy difference of approximately 50 kJ/mol comparing compounds with ortho CF_3 groups and compounds without adjacent CF_3 groups.[44] Based on this information, it was hypothesized that steric bulk and reaction time could be used to direct •CF_3 radical substitution of phen and limit the number of possible isomers. To test this hypothesis, phen-2-1 was used as the starting material and four reactions were performed with different reactions times, ranging from 20 minutes to 10 hours.

As shown in **Scheme 3.2**, by starting with phen-2-1, two of the 8 positions are blocked from substitution. In addition, the 3 and 8 positions are less likely to be substituted due to the steric bulk of CF_3 groups. This suggests that the most probable positions to be substituted are the 4, 5, 6, and 7 positions. Due to the inherent symmetry of phen, when reaction conditions are controlled for a single substitution, there are only two likely major products of the reaction, phen-3-1 and 2,4,9-tris(trifluoromethyl)-1,10-phenanthroline (phen-3-2). It was found that varying the reaction time while keeping pressure of CF_3I constant allowed for control over the number of CF_3 substitutions. While a 20 min reaction (R1) targeted compounds with 3 substitutions, there was

unreacted phen-2-1 (**Figure 3.3** R1). By increasing reaction time to 40 minutes (R2), the major

product was phen-3-1 (82% of crude measured by NMR spectroscopy, **Figure 3.3** R2), the starting

material was consumed, and a small amount of phen-4-1 was present (6% of crude). From this

reaction, phen-3-1 was isolated in 63% yield, which is a major increase from the 0.16% yield in

Method 1. Interestingly, phen-3-2 was only a very minor product in this reaction (approximately

2% by NMR spectroscopy). This can likely be explained due to the 5,6-positions being

significantly less sterically encumbered and more open to CF_3 radical addition than the 4,7-

positions.

Since phen-3-1 does not lead to the formation of phen-4-2, the most likely tetra-substituted

compound to be formed was phen-4-1. Surprisingly, increasing the reaction time to 3 h (R3) only

yielded a small amount more phen-4-1 (**Table 3.3**, **Figure 3.3**). It required a 10 h reaction (R4) to

increase the conversion to the point that it was the major product (60% by ^{19}F NMR spectroscopy)

as shown in **Figure 3.3** and **Table 3.3**.

3.1.4   Isolation of phen(CF$_3$)$_n$ compounds from Method 2

One stage of HPLC separation in 100% MeOH yielded 5 fractions, in which the CF_3 phen

derivatives are well separated (**Figure 3.4**). This is significantly improved from the multiple stages

of HPLC required in the Method 1 separation.

3.1.5   Characterization of phen(CF$_3$)$_n$ by NMR Spectroscopy and SC-XRD

Single crystals for the compounds phen-3-1, phen-3-2, phen-4-1, phen-4-2, phen-4-3, and

phen-5-1 were grown from dichloromethane or methanol. NMR spectroscopy and SC-XRD

allowed for the assignment of the structures of all of these compounds. NMR spectra can be found

in Appendix 2. Additionally, the solid-state packing was examined (**Figure 3.5 – Figure 3.9**).

phen-4-1: The four singlets in the ^{19}F NMR spectrum of phen-4-1 suggests the compound is substituted with four non-adjacent CF_3 groups. The ^{1}H NMR spectrum allows for the elucidation of the structure further by revealing there must be two adjacent protons and two protons that are not adjacent to any others. The only possible structural assignment for this molecule is 2,4,6,9-tetra(trifluoromethyl)-1,10-phenanthroline, which was confirmed by SC-XRD as shown in **Figure 3.1**.

phen-4-2: Two singlets in the ^{19}F NMR spectrum and in the ^{1}H NMR spectrum of phen-4-2 suggest the compound is a symmetric phen derivative with four CF_3 substitutions. The singlets in the ^{19}F and ^{1}H NMR spectra also show that there are no coupled protons or CF_3 groups suggesting that there are no adjacent groups or if there are, they are symmetrically equivalent. In ^{19}F NMR spectroscopy, adjacent CF_3 groups on an aromatic molecule that are non-equivalent typically produce a quartet, which was not observed. The two possible assignments for this were 2,4,7,9-tetra(trifluoromethyl)-1,10-phenanthroline and 2,5,6,9-tetra(trifluoromethyl)-1,10-phenanthroline. SC-XRD confirmed that phen-4-2 was 2,4,7,9-tetra(trifluoromethyl)-1,10-phenanthroline as shown in **Figure 3.1**.

phen-3-1: The ^{19}F NMR spectrum of phen-3-1 contains three singlets, which suggests the compound contains three non-adjacent CF_3 groups. From the ^{1}H NMR spectrum, it can be determined that there are two sets of coupled protons, resulting in four distinct doublets. This evidence narrows down the possible assignments to 2,4,9-tris(trifluoromethyl)-1,10-phenanthroline or 2,5,9-tris(trifluoromethyl)-1,10-phenanthroline. The structure of phen-3-1 was determined to be 2,5,9-tris(trifluoromethyl)-1,10-phenanthroline by SC-XRD as shown in **Figure 3.1**.

phen-3-2: The ^{19}F NMR spectrum of phen-3-2 contains a singlet for one CF_3 group and a singlet for two CF_3 groups that are accidentally isochronous. The ^{1}H NMR spectrum contains three doublets that each represent a single proton and a multiplet resulting from two protons. The structure of phen-3-2 was determined to be 2,4,9-tris(trifluoromethyl)-1,10-phenanthroline by SC-XRD as shown in **Figure 3.1**.

phen-5-1: The splitting in the ^{19}F NMR spectrum of phen-5-1, three singlets and two quartets, suggests that there are three non-adjacent CF_3 groups and two coupled (adjacent) CF_3 groups, for a total of five substitutions. This structure was confirmed to be 2,4,5,7,9-pentakis(trifluoromethyl)-1,10-phenanthroline by SC-XRD.

phen-4-3: The compound phen-4-3 was isolated by crystallization from dichloromethane out of fraction 4. The compound phen-4-3, as shown in **Figure 3.1**, represents an interesting substitution pattern with four CF_3 substitutions where only one CF_3 is substituted ortho to a nitrogen. This substitution pattern is very similar to phen-4-1 with the exception of the CF_3 substituted at the 9-position being shifted over to the 8-position on phen.

2-OH-phen-4-1: The ^{19}F NMR spectrum for 2-OH-phen-4-1 shows 4 singlets, meaning that there are no adjacent CF_3 groups on the molecule. There are also four singlets in the ^{1}H NMR spectrum, similar to phen-4-1. The distinctive difference is that one of the singlets in the ^{1}H NMR spectrum is significantly de-shielded and very broad compared to the rest of the protons, suggesting a hydroxyl group is present on the molecule, as shown in **Figure 3.1**. This structure is confirmed by the SC-XRD structure of the Cu(I) complex formed with the ligand shown in Appendix 2 Figure A2.21.

NMR Data for phen(CF$_3$)$_n$ compounds:

phen-2-1:^{19}F NMR: δ −69.9 (singlet, 2 CF$_3$). ^{1}H NMR: δ 8.49 (d, J = 8.3 Hz, 2 H); 8.03 (d, J =8.3 Hz, 2H); 7.99 (singlet, 2H).

phen-3-1: ^{19}F NMR: δ −63.5 (singlet, 1 CF$_3$); −70.3 (singlet, 1 CF$_3$); −70.3 (singlet, 1 CF$_3$). ^{1}H NMR: δ 8.81 (d, J = 8.7, 2H); 8.32 (d, J = 8.7 2H); 8.31 (singlet, 1H), 8.14 (m, 2H).

phen-3-2: ^{19}F NMR: δ −63.9 (singlet, 1 CF$_3$); −70.1 (singlet, 2 CF$_3$). δ 8.55 (doublet, J = 8.3 Hz 1 H); 8.32 (m, 2H); 8.16 (d, J = 9.3 Hz, 1H); 8.11 (d, J = 8.4 Hz, 1 H).

phen-4-1: ^{19}F NMR: δ −63.4 (singlet, 1 CF$_3$); −63.7 (singlet, 1 CF$_3$) −70.4 (singlet, 1 CF$_3$); −70.5 (singlet, 1 CF$_3$). ^{1}H NMR: δ 8.86 (d, J = 8.8 Hz 1 H); 8.69 (singlet, 1H); 8.38 (singlet, 1H); 8.21 (d, J = 8.7 Hz, 1 H).

phen-4-2: ^{19}F NMR: δ −63.8 (singlet, 2 CF$_3$). −70.3 (singlet, 2 CF$_3$). ^{1}H NMR: δ 8.48 (singlet, 2 H); 8.36 (singlet, 2H).

phen-4-3: ^{19}F NMR: δ −63.4 (singlet, 1 CF$_3$); −63.5 (singlet, 1 CF$_3$); −65.3 (singlet, 1 CF$_3$); −70.3 (singlet, 1 CF$_3$). ^{1}H NMR: δ 9.62 (singlet, 1H); 8.88 (singlet, 1H); 8.69 (singlet, 1H); 8.42 (singlet, 1H).

phen-5-1: ^{19}F NMR: δ −59.0 (quartet, 1 CF$_3$); −60.3 (quartet, 1 CF$_3$); −63.6 (singlet, 1 CF$_3$); −70.6 (singlet, 1 CF$_3$); −70.7 (singlet, 1 CF$_3$). ^{1}H NMR: δ 8.84 (singlet, 1H); 8.42 (singlet, 1H); 8.39 (singlet, 1H).

2-OH-phen-4-1: ^{19}F NMR: δ −63.0 (singlet, 1 CF$_3$); −64.1 (singlet, 1 CF$_3$) −69.5 (singlet, 1 CF$_3$); −70.6 (singlet, 1 CF$_3$). ^{1}H NMR: δ 10.89 (singlet, 1 H); 8.54 (singlet, 1H); 8.33 (singlet, 1H); 8.29 (singlet, 1 H).

The molecules in phen-3-1 (**Figure 3.5**), phen-3-2 (**Figure 3.6**), phen-4-2 (**Figure 3.7**), are packed in a slip stacked formation within columns, but the columns are oriented in a herringbone

fashion. The compound phen-4-3 packs in a brick layered orientation (**Figure 3.8**). The compound phen-5-1 is packed in a herringbone fashion without significant π-π overlap between adjacent molecules (**Figure 3.9**). The compounds phen-3-1, phen-4-2, and phen-4-3 adopt opposite orientations within columns, while phen-3-2 is oriented in the same direction throughout the columns. The packing of phen-4-1 was not examined due to the low quality of the structure. Interestingly, all of the compounds that are substituted at the 2,9-positions exhibit herringbone packing. The compound phen-2-1 also exhibits herringbone packing.[45] The inter-planar distances range between 3.4 to 3.8 Å with phen-3-2 exhibiting the closest packing (**Table 3.4**).

3.2   Cyclic Voltammetry of phen(CF$_3$)$_n$ compounds

Quasi-reversible electrochemistry was obtained for phen-2-1, phen-3-1, phen-3-2, phen-4-1, and phen-4-2 (**Figure 3.10**). $E_{1/2}$ values are reported in (**Table 3.2**). Unexpectedly, there are large differences (greater than 100 mV) between the different tri-substituted isomers (phen-3-1 vs phen-3-2) and the different tetra-substituted isomers (phen-4-1 vs phen-4-2) of phen. This variation in $E_{1/2}$ of more than 100 mV between isomers is not typical for PAHs.[42-43] Based on their substitution patterns, it seems that the larger changes in $E_{1/2}$ between phen isomers can be attributed to the compounds that have a CF$_3$ directly para to a nitrogen.

3.3   Trifluoromethylated phen Ligands in Homoleptic Copper(I) Complexes

3.3.1   Synthesis and Characterization of Copper(I) Complexes Results

The ligands shown in **Scheme 3.3** were synthesized in a single step reaction and were isolated via HPLC, solubility differences and crystallization techniques as described above. The copper(I) complexes were synthesized as described in Experimental Section 3.4.9-3.4.12. NMR spectra were collected for the ligands and for the copper complexes and mass spectra were collected for the copper complexes (Appendix 2 Figures A2.22 to A2.35). There is a very slight

109

shift in the ^{19}F NMR spectra from the phen-3-1 ligand in comparison to the complex (**Figure 3.11**). A similar result is observed for phen-4-1 and phen-4-2, and phen-2-1. In the case of phen-3-1, the CF$_3$ groups substituted at the 2,9-positions (approximately -70 ppm) become accidentally isochronous when the ligand is bound in the Cu(I) complex. A much more noticeable shift is observed in the ^{1}H NMR spectra comparing ligand and complex (**Figure 3.11**).

SC-XRD structures were obtained for [Cu(phen-3-1)$_2$]SO$_3$CF$_3$ and [Cu(phen-4-1)$_2$]SO$_3$CF$_3$ as shown in **Figure 3.12**. High quality single crystals of [Cu(phen-4-2)$_2$]SO$_3$CF$_3$ were not obtained. The dihedral ligand angle for [Cu(phen-3-1)$_2$]$^+$ is 86.1°. The dihedral ligand angle for [Cu(phen-4-1)$_2$]$^+$ is 85.4°. The Cu-N bond lengths for [Cu(phen-4-1)$_2$]$^+$ are all 2.05 Å. The Cu-N bond lengths for [Cu(phen-3-1)$_2$]$^+$ are 2.04 Å, 2.05 Å, 2.04 Å, 2.03 Å.

When measured in a 0.1M TBAPF$_6$ dichloromethane solution, the $E_{1/2}$ for [Cu(phen-3-1)$_2$]$^+$ was 1.69 V, approximately 140 mV more positive than [Cu(phen-2-1)$_2$]$^+$ (**Figure 3.13**).[32] [Cu(1,10-phen-4-1)$_2$]$^+$ did not show reversible electrochemical behavior, however an oxidation peak was observed at 2.03 V (**Figure 3.14**).

3.3.2 Electronic Absorption and Emission Spectroscopy Results

The absorption spectra of the trifluoromethylated phen [Cu(NN)$_2$]$^+$ complexes (**Scheme 3.3**) investigated here display MLCT absorption maxima at 463, 464, 481 and 482 nm for [Cu(phen-2-1)$_2$]$^+$, [Cu(phen-3-1)$_2$]$^+$, [Cu(phen-4-1)$_2$]$^+$, and [Cu(phen-4-2)$_2$]$^+$, respectively (**Figure 3.15** A, B, C). A higher energy MLCT transition is also observed at 341, 338, 339 and 351 nm for [Cu(phen-2-1)$_2$]$^+$, [Cu(phen-3-1)$_2$]$^+$, [Cu(phen-4-1)$_2$]$^+$, and [Cu(phen-4-2)$_2$]$^+$, respectively (**Figure 3.15** A, B, C). Lastly, a low energy tail is observed in each complex from 500 to 600 nm. The emission spectra for [Cu(phen-2-1)$_2$]$^+$ and [Cu(phen-3-1)$_2$]$^+$ depict a broad featureless transition with maxima near 685 and 718 nm, respectively, assignable to a ligand-to-

metal charge transfer (LMCT) transition. The excitation profiles (dotted traces, **Figure 3.15** A, B) for $[Cu(phen-2-1)_2]^+$ and $[Cu(phen-3-1)_2]^+$ complexes overlap well with their corresponding absorption spectra replicating all spectral features. The $[Cu(phen-4-1)_2]^{2+}$ and $[Cu(phen-4-2)_2]^{2+}$ show evidence of decomposition upon long-term exposure to light and thus their emission spectra were not collected (Appendix 2 Figure A2.36).

3.3.3 Pump Probe Transient Absorption Spectroscopy Results

The pump-probe transient spectra of $[Cu(phen-2-1)_2]^+$ and $[Cu(phen-3-1)_2]^+$ are shown in **Figure 3.16** A and B, respectively. The features of the $[Cu(NN)_2]^+$ complexes consist of two photoinduced excited-state absorption (ESA) transitions from ~350 to 400 nm and from ~500 to 750 nm, as well as a negative peak ranging from 400 to 500 nm. The maxima of the two ESAs appear at 365 and 371 nm as well as 532 and 535 nm for $[Cu(phen-2-1)_2]^+$ and $[Cu(phen-3-1)_2]^+$, respectively. The maxima of the negative signal of $[Cu(phen-2-1)_2]^+$ and $[Cu(phen-3-1)_2]^+$ are observed at 469 and 463 nm, respectively. The excited state "double-peak" absorption from 500 to 625 nm has previously been assigned to a reduced phenanthroline (phen⁻) $\pi^*{\rightarrow}\pi^*$ ligand localized transition in $[Cu(NN)_2]^+$ complexes.[46] For this reason the ESA region from ~500 to 625 is enhanced to highlight important spectral changes in the temporal response at these wavelengths (**Figure 3.16** insets). The negative signal is assigned to the depletion or bleach of the ground state (GSB). The long, low amplitude featureless absorption from 625 to 750 nm has been assigned to LMCT transition. Nanosecond flash photolysis transient absorption spectra for the $[Cu(phen-2-1)_2]^+$ and $[Cu(phen-3-1)_2]^+$ complexes are consistent with the final spectra from the pump-probe transient absorption experiment inferring that no intermediate excited state exists between the two experiments. The time constants from the multi-exponential fitting of the pump-probe transient absorption and nanosecond flash photolysis experiments are summarized in **Table 3.4**.

The pump-probe transient spectra of $[Cu(phen-4-1)_2]^+$ and $[Cu(phen-4-2)_2]^+$ are shown in **Figure 3.17** A and **Figure 3.17** B, respectively. The excited state features for $[Cu(phen-4-1)_2]^+$ and $[Cu(phen-4-2)_2]^+$ are similar to $[Cu(phen-2-1)_2]^+$ and $[Cu(phen-3-1)_2]^+$ for the most part consisting of two photoinduced ESA transitions from ~350 to 400 nm as well as from ~500 to 750 nm and a negative peak ranging from 400 to 500 nm. The assignment of the negative peak from 400 to 500 nm is to the GSB, the ESA from ~500 to 625 is the phen⁻ absorption and 625 to 750 nm is the LMCT absorption. A notable difference is observed for the $[Cu(phen-4-1)_2]^+$ and $[Cu(phen-4-2)_2]^+$ compared with the $[Cu(phen-2-1)_2]^+$ and $[Cu(phen-3-1)_2]^+$ is a second negative absorption observed between 530 to 550 nm. Due to the low amplitude of this second negative absorption as well as the shaped phen⁻ ESA, the second negative absorption is ascribed to the tail of the GSB overlapping with the reduced phen⁻ ESA. Time constants from the multi-exponential fitting of the pump-probe transient absorption and nanosecond flash photolysis experiments are summarized in **Table 3.4**.

In order to understand the results of the new complexes reported here, it was necessary to collect spectroscopic data of the parent complex, $[Cu(dmp)_2](PF_6)$, for comparison. The electronic absorption spectrum of $[Cu(dmp)_2]^+$ features a broad transition with a maximum at 457 nm, a higher energy shoulder near 375 nm and a tail from 500 to 600 nm. The emission spectrum displays a broad transition with a maximum near 750 nm. The excitation spectrum of $[Cu(dmp)_2]^+$ reveals a transition at 434 nm (blue shifted relative to the absorption maxima) with a continuous intensity into the ultraviolet region. While many of the spectral features of the CF_3–derivatized complexes are similar to that of the parent complex (see **Figure 3.15**), there is a noticeable difference in the intensity of the highest energy MLCT near 375 nm. Most notably, this transition has a reduced intensity in the CF_3 complexes. The intensity of this peak is sensitive to the extent of distortion in

the excited state. Pump-probe transient absorption spectra obtained at different time delays for $[Cu(dmp)_2]^+$ (**Figure 3.18 B**) also exhibit two ESA transitions from 350 to 400 nm and from 500 to 750 nm and a GSB ranging from 400 to 500 nm. The maxima of the two ESAs occur at 370 nm and 520 nm. The two ESA peaks from 500 to 625 nm are enhanced to highlight important spectral changes in the temporal response at these wavelengths (**Figure 3.18 C**). Again, the lower energy ESA from ~625 to >750 nm is an LMCT absorption. The flash photolysis transient absorption spectra for $[Cu(dmp)_2]^+$ also show the same features as the pump-probe spectra (Appendix 2 Figure A2.26). Again, all time constants from the multi-exponential fitting of the pump-probe transient absorption and nanosecond flash photolysis experiments can be found in **Table 3.4**. The steady-state absorption and emission, as well as time-resolved transient absorption experiments of $[Cu(dmp)_2](PF_6)$, are consistent with previous reports.

3.3.4 Synthesis and Characterization Discussion

The isolation of phen derivatives with different numbers of CF_3 substituents, as well as derivatives with the same number of CF_3 groups but different substitution patterns, allowed for a systematic study of the metal-ligand interaction. To overcome the poor ligand strength of the tetra-substituted trifluoromethylated ligands, copper(I) trifluoromethanesulfonate toluene complex was used as the copper(I) starting material. It was hypothesized that by using copper(I) trifluoromethanesulfonate toluene complex as the starting material, the combination of a weak anion and the very weakly coordinating toluene ligand would provide the right conditions for ligand exchange with the trifluoromethylated phen ligands. This reaction was performed with phen-4-1, phen-4-2, phen-3-1, and phen-2-1 to form the complexes $[Cu(phen-4-1)_2]SO_3CF_3$, $[Cu(phen-4-2)_2]SO_3CF_3$, $[Cu(phen-3-1)_2]SO_3CF_3$, and $[Cu(phen-2-1)_2]SO_3CF_3$, respectively.

The $[Cu(phen-4-1)_2]^+$ complex shown on the right in **Figure 3.19** shows significantly more space being occupied by the CF_3 groups in comparison to the CH_3 groups in the $[Cu(dmp)_2]^+$ complex. This likely has a significant impact on the pseudo-Jahn-Teller distortion that occurs in the excited state.

When comparing the Cu(I) complex single-crystal structures, the ligand dihedral angles decrease as more CF_3 groups are added. Kovalevsky et al. obtained crystal structures for $[Cu(phen-2-1)_2]SO_3CF_3$ in two different space groups.[30] The structure that has the space group $P2_1/c$ has a dihedral ligand angle of 89.5° while the $C2/c$ structure has dihedral angle of 88.5°. The dihedral ligand angles for $[Cu(phen-3-1)_2]SO_3CF_3$ and $[Cu(phen-4-1)_2]SO_3CF_3$ decrease to 86.1° and 85.4°, respectively. It is likely that the 2,9-substituted CF_3 groups interact with CF_3 groups in the 4, 5, or 6-positions on the opposite ligand, causing the decrease in dihedral angle in the structure. While it is unlikely that this small change has such a dramatic effect, the decrease in dihedral ligand angle does correlate with the decreased excited-state lifetimes for the trifluoromethylated compounds as shown below.

Previous literature, shown in **Table 3.5**, shows that $[Cu(phen-2-1)_2]^+$ has the most positive Cu(II/I) redox potential value at 1.55 V vs SCE of all reported $[Cu(NN)_2]^+$ complexes.[29,32] It was assumed that this is due to the steric bulk at the 2,9-positions and the electron withdrawing nature of two CF_3 groups stabilized the pseudo tetrahedral copper(I) state. It was hypothesized that the increased electron withdrawing character of phen-3-1 and phen-4-1 would increase the redox potential even more. The $E_{1/2}$ for $[Cu(phen-3-1)_2]^+$ was 1.69 V, approximately 140 mV more positive than $[Cu(phen-2-1)_2]^+$ (**Figure 3.13**). To the best of the author's knowledge, this is the highest recorded Cu(II/I) redox potential for a bis(phen)copper(I) complex. $[Cu(phen-4-1)_2]^+$ did not show reversible electrochemical behavior (**Figure 3.14**). The non-reversible behavior is likely

due to the decomposition of $[Cu(phen-4-1)_2]^+$. This would be consistent with the decomposition of $[Cu(phen-4-1)_2]^+$ when it was studied by pump probe transient absorption spectroscopy, which was attributed to the strong electron withdrawing nature and poor coordination of the phen-4-1 ligand.

3.3.5 Steady-State Absorption and Emission Discussion

The steady-state absorption and emission spectroscopy of $[Cu(NN)_2]^+$ are well documented to comprise multiple MLCT transitions ranging from 350 – 650 nm. The lowest energy MLCT transitions occur between 500 – 650 nm and are less intense in comparison to the other CT transitions because they are formally forbidden in a pseudo T_d symmetry (where $\theta \approx 90°$). The primary MLCT transitions are found from ~425 to 485 nm and are thought to be more intense due to the vibronic coupling of low energy Cu–N torsional modes to the electronic transition. The primary MLCT transitions are not symmetry forbidden as low energy transitions. Higher energy MLCT transitions are found from ~350 to ~425 nm and are symmetry forbidden, similar to the low energy transitions in ideal T_d geometry.[6,15] The higher energy MLCT shoulder near 375 nm and low energy MLCT tail are highly sensitive to the degree of distortion, which makes them good spectral areas for comparison. The sharpness of the two primary MLCT transitions as seen in $[Cu(phen-2-1)_2]^+$, $[Cu(phen-3-1)_2]^+$, and $[Cu(phen-4-1)_2]^+$ suggest that minimal distortion occurs as no higher energy shoulder is observed (**Figure 3.15**). The $[Cu(dmp)_2]^+$ and $[Cu(phen-4-2)_2]^+$ complexes feature visibly broader and less resolved absorption spectra.

The emission maximum and QY are also important indicators of excited-state distortion. The emission maximum and QY for the trifluoromethylated phen complexes for which emission could be collected, as well as the dmp analogue, exhibit a clear trend. Ordering the complexes starting with the highest energy emission and QY produces a sequence of $[Cu(phen-2-1)_2]^+$,

$[Cu(phen-3-1)_2]^+$, and $[Cu(dmp)_2]^+$. This emission trend is surprising as one may imagine from previous literature that the addition of a third CF_3 group ($[Cu(phen-3-1)_2]^+$ complex) should exhibit a greater than or equal emission QY and Stokes shift relative to $[Cu(phen-2-1)_2]^+$ complex (a ligand with two CF_3 groups).[29] Similarly, this same trend is also observed when comparing the excitation profiles to the absorption spectrum of $[Cu(phen-2-1)_2]^+$, which overlap perfectly. However, the absorption spectra and excitation profile for $[Cu(dmp)_2]^+$ do not overlap, indicating a change in structure from the Franck-Condon state (initial structure upon electronic absorption) and the emitting state. Thus, the absorption, excitation, and emission spectra of the CF_3 phen complexes indicate that the fluorinated ligands lead to a smaller pseudo-Jahn-Teller distortion relative to $[Cu(dmp)_2]^+$.

Numerous time-resolved experiments (absorption and emission), as well as DFT calculations, have been performed on $[Cu(dmp)_2]^+$ and derivatives. These experiments have made the spectroscopic and kinetic assignments possible, in addition to identifying the GSB and phen$^-$ regions as the most prominent spectral and dynamic indicators for excited-state pseudo-Jahn-Teller distortion.[14,16-17,25] The discussion will focus heavily on the spectral shape and dynamics of these regions. Kinetic analysis of phen$^-$ ESA and GSB spectral regions reveals the presence of three time constants in $[Cu(dmp)_2]^+$, a sub-picosecond time constant, a tens of picosecond time constant and a long ns time constant. The solvent dependence of the sub-picosecond time constant as well as computational modeling have led to the assignment of an excited-state pseudo-Jahn-Teller distortion from $\sim T_d$ to D_2 (coincident with internal conversion).[17] There was an increase in the intensity of the phen$^-$ region in the first 1 ps following excitation which continued to blue shift yielding a "double-peak" transition at 524 and 563 nm (**Figure 3.18 C**). The GSB dynamics depict an initial narrowing of the GSB from 460 to 500 nm in the first 2.5 picoseconds followed by a blue

shift. TDDFT calculations of singlet MLCT energy as a function of θ reveal that the energy of the 3rd singlet state (S_3, state with the highest transition oscillator strength) increases as a function of θ.[18] These calculations also indicate that the excited-state distortion occurs during internal conversion (IC) from the S_3 to S_1 (without a significant population of the S_2) with a time constant of ~300 fs. Similarly, the longer picosecond time constant is attributed to intersystem crossing (ISC) due to the lack of solvent dependence and computational results. Moreover, TDDFT ground-state projections of the singlet and triplet MLCT energy(s) demonstrate that as θ decreases from 90°, the ground state energy increases and the lowest triplet energy decreases, which together produces a large red shift in emission spectra.[15] All GSB and ESA features eventually returned to 0 with a time constant of 66.6 ± 2.1 ns which is assigned as the electron-hole recombination to regenerate the ground state complex (Appendix 2 Figure A2.36).

Based on the steady-state absorption and emission spectra of $[Cu(dmp)_2]^+$ compared with the CF_3 derivatives, a number of differences in the shape of excited state spectra as well as dynamics were anticipated. A major difference can be found in the early spectra and kinetics of CF_3 complexes. The first resolved spectrum at 300 fs following excitation of $[Cu(phen-2-1)_2]^+$ features a narrow single transition at 530 nm, while the $[Cu(phen-3-1)_2]^+$ already has a nicely resolved "double-peak". Both of these first spectra were unlike the broad ESA transition in $[Cu(dmp)_2]^+$ obtained at a similar pump-probe delay. Moreover, the transient spectra of $[Cu(phen-2-1)_2]^+$ and $[Cu(phen-3-1)_2]^+$ only show a modest increase in intensity with a smooth transition to the blue, producing multiple isosbestic points in the process (**Figure 3.16** A, B). Further kinetic analysis of the $[Cu(phen-2-1)_2]^+$ and $[Cu(phen-3-1)_2]^+$ complexes did not reveal a sub-picosecond kinetic phase in the $phen^-$ ESA region (**Table 3.4**). The picosecond kinetics fit well to a single exponential process with time constants of 69 ± 5 and 6.0 ± 2.3 ps for $[Cu(phen-2-1)_2]^+$ and

[Cu(phen-3-1)$_2$]$^+$, respectively. It is suspected that the "double-peak" spectral signature of the phen$^-$ is maintained at longer pump-probe delays, but that the laser line obscures the higher energy peak. The GSB of [Cu(phen-2-1)$_2$]$^+$ and [Cu(phen-3-1)$_2$]$^+$ from 400 – 500 nm also displayed differences in comparison to [Cu(dmp)$_2$]$^+$. The GSB of [Cu(phen-2-1)$_2$]$^+$ and [Cu(phen-3-1)$_2$]$^+$ did not exhibit narrowing or a shift in wavelength, while the GSB of [Cu(dmp)$_2$]$^+$ exhibited both of these spectral changes. Furthermore, unlike the phen$^-$ ESA where [Cu(phen-2-1)$_2$]$^+$ and [Cu(phen-3-1)$_2$]$^+$ exhibited similar changes, the GSB of [Cu(phen-2-1)$_2$]$^+$ and [Cu(phen-3-1)$_2$]$^+$ displayed large differences in the magnitude of the bleach recovery. The GSB of [Cu(phen-2-1)$_2$]$^+$ was resolved by the first transient spectra at 300 fs and exhibited a 48% recovery (at 462 nm) with a time constant of 69 ± 5 ps. The GSB of [Cu(phen-3-1)$_2$]$^+$ was also resolved by the first transient spectra at 300 fs though unlike [Cu(dmp)$_2$]$^+$ and [Cu(phen-2-1)$_2$]$^+$, only a 5% recovery (462 nm) of the GSB was observed with a time constant of 6.0 ± 2.3 ps. The single wavelength kinetic time constants for the changes in the GSB as well as the phen$^-$ ESA are displayed in **Table 3.4**. These differences in temporal and spectral response are undoubtedly due to differences in structural relaxation following MLCT excitation.

A more in-depth insight into these spectroscopic differences in the GSB kinetics may be explained by the DFT optimized structures (Appendix 2 Table A2.3). The excited state S$_n$ and S$_1$ optimization of [Cu(phen-2-1)$_2$]$^+$ yielded a θ of 90°, thus predicting that the distortion will occur during ISC (not during IC as seen in other Cu(I) complexes), which occurs between the S$_1$ ($\theta = 90°$) and T$_1$ ($\theta = 70.6°$). Excited state optimization of [Cu(phen-3-1)$_2$]$^+$ revealed that the distortion begins from the initially prepared Frank-Condon ($\theta = 90°$) states with most of the distortion occurring during adiabatic relaxation of S$_n$ ($\theta = 80°$) and then IC to S$_1$ ($\theta = 78.3°$). A second smaller distortion occurs during ISC for T$_1$ ($\theta = 74.9°$). Based on earlier discussion of [Cu(dmp)$_2$]$^+$

dynamics and DFT optimizations, the picosecond time constant in both $[Cu(phen-2-1)_2]^+$ and $[Cu(phen-3-1)_2]^+$ is ascribed to ISC. As mentioned earlier, the pseudo-Jahn-Teller distortion in $[Cu(phen-2-1)_2]^+$ is likely coincident with ISC, while in $[Cu(phen-3-1)_2]^+$ the distortion is coincident with IC, which occurs faster than the instrument response (earlier than 300 fs). The nanosecond flash photolysis of $[Cu(phen-2-1)_2]^+$ and $[Cu(phen-3-1)_2]^+$ resulted in the same unexpected trend as the emission results. Again the $[Cu(phen-2-1)_2]^+$ had the longest observed lifetime followed by $[Cu(phen-3-1)_2]^+$ and $[Cu(dmp)_2]^+$ (**Table 3.4**). This trend is also contradictory to the calculated trend for θ where the T_1 of $[Cu(phen-3-1)_2]^+$ is less distorted than $[Cu(phen-2-1)_2]^+$. The observed time-resolved dynamics and emission trend is that addition of CF_3 groups past two decreases the excited state lifetime. This suggests that previously observed trends of increased excited-state lifetime with increased steric bulk can be affected, and even reversed, when electron-withdrawing substituents are used.

The observations of $[Cu(phen-2-1)_2]^+$ and $[Cu(phen-3-1)_2]^+$ are consistent with earlier reports of $[Cu(phen-2-1)_2]^+$ where it was also noticed that the emission maxima and QY correlate with results for structurally inhibited complexes while the excited-state lifetime is much shorter.[24] For example, $[Cu(dsbp)_2]^+$ and $[Cu(dsbtmp)_2]^+$, where dsbp and dsbtmp are 2,9-di-sec-butyl-1,10-phenanthroline and 2,9-di-sec-butyl-2,3,7,8-tetramethyl-1,10-phenanthroline, reported by Castellano and co-workers exhibit emission maxima of 690 and 631 nm, respectively, and QY of 4.5×10^{-3} and 6.3×10^{-2}, respectively.[47] Transient absorption of these complexes yielded three kinetic time constants of $0.1-0.4$ ps (τ_1), $6-10$ ps (τ_2) and 380 ns (τ_3) for dsbp and $0.1-0.4$ ps (τ_1), $2-4$ ps (τ_2), and 2.8 μs (τ_3) for dsbtmp complexes in dichloromethane.[25,47] They did not report θ for $[Cu(dsbp)_2]^+$. While the emission maxima and quantum yield of $[Cu(phen-2-1)_2]^+$ and $[Cu(dsbp)_2]^+$ are nearly identical, the excited-state kinetics are substantially different. Recall, for

$[Cu(phen-2-1)_2]^+$, τ_2 is 69 ps and τ_{em} is 98 ns. Thus, while τ_2 is longer (representing ISC), the excited lifetime is not longer, suggesting that the potential energy surfaces for the CF_3 phen complexes are significantly different than the dialkylphenanthroline complexes.

Photodecomposition was observed in each of the complexes, $[Cu(phen-4-1)_2]^+$ and $[Cu(phen-4-2)_2]^+$. The decomposition is most likely caused by the sigma bond inductive withdrawing nature of CF_3 groups on the coordinating phen nitrogen p orbitals, which causes phen-4-1 and phen-4-2 compounds to be worse coordinating ligands. This weak coordination is further evidenced by the longer Cu–N bond lengths of $[Cu(phen-4-1)_2]^+$ compared to $[Cu(phen-3-1)_2]^+$. A consequence of this weaker coordination is seen upon photoexcitation where any low energy Cu–N torsional or bond elongation is breaking the unreduced ligand bonds to copper resulting in bond dissociation. This observation is consistent with trifluoromethylated bipyridine complexes of ruthenium (II) where tetra-trifluoromethylated bipyridine complexes could not be synthesized.[31] Due to the decomposition of $[Cu(phen-4-1)_2]^+$ and $[Cu(phen-4-2)_2]^+$, the observed emission and excitation spectra of these complexes strongly resembles the free ligands (Appendix 2 Figures A2.37-39). The pump-probe transient absorption of both $[Cu(phen-4-1)_2]^+$ and $[Cu(phen-4-2)_2]^+$ complexes is reminiscent of $[Cu(phen-2-1)_2]^+$. Clean isosbestic points are observed at 507 and 573 nm for $[Cu(phen-4-1)_2]^+$ (**Figure 3.17** A), while the $[Cu(phen-4-2)_2]^+$ complex (**Figure 3.17** B) does not have any isosbestic points in the phen$^-$ region. As mentioned in the results section, the strong ground-state overlap with the ESA distorts the phen$^-$ double peak. The formation of the bleach at ~540 nm occurs simultaneously with the blue shift in $[Cu(phen-4-1)_2]^+$ and $[Cu(phen-4-2)_2]^+$ ESA. Surprisingly, the GSB region of $[Cu(phen-4-1)_2]^+$ and $[Cu(phen-4-2)_2]^+$ did not exhibit any major spectral changes on the picosecond time scale suggesting that all the spectral differences originate from the ESA. The kinetic analysis of the single time constant for $[Cu(phen-4-1)_2]^+$ is

consistent with [Cu(phen-3-1)$_2$]$^+$ and is assigned to ISC. Unlike all other CF$_3$ complexes [Cu(phen-4-2)$_2$]$^+$ features important differences. As mentioned in the steady-state results section, the electronic absorption of [Cu(phen-4-2)$_2$]$^+$ shares more similarities with [Cu(dmp)$_2$]$^+$ than with CF$_3$ complexes. The pump-probe transient absorption kinetics also have observable differences. The single wavelength as well as global fitting kinetic of [Cu(phen-2-1)$_2$]$^+$, [Cu(phen-3-1)$_2$]$^+$ and [Cu(phen-4-1)$_2$]$^+$ all exhibit one time constant on the ultrafast time scale yet a second short time constant is only observed in single wavelength fitting of [Cu(phen-4-2)$_2$]$^+$ (**Table 3.4**). The assignment of the ~4 ps time constant is ISC with the 160 ps assigned as a bifurcation leading to decomposition. Again, only a single ns flash photolysis and time-correlated single-wavelength kinetics could be obtained for the [Cu(phen-4-1)$_2$]$^+$ and no flash photolysis data for [Cu(phen-4-2)$_2$]$^+$. The observed lifetime for [Cu(phen-4-1)$_2$]$^+$ was 17 ns, which is shorter than the excited-state lifetime of the other copper complexes (>66 ns; **Table 3.4**). This result is unexpected as the decreased excited-state distortion observed in the ground state absorption and DFT excited state optimized structures would suggest a long-lived excited-state lifetime of the copper complex. The observation of the shorter lifetime is attributed to an observed rate of the photodecomposition reaction in [Cu(phen-4-1)$_2$]$^+$ complex being much faster than the relaxation of ^{3}MLCT to the ground state.

3.3.6   Conclusions

In summary, two methods for the synthesis of trifluoromethylated phenanthroline derivatives was reported. It was found that the electrochemical properties of the compound are heavily dependent on the substitution pattern. Additionally, the synthesis and characterization of trifluoromethylated copper(I) phen complexes were reported. In aggregate, the sum total of the steady state spectra, time-resolved experimentation and DFT calculations all point to inhibition of

excited state pseudo-Jahn-Teller distortion from the substitution of the 2,9 methyl groups for the CF$_3$ groups. The finding resembles previous observations of copper(I) complexes with enhanced bulk in the 2,9 phen positions with the caveat that the trifluoromethylation changes the potential energy surface to favor a θ ~90°. If trifluoromethylation simply enhanced the steric bulk restricting pseudo-Jahn-Teller distortion then we would expect similar emission maxima, emission QY and ns flash photolysis lifetimes for all complexes which are not experimentally observed. The observed time-resolved dynamics and emission trend that addition of CF$_3$ groups past two decreases the excited-state lifetime is contrary to the traditional understanding of $[Cu(NN)_2]^+$ complexes. In aggregate, these results outline the need for further high level dynamic theory computations and experimental vibrational investigation into copper(I) complexes where the 2,9 phen positions constituents alter both the sterics and electronics of the excited state.

3.4 Experimental

3.4.1 Materials and Instrumentation

The following reagents and solvents were obtained from the indicated sources and were used as received or were purified/treated/stored as indicated. Phenanthridine, (Aldrich, 99%). Trifluoromethyl iodide, 98% (SynQuest). HPLC grade methanol (Fisher Scientific), ACS grade dichloromethane (Sigma), chloroform-d (Cambridge Isotopes Laboratories, 99.8%) sodium thiosulfate (Malinckrodt), and hexafluorobenzene (Synquest Labs, 99.8%).

3.4.2 High Performance Liquid Chromatography

HPLC was conducted using a Shimadzu liquid chromatography instrument (CBM-20A control module, SPD-20A UV-vis detector set to 300 nm, LC-6AD pump, manual injector valve.) The HPLC column utilized was a 10 mm I.D. x 250 nm COSMOSIL Buckyprep column. The eluent was ACS grade methanol at a flow rate of 5 mL min^{-1}.

3.4.3 ^{1}H and ^{19}F NMR Analysis:

^{1}H and ^{19}F NMR analyses were acquired on a Varian INOVA instrument. ^{1}H NMR spectra were acquired at 400 MHz (CDCl$_3$ or CD$_2$Cl$_2$). ^{19}F NMR spectra were acquired at 376 MHz (CDCl$_3$ or CD$_2$Cl$_2$).^{19}F NMR spectra were referenced to a hexafluorobenzene ($-\delta = 164.9$) internal standard.

3.4.4 Cyclic voltammetry (CV):

CV measurements were carried out in a nitrogen atmosphere glovebox on a PAR 263 potentiostat/galvanostat. CV measurements of phen(CF$_3$)$_n$ compounds utilitzed 0.1 M tetrabutylammonium perchlorate, recrystallized from ethyl acetate, in dimethoxyethane with platinum working and counter electrodes and a silver quasi-reference electrode at a scan rate of 100 mVs^{-1} using ferrocene as an internal standard. CV measurements for copper(I) complexes utilized 0.1 M tetrabutylammonium hexafluorophosphate in dichloromethane with platinum working and counter electrodes and a silver quasi-reference electrode at a scan rate of 300 mVs^{-1} using ferrocene as an internal standard.

3.4.5 Synthesis of 2,9-bis(trichloromethyl)-1,10-phenanthroline:

Based on literature prep.[41] Neocuproine hemihydrate (500 mg, 2.30 mmol, 1 eq.) and N-chlorosuccinimide (4.61 g, 34.52 mmol, 15 eq.) were added to a 300 mL round bottom flask. Chloroform (150 mL) was added to the flask and the reaction mixture was refluxed for 6 h followed by cooling to room temperature. The solvent was removed *in vacuo* resulting in a yellow solid. Saturated sodium carbonate (100 mL) and chloroform (40 mL) were then added. The product was extracted into chloroform (2x20 mL). The organic layer was then washed with DI water, 6x50 mL. The solvent was again removed *in vacuo* resulting in a yellow solid. The product was then purified on silica (eluent 2:1 chloroform/hexanes).

3.4.6 Synthesis of phen-2-1:

Based on a modified literature prep.[41] 2,9-bis(trichloromethyl)-1,10-phenanthroline (150 mg, 0.36 mmol) was combined with antimony (III) fluoride (1.5 grams, 8.4 mmol) and ground with a mortar and pestle. The mixture was then added to a 50 mL round-bottom flask and fitted with a reflux condenser under $N_{2(g)}$. Heat was applied until a melt formed. The mixture was heated for one more minute and allowed to cool to room temperature. Sodium hydroxide (5M) was added to the flask and transferred to a separatory funnel. Dichloromethane, 50 mL, was added and transferred to a separatory funnel. The product was extracted with dichloromethane (3x20 mL), dried on sodium sulfate, and passed through silica gel. The solvent was removed *in vacuo* resulting in a white crystalline solid (39% yield). ^{19}F NMR: **δ** −69.9 (singlet, 6F). ^{1}H NMR: **δ** 8.5 (doublet, $J = 8$ Hz, 2H); 8.0 (doublet, $J = 8$ Hz, 2H); 8.0 (singlet, 2H).

3.4.7 Trifluoromethylation of phen Method 1

The compound 1,10-phenanthroline monohydrate (251.5 mg, 1.27 mmol) was added to a glass ampoule. CF$_3$I gas (10 eq.) was introduced, cooled to -78 °C and the ampoule was sealed under vacuum (10^{-4} torr). The ampoule was heated to 330 °C for 10 h and subsequently cooled to room temperature. The ampoule was opened, and soluble trifluoromethylated phen derivatives were extracted with dichloromethane. The dichloromethane solution was washed with a 10% solution of sodium thiosulfate to remove iodine. This sealed ampoule reaction was performed by former Strauss Boltalina Research Group postdoctoral researcher, Dr. Igor Kuvychko.

3.4.8 Trifluoromethylation of phen Method 2

Method 2 Reaction 1 (R1, 20 min): phen-2-1 (20 mg, 0.063 mmols) was added to a 38 mL glass ampoule (2 cm inner diameter, 12 cm length). CF$_3$I gas (600 torr) was introduced, cooled to -78 °C and the ampoule was sealed under vacuum (10^{-4} torr). The ampoule was allowed to return to

room temperature and was then heated to 330 °C for 20 min and subsequently cooled to room temperature. The ampoule was opened, and soluble trifluoromethylated products were extracted with dichloromethane. The solvent and iodine were then removed *in vacuo*. One stage of HPLC separation in 100% MeOH yielded 5 fractions as shown in **Figure 3.4**.

Method 2 Reaction 2 (R2, 40 min): phen-2-1 (20 mg, 0.063 mmols) was added to a 52 mL glass ampoule (2 cm inner diameter, 16.5 cm length). CF_3I gas (600 torr) was introduced, cooled to -78 °C and the ampoule was sealed under vacuum (10^{-4} torr). The ampoule was allowed to return to room temperature and was then heated to 330 °C for 40 min and subsequently cooled to room temperature. The ampoule was opened, and soluble trifluoromethylated products were extracted with dichloromethane. The solvent and iodine were then removed *in vacuo*. One stage of HPLC separation in 100% MeOH yielded 5 fractions. The predominant fraction (13-14.5 min) yielded only phen-3-1 (26.4 mg, 63% yield). Other fractions included starting material, phen-4-1 and phen-4-2.

Method 2 Reaction 3 (R3, 3 h): phen-2-1 (20 mg, 0.063 mmols) was added to a 53 mL glass ampoule (2 cm inner diameter, 17 cm length). CF_3I gas (600 torr) was introduced, cooled to -78 °C and the ampoule was sealed under vacuum (10^{-4} torr). The ampoule was allowed to return to room temperature and was then heated to 330 °C for 3 h and subsequently cooled to room temperature. The ampoule was opened, and soluble trifluoromethylated products were extracted with dichloromethane. The solvent and iodine were then removed *in vacuo*.

Method 2 Reaction 4 (R4, 10 h): phen-2-1 (20 mg, 0.063 mmols) was added to a 56 mL glass ampoule (2 cm inner diameter, 18 cm length). CF_3I gas (600 torr) was introduced, cooled to -78 °C and the ampoule was sealed under vacuum (10^{-4} torr). The ampoule was allowed to return to room temperature and was then heated to 330 °C for 10 h and subsequently cooled to room

temperature. The ampoule was opened, and soluble trifluoromethylated products were extracted with dichloromethane. The solvent and iodine were then removed *in vacuo*. Preliminary HPLC separation in 100% MeOH was performed as shown in **Figure 3.4**. The predominant fraction (14.4-15.6 min) yielded phen-4-1. Other fractions included starting material, phen-3-1 and phen-4-2.

Danger! High pressure can be generated in the ampoule leading to explosive ampoule failure. The maximum pressure inside the ampoule at high temperature has to be calculated. Depending on the size and wall thickeness of the ampoule the maximum allowable pressure changes, so a conservative limit of 2-3 bar must be set. The burst pressure for a glass ampoule is largely determined by the quality of seal, so care must be taken during the sealing step. Use shields and personal protection at all times. Only experienced personnel should perform these operations.

3.4.9   Synthesis of [Cu(phen-4-1)$_2$]SO$_3$CF$_3$

A 0.041 M solution of phen-4-1 in dichloromethane-d$_2$ (0.5 mL, 0.021 mmol) was added to an air-free NMR tube with 0.9 mL of dichloromethane-d$_2$. The ^{19}F NMR and the ^{1}H NMR spectra of the ligand were recorded. Copper(I) trifluoromethanesulfonate toluene complex (55 mg, 0.106 mmol) was added to the NMR tube and the NMR spectra were recorded again. The mixture was filtered and dried *in vacuo* yielding a dark orange solid (7.5 mg, 0.0067 mmol, 65% yield). Single crystals of [Cu(phen-4-1)$_2$]SO$_3$CF$_3$ suitable for diffraction were grown by slow evaporation of an anhydrous dichloromethane solution. ^{19}F NMR: δ −62.5 (singlet, 3F); −62.9 (singlet, 3F) −69.9 (singlet, 3F); −70.0 (singlet, 3F). ^{1}H NMR: δ 9.3 (doublet, $J = 8$ Hz, 1H); 9.0 (singlet, 1H); 8.8 (singlet, 1H); 8.6 (doublet, $J = 9$ Hz, 1H). ESI+ MS (*m/z*): 967.08 (calc. mass: 966.97).

3.4.10 Synthesis of [Cu(phen-3-1)$_2$]SO$_3$CF$_3$

A 0.0275 M solution of phen-3-1 in dichloromethane-d$_2$ (0.5 mL, 0.0138 mmol) was added to an air-free NMR tube. Copper(I) trifluoromethanesulfonate toluene complex (40 mg, 0.077 mmol) was added and placed on a rotating motor to provide mixing. The mixture was filtered and dried *in vacuo* yielding a dark orange solid (4.8 mg, 0.0049 mmol, 71% yield). Single crystals of [Cu(phen-3-1)$_2$]SO$_3$CF$_3$ suitable for diffraction were grown by slow evaporation of an anhydrous dichloromethane and diethyl ether mixture. ^{19}F NMR: δ −62.8 (singlet, 3F); −70.1 (singlet, 6F). ^{1}H NMR: δ 9.2 (doublet, *J* = 9 Hz, 1H); 9.2 (doublet, *J* = 9 Hz, 1H); 8.9 (singlet, 1H), 8.5 (multiplet, 2H). ESI+ MS (*m/z*): 831.17 (calc. mass: 830.99).

3.4.11 Synthesis of [Cu(phen-4-2)$_2$]SO$_3$CF$_3$

A 0.037 M solution of phen-4-2 in dichloromethane-d$_2$ (0.1 mL, 3.7 μmol) was added to an air-free NMR tube with 0.9 mL of dichloromethane-d$_2$. Copper(I) trifluoromethanesulfonate toluene complex (10 mg, 0.019 mmol) was added to the NMR tube and the NMR spectra were recorded again. The mixture was filtered and dried *in vacuo* yielding a dark orange solid (0.3 mg, 0.27 μmol, 15% yield). ^{19}F NMR: δ −62.9 (singlet, 6F). −69.7 (singlet, 6F). ^{1}H NMR: δ 8.8 (singlet, 2H); 8.8 (singlet, 2H). ESI+ MS (*m/z*): 966.90 (calc. mass: 966.97).

3.4.12 Synthesis of [Cu(phen-2-1)$_2$]SO$_3$CF$_3$

A 0.14 M solution of phen-2-1 in dichloromethane-d$_2$ (0.1 mL, 0.014) was added to an air-free NMR tube with 0.5 mL of dichloromethane-d$_2$. Copper(I) trifluoromethanesulfonate toluene complex (16 mg, 0.031 mmol) was added and placed on a rotating motor to provide mixing. The mixture was filtered and dried *in vacuo* yielding a dark orange solid (3.5 mg, 0.0041 mmol, 59% yield). ^{19}F NMR: δ −69.9 (singlet, 6F). ^{1}H NMR: δ 9.0 (doublet, *J* = 8 Hz, 2H); 8.4 (singlet, 2H); 8.4 (doublet, *J* = 8 Hz, 2H). ESI+ MS (*m/z*): 695.25 (calc. mass: 695.02).

3.4.13 SC-XRD

Single crystal data for phen-3-1, phen-3-2, phen-4-1, phen-4-2, phen-4-3, phen-5-1, [Cu(phen-4-1)$_2$]SO$_3$CF$_3$ and [Cu(phen-3-1)$_2$]SO$_3$CF$_3$ was collected on the Advanced Photon Source synchrotron instrument at Argonne National Laboratory, Argonne, IL on beamline 15ID-D with a wavelength of λ=0.41328 Å, employing a diamond 1 1 1 monochromator and Bruker D8 goniometer. The structures were solved using direct methods and refined by a full-matrix weighted least-squares process. Standard Bruker control and integration software (APEX 3) was employed, and Bruker SHELXTL software was used with Olex 2 for structure solution, refinement and molecular graphics. All single crystals were grown by the author of this dissertation. All structures were collected by the author with either Strauss Boltalina lab group member Nicholas DeWeerd or Colin Brook at Argonne National Laboratory. The X-ray structures phen-3-1, phen-4-1, phen-4-2, phen-3, phen-5-1, and [Cu(phen-4-1)$_2$]SO$_3$CF$_3$ were solved by Nicholas DeWeerd. The X-ray structures for phen-3-2 and [Cu(phen-3-1)$_2$]SO$_3$CF$_3$ were solved by the author with some assistance from Nicholas DeWeerd. All analysis of the X-ray structures was performed by the author of this dissertation. Crystallographic data can be found in Appendix 2 Table A2.1.

Table 3.1. Packing distances between molecules.

Compound	Packing distance (Å)
phen-2-1[a,d]	3.77
phen-3-1[b]	3.54
phen-3-2[a]	3.40
phen-4-2[b]	3.56
phen-4-3[b]	3.53
phen-5-1[b]	3.74

[a] Packing distance measured by generating a centroid of one molecule and a plane from the adjacent molecule and measuring the distance from the centroid to the plane. CF_3 groups and hydrogens were not included for generation of planes or centroids.
[b] Packing distance measured by generating a plane of one molecule to the plane generated from the core of its nearest neighbor.
[c] The structure of phen-4-1 not of high enough quality to examine the packing.
[d] phen-2-1 structure from Kovalevsky et al.[45] CCDC deposition number: 222330

Table 3.2. Phenanthridine, phenanthridine$(CF_3)_n$ compounds, phen$(CF_3)_n$ compounds, abbreviations and reduction potentials.

compound	Abbreviation	$E_{1/2}$ [V] vs. Fe(Cp)$_2$	Number of CF$_3$ Groups
2,9-bis(trifluoromethyl)-1,10-phenanthroline	**phen-2-1**	−2.20	2
2,5,9-tris(trifluoromethyl)-1,10-phenanthroline	**phen-3-1**	−1.94	3
2,4,9-tris(trifluoromethyl)-1,10-phenanthroline	**phen-3-2**	−1.81	3
2,4,6,9-tetra(trifluoromethyl)-1,10-phenanthroline	**phen-4-1**	−1.71	4
2,4,7,9-tetra(trifluoromethyl)-1,10-phenanthroline	**phen-4-2**	−1.60	4

[a]Cyclic voltammetry; 0.1 M N(n-Bu)$_4$ClO$_4$ in dimethoxyethane; platinum working and counter electrodes; silver wire quasi-reference electrode; 100 mv^{-s}; ferrocene (Fe(Cp)$_2$) internal standard.

Table 3.3. Percentages of phen-3-1 and phen-4-1 in each crude reaction

reaction	reaction time	phen-3-1	phen-4-1
R1[b]	20 min	60%	6.6 %
R2	40 min	82%	16%
R3	3 h	61%	33%
R4[c]	10 h	22%	60%

[a]Percentages determined by integrating the ^{19}F NMR peaks.
[b]R1 contained phen-2-1 (26%).
[c]R4 contained approximately 18% unidentified isomers

Table 3.4. Absorbance, excited-state absorbance, and emission global fitting lifetimes as well as emission quantum yield.

	$[Cu(dmp)_2]^+$	$[Cu(phen-2-1)_2]^+$	$[Cu(phen-3-1)_2]^+$	$[Cu(phen-4-1)_2]^+$	$[Cu(phen-4-2)_2]^+$
λ_{max} (nm)	457	463	464	481	482
τ_1 (ps)	0.3 (Fixed)[a]	–	–	–	4[a]
τ_2 (ps)	54 ± 15	69 ± 5	6.0 ± 2.3	10.0 ± 7.0	150 ± 20
τ_3 (ns)	66.6 ± 2.1	106 ± 2	68.3 ± 0.6	15.5 ± 1.7[b]	–
τ_{em} (ns)	52.0 ± 1.4	98 ± 2	82 ± 2[b]	17.9 ± 2.2[b]	–
Φ_p	3.5 x 10^{-4}	4.0 x 10^{-3}	1.1 x 10^{-3}	–	–

[a] τ_1 is fixed from single wavelength kinetic time constant to yield a more accurate fit of τ_2.
[b] Time constant found in single wavelength kinetics.

Table 3.5. $Cu^{II/I}$ redox potentials for copper(I) phen compounds.

Compound	$Cu^{II/I}$ (V vs SCE)
[Cu(phen)$_2$]$^+$	0.19[b]
[Cu(dmp)$_2$]$^+$	0.50[b]
[Cu(1,10-phen-2-1)$_2$]$^+$	1.55[b]
[Cu(1,10-phen-3-1)$_2$]$^+$	1.69[c]

[a]All measurements were recorded in PF_6^- electrolyte in dichloromethane.
[b]Data from Scaltrito et al.[32]
[c]This work
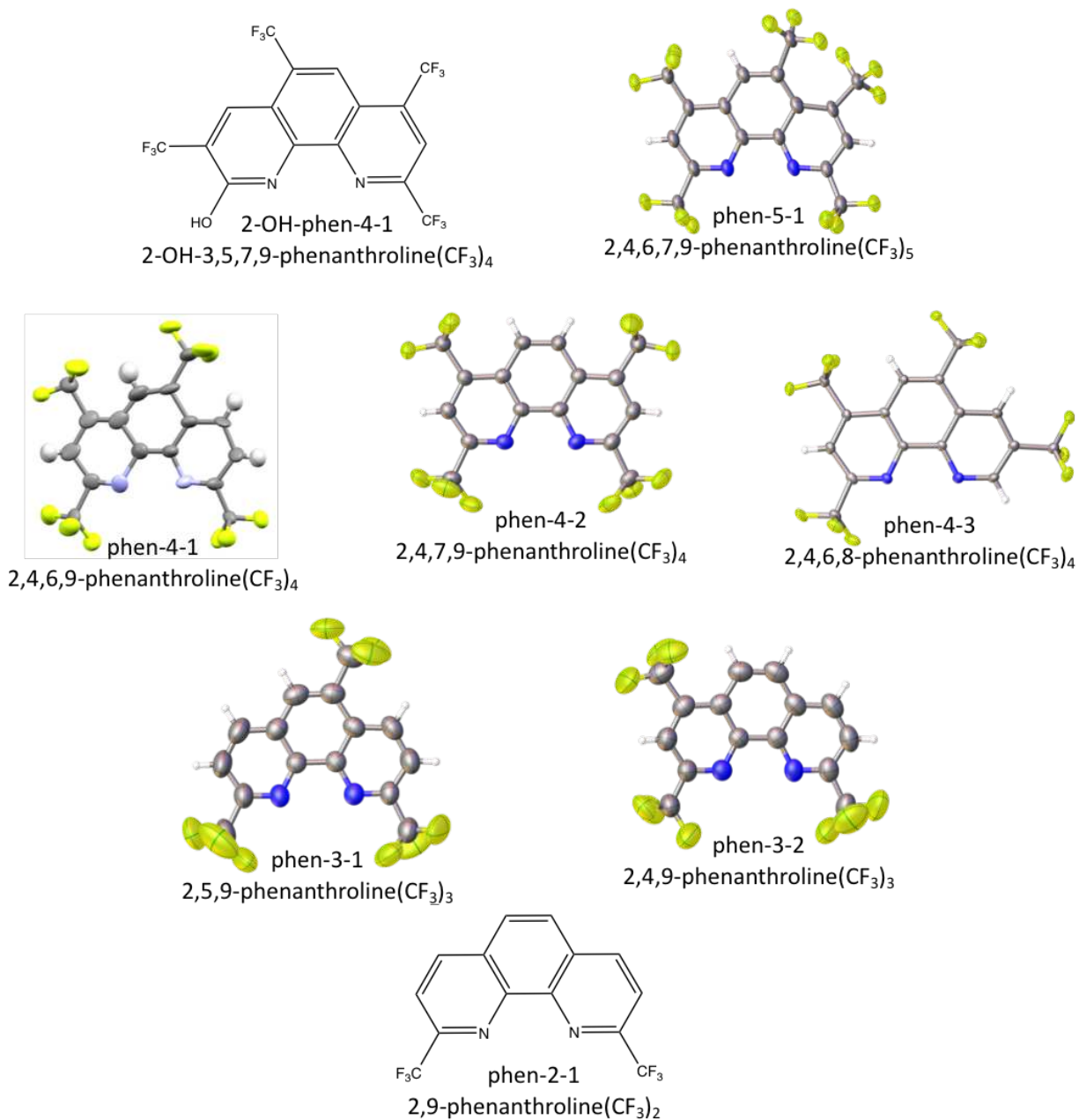
Figure 3.1. Structures and common names of phen(CF$_3$)$_n$ compounds. Thermal ellipsoid plots at the 50% probability level shown phen-4-1, phen-4-2, phen-4-3, phen-3-1, phen-3-2, phen-5-1.
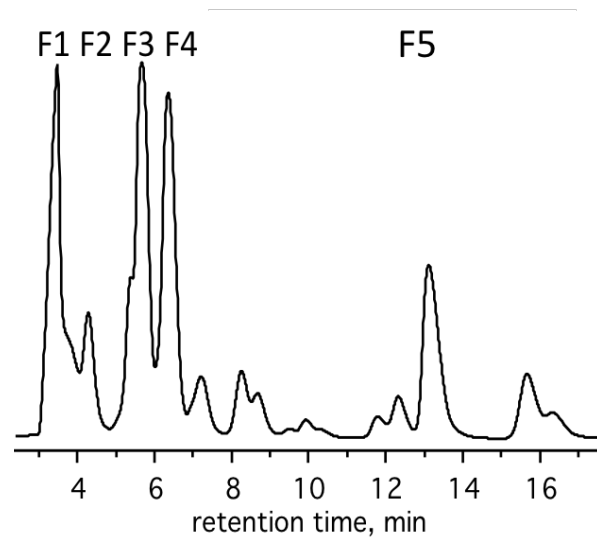
Figure 3.2. HPLC chromatogram of trifluoromethylation of phen, Method 1, with semi-preparative Buckyprep stationary phase and acetonitrile as the eluent at 5 mL min^{-1}, showing 5 major fractions from 3 minutes to 17 minutes.
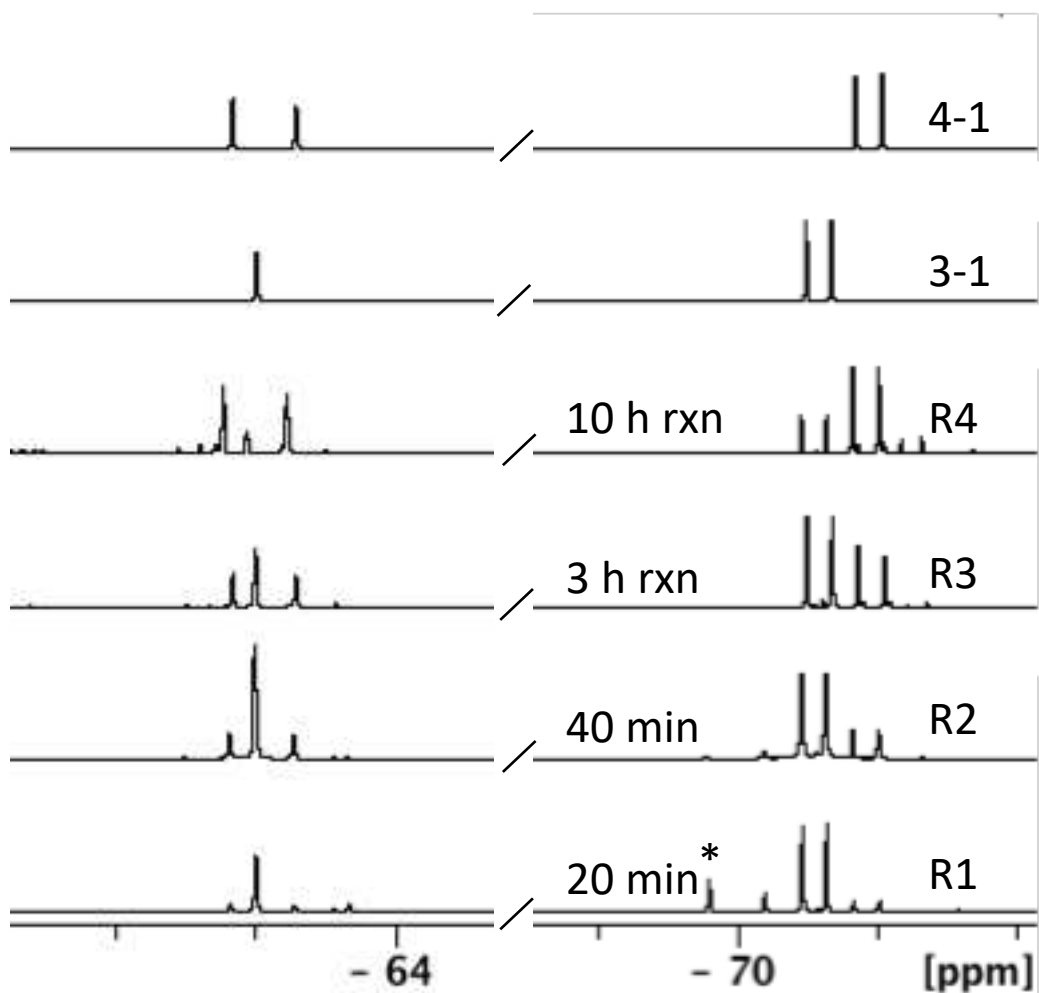
Figure 3.3. Stacked ^{19}F NMR spectra of crude reactions at 20 minutes (R1), 40 min (R2), 3 h (R3), 10 h (R4), as well as pure phen-3-1 (3-1) and phen-4-1 (4-1). The asterisk designates unconsumed starting material, phen-2-1.
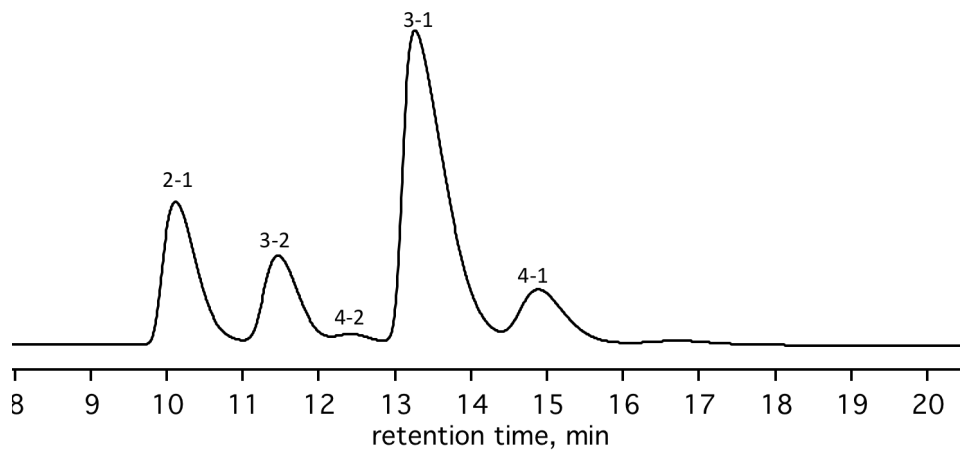
Figure 3.4. HPLC chromatogram of trifluoromethylation of phen, Method 2 with semi-preparative Buckyprep stationary phase and methanol as mobile phase flowing at 5 mL min^{-1}. The peaks are labeled with the corresponding compound abbreviated (i.e. 2-1 represents phen-2-1).
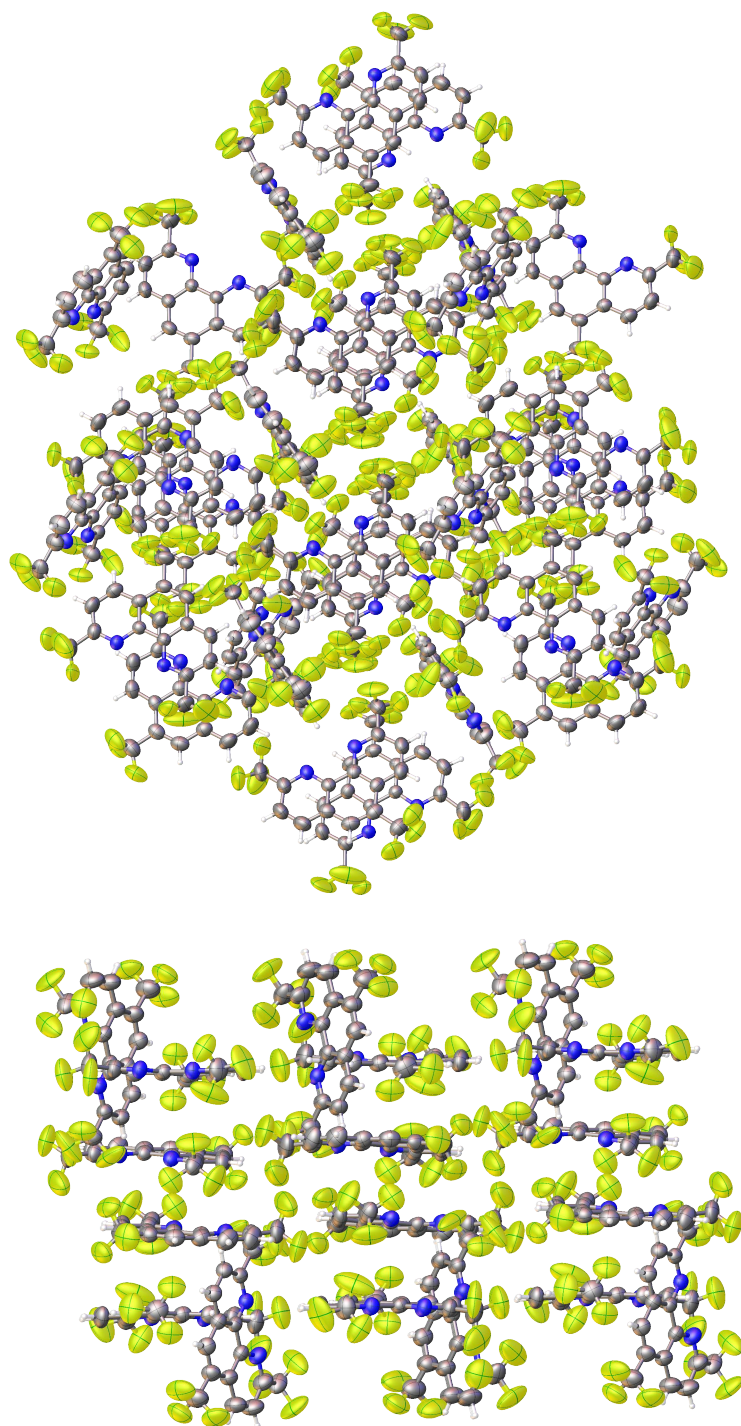
Figure 3.5. Top view of phen-3-1 packing (top). Side view of phen-3-1 packing (bottom).
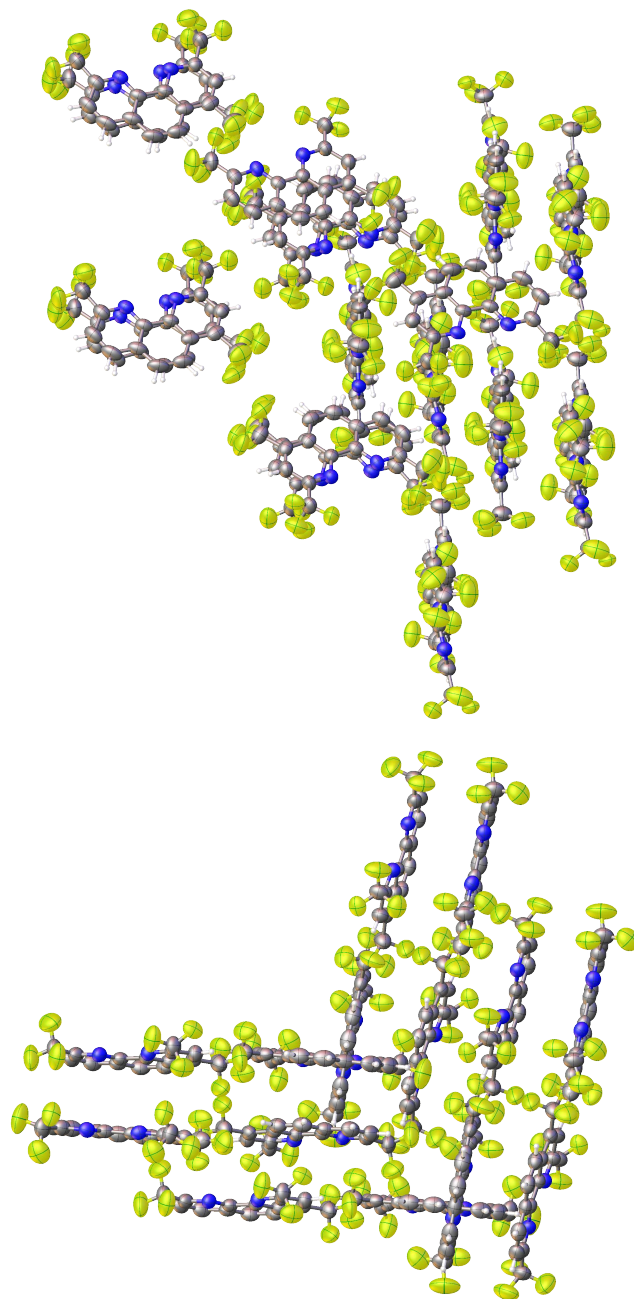
Figure 3.6. Top view of phen-3-2 packing (top). Side view of phen-3-2 packing (bottom).
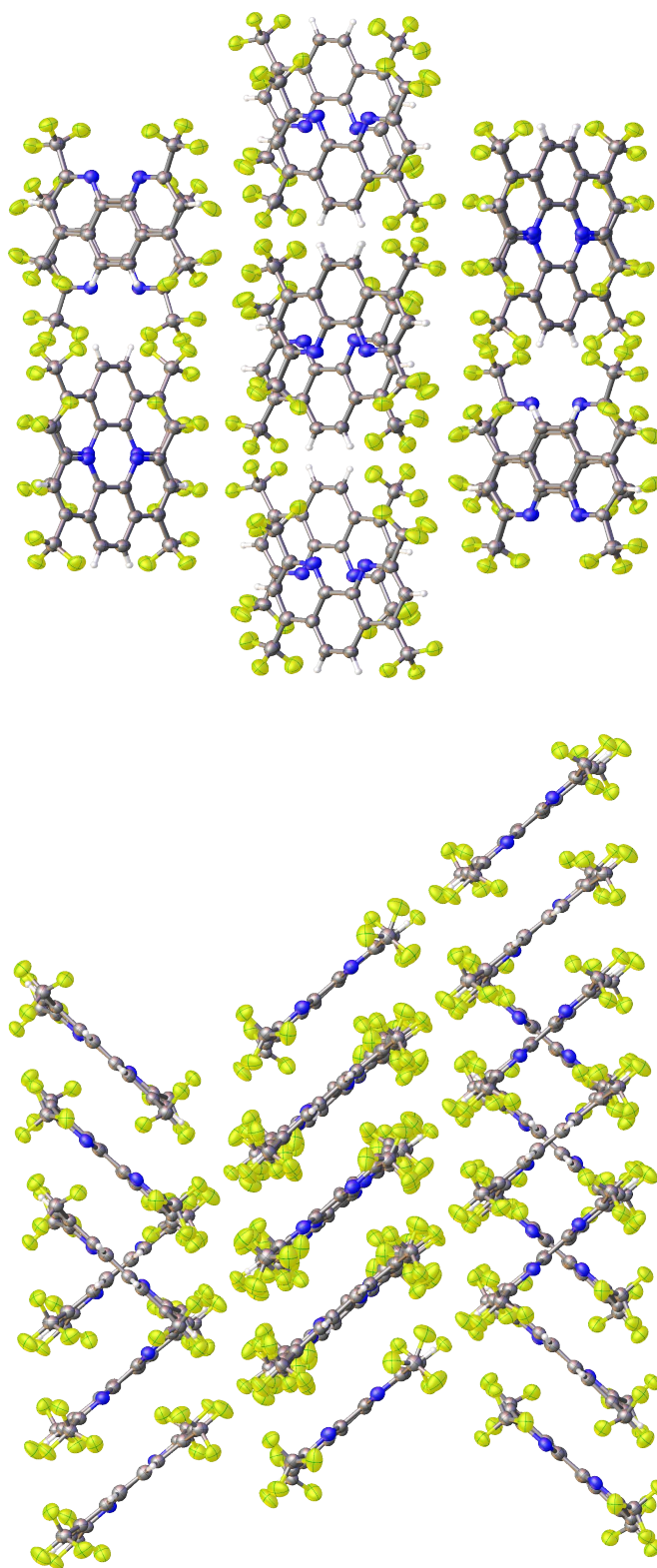
Figure 3.7. Top view of phen-4-2 packing (top). Side view of phen-4-2 packing (bottom).
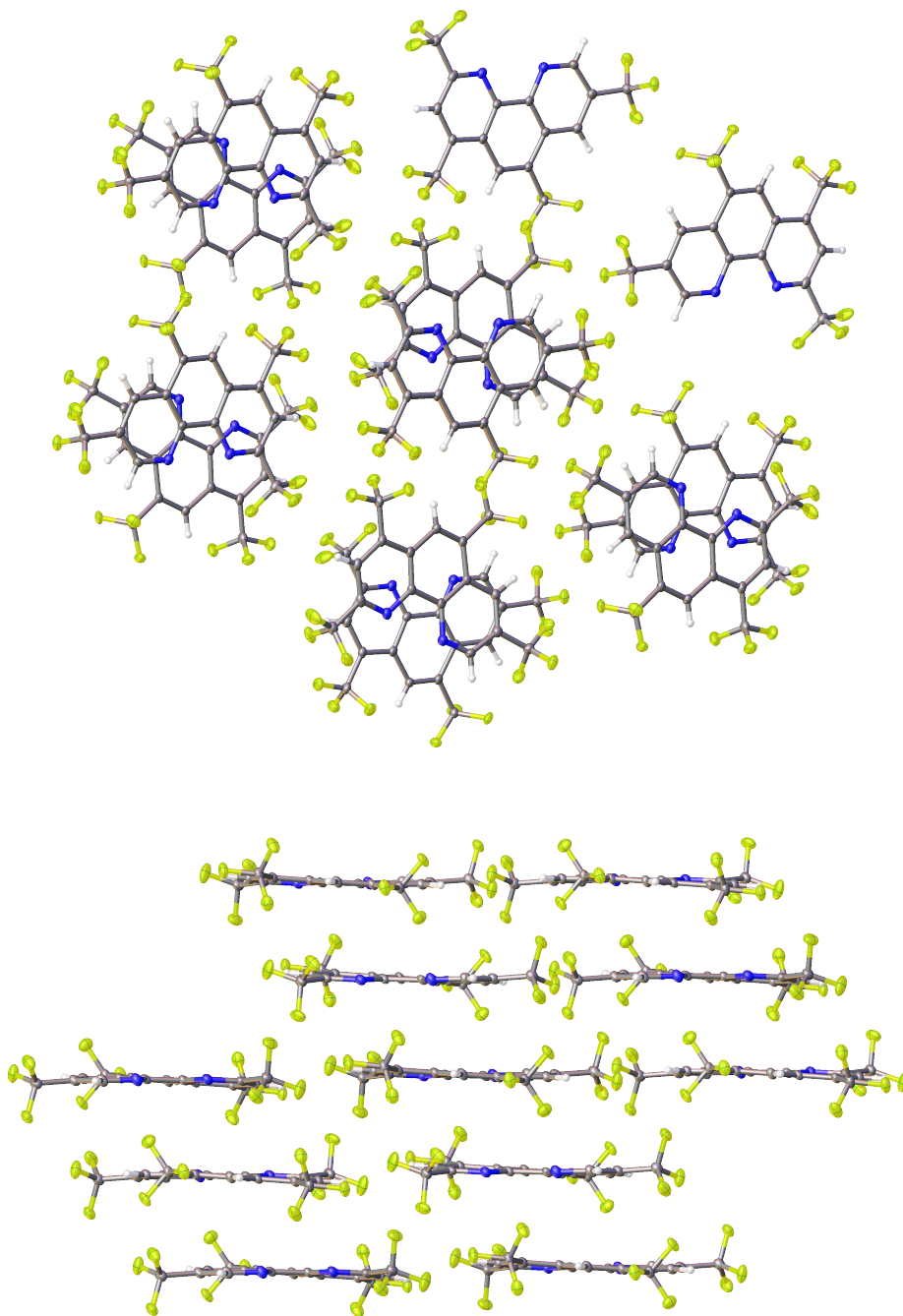
Figure 3.8. Top view of phen-4-3 packing (top). Side view of phen-4-3 packing (bottom).
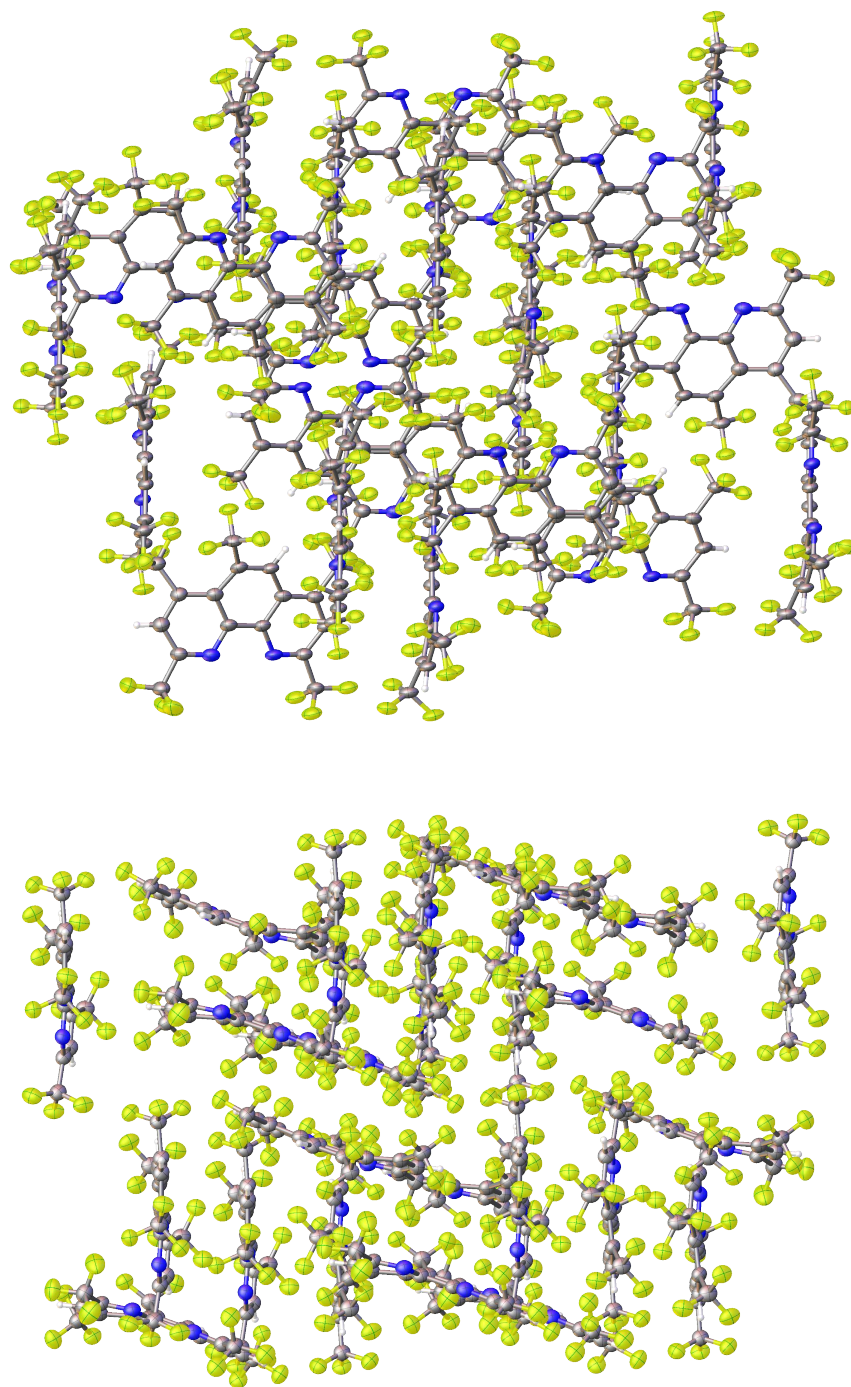
Figure 3.9. Top view of phen-5-1 packing (top). Side view of phen-5-1 packing (bottom).
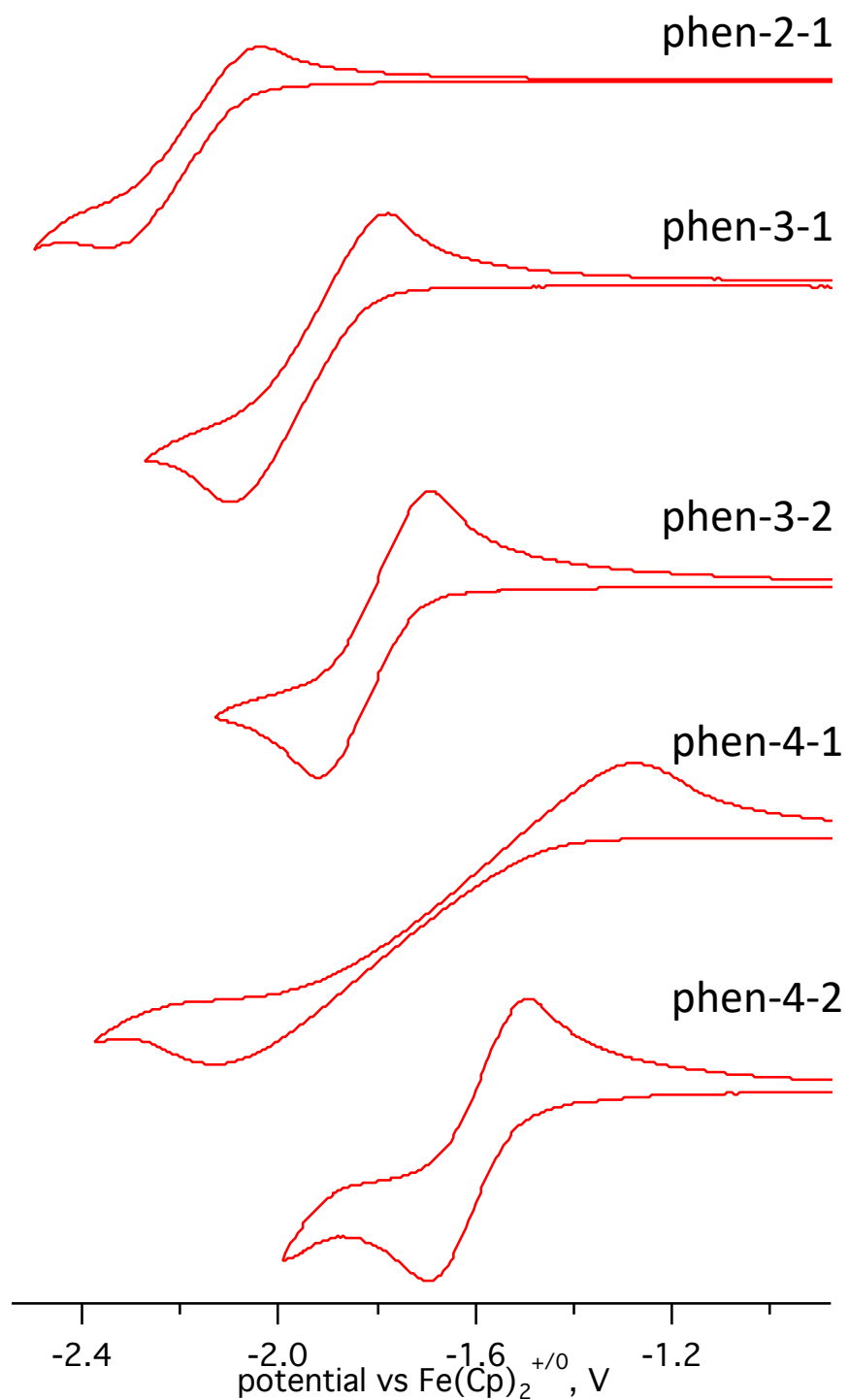
Figure 3.10. Cyclic voltammetry of trifluoromethylated phen derivatives versus $Fe(Cp)_2$, 0.1 M $N(nBu)_4ClO_4$ in dimethoxyethane, 100 mVs^{-1}.
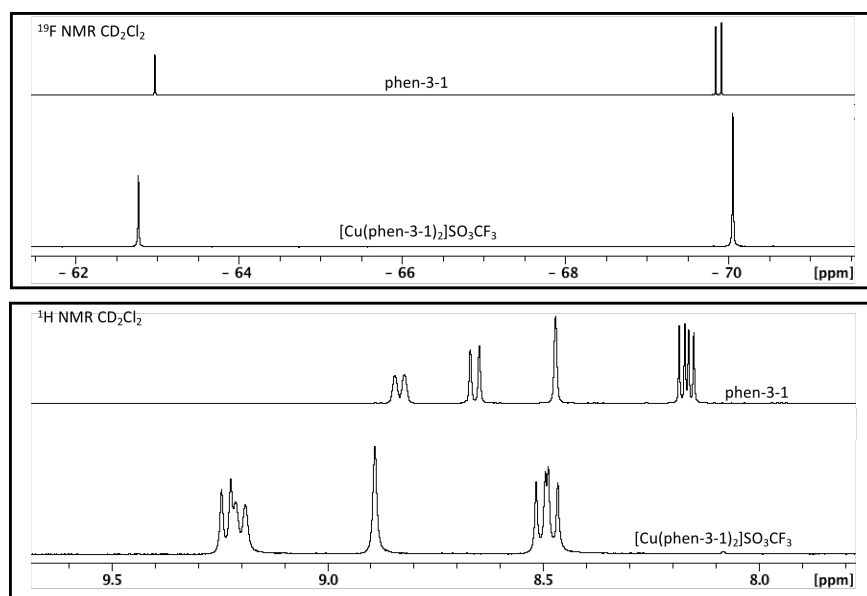
Figure 3.11. (Top) ^{19}F NMR spectra of phen-3-1 and [Cu(phen-3-1)$_2$]SO$_3$CF$_3$. (Bottom) ^{1}H NMR spectra of phen-3-1 and [Cu(phen-3-1)$_2$]SO$_3$CF$_3$.
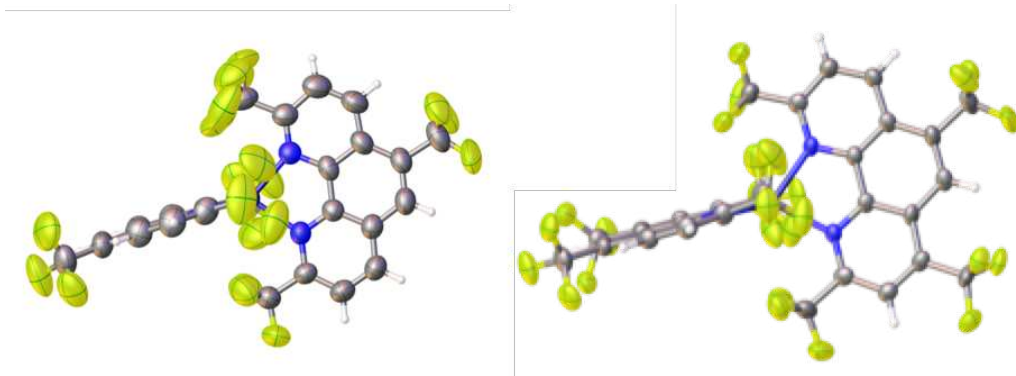
Figure 3.12. Single crystal XRD structures for [Cu(phen-3-1)$_2$]$^+$ (Left) and [Cu(phen-4-1)$_2$]$^+$ (Right). Triflate anions not shown for clarity. Thermal ellipsoids are plotted at a default 50% probability.
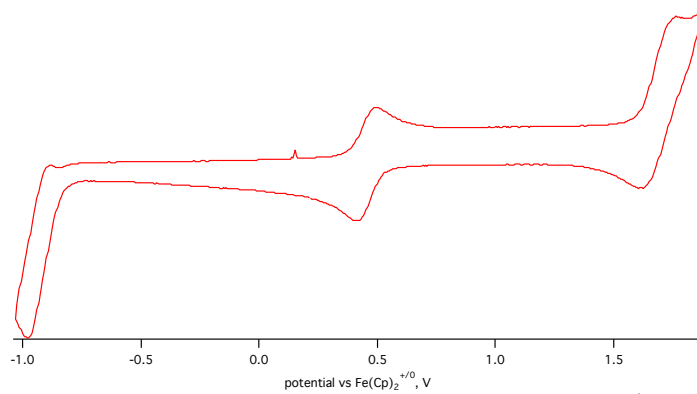
Figure 3.13. Cyclic voltammetry of [Cu(phen-3-1)$_2$]$^+$ versus SCE (Fe(Cp)$_2$=0.45 V), 0.1 M N(nBu)$_4$PF6 in dichloromethane, 300 mVs^{-1}.
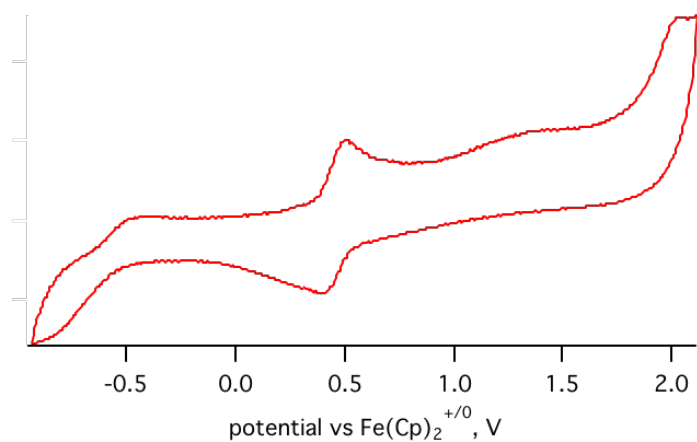
Figure 3.14. Cyclic voltammetry of [Cu(phen-4-1)$_2$]$^+$ versus SCE (Fe(Cp)$_2$=0.45 V), 0.1 M N(nBu)$_4$PF6 in dichloromethane, 300 mVs^{-1}.
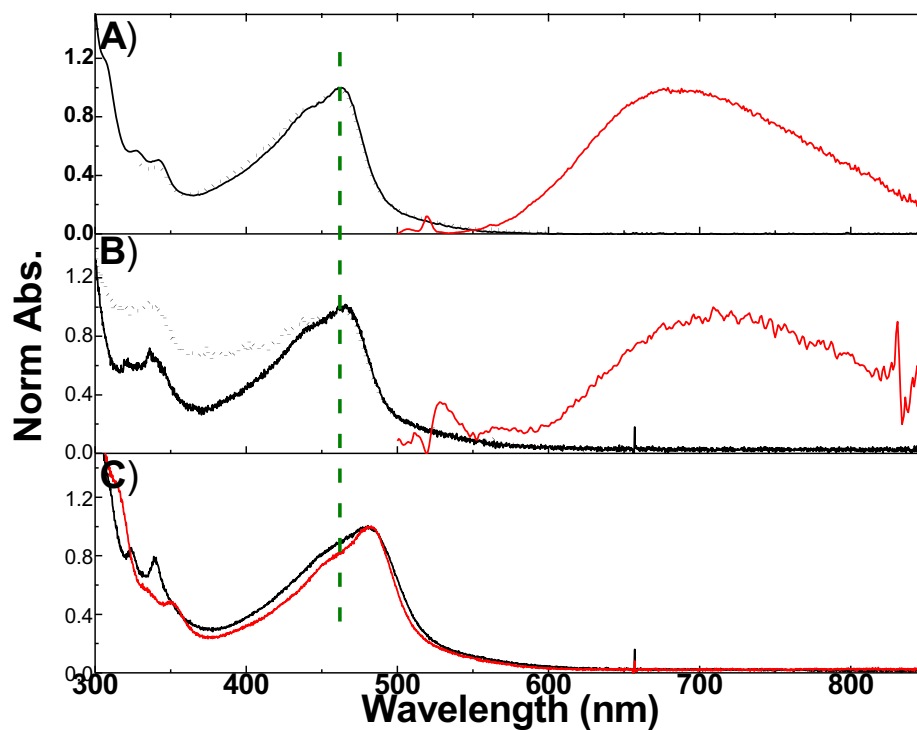
Figure 3.15. (A) Normalized electronic absorption (black solid line), emission (red) and excitation (black scatter line) spectra for [Cu(phen-2-1)$_2$]OTf in 1,2-dichloroethane. (B) Normalized electronic absorption (solid black), emission (red) and excitation (scatter black) spectra for [Cu(phen-3-1)$_2$]OTf in 1,2-dichloroethane. (C) Normalized electronic absorption of [Cu(phen-4-1)$_2$]OTf (black) and [Cu(phen-4-2)$_2$]OTf (red) in 1,2-dichloroethane. The dashed green line is added to highlight differences in the absorption spectra.
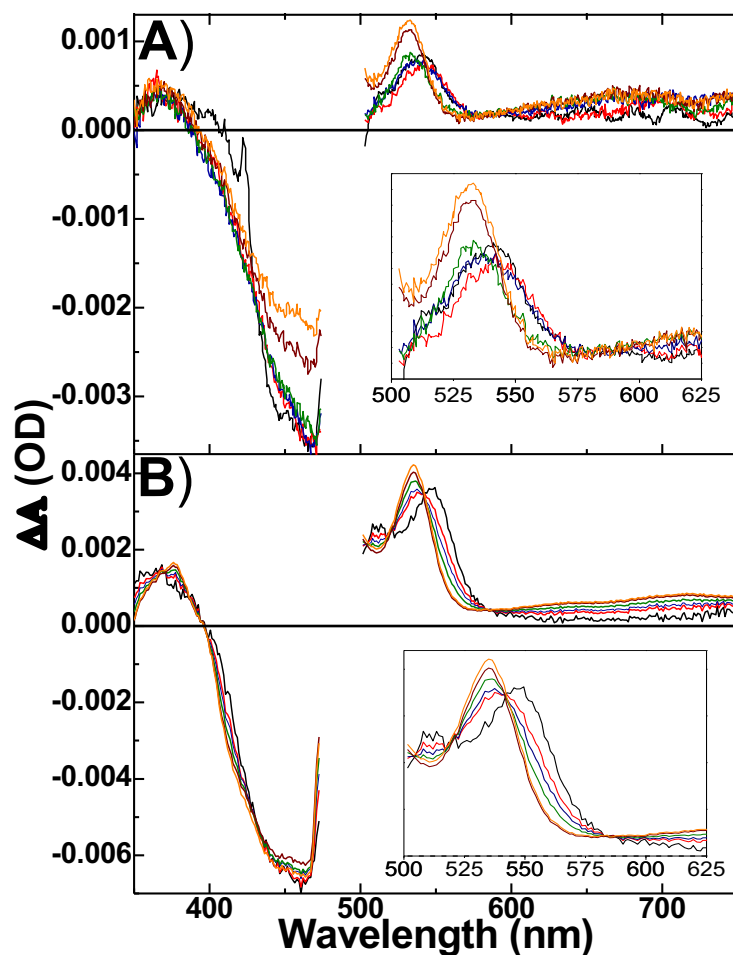
Figure 3.16. Ultrafast pump probe transient absorption spectra for [Cu(phen-2-1)$_2$]OTf (A) and [Cu(phen-3-1)$_2$]OTf (B) collected in 1,2-dichloroethane. Insets: Enhanced 500 to 625 nm region for [Cu(phen-2-1)$_2$]OTf and [Cu(phen-3-1)$_2$]OTf to highlight spectral changes. The spectra are taken at 0.3 ps (black), 0.75 ps (red), 2.5 ps (blue), 10 ps (green), 50 ps (brown), 100 ps (orange).
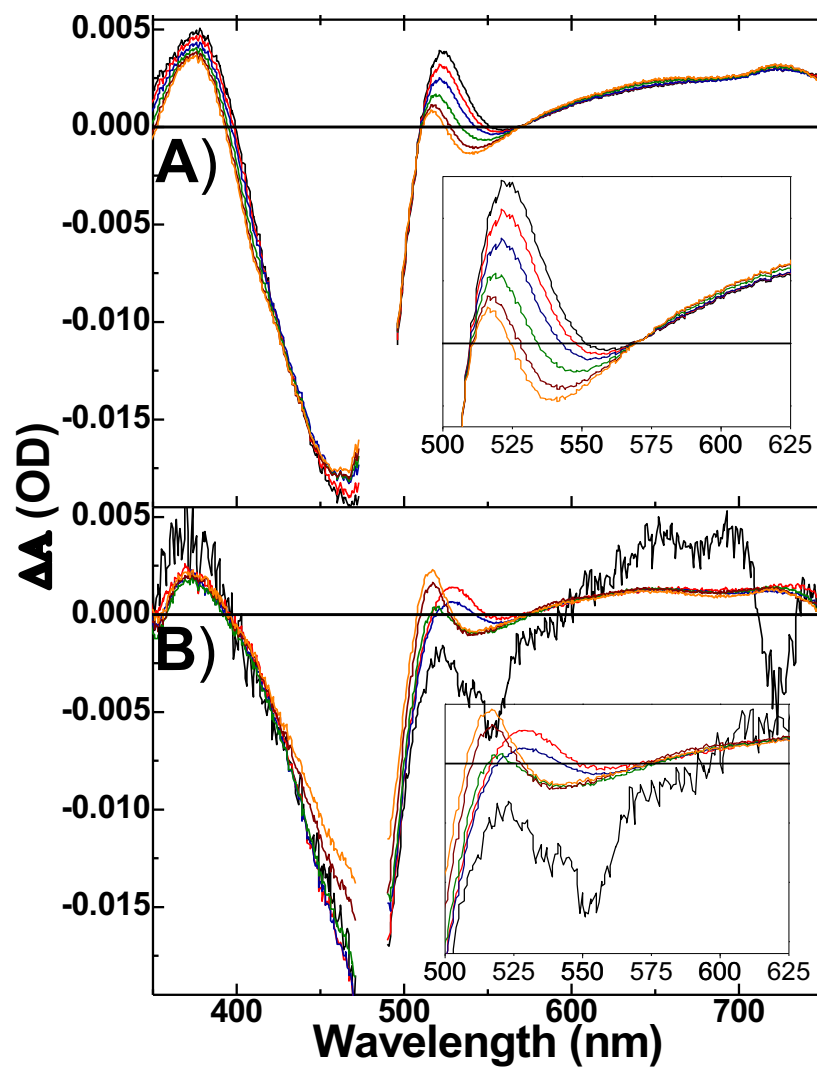
Figure 3.17. Ultrafast pump-probe transient absorption spectra for [Cu(phen-4-1)$_2$]OTf (A) and [Cu(phen-4-2)$_2$]OTf (B) collected in 1,2-dichloroethane. Insets: Enhanced 500 to 625 nm region for [Cu(phen-4-1)$_2$]OTf and [Cu(phen-4-2)$_2$]OTf to highlight spectral changes. The spectra are obtained at pump-probe delays of 0.3 ps (black), 0.75 ps (red), 2.5 ps (blue), 10 ps (green), 50 ps (brown), and 100 ps (orange).
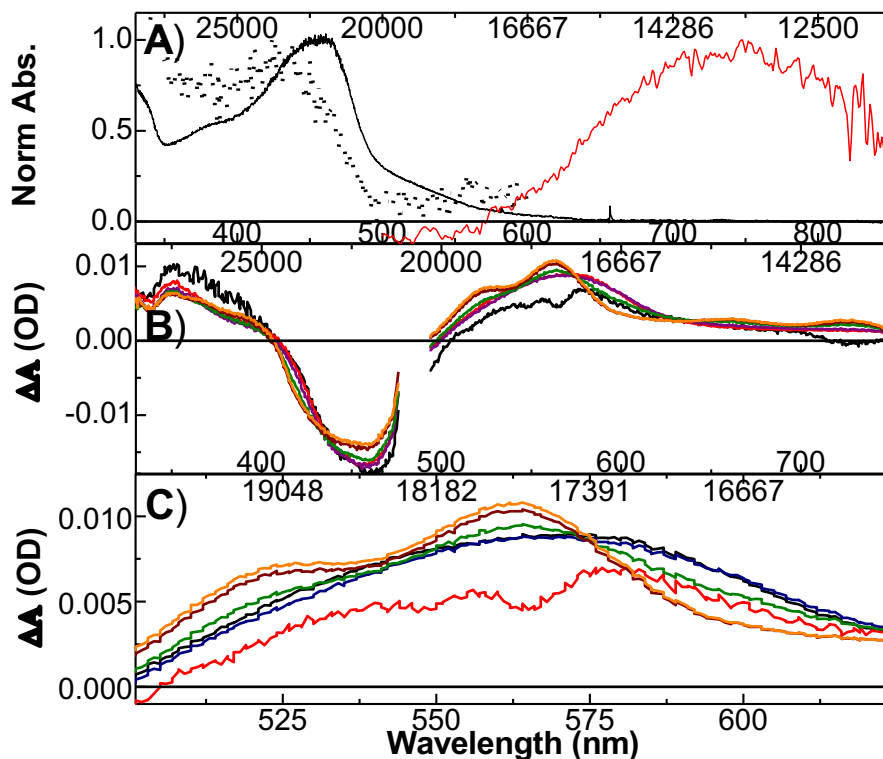
Figure 3.18. (A) Normalized electronic absorption (black solid line), emission (red solid line) and excitation (black scatter line) spectra for [Cu(dmp)$_2$](PF$_6$) in 1,2-dichloroethane. (B) Ultrafast pump probe transient absorption spectra for [Cu(dmp)$_2$]PF$_6$ collected in 1,2-dichloroethane. (C) Enhanced 500 to 625 nm region for [Cu(dmp)$_2$]PF$_6$ collected in 1,2-dichloroethane. The selected spectra are taken at 0.3 ps (black), 0.75 ps (red), 2.5 ps (blue), 10 ps (green), 50 ps (brown), 100 ps (orange) time delays.
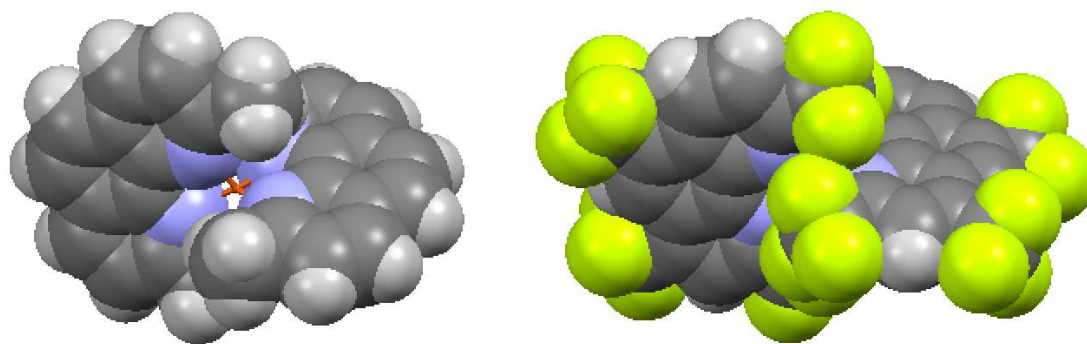
Figure 3.19. Space filling models of [Cu(dmp)$_2$]$^+$ (left)[48] and [Cu(phen-4-1)$_2$]$^+$ (right). Note the viewing angle has been moved to highlight the 2,9 substituents.
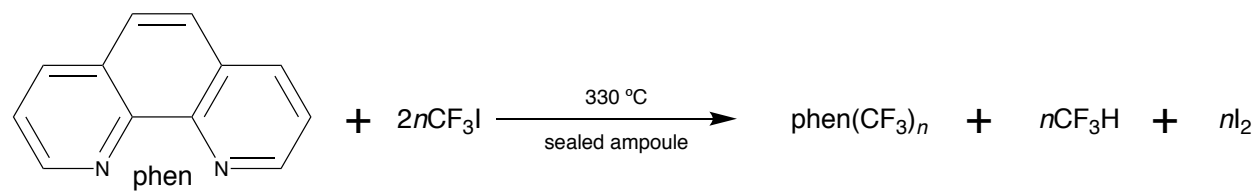
Scheme 3.1. Trifluoromethylation of phen.
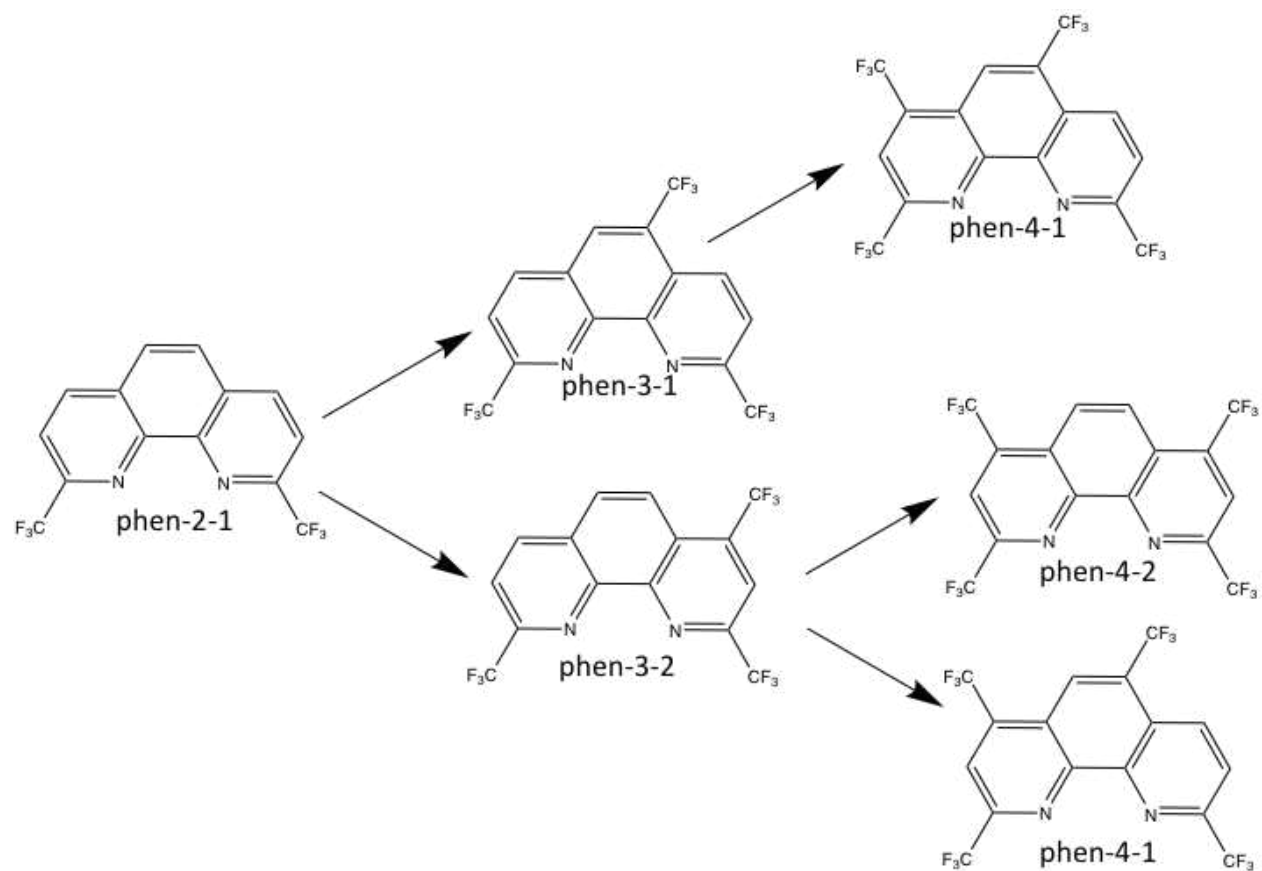
Scheme 3.2. Flow diagram with most likely products from Method 2 based on steric considerations.
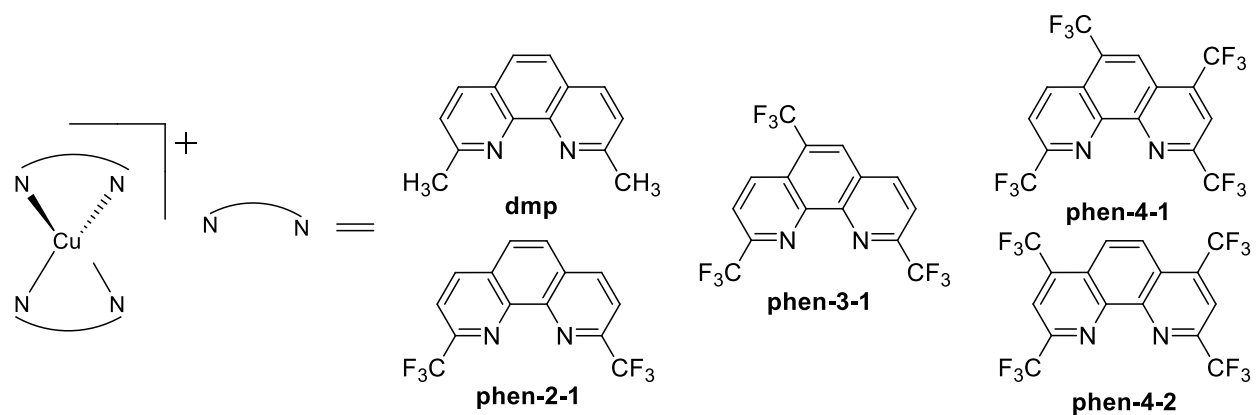
Scheme 3.3. Bond line structure(s) of $[\text{Cu(NN)}_2]^+$ (left) complexes utilized in this study. Here NN is 2,9-dimethyl-1,10-phenanthroline, phen-2-1, phen-3-1, phen-4-1, and phen-4-2.

CHAPTER 3 REFERENCES

1.   Bessho, T.; Constable, E. C.; Graetzel, M.; Hernandez Redondo, A.; Housecroft, C. E.; Kylberg, W.; Nazeeruddin, M. K.; Neuburger, M.; Schaffner, S. An element of surprise—efficient copper-functionalized dye-sensitized solar cells. *Chem. Commun.* **2008**, 3717-3719.

2.   Lv, L.; Liu, K.; Yuan, K.; Zhu, Y.; Wang, Y. Thermally activated delayed fluorescence processes for Cu(i) complexes in solid-state: a computational study using quantitative prediction. *RSC Adv.* **2018**, *8*, 28421-28432.

3.   Sandroni, M.; Kayanuma, M.; Planchat, A.; Szuwarski, N.; Blart, E.; Pellegrin, Y.; Daniel, C.; Boujtita, M.; Odobel, F. First Application of the HETPHEN Concept to New Heteroleptic Bis(diimine) Copper(I) Complexes as Sensitizers in Dye Sensitized Solar Cells. *Dalton Trans.* **2013**, *42*, 10818-10827.

4.   Ahn, B.-T.; McMillin, D. R. Studies of Photoinduced Electron transfer from Bis(2,9-dimethyl-1,10-Phenanthroline)Copper(I). *Inorg. Chem.* **1978**, *17*, 2253-2258.

5.   McMillin, D. R.; Buckner, M. T.; Ahn, B. T. A Light-Induced Redox Reaction of Bis(2,9-dimethyl-1,10-phenanthroline)Copper(I). *Inorg. Chem.* **1977**, *16*, 943-945.

6.   Blaskie, M. W.; McMillin, D. R. Photostudies of Copper(I) Systems. 6. Room-Temperature Emission and Quenching Studies of Bis(2,9-dimethyl-1,10-Phenanthroline)Copper(I). *Inorg. Chem.* **1980**, *19*, 3519-3522.

7.   Mara, M. W.; Fransted, K. A.; Chen, L. X. Interplays of Excited State Structures and Dynamics in Copper(I) Diimine Complexes: Implications and Perspectives. *Coord. Chem. Rev.* **2015**, *282–283*, 2-18.

8.   Prier, C. K.; Rankic, D. A.; MacMillan, D. W. C. Visible Light Photoredox Catalysis with Transition Metal Complexes: Applications in Organic Synthesis. *Chem. Rev.* **2013**, *113*, 5322-5363.

9.   Wagenknecht, P. S.; Ford, P. C. Metal Centered Ligand Field Excited States: Their Roles in the Design and Performance of Transition Metal Based Photochemical Molecular Devices. *Coord. Chem. Rev.* **2011**, *255*, 591-616.

10.   Auböck, G.; Chergui, M. Sub-50-fs Photoinduced Spin Crossover in [Fe(bpy)3]2+. *Nat. Chem.* **2015**, *7*, 629-633.

11.   Kober, E. M.; Meyer, T. J. An Electronic Structural Model for the Emitting MLCT Excited States of $Ru(bpy)_3^{2+}$ and $Os(bpy)_3^{2+}$. *Inorg. Chem.* **1984**, *23*, 3877-3886.

12.   Yaghoobi Nia, N.; Farahani, P.; Sabzyan, H.; Zendehdel, M.; Oftadeh, M. A Combined Computational and Experimental Study of the [Co(bpy)3]2+/3+ Complexes as One-Electron Outer-Sphere Redox Couples in Dye-Sensitized Solar Cell Electrolyte Media. *Phys. Chem. Chem. Phys.* **2014**, *16*, 11481-11491.

13.   Buckner, M. T.; McMillin, D. R. Photoluminescence from Copper(I) Complexes with Low-Lying Metal-to-Ligand Charge Transfer Excited States. *Chem. Commun.* **1978**, 759-761.

14.   Palmer, C. E. A.; McMillin, D. R.; Kirmaier, C.; Holten, D. Flash Photolysis and Quenching Studies of Copper(I) Systems in the Presence of Lewis Bases: Inorganic exciplexes? *Inorg. Chem.* **1987**, *26*, 3167-3170.

15.   Siddique, Z. A.; Yamamoto, Y.; Ohno, T.; Nozaki, K. Structure-Dependent Photophysical Properties of Singlet and Triplet Metal-to-Ligand Charge Transfer States in Copper(I) Bis(diimine) Compounds. *Inorg. Chem.* **2003**, *42*, 6366-6378.

16.   Chen, L. X.; Shaw, G. B.; Novozhilova, I.; Liu, T.; Jennings, G.; Attenkofer, K.; Meyer, G. J.; Coppens, P. MLCT State Structure and Dynamics of a Copper(I) Diimine Complex Characterized by Pump−Probe X-ray and Laser Spectroscopies and DFT Calculations. *J. Am. Chem. Soc.* **2003**, *125*, 7022-7034.

17.   Shaw, G. B.; Grant, C. D.; Shirota, H.; Castner, E. W.; Meyer, G. J.; Chen, L. X. Ultrafast Structural Rearrangements in the MLCT Excited State for Copper(I) bis-Phenanthrolines in Solution. *J. Am. Chem. Soc.* **2007**, *129*, 2147-2160.

18.   Du, L.; Lan, Z. Ultrafast Structural Flattening Motion in Photoinduced Excited State Dynamics of a Bis(diimine) Copper(I) Complex. *Phys. Chem. Chem. Phys.* **2016**, *18*, 7641-7650.

19.   Iwamura, M.; Takeuchi, S.; Tahara, T. Ultrafast Excited-State Dynamics of Copper(I) Complexes. *Acc. Chem. Res.* **2015**, *48*, 782-791.

20.   Brown-Xu, S.; Fumanal, M.; Gourlaouen, C.; Gimeno, L.; Quatela, A.; Thobie-Gautier, C.; Blart, E.; Planchat, A.; Riobé, F.; Monnereau, C.; Chen, L. X.; Daniel, C.; Pellegrin, Y. Intriguing Effects of Halogen Substitution on the Photophysical Properties of 2,9-(Bis)halo-Substituted Phenanthrolinecopper(I) Complexes. *Inorg. Chem.* **2019**, *58*, 7730-7745.

21.   Soulis, K.; Gourlaouen, C.; Daniel, C.; Quatela, A.; Odobel, F.; Blart, E.; Pellegrin, Y. New luminescent copper(I) complexes with extended π-conjugation. *Polyhedron* **2018**, *140*, 42-50.

22.   Everly, R. M.; Ziessel, R.; Suffert, J.; McMillin, D. R. Steric Influences on the Photoluminescence from Copper(I) Phenanthrolines in Rigid Media. *Inorg. Chem.* **1991**, *30*, 559-561.

23.   Ichinaga, A. K.; Kirchhoff, J. R.; McMillin, D. R.; Dietrich-Buchecker, C. O.; Marnot, P. A.; Sauvage, J. P. Charge-Transfer Absorption and Emission of Cu(NN)2+ Systems. *Inorg. Chem.* **1987**, *26*, 4290-4292.

24.   Cunningham, C. T.; Cunningham, K. L. H.; Michalec, J. F.; McMillin, D. R. Cooperative Substituent Effects on the Excited States of Copper Phenanthrolines. *Inorg. Chem.* **1999**, *38*, 4388-4392.

25.   McCusker, C. E.; Castellano, F. N. Design of a Long-Lifetime, Earth-Abundant, Aqueous Compatible Cu(I) Photosensitizer Using Cooperative Steric Effects. *Inorg. Chem.* **2013**, *52*, 8114-8120.

26.   Lockard, J. V.; Kabehie, S.; Zink, J. I.; Smolentsev, G.; Soldatov, A.; Chen, L. X. Influence of Ligand Substitution on Excited State Structural Dynamics in Cu(I) Bisphenanthroline Complexes. *J. Phys. Chem. B* **2010**, *114*, 14521-14527.

27.   Brunner, F.; Klein, Y. M.; Keller, S.; Morris, C. D.; Prescimone, A.; Constable, E. C.; Housecroft, C. E. The beneficial effects of trifluoromethyl-substituents on the photoconversion efficiency of copper(i) dyes in dye-sensitized solar cells. *RSC Adv.* **2015**, *5*, 58694-58703.

28.   Benari, M. D.; Hefter, G. T. Electrochemical Characteristics of the Copper(II)-Copper(I) Redox Couple in Dimethyl Sulfoxide Solutions. *Aust. J. Chem.* **1990**, *43*, 1791-1801.

29.   Miller, M. T.; Gantzel, P. K.; Karpishin, T. B. A photoluminescent copper(I) complex with an exceptionally high Cu-II/Cu-I redox potential: Cu(bfp)(2) (+) (bfp = 2,9-bis(trifluoromethyl)-1,10-phenanthroline). *Angew. Chem. Int. Ed.* **1998**, *37*, 1556-1558.

30.   Kovalevsky, A. Y.; Gembicky, M.; Coppens, P. Cu(I)(2,9-Bis(trifluoromethyl)-1,10-phenanthroline)2+ Complexes: Correlation between Solid-State Structure and Photoluminescent Properties. *Inorg. Chem.* **2004**, *43*, 8282-8289.

31.   Furue, M.; Maruyama, K.; Oguni, T.; Naiki, M.; Kamachi, M. Trifluoromethyl-Substituted 2,2'-Bipyridine Ligands. Synthetic Control of Excited-State Properties of Ruthenium(II) Tris-Chelate Complexes. *Inorg. Chem.* **1992**, *31*, 3792-3795.

32.   Scaltrito, D. V.; Thompson, D. W.; O'Callaghan, J. A.; Meyer, G. J. MLCT excited states of cuprous bis-phenanthroline coordination compounds. *Coord. Chem. Rev.* **2000**, *208*, 243-266.

33.   Accorsi, G.; Listorti, A.; Yoosaf, K.; Armaroli, N. 1,10-Phenanthrolines: versatile building blocks for luminescent molecules, materials and metal complexes. *Chem. Soc. Rev.* **2009**, *38*, 1690-1700.

34.   Alreja, P.; Kaur, N. Recent advances in 1,10-phenanthroline ligands for chemosensing of cations and anions. *RSC Adv.* **2016**, *6*, 23169-23217.

35.   Bencini, A.; Lippolis, V. 1,10-Phenanthroline: A versatile building block for the construction of ligands for various purposes. *Coord. Chem. Rev.* **2010**, *254*, 2096-2180.

36.   Nagib, D. A.; MacMillan, D. W. C. Trifluoromethylation of arenes and heteroarenes by means of photoredox catalysis. *Nature* **2011**, *480*, 224-228.

37.   Ji, Y. N.; Brueckl, T.; Baxter, R. D.; Fujiwara, Y.; Seiple, I. B.; Su, S.; Blackmond, D. G.; Baran, P. S. Innate C-H trifluoromethylation of heterocycles. *Proc. Natl. Acad. Sci. U.S.A.* **2011**, *108*, 14411-14415.

38.   Ye, Y. D.; Sanford, M. S. Merging Visible-Light Photocatalysis and Transition-Metal Catalysis in the Copper-Catalyzed Trifluoromethylation of Boronic Acids with CF3I. *J. Am. Chem. Soc.* **2012**, *134*, 9034-9037.

39.   Li, G. B.; Zhang, C.; Song, C.; Ma, Y. D. Progress in copper-catalyzed trifluoromethylation. *Beilstein J. Org. Chem.* **2018**, *14*, 155-181.

40.   Zhu, C. L.; Zhang, Y. Q.; Yuan, Y. A.; Xu, H. Copper-Catalyzed Aerobic C-H Trifluoromethylation of Phenanthrolines. *Synlett* **2015**, *26*, 345-349.

41.   Beer, R. H.; Jimenez, J.; Drago, R. S. Syntheses of 2,9-bis(halomethyl-1,10-phenanthrolines: potential robust ligands for metal oxidation catalysts. *J. Org. Chem.* **1993**, *58*, 1746-1747.

42.   Kuvychko, I. V.; Castro, K. P.; Deng, S. H. M.; Wang, X.-B.; Strauss, S. H.; Boltalina, O. V. Taming Hot CF3 Radicals: Incrementally Tuned Families of Polyarene Electron Acceptors for Air-Stable Molecular Optoelectronics. *Angew. Chem. Int. Ed.* **2013**, *52*, 4871-4874.

43.   Castro, K. P.; Clikeman, T. T.; DeWeerd, N. J.; Bukovsky, E. V.; Rippy, K. C.; Kuvychko, I. V.; Hou, G.-L.; Chen, Y.-S.; Wang, X.-B.; Strauss, S. H.; Boltalina, O. V. Incremental Tuning Up of Fluorous Phenazine Acceptors. *Chem. Eur. J.* **2016**, *22*, 3930-3936.

44.   Kuvychko, I. V.; Clikeman, T.; Dubceac, C.; Chen, Y. S.; Petrukhina, M. A.; Strauss, S. H.; Popov, A. A.; Boltalina, O. V. Understanding Polyarene Trifluoromethylation with Hot CF3 Radicals Using Corannulene. *Eur. J. Org. Chem.* **2018**, 4233-4245.

45.   A. Y. Kovalevsky, M. G., P. Coppens CCDC 222330: Experimental Crystal Structure Determination. *CSD Communication* **2004**.

46.   Gordon, K. C.; McGarvey, J. J. Time-Resolved Resonance Raman Spectroscopy of Bis(2,9-dimethyl-1,10-phenanthroline)Copper(1+) in Solution. *Inorg. Chem.* **1991**, *30*, 2986-2989.

47.   Garakyaraghi, S.; Danilov, E. O.; McCusker, C. E.; Castellano, F. N. Transient Absorption Dynamics of Sterically Congested Cu(I) MLCT Excited States. *J. Phys. Chem. A* **2015**, *119*, 3181-3193.

48.   Kovalevsky, A. Y.; Gembicky, M.; Novozhilova, I. V.; Coppens, P. Solid-State Structure Dependence of the Molecular Distortion and Spectroscopic Properties of the Cu(I) Bis(2,9-dimethyl-1,10-phenanthroline) Ion. *Inorg. Chem.* **2003**, *42*, 8794-8802.

CHAPTER 4. POLYTRIFLUOROMETHYLATION OF PHENANTHRIDINE: SYNTHESIS,

ISOLATION, STRUCUTRAL STUDIES AND ELECTROCHEMICAL PROPERTIES

Eight new trifluoromethyl (CF_3) phenanthridine (PHRD) compounds, of which four are

PHRD derivatives with three CF_3 substitutions and four are PHRD derivatives with four CF_3

substitutions have been identified and structurally characterized. The compounds and their

abbreviations are shown in **Figure 4.1**. The structure and numbering scheme for PHRD is shown

in **Figure 4.2**. Of the eight compounds, six have been structurally characterized by single crystal

X-ray diffraction (SC-XRD). Five compounds have been studied with cyclic voltammetry (CV).

4.1   Introduction

The PHRD core is found in many natural products, biologically active molecules, and drug

molecules including promising anti-cancer agents (**Figure 4.3**).[1-6] Sanguinarine and chelerythrine

are naturally occurring PHRD derivatives with anti-cancer activity. Chelerythrine has also

exhibited antibacterial, antifungal, and anti-inflammatory properties.[1] The PHRD derivative

reported by Wan et al. (**Figure 4.3**, compound 8a, right) was shown to have higher antitumor

activity and solubility with less side effects compared to the naturally occurring

benzophenanthridine, sanguinarine.[6] The higher solubility is attributed to the lack of the fourth

aromatic ring that is found in sanguinarine. The PHRD core can also be found in ligands for metal

complexes (**Figure 4.4**, left and middle), which have been used as sensitizers for organic light

emitting diodes (OLED).[7-9] Additionally, the PHRD motif can be found in dye sensitized solar

cells (DSSCs) as organic dyes (**Figure 4.4**, right) with reported efficiency up to 8%.[10]

The CF_3 group can also be found in many drugs and drug candidates as it has been shown

to lead to higher lipophilicity which can improve membrane permeability, bioavailability, and

potency.[11-13] The presence of a CF_3 group in a drug candidate can improve stability and selectivity. This is accomplished through a variety of ways including modifying the pKa of the molecule which impacts hydrogen bonding interactions, introducing a steric effect due to the larger van der Waals radius of a CF_3 group, and/or by modifying the conformation of the molecule.[11] With this in mind, many research groups are interested in incorporating CF_3 groups into the PHRD core.

To date, there have been trifluoromethylated PHRD derivatives containing one or two CF_3 groups.[14-19] As shown in **Scheme 4.1**, the reported methods employed for the synthesis of these PHRD$(CF_3)_n$ derivatives include i) rhodium catalyzed [2+2+2] cycloaddition reactions between a trifluoromethylated diyne and various alkynes;[17] ii) cyclization of trifluoroacetimidoyl chlorides via photoredox generated radical or palladium catalyzed C-H bond functionalization;[18-19] iii) cyclization of a 2-isocyano-1,1'-biphenyl derivative after addition of a •CF_3 radical;[12,15,20-21] iv) Suzuki coupling of *N*-aryltrifluoroacetimidoyl chlorides and arylboronic acids.[16] All four of these methods have generally high yields ranging from 50-90 % depending on the substrate substituents. Methods ii, iii, and iv have been shown to produce PHRD derivatives with two CF_3 substituents when one of the starting material R-groups is a CF_3 (**Table 4.1**). It should be noted that for each case with two CF_3 substituents, the positions are limited in that one of the CF_3 groups is always located at the 6-position. Although there were multiple reports of PHRD derivatives with two CF_3 groups, PHRD derivatives with more than two CF_3 groups have not been reported to the best of the author's knowledge.

While PHRD derivatives with three and four CF_3 substituents have not yet been reported, the presence of electron-withdrawing groups in polycyclic aromatic hydrocarbons (PAH) is known to enhance air-stability and metabolic stability while improving electron-acceptor properties and charge carrier mobilities. It is of interest to synthesize and study PHRD derivatives with more than

two CF_3 substituents so that the effects of higher substitution and different substitution patterns can be evaluated. In this work, it is demonstrated that direct substitution of multiple hydrogen atoms with CF_3 groups can be achieved with PHRD. To the author's knowledge, this is the first instance that PHRD has been post-synthetically substituted with CF_3 groups by direct treatment with CF_3I gas and it is the first report of PHRD derivatives with more than two CF_3 groups.

4.2   Results and Discussion

4.2.1   Trifluoromethylation of PHRD

In an effort to synthesize PHRD derivatives with more than two CF_3 substituents, an efficient method for the polytrifluoromethylation of PHRD was employed through the substitution of aromatic hydrogen atoms with $CF_3 \bullet$ radicals, which are generated by homolysis of CF_3I in the gas-phase (**Scheme 4.2**). This method is known to produce a large number of compounds with a different number of substitutions and different substitution patterns, which in turn allows for the study of multiple compounds without the need to develop syntheses for each compound. In addition to the trifluoromethylation of multiple PAHs,[22] the Strauss-Boltalina research group has previously shown that this is an efficient method for the trifluoromethylation another hetero-PAH, phenazine (PHNZ).[23]

For the trifluoromethylation of PHRD, one equiv. of PHRD (193.5 mg, 1.08 mmol) and ten equiv. of CF_3I (g) were added to a glass ampoule which was subsequently sealed and heated to 330 ºC for 6 h. This reaction was performed by former Strauss Boltalina Research Group postdoctoral researcher, Dr. Igor Kuvychko. Soluble products were extracted with dichloromethane and iodine was removed by washing with an aqueous sodium thiosulfate solution resulting in 413.7 mg of oily material. Mass spectrometry of the crude mixture revealed PHRD with five and six substitutions but these molecules were not isolated or observed by NMR

spectroscopy. Analyte suppression is likely the reason that the mass spectrum is not representative of the overall mixture, as compounds with more electron withdrawing groups are more easily ionized than compounds with less electron withdrawing groups. The crude mixture was then purified by HPLC. From the twelve fractions, eight new compounds were identified and structurally characterized via NMR spectroscopy and/or SC-XRD. The twelve fractions resulted in a sum of 181.9 mg (0.44 mmol based on 3.5 substitutions) after HPLC separation.

4.2.2   Isolation of PHRD(CF$_3$)$_n$ Compounds

The separation of PHRD(CF$_3$)$_n$ derivatives was carried out on a COSMOSIL Buckyprep HPLC semi-preparative column. While this particular column was originally designed for the separation of fullerenes, the pyrene stationary phase has proven to be useful in the separation and isolation of PAHs as well. The Strauss Boltalina Research Group has found the Buckyprep stationary phase to be successful in the separation of trifluoromethyl PAH derivatives, even allowing for the separation of isomers with similar structures. Initial separation was attempted with acetonitrile as the eluent, but it was found that switching the eluent from acetonitrile to methanol had a significant impact by increasing the retention times for many compounds and allowing for better separation (**Figure 4.5** and **Figure 4.6**).

Separation in methanol afforded twelve major fractions (**Figure 4.6**): Fraction 1 (8.3 – 9.0 min, 4.2 mg); Fraction 2 (9.0 – 9.8 min, 18.8 mg); Fraction 3 (9.8 – 10.7 min, 43.6 mg); Fraction 4 (10.7 – 11.6 min, 22.8 mg); Fraction 5 (12.0 – 12.9 min, 17.5 mg); Fraction 6 (12.9 – 14.5 min, 17 mg); Fraction 7 (14.5 – 15.5 min, 1.4 mg); Fraction 8 (16.5 – 17.8 min, 17.1 mg); Fraction 9 (18.4 – 19.4 min, 13.7 mg); Fraction 10 (21.0 – 22.3 min, 12.4 mg); Fraction 11 (22.8 – 24.5 min, 8.6 mg); Fraction 12 (24.5 – 26.9 min, 4.8 mg). After HPLC separation, NMR analysis was performed and the purest fractions were selected for single crystal growth.

PHRD-3-1 was crystallized from Fraction 1. Fraction 4 produced single crystals of PHRD-4-2 as well as multiple unidentified compounds. Fraction 6 produced crystals of PHRD-3-2. PHRD-3-3 was crystallized from Fraction 9. Fraction 10 produced PHRD-4-4 (F10a) and single crystals of PHRD-3-4 (F10b). Fraction 11 was mainly composed of PHRD-4-3, but high quality single crystals were not produced. Fraction 12 produced single crystals of PHRD-4-1 by slow evaporation of $CDCl_3$. All single crystals were grown by slow evaporation of methanol, with the exception of PHRD-4-1.

^{19}F NMR spectra for fractions 2, 3, 4, 5, 7, and 8 are shown in **Figure 4.7**. Fraction 2 contains at least three major compounds with several minor compounds. Based on integrated peaks in the ^{19}F NMR spectrum, F2 appears to be composed of compounds with three substitutions. Fraction 3 contains multiple compounds based on the ^{19}F NMR spectrum and it appears that it is mostly composed of compounds with four substitutions. F5 is a mixture of at least three compounds, with the major component having four substitutions. F7 appears to have one major compound with four substitutions and several minor compounds. F8 appears to contain at least three major compounds and it is mostly composed of compounds with three substitutions.

In general, compounds with four CF_3 substitutions eluted later than compounds with 3 CF_3 substitutions. The exception to this rule was the minor compound PHRD-4-2, which happens to have a twisted core. With this in mind, PHRD-3-1 was the first compound to elute and it also has a twisted core. The phenomenon of compounds with a twisted core eluting first can most likely be attributed to less π-π interaction with the pyrene stationary phase in the COSMOSIL Buckyprep columns.

4.2.3   SC-XRD: Structural Assignments and Packing of PHRD(CF$_3$)$_n$ derivatives

The lack of symmetry in the PHRD core leads to difficulty in structural assignment from

NMR spectroscopy alone. While ^{19}F NMR spectroscopy can provide the number of CF_3 groups for these PHRD derivatives, very little information on the position of substitutions can be determined. Considering this, SC-XRD was used to identify the majority of the PHRD derivatives, with the exception of PHRD-4-4 (F10a) and PHRD-4-3 (F11). The preliminary structures of PHRD-4-4 (F10a) and PHRD-4-3 (F11) have been determined by comparing their ^{19}F and ^{1}H NMR signals with the NMR signals of compounds identified by SC-XRD (described in Section 4.2.4).

Single crystals of six compounds have been grown by slow evaporation of methanol or chloroform. PHRD-3-1 (**Figure 4.8**), PHRD-3-2 (**Figure 4.9**), PHRD-3-3 (**Figure 4.10**) and PHRD-3-4 (**Figure 4.11**) all exhibit significant core overlap, while adjacent molecules adopt opposite orientations within columns. PHRD-4-1 is oriented in the same direction throughout the columns (**Figure 4.12**), while PHRD-4-2 is oriented with a flip along the z-axis between molecules, rather than a complete inversion (**Figure 4.13**). The 4-position is the most commonly substituted position. Following the 4-position, the 6, and 7-positions are also commonly substituted.

PHRD-4-1, PHRD-3-2, PHRD-3-3, and PHRD-3-4 all have rigidly flat cores, while PHRD-3-1 and PHRD-4-2 have twisted cores, with torsional angles of 16.52 º and 15.77 º, respectively. The torsion in PHRD-3-1 and PHRD-4-2 can be attributed to steric interaction of a CF_3 group at the 1-position and the H atom at the 10-position, also known as the bay positions. This is expected due to the bulk of the CF_3 groups and it has been observed in other PAHs such perylene diimide.[24] The compounds with flat cores do not have CF_3 groups substituted at the bay positions.

PHRD-3-1, PHRD-3-3, PHRD-4-1, and PHRD-4-2 are packed in a slip stacked

conformation within columns, but the columns are oriented in a herringbone fashion (**Figure 4.8**, **Figure 4.10**, **Figure 4.12**, **Figure 4.13**). The herringbone angle in PHRD-3-1 is significantly less than that in PHRD-4-1 and PHRD-3-3. PHRD-3-2 and PHRD-3-4 exhibit brick layered packing (**Figure 4.9** and **Figure 4.11**). As the number of CF_3 groups is increased from 3 to 4, the packing distance between molecules is increased (**Table 4.2**).

4.2.4 NMR spectroscopy of PHRD(CF_3)$_n$ compounds

^{1}H and ^{19}F NMR data by itself is generally not enough information to determine the structure of the PHRD(CF_3)$_n$ compounds. However, NMR data from compounds that have already been structurally characterized by SC-XRD can be useful in elucidating the structures of compounds which did not produce high quality single crystals. For the following discussion, it may be helpful to refer to the numbering scheme for PHRD found in **Figure 4.2**.

By examining the ^{19}F NMR spectra of the PHRD derivatives in combination with the substitution patterns from crystal structures, some NMR peak positions can be tentatively assigned to substitutions at specific positions. For instance, each of the compounds PHRD-3-1, PHRD-3-2, PHRD-3-3, and PHRD-4-1 are substituted at the 4-position. This is the only position that is consistently substituted in each of these compounds (**Figure 4.14**) and all of these compounds have a peak at −63 ppm in their ^{19}F NMR spectra. It can be assumed that this peak is the result of a CF_3 group substituted at the 4-position.

PHRD-3-1, PHRD-3-2, PHRD-4-1 all have a peak near −67 ppm (^{19}F NMR) in common and they are all substituted at the 6-position, which suggests that a peak near −67 ppm is the result of substitution at the 6-position.

Additionally, PHRD-3-1 is the only compound with a bay position substituted, and it is the only compound with a peak near −59 ppm (**Figure 4.14**), so it can be assumed that a peak near

−59 ppm is the result of CF_3 substitution at bay position.

Examination of the ^{1}H NMR spectra of known compounds shows that PHRD-3-3, the only known compound with a proton at the 6-position, has a signal near 10 ppm in its ^{1}H NMR spectrum (**Figure 4.15**).

The structure of PHRD-4-3 was preliminarily assigned by comparing NMR spectra of other $PHRD(CF_3)_n$ derivatives as discussed above. The four singlets in the ^{19}F NMR spectrum suggests that there will be four CF_3 groups that are not adjacent to one another (**Figure 4.14**). The ^{1}H NMR spectrum shows three singlets and two doublets (**Figure 4.15**), suggesting that there are only two adjacent protons. There is not a peak near 10 ppm, which would be indicative of a proton being present at the 6-position so there is likely a CF_3 group at the 6-position of PHRD-4-3. There is a peak near −63 ppm in the ^{19}F NMR spectrum, which suggests the 4-position is substituted. There is not a peak near −59 ppm, which would be indicative of a CF_3 at a bay position (reference PHRD-3-1, **Figure 4.14**). Based on this information, the most likely structures are 2,4,6,9-phenanthridine$(CF_3)_4$ or 2,4,6,8-phenanthridine$(CF_3)_4$. Since PHRD-4-1 is 2,4,6,8-phenanthridine$(CF_3)_4$, the structure of PHRD-4-3 has been assigned as 2,4,6,9-phenanthridine$(CF_3)_4$.

The structure of PHRD-4-4 was preliminarily assigned by comparing the NMR spectra of other $PHRD(CF_3)_n$ derivatives as discussed above. The four singlets in the ^{19}F NMR spectrum suggests that there will be four CF_3 groups that are not adjacent to one another. The five singlets in the ^{1}H NMR spectrum suggest that there are five protons that are not adjacent to one another. Based on this information alone, the possible assignments include 2,4,7,9-phenanthridine$(CF_3)_4$, 2,4,8,10-phenanthridine$(CF_3)_4$, 1,3,8,10-phenanthridine$(CF_3)_4$, or 1,3,7,9-phenanthridine$(CF_3)_4$. There is a peak at 10 ppm in the ^{1}H NMR spectrum which suggests there is a proton at the 6-

position. There is a peak near −63 ppm in the ^{19}F NMR spectrum, which suggests the 4-position is substituted, which eliminates 1,3,8,10-phenanthridine(CF$_3$)$_4$ and 1,3,7,9-phenanthridine(CF$_3$)$_4$ as possibilities. Additionally, since there is not a peak near −59 ppm, it can be assumed that there is not a CF$_3$ at the 1-position (bay) (reference PHRD-3-1). While 2,4,8,10-phenanthridine(CF$_3$)$_4$ is still a possibility, it is likely that substitution of the 10-position (bay) would result in a chemical environment that is comparable to substitution of the 1-position (i.e. a downfield chemical shift). In addition, the ^{1}H NMR signals in the spectrum of PHRD-4-4 indicate that there are two sets of protons with similar chemical environments. The peaks at 9.16 and 9.11 ppm represent one set of similar protons, while the peaks at 8.45 and 8.39 ppm represent another set of protons. One set of protons with a similar chemical environment are at the 1 and 10-positions and the other set of protons are at the 3 and 8-positions. The singlets in this region of the ^{1}H NMR spectra of PHRD-3-3 and PHRD-3-2 are also assigned to either the 1 or 3 positions (**Figure 4.15**). The preliminary assignment for PHRD-4-4 is 2,4,7,9-phenanthridine(CF$_3$)$_4$.

Fraction 5 and fraction 7 are each composed of a single major component with multiple minor components. The exact structures for these major components were not completely identified, but some information was extracted from the NMR spectra. Based on the singlets in the ^{19}F NMR spectra, the major components in each fraction are isomers with four non-adjacent CF$_3$ substitutions (**Figure 4.16** and **Figure 4.17**, respectively). Both have peaks near −59 ppm in their ^{19}F NMR spectra which suggests that they are both substituted at a bay position. Neither have a peak in their ^{1}H NMR spectra near 10 ppm (**Figure 4.16**), which suggests that the 6-position is substituted in both molecules. Based on the ^{1}H NMR spectrum, the major component in F5 contains four protons that are each adjacent to another proton, and a single proton that is not adjacent to any other protons. Based on the ^{1}H NMR spectrum (**Figure 4.17**), the major component

in fraction 7 has two protons that are adjacent to each other and three non-adjacent protons.

NMR Data for PHRD(CF₃)ₙ Compounds

PHRD-3-1 (F1, 1,4,6-phenanthridine(CF₃)₃): ^{19}F NMR: δ −59.0 (s, 1 CF₃); −63.3 (singlet, 1 CF₃); −66.9 (singlet, 1 CF₃). ^{1}H NMR: δ 8.89 (d, J = 8.6 Hz, 1H); 8.50 (d, J = 8.2 Hz, 1H); 8.27 (ABq, Δv_{AB} = 33.2 Hz, J_{AB} = 8.1 Hz, 2H); 8.00 (t, J = 7.4 Hz, 1H); 7.93 (t, J = 7.4 Hz, 1H). 92 mol% pure.

PHRD-3-2 (F6, 2,4,6-phenanthridine(CF₃)₃): ^{19}F NMR: δ −63.3 (singlet, 1 CF₃); −65.6 (singlet, 1 CF₃); −67.1 (singlet, 1 CF₃). ^{1}H NMR: δ 9.11 (singlet, 1H); 8.80 (d, J = 8.7 1H); 8.52 (d, J = 8.7 2H); 8.35 (singlet, 1H); 8.09 (t, 1H); 7.95 (t, 1H). 69% pure.

PHRD-3-3 (F9, 2,4,7-phenanthridine(CF₃)₃): ^{19}F NMR: δ −60.7 (singlet, 1 CF₃); −63.2 (singlet, 1 CF₃); −65.4 (singlet, 1 CF₃). ^{1}H NMR: δ 9.96 (s, 1H); 9.11 (s, 1H); 8.94 (d, J = 8.8 Hz, 1H), 8.37 (s, 1H); 8.21 (d, J = 7.3 Hz, 1H); 8.08 (t, J = 8.2 Hz, 1H). 84 mol% pure.

PHRD-3-4 (F10 b, 3,7,9-phenanthridine(CF₃)₃): X-ray structure only

PHRD-4-1 (F12, 2,4,6,8-phenanthridine(CF₃)₄): ^{19}F NMR: δ −63.3 (singlet, 1 CF₃); −65.6 (s, 1 CF₃); −65.9 (s, 1 CF₃); −66.9 (s, 1 CF₃). ^{1}H NMR: δ 9.13 (singlet, 1 H); 8.93 (d, J = 8.7, 1 H); 8.76 (s, 1 H), 8.43 (s, 1 H); 8.28 (d, J = 8.7 Hz, 1 H). 80 mol% pure.

PHRD-4-2 (F4 b, 1,4,7,9-phenanthridine(CF₃)₄): X-ray structure only

PHRD-4-3 (F11, 2,4,6,9-phenanthridine(CF₃)₄): ^{19}F NMR: δ −63.3 (singlet, 1 CF₃); −65.6 (singlet, 1 CF₃); −66.1 (singlet, 1 CF₃); −67.1 (singlet, 1 CF₃). ^{1}H NMR: δ 9.12 (s, 1H); 9.03 (s, 1H); 8.66 (d, J = 9.6 Hz, 1H), 8.43 (singlet, 1H); 8.16 (d, J = 8.3 Hz, 1H). 82 mol% pure.

PHRD-4-4 (F10 a): ^{19}F NMR: δ −61.0 (s, 1 CF₃); −63.2 (s, 1 CF₃); −65.4 (s, 1 CF₃); −65.9 (s, 1 CF₃). ^{1}H NMR: δ 10.00 (s, 1H); 9.17 (s, 1H); 9.11 (s, 1H); 8.45 (s, 1H); 8.39 (s, 1H). 86 mol% pure.

The purity of the compounds was determined by examining the ^{19}F NMR spectra, which in general have very narrow resonances, and estimating the level of impurities from any observable low-intensity resonances near the baseline.

4.2.5   Cyclic Voltammetry

Quasi-reversible electrochemical behavior was observed for PHRD, PHRD-3-1, PHRD-3-3 and PHRD-4-1 (**Figure 4.18**). $E_{1/2}$ values are reported in **Table 4.3**. Cyclic voltammetry was reported for 6-trifluoromethyl-phenanthridine by Lübbesmeyer et al., but it did not appear to be reversible.[15] Quasi-reversible electrochemical behavior for PHRD-4-3 and PHRD-4-4 was not observed (**Figure 4.18**).

It was previously reported by the Strauss Boltalina Research Group that as CF$_3$ groups are added to PHNZ, the change in $E_{1/2}$ per CF$_3$ group is attenuated compared to anthracene (ANTH, the carbon analog of PHNZ).[23] The same does not appear to hold true for PHRD compared to phenanthrene, 0.32 V per CF$_3$ versus 0.28 V per CF$_3$, respectively (**Figure 4.19**). With the added data of PHRD and 1,10-phenanthroline (phen, Chapter 3 Section 3.2), it appears that there is not a predictable trend in $E_{1/2}$ per CF$_3$ group when comparing all carbon analogs vs hetero-PAHs, as was suggested previously.[23]

It is interesting to note that PHRD-3-1 and PHRD-3-3 show a difference in $E_{1/2}$ of 0.05 V, while having significantly different substitution patterns. PHRD-3-1 has a CF$_3$ group ortho to the nitrogen and a CF$_3$ group substituted at the bay position, while PHRD-3-3 does not share either of these characteristics. Consequently, PHRD-3-3 has a flat core, while PHRD-3-1 has a bent core. This suggests that the number of CF$_3$ substitutions has a significantly larger effect on the electrochemistry than the position of the CF$_3$ groups for PHRD derivatives.

A similar trend was observed in PHNZ.[23] PHNZ-3-1 and PHNZ-3-2 as well as PHNZ-4-1

and PHNZ-4-2 each had differences in $E_{1/2}$ of 0.05 V for isomers with different substitution patterns, while the average difference per CF_3 group was reported to be 0.20 V. For phen$(CF_3)_n$ derivatives (Chapter 3), the average difference per CF_3 group was 0.27 V, but the differences between isomers with the same number of substituents was 0.13 V for phen-3-1 and phen-3-2 and 0.11 V for phen-4-1 and phen-4-2. PHRD and PHNZ have significantly lower variance in $E_{1/2}$ between isomers with the same number of CF_3 groups. In phen isomers, the larger differences can be attributed to CF_3 groups that were para in relation to a nitrogen. PHRD and PHNZ do not have positions available that are para to nitrogen, thus the larger difference in $E_{1/2}$ for isomers of the same number of CF_3 substituents is not observed. Overall this suggests that generally, isomeric differences have minimal effect on the electronic properties, but special circumstances such as CF_3 position relative to a heteroatom can have a significant effect on the electronic properties of hetero-PAHs.

4.3 Summary and Outlook

In summary, a one-step method for the preparation and chromatographic separation of tris and tetra-trifluoromethylated PHRD derivatives is reported. SC-XRD and NMR spectroscopy allowed for the assignment of eight new PHRD$(CF_3)_n$ compounds. The electronic properties of PHRD were tuned by the number of CF_3 groups; on average, the $E_{1/2}$ increased 0.32 V per CF_3 group. It was found that the electrochemistry ($E_{1/2}$) is significantly impacted by the number of CF_3 groups, but not as heavily impacted by substitution pattern for PHRD. This method demonstrates the possibility for direct trifluoromethylation of PHRD. While this particular reaction was not intended to target specific isomers, direct trifluoromethylation could be explored by starting with a PHRD$(CF_3)_2$ substrate to improve selectivity and yields.

4.4 Experimental

4.4.1 Materials and Methods

The following reagents and solvents were obtained from the indicated sources and were used as received or were purified/treated/stored as indicated. Phenanthridine, (Aldrich, 99%). Trifluoromethyl iodide, 98% (SynQuest). HPLC grade methanol (Fisher Scientific), ACS grade dichloromethane (Sigma), chloroform-d (Cambridge Isotopes Laboratories, 99.8%) sodium thiosulfate (Malinckrodt), and hexafluorobenzene (Synquest Labs, 99.8%).

4.4.2 High Performance Liquid Chromatography

HPLC was conducted using a Shimadzu liquid chromatography instrument (CBM-20A control module, SPD-20A UV-vis detector set to 300 nm, LC-6AD pump, manual injector valve.) The HPLC column utilized was a 10 mm I.D. x 250 nm COSMOSIL Buckyprep column. The eluent was ACS grade methanol at a flow rate of 5 mL min^{-1}.

4.4.3 NMR Analysis

^{1}H and ^{19}F NMR analyses were acquired on a Varian INOVA instrument. ^{1}H NMR spectra were acquired at 400 MHz (CDCl$_3$ solvent). ^{19}F NMR spectra were acquired at 376 MHz (CDCl$_3$ solvent).^{19}F NMR spectra were referenced to a hexafluorobenzene ($-\delta = 164.9$) internal standard.

4.4.4 Cyclic voltammetry (CV):

CV measurements were carried out in a nitrogen atmosphere glovebox on a PAR 263 potentiostat/galvanostat. CV measurements utilized 0.1 M tetrabutylammonium perchlorate, recrystallized from ethyl acetate, in dimethoxyethane with platinum working and counter electrodes and a silver quasi-reference electrode at a scan rate of 100 mVs^{-1} using ferrocene as an internal standard.

4.4.5 Trifluoromethylation of PHRD:

The compound PHRD (193.5 mg, 1.08 mmol) was added to a 330.6 mL glass ampoule.

CF₃I gas (600 torr, 10.8 mmol) was introduced, cooled to −78 °C and the ampoule was sealed under vacuum (10^{-4} torr). The ampoule was heated to 330 °C for 7.5 h and subsequently cooled to room temperature. The ampoule was opened, and soluble trifluoromethylated PHRD derivatives were extracted with dichloromethane. The dichloromethane solution was washed with a 10% solution of sodium thiosulfate to remove iodine.

Danger! High pressure can be generated in the ampoule leading to explosive ampoule failure. The maximum pressure inside the ampoule at high temperature has to be calculated. Depending on the size and wall thickness of the ampoule the maximum allowable pressure changes, so a conservative limit of 2-3 bar must be set. The burst pressure for a glass ampoule is largely determined by the quality of seal, so care must be taken during the sealing step. Use shields and personal protection at all times. Only experienced personnel should perform these operations.

4.4.6   SC-XRD

Single crystal data for PHRD-3-1, PHRD-3-2, PHRD-3-3, PHRD-3-4, PHRD-4-1, PHRD-4-2, PHRD-4-3, and PHRD-4-4 was collected on the Advanced Photon Source synchrotron instrument at Argonne National Laboratory, Argonne, IL on beamline 15ID-D with a wavelength of λ=0.41328 Å, employing a diamond 1 1 1 monochromator and Bruker D8 goniometer. The structures were solved using direct methods and refined by a full-matrix weighted least-squares process. Standard Bruker control and integration software (APEX 3) was employed, and Bruker SHELXTL software was used with Olex 2 for structure solution, refinement and molecular graphics. All single crystals were grown by the author of this dissertation. All structures were collected by the author with either Strauss Boltalina lab group member Nicholas DeWeerd or Colin Brook at Argonne National Laboratory. The X-ray structures in this Chapter were solved by

Nicholas DeWeerd or they were solved by the author with assistance from Nicholas DeWeerd. All analysis of the X-ray structures was performed by the author of this dissertation. Crystallographic data can be found in Appendix 3 Table A3.1.

Table 4.1. PHRD derivatives with two CF$_3$ groups.
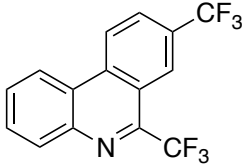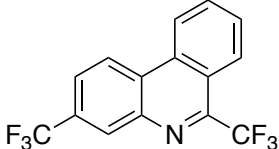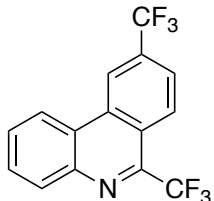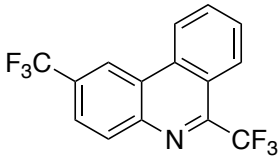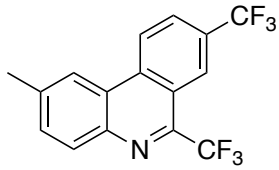
PHRD(CF$_3$)$_2$ Derivative	Reference, Identifier, and Yield	Synthesis Method
	Fu et al., compound 2h, 70%[18] Zhu et al., compound 2g, 80%[19] Q. Wang et al., compound 2f, 63%[21]	Method ii Method ii Method iii
	Fu et al., compound 2p, 80%[18] Zhu et al., compound 2o, 79%[19] Cheng et al., compound 3h, 70%[20] W. Wang et al., compound 22, 82%[16]	Method ii Method ii Method iii Method iv
	W. Wang et al., compound 14, 87%[16]	Method iv
	Q. Wang et al., compound 2n, 59%[21]	Method iii
	Lübbesmeyer et al., compound 3k, 80%[15]	Method iii

Table 4.2. Packing distances between molecules.

Compound	Packing distance (Å)
PHRD[a,c]	3.47
PHRD-3-1[a]	3.67
PHRD-3-2[b]	3.51
PHRD-3-3[a]	3.77
PHRD-3-4[b]	3.61
PHRD-4-1[b]	3.79
PHRD-4-2[a]	4.11

[a] Packing distance measured by generating a centroid of one molecule and a plane from the adjacent molecule and measuring the distance from the centroid to the plane. CF_3 groups and hydrogens were not included for generation of planes or centroids.
[b] Packing distance measured by generating a plane of one molecule to the plane generated from the core of its nearest neighbor.
[c] PHRD structure from Orola et al.[25] CCDC deposition number: 816162

Table 4.3. PHRD, PHRD $(CF_3)_n$ compounds, abbreviations and reduction potentials.

compound	Abbreviation	$E_{1/2}$ [V] vs. Fe(Cp)$_2$	Number of CF$_3$ Groups
phenanthridine	**PHRD**	−2.87	0
1,4,6-tris(trifluoromethyl)phenanthridine	**PHRD-3-1**	−1.85	3
2,4,7-tris(trifluoromethyl)phenanthridine	**PHRD-3-3**	−1.90	3
2,4,6,8-tetra(trifluoromethyl)phenanthridine	**PHRD-4-1**	−1.64	4

[a]Cyclic voltammetry; 0.1 M N(n-Bu)$_4$ClO$_4$ in dimethoxyethane; platinum working and counter electrodes; silver wire quasi-reference electrode; 100 mv^{-s}; ferrocene (Fe(Cp)$_2$) internal standard.

PHRD-3-1
1,4,6-phenanthridine(CF$_3$)$_3$

PHRD-4-1
2,4,6,8-phenanthridine(CF$_3$)$_4$

PHRD-3-2
2,4,6-phenanthridine(CF$_3$)$_3$

PHRD-4-2
1,4,7,9-phenanthridine(CF$_3$)$_4$

PHRD-3-3
2,4,7-phenanthridine(CF$_3$)$_3$

PHRD-4-3
2,4,6,9-phenanthridine(CF$_3$)$_4$

PHRD-3-4
3,7,9-phenanthridine(CF$_3$)$_3$

PHRD-4-4
2,4,7,9-phenanthridine(CF$_3$)$_4$
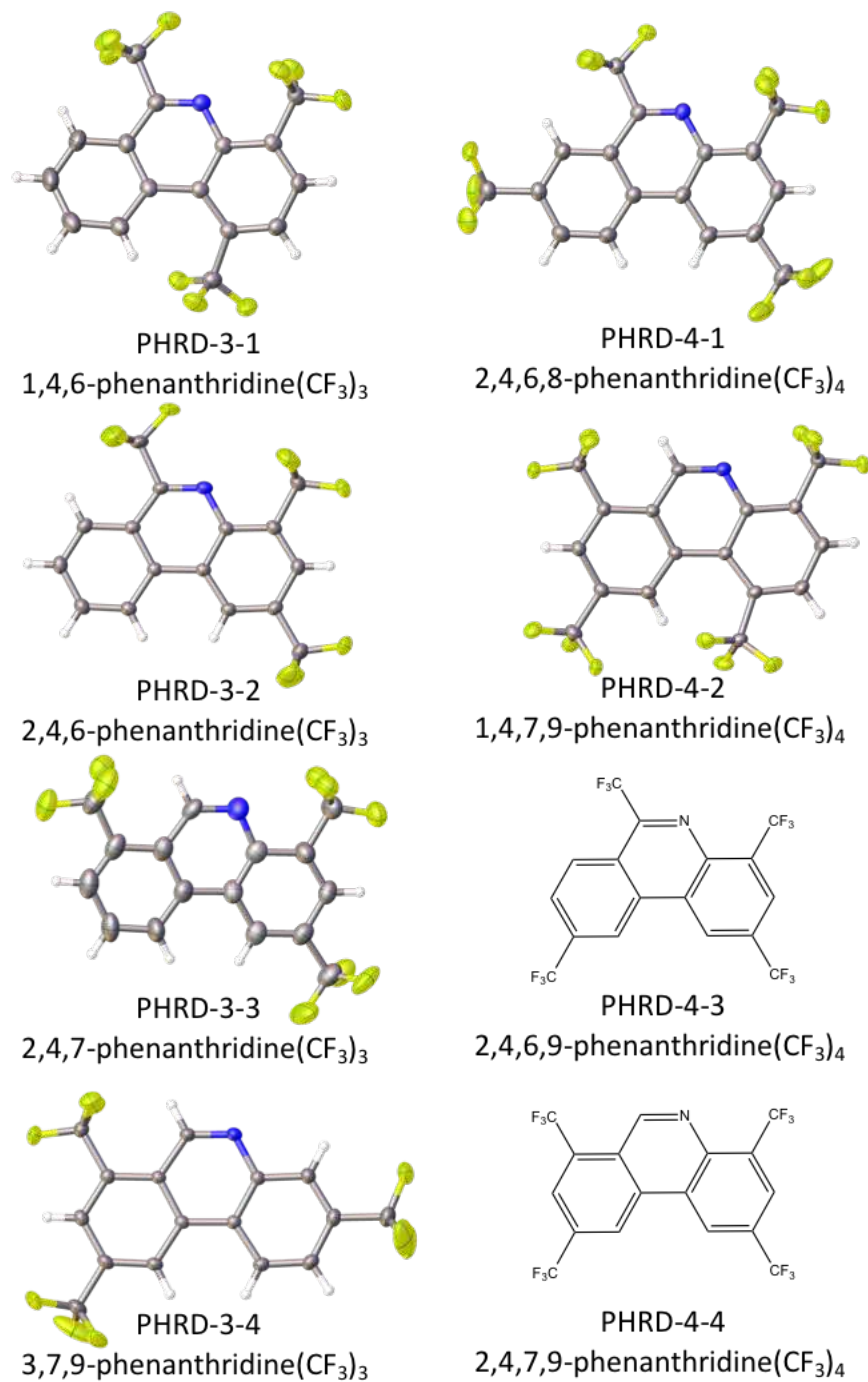
Figure 4.1. Structures and common names of PHRD(CF$_3$)$_n$ compounds. Thermal ellipsoid plots at the 50% probability level shown PHRD-3-1, PHRD-3-2, PHRD-3-3, PHRD-3-4, PHRD-4-1, PHRD-4-2.

181
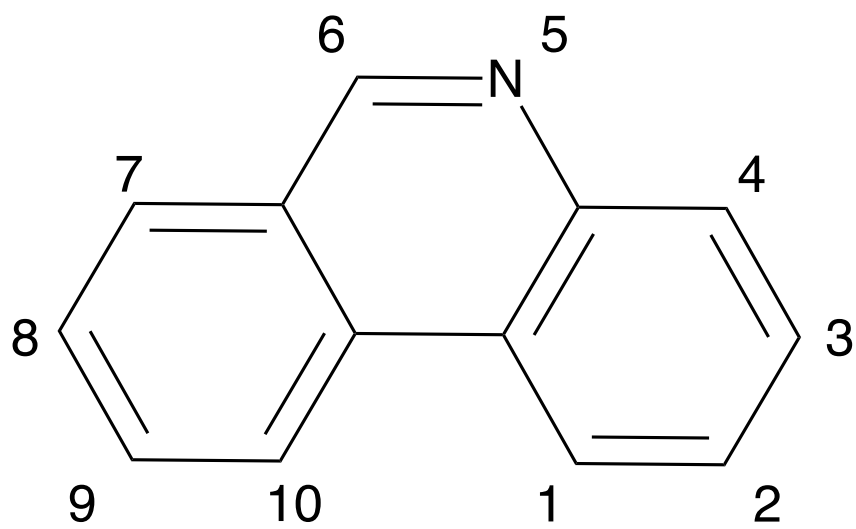
Figure 4.2. Numbering scheme for PHRD.
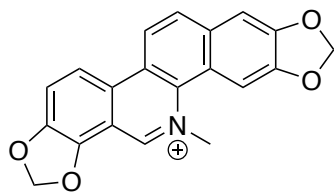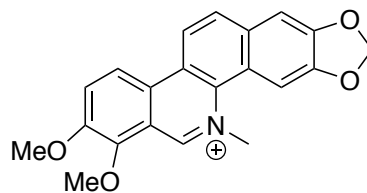
sanguinarine   chelerythrine   Wan et al.
                                              compound 8a
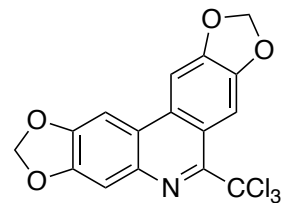
Figure 4.3. Structures for naturally occurring sanguinarine and chelerythrine, as well as compound 8a reported by Wan et al.[6] the molecule 8a was designed to be a more soluble derivative of sanguinarine and it exhibits promising antitumor properties with less side effects than sanguinarine.
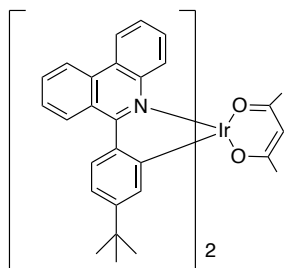
(TP-BQ)2Ir(acac)
OLED sensitizer
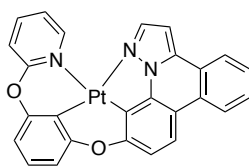
ZPt1
OLED sensitizer
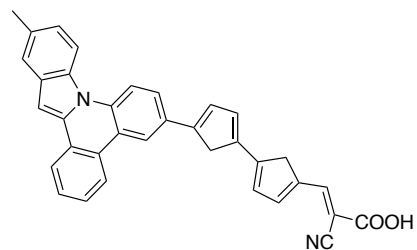
JK-61
DSSC organic dye

Figure 4.4. Examples of the PHRD motif as OLED sensitizers and DSSC dyes.
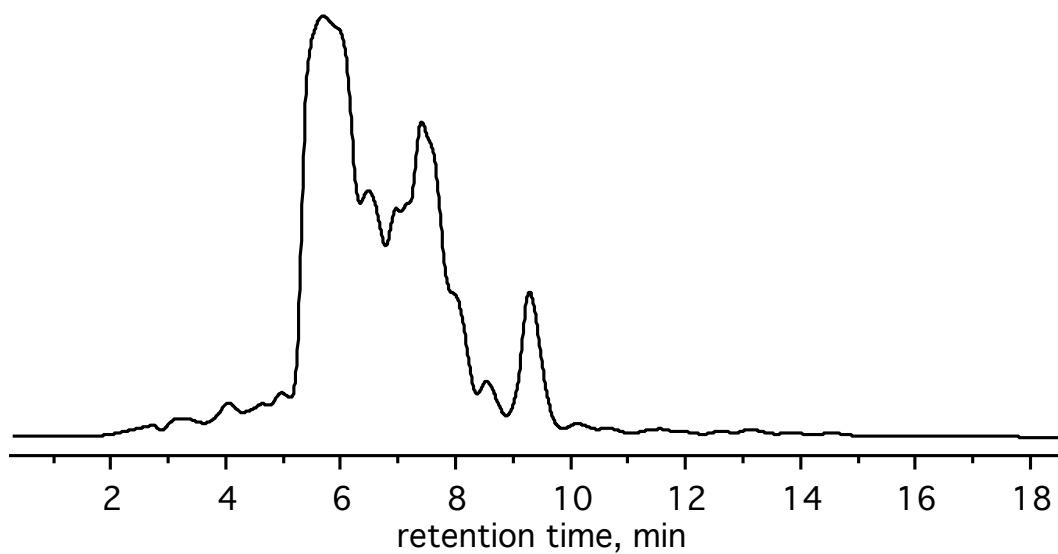
Figure 4.5. HPLC chromatogram of PHRD reaction. Eluent is acetonitrile at 5 mL/min on Cosmosil Buckprep semi-preparative at 300 nm.
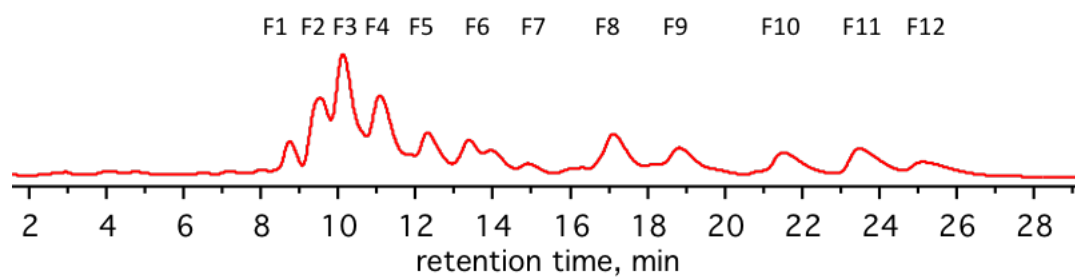
Figure 4.6. HPLC chromatogram of PHRD reaction. Eluent is methanol at 5 mL/min Cosmosil Buckprep semi-preparative at 300 nm.
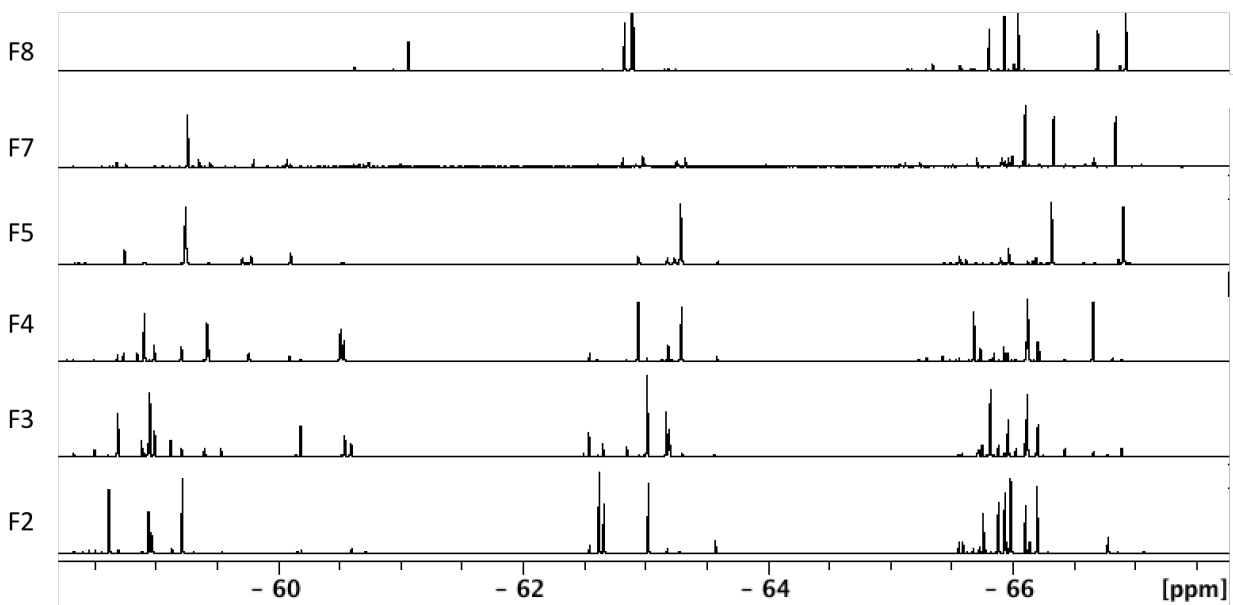
Figure 4.7. ^{19}F NMR spectra of PHRD fractions 2, 3, 4, 5, 7, and 8.
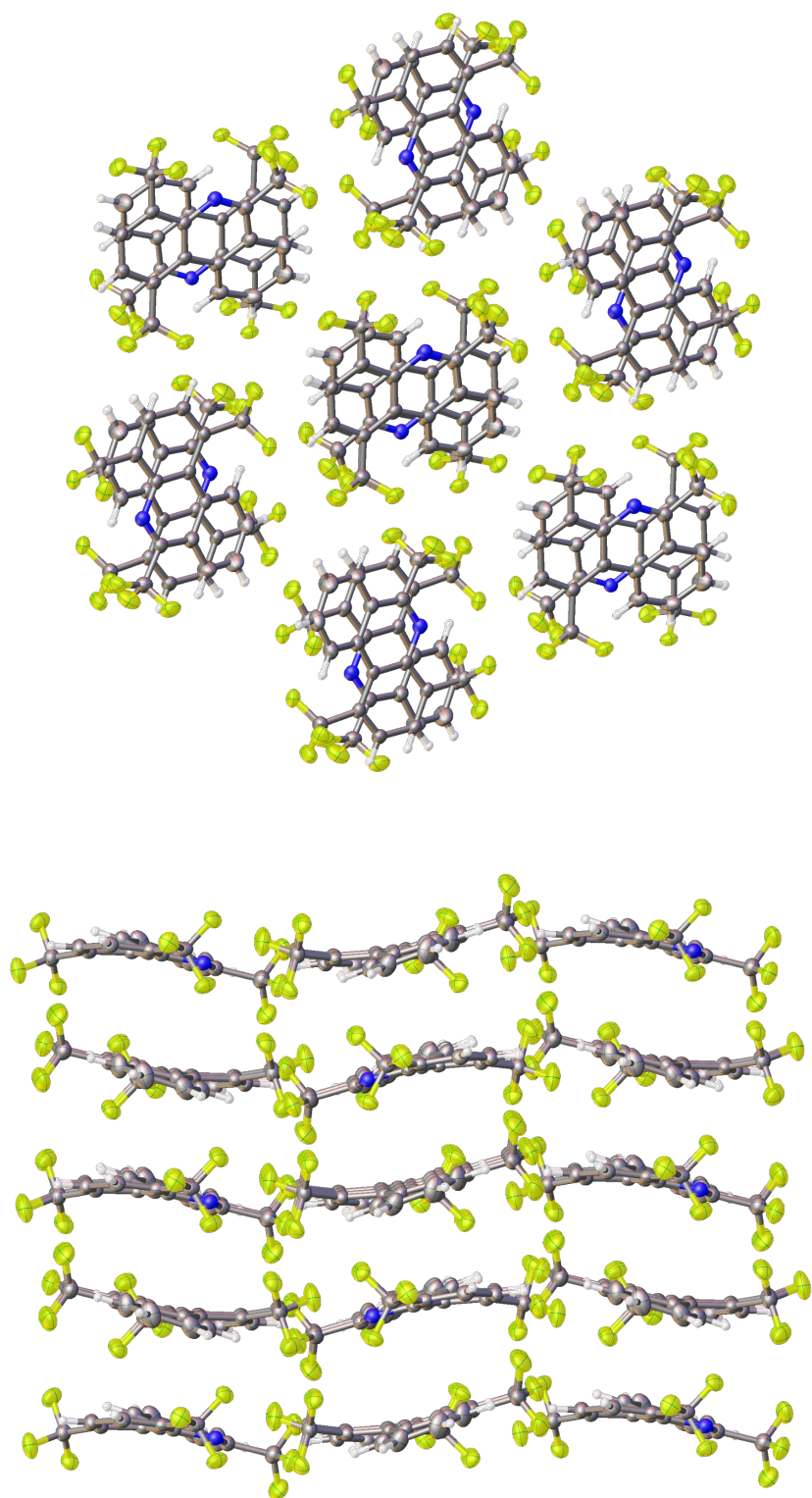
Figure 4.8. Top view of PHRD-3-1 packing (top). Side view of PHRD-3-1 packing (bottom).
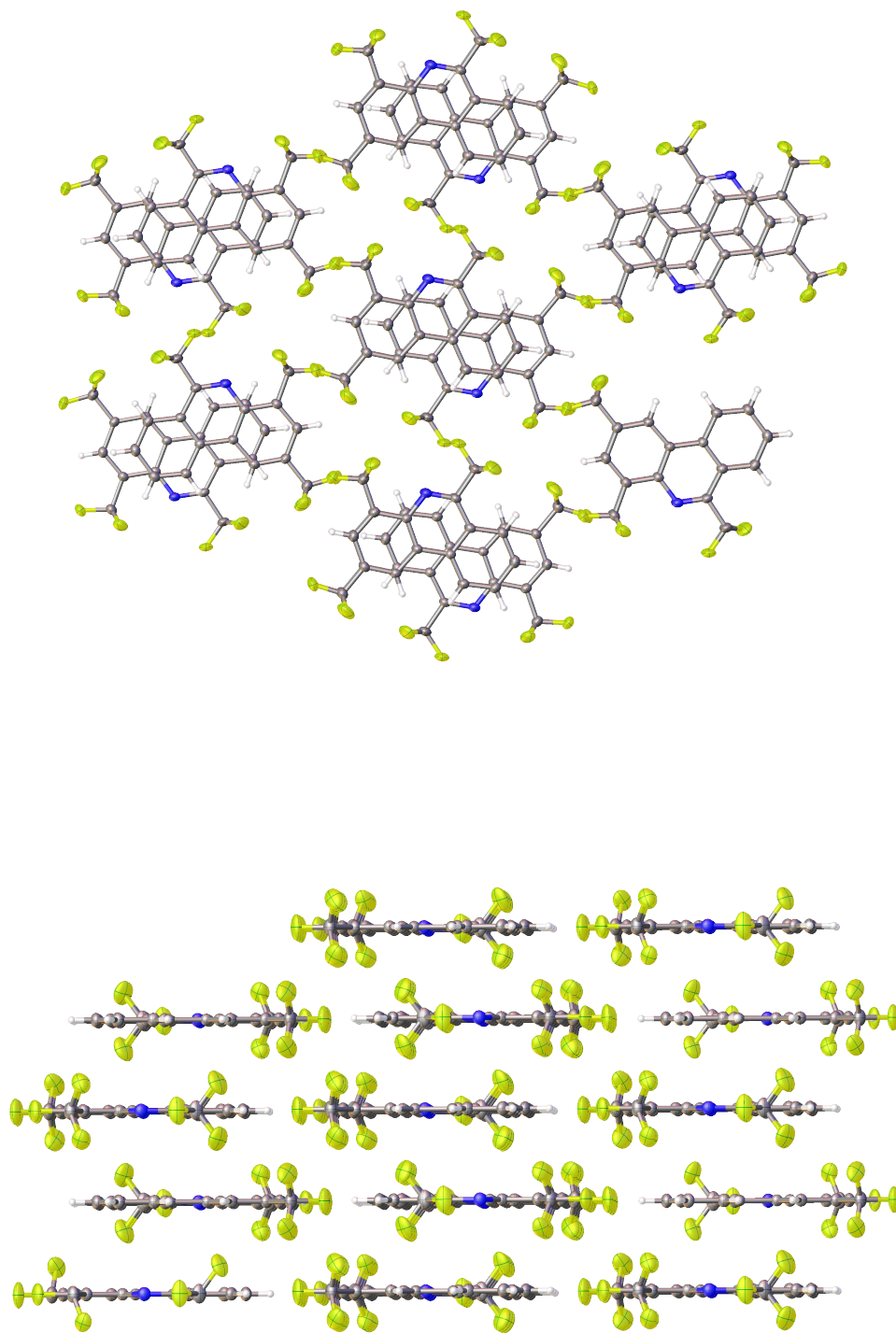
Figure 4.9. Top view of PHRD-3-2 packing (top) Side view of PHRD-3-2 packing (bottom)
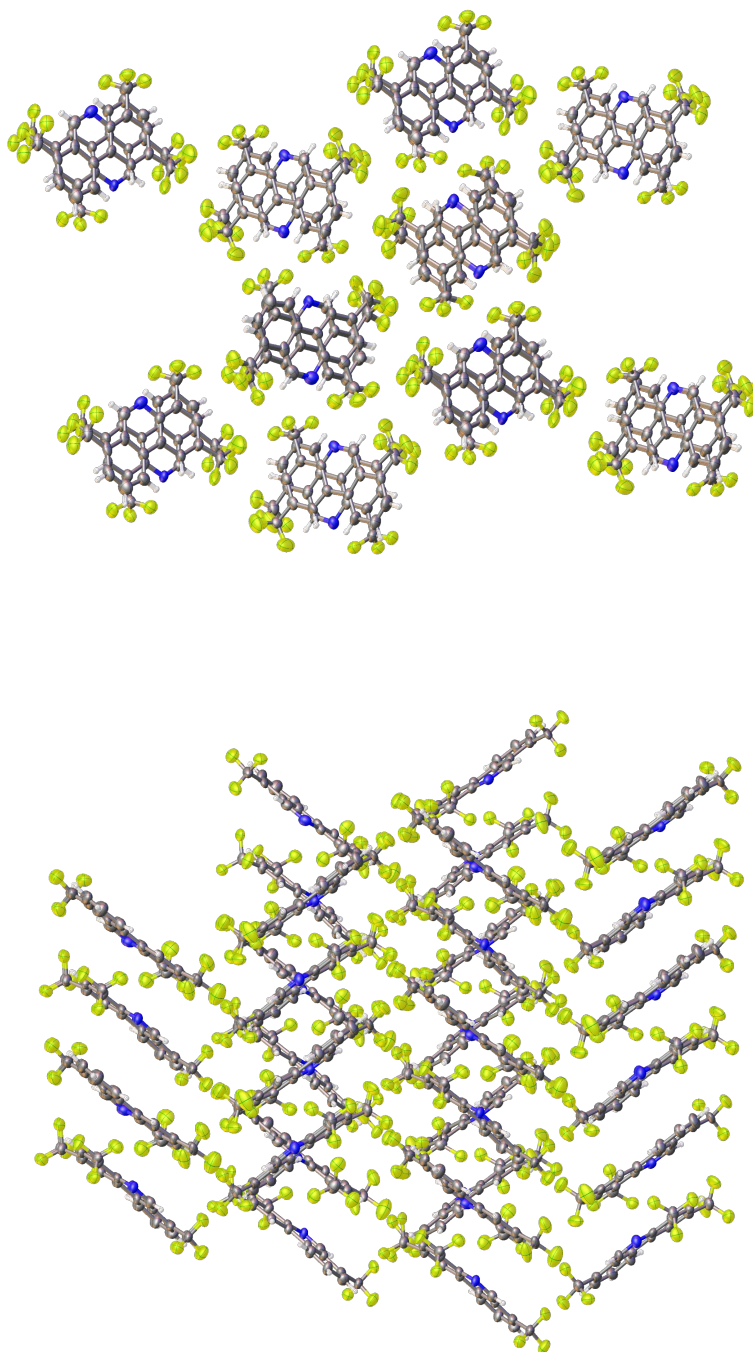
Figure 4.10. Top view of PHRD-3-3 packing (top). Side view of PHRD-3-3 packing (bottom).
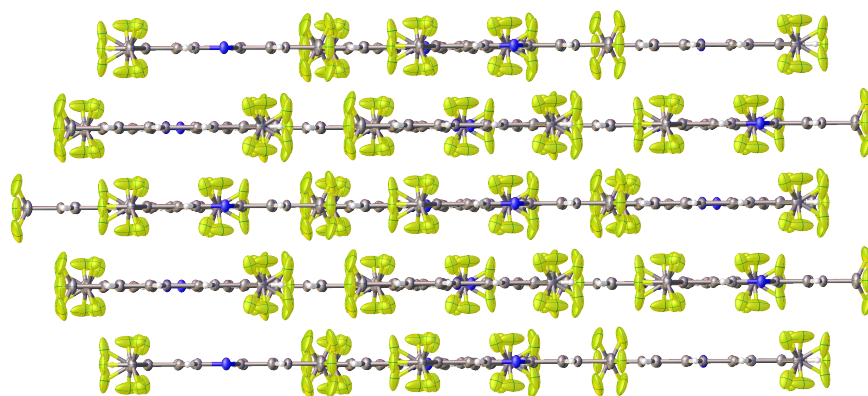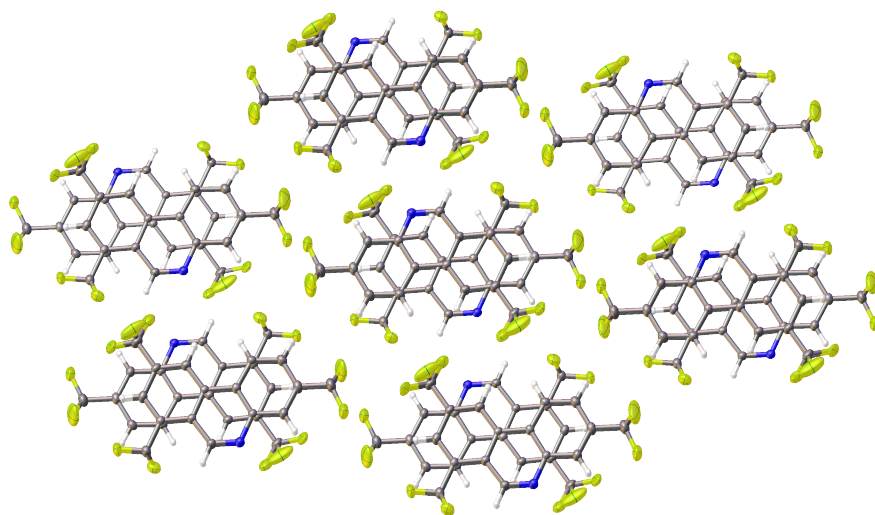
Figure 4.11. Top view of PHRD-3-4 packing (top). Side view of PHRD-3-4 packing (bottom).
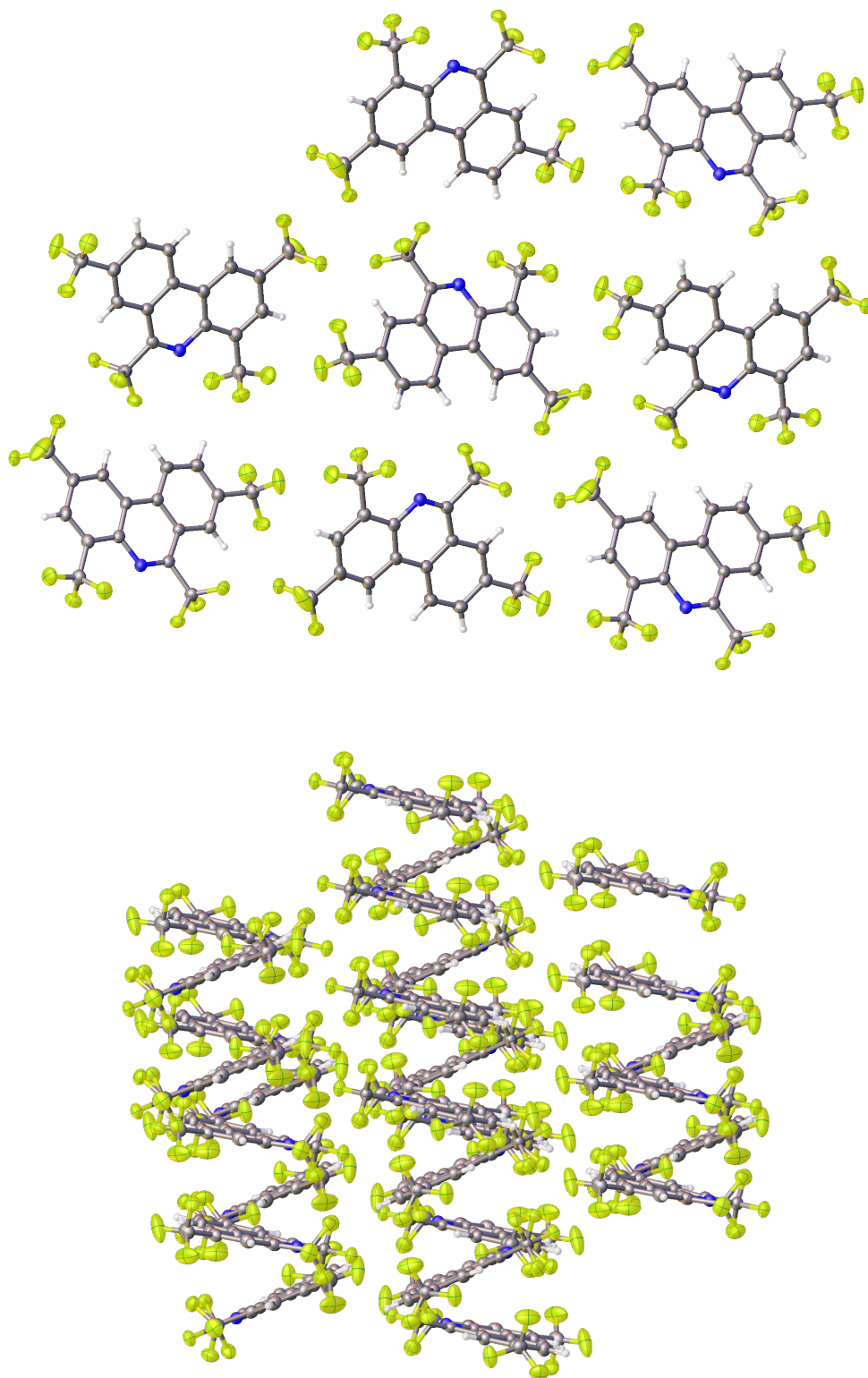
Figure 4.12. Top view of PHRD-4-1 packing (top). Side view of PHRD-4-1 packing (bottom).
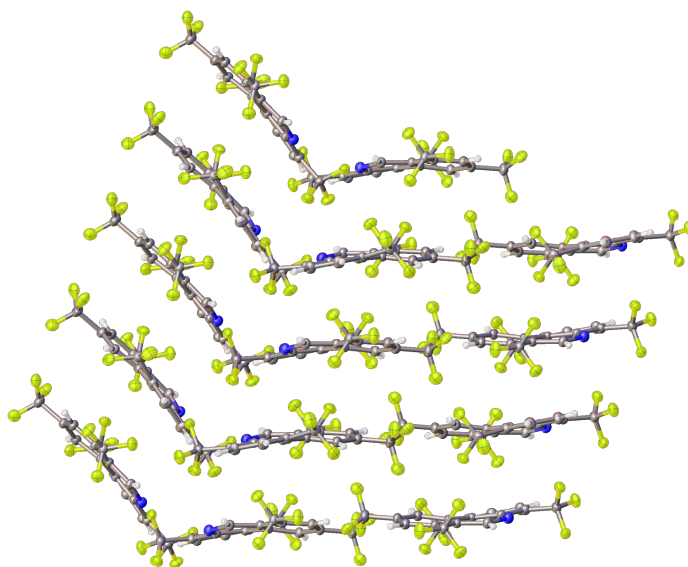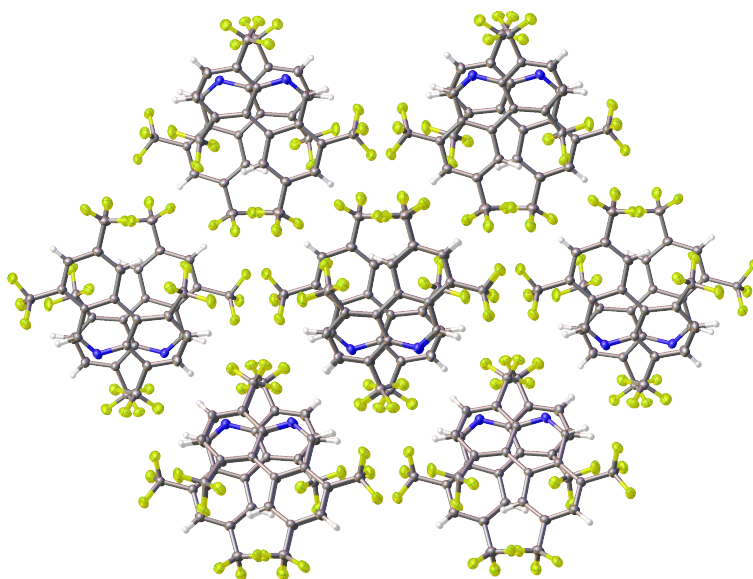
Figure 4.13. Top view of PHRD-4-2 packing (top). Side view of PHRD-4-2 packing (bottom).
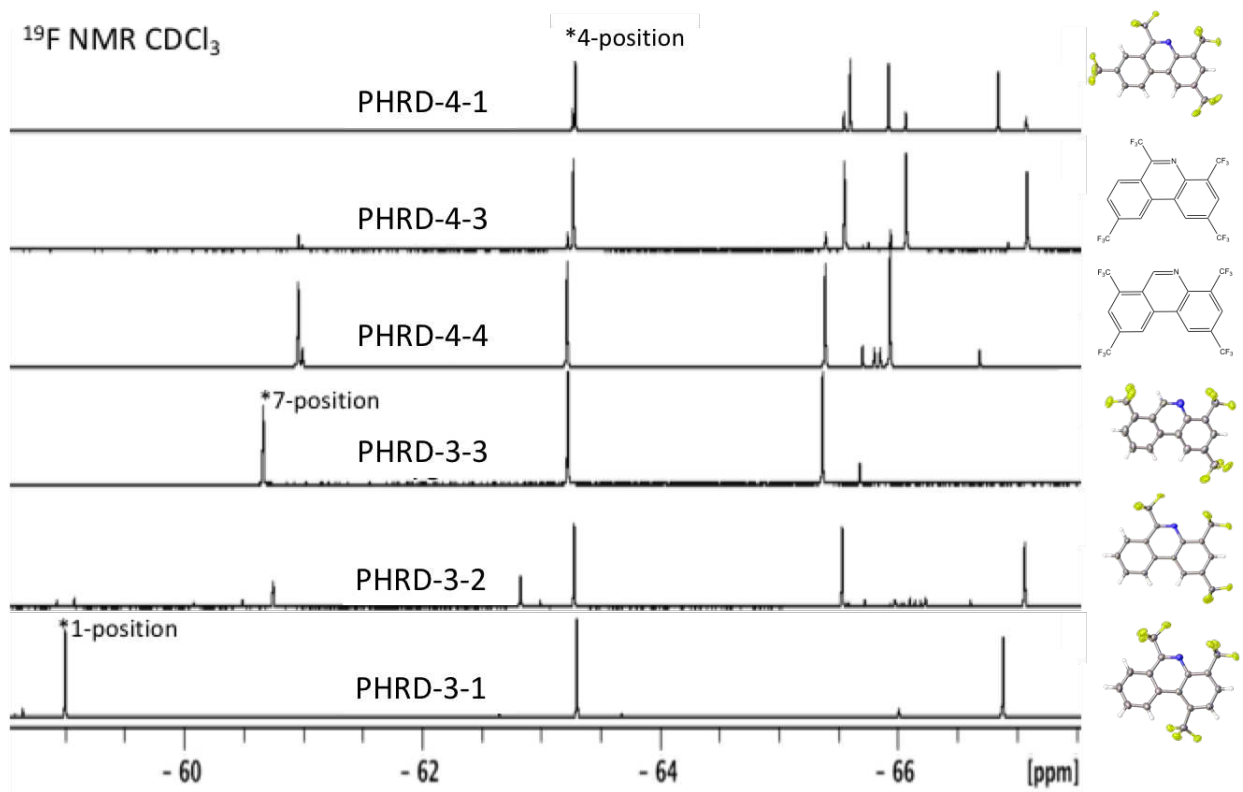
Figure 4.14. ^{19}F NMR spectra of PHRD-3-1, PHRD-3-2, PHRD-3-3, PHRD-4-1, PHRD-4-3, and PHRD-4-4 with their structures or preliminary structures.
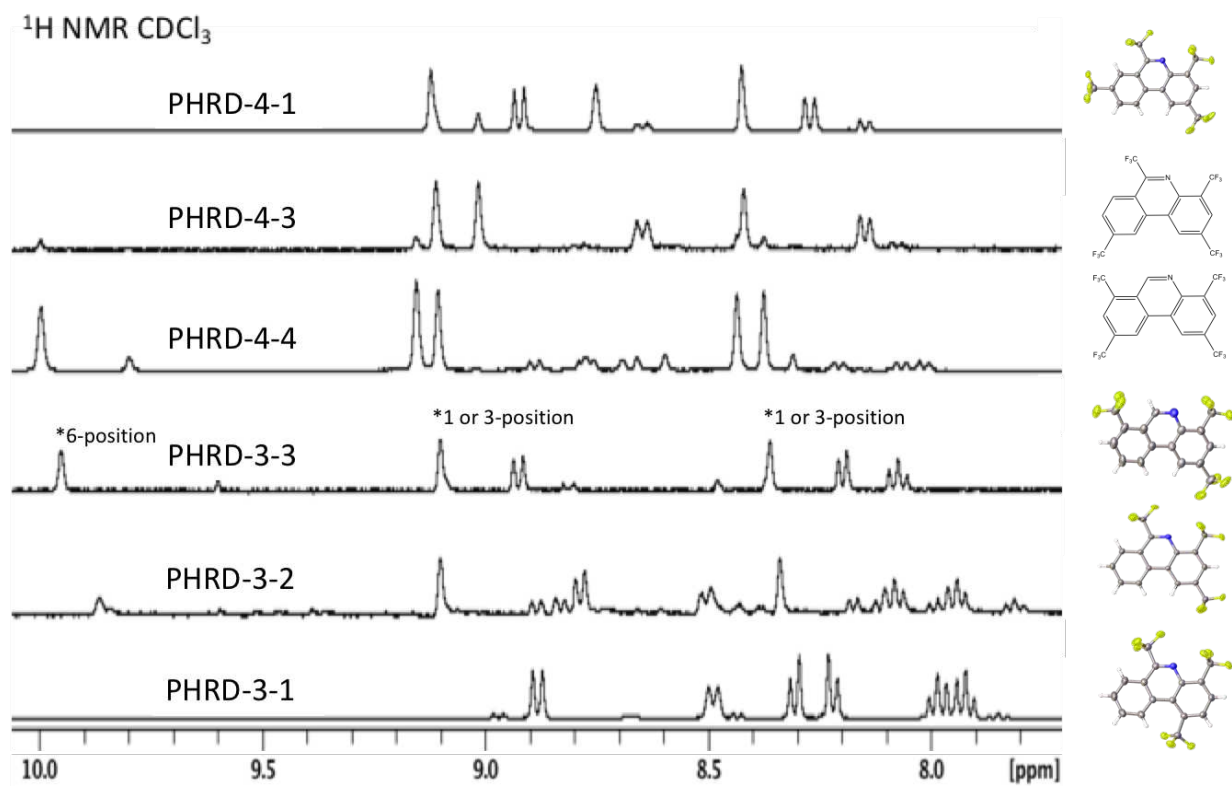
Figure 4.15. ^{1}H NMR spectra of PHRD-3-1, PHRD-3-2, PHRD-3-3, PHRD-4-1, PHRD-4-3, and PHRD-4-4 with their structures or preliminary structures.
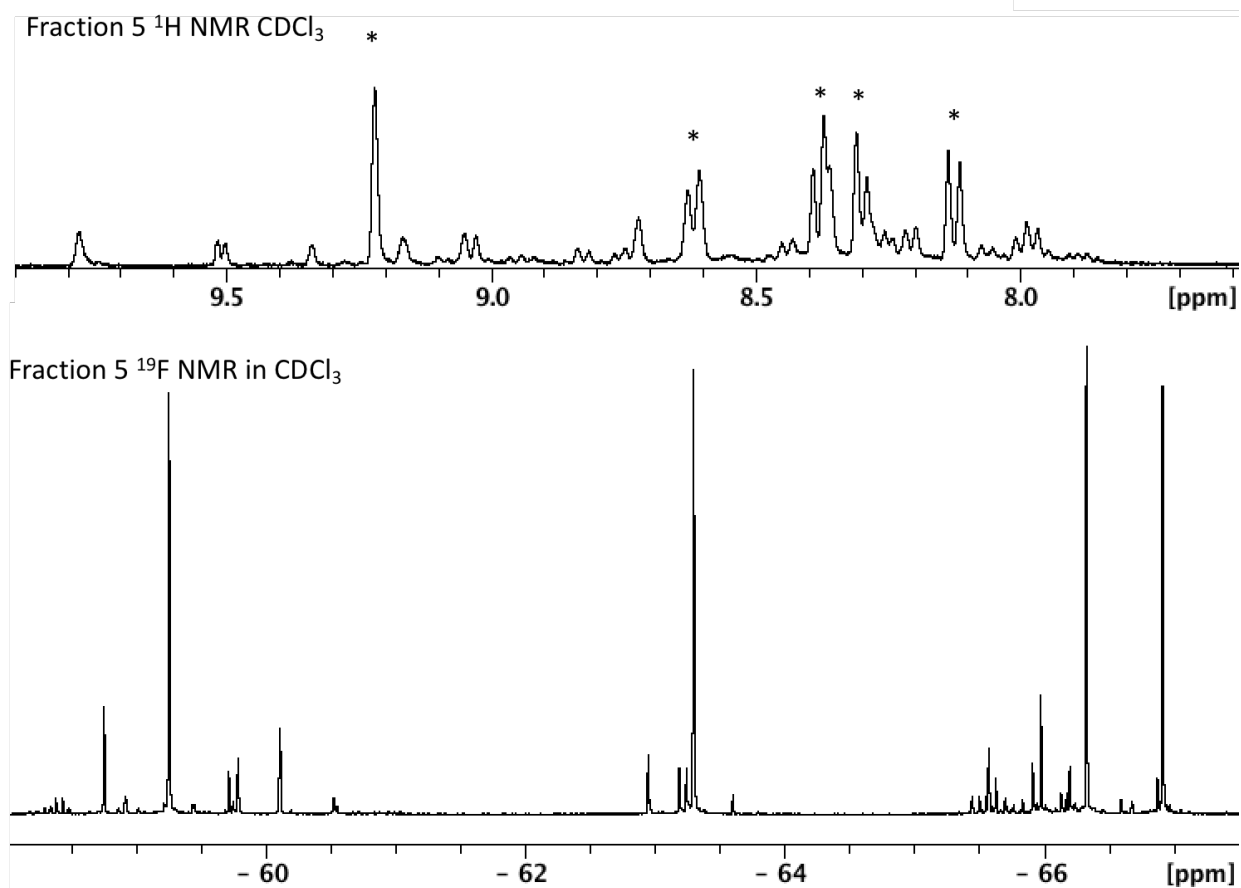
Figure 4.16. ¹H and ¹⁹F NMR spectra for Fraction 5.
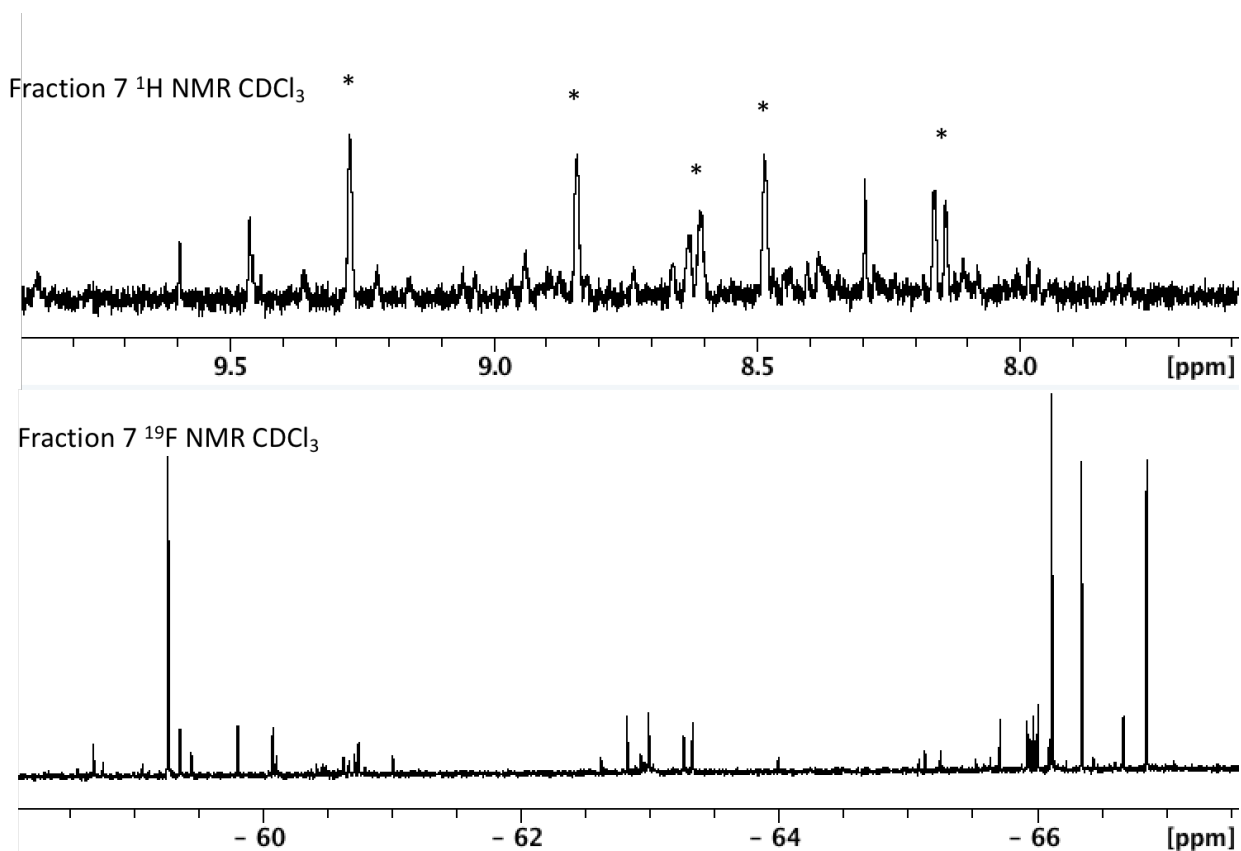
Figure 4.17. ^{1}H and ^{19}F NMR spectra for Fraction 7. NMR signals from the major compound in F7 are indicated by asterisks (*) in the ^{1}H NMR spectrum.
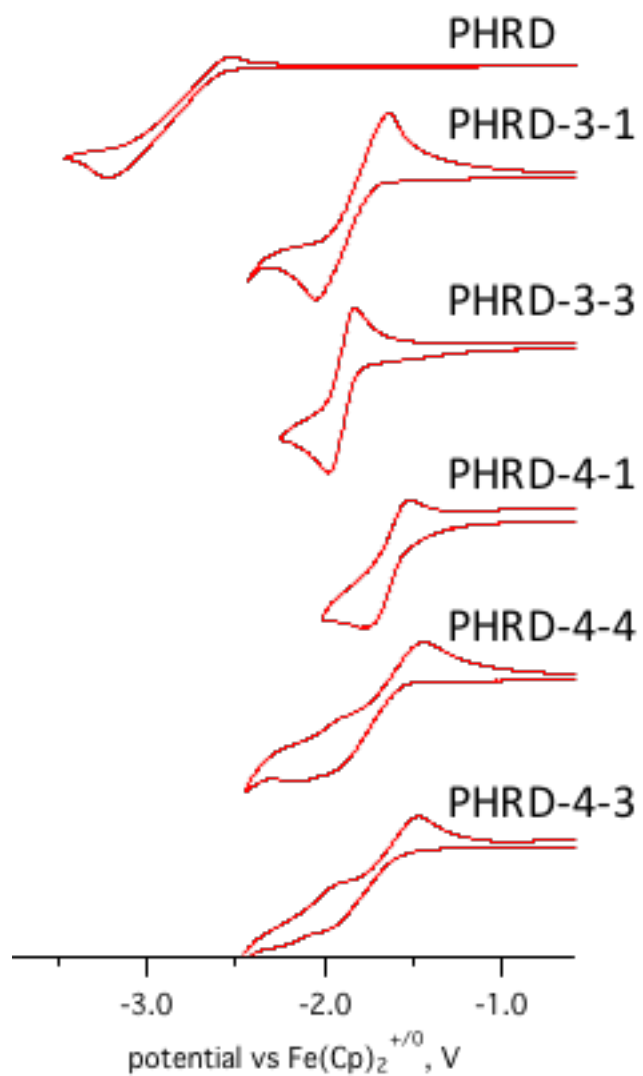
Figure 4.18. Cyclic voltammetry of PHRD, PHRD-3-1, PHRD-3-3, PHRD-4-1, PHRD-4-4, and PHRD-4-3 versus Fe(Cp)$_2$, 0.1 M N(nBu)$_4$ClO$_4$ in dimethoxyethane, 100 mVs^{-1}.
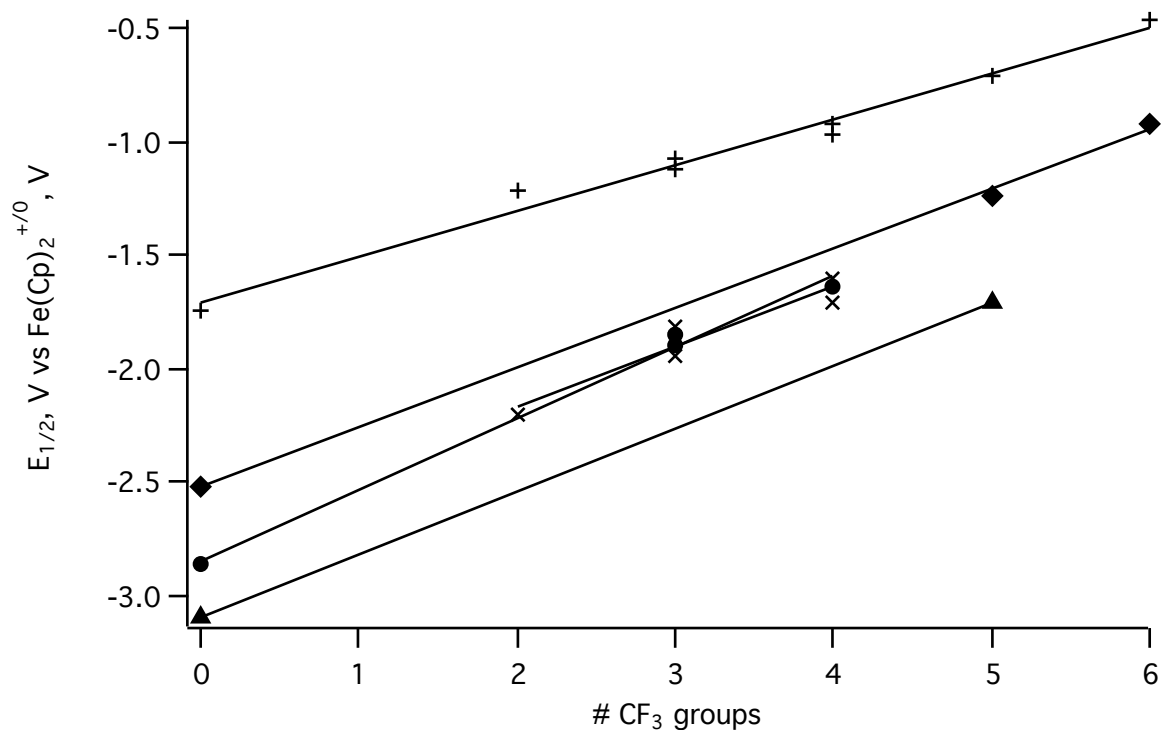
Figure 4.19. $E_{1/2}$ as a function of the number of CF_3 groups for PHNZ(+),[23] ANTH($\blacklozenge$),[26] PHRD($\bullet$),[This work] phenanthrene ($\blacktriangle$),[26] and phen (x).[This work] Measured via cyclic voltammetry versus Fe(Cp)$_2$, 0.1 M N(nBu)$_4$ClO$_4$ in dimethoxyethane. Slope for PHNZ slope = 0.20 V per CF_3, ANTH slope=0.26 V per CF_3, PHRD slope=0.32 V per CF_3, phenanthrene slope = 0.28 V per CF_3, phen slope = 0.27 V per CF_3.

i) [2+2+2] cycloaddition reaction
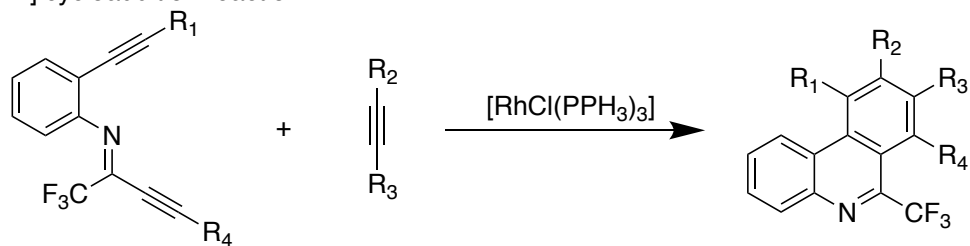
ii) trifluoroacetimidoyl chloride cyclization
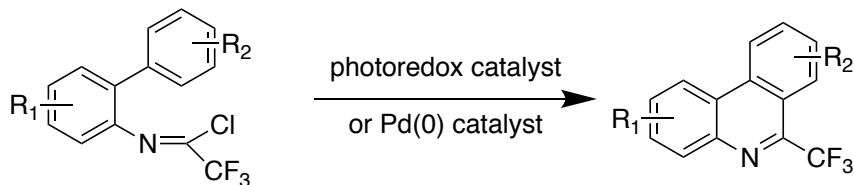
iii) isocyano cyclization
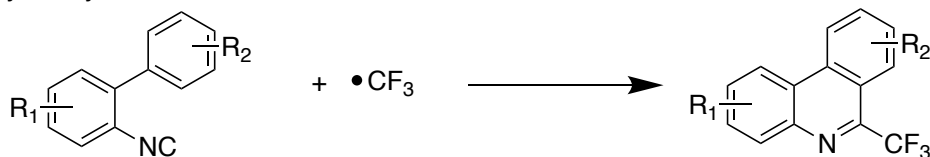
iv) Suzuki coupling
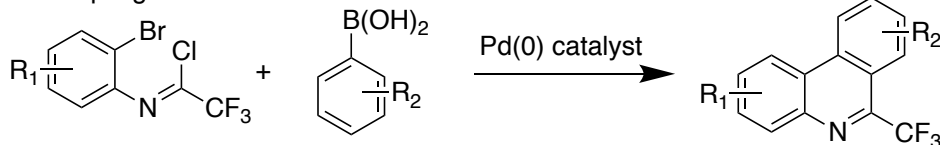
Scheme 4.1. Literature methods for the synthesis of trifluoromethylated PHRD derivatives: i) [2+2+2] cycloaddition;[17] ii) trifluoroacetimidoyl chloride cyclization;[18-19] iii) isocyano cyclization;[12,15,20-21] iv) Suzuki coupling.[16]
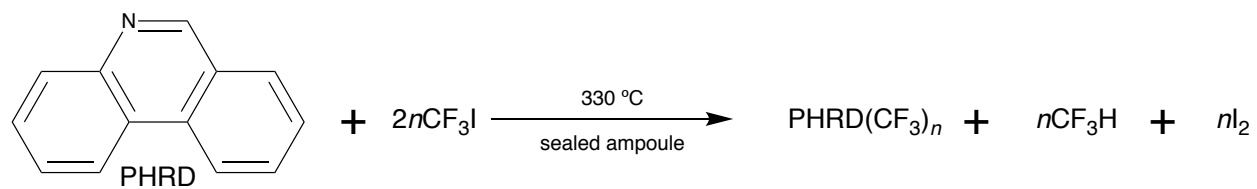
Scheme 4.2. Trifluoromethylation of PHRD.

CHAPTER 4 REFERENCES

1.   Tumir, L.-M.; Radić Stojković, M.; Piantanida, I. Come-back of phenanthridine and phenanthridinium derivatives in the 21st century. *Beilstein J. Org. Chem.* **2014**, *10*, 2930-2954.

2.   Phillips, S. D.; Castle, R. N. A review of the chemistry of the antitumor benzo[c]phenanthridine alkaloids nitidine and fagaronine and of the related antitumor alkaloid coralyne. *J. Heterocycl. Chem.* **1981**, *18*, 223-232.

3.   Ishikawa, T. Benzo[c]phenanthridine bases and their antituberculosis activity. *Med. Res. Rev.* **2001**, *21*, 61-72.

4.   Stevens, N.; O'Connor, N.; Vishwasrao, H.; Samaroo, D.; Kandel, E. R.; Akins, D. L.; Drain, C. M.; Turro, N. J. Two Color RNA Intercalating Probe for Cell Imaging Applications. *J. Am. Chem. Soc.* **2008**, *130*, 7182-7183.

5.   Azad, I.; Ahmad, R.; Khan, T.; Saquib, M.; Hassan, F.; Akhter, Y.; Khan, A. R.; Nasibullah, M. Phenanthridine derivatives as promising new anticancer agents: synthesis, biological evaluation and binding studies. *Future Medicinal Chemistry* **2020**, *12*, 709-739.

6.   Wan, M.; Zhang, L.; Chen, Y.; Li, Q.; Fan, W.; Xue, Q.; Yan, F.; Song, W. Synthesis and Anticancer Activity Evaluation of Novel Phenanthridine Derivatives. *Front Oncol* **2019**, *9*, 274-274.

7.   Ohsawa, T.; Sasabe, H.; Watanabe, T.; Nakao, K.; Komatsu, R.; Hayashi, Y.; Hayasaka, Y.; Kido, J. A Series of Imidazo[1,2-f]phenanthridine-Based Sky-Blue TADF Emitters Realizing EQE of over 20%. *Advanced Optical Materials* **2019**, *7*, 1801282.

8.   Zhao, D.; Tang, X.; Liu, X.-Y.; Fan, J.; Liao, L.-S. Highly luminescent platinum(II) complexes based on pyrazolo[1,5-f]phenanthridine-containing ligands. *Org. Electron.* **2017**, *50*, 473-479.

9.   Jiang, B.; Gu, Y.; Qin, J.; Ning, X.; Gong, S.; Xie, G.; Yang, C. Deep-red iridium(iii) complexes cyclometalated by phenanthridine derivatives for highly efficient solution-processed organic light-emitting diodes. *J. Mater. Chem. C.* **2016**, *4*, 3492-3498.

10.   Baik, C.; Kim, D.; Kang, M.-S.; Song, K.; Kang, S. O.; Ko, J. Synthesis and photovoltaic properties of novel organic sensitizers containing indolo[1,2-f]phenanthridine for solar cell. *Tetrahedron* **2009**, *65*, 5302-5307.

11.   Purser, S.; Moore, P. R.; Swallow, S.; Gouverneur, V. Fluorine in medicinal chemistry. *Chem. Soc. Rev.* **2008**, *37*, 320-330.

12.   Zhang, B.; Mück-Lichtenfeld, C.; Daniliuc, C. G.; Studer, A. 6-Trifluoromethyl-Phenanthridines through Radical Trifluoromethylation of Isonitriles. *Angew. Chem. Int. Ed.* **2013**, *52*, 10792-10795.

13.   Shah, P.; Westwell, A. D. The role of fluorine in medicinal chemistry. *Journal of Enzyme Inhibition and Medicinal Chemistry* **2007**, *22*, 527-540.

14.   Tang, X.; Song, S.; Liu, C.; Zhu, R.; Zhang, B. Light triggered addition/annulation of 2-isocyanobiphenyls toward 6-trifluoromethyl-phenanthridines under photocatalyst-free conditions. *RSC Adv.* **2015**, *5*, 76363-76367.

15.   Lübbesmeyer, M.; Leifert, D.; Schäfer, H.; Studer, A. Electrochemical initiation of electron-catalyzed phenanthridine synthesis by trifluoromethylation of isonitriles. *Chem. Commun.* **2018**, *54*, 2240-2243.

16.   Wang, W.-Y.; Feng, X.; Hu, B.-L.; Deng, C.-L.; Zhang, X.-G. Synthesis of 6-(Trifluoromethyl)phenanthridines via Palladium-Catalyzed Tandem Suzuki/C–H Arylation Reactions. *J. Org. Chem.* **2013**, *78*, 6025-6030.

17.   Li, Y.; Zhu, J.; Zhang, L.; Wu, Y.; Gong, Y. Synthesis of Fluorine-Containing Multisubstituted Phenanthridines by Rhodium-Catalyzed Alkyne [2+2+2] Cycloaddition and Tandem sp2 C-H Difluoromethylenation. *Chem. Eur. J.* **2013**, *19*, 8294-8299.

18.   Fu, W.; Zhu, M.; Xu, F.; Fu, Y.; Xu, C.; Zou, D. An approach to 6-trifluoromethyl-phenanthridines through visible-light-mediated intramolecular radical cyclization of trifluoroacetimidoyl chlorides. *RSC Adv.* **2014**, *4*, 17226-17229.

19.   Zhu, M.; Fu, W.; Zou, G.; Xu, C.; Wang, Z. Palladium-catalyzed intramolecular C−H bond functionalization of trifluoroacetimidoyl chloride derivatives: Synthesis of 6-trifluoromethyl-phenanthridines. *J. Fluorine Chem.* **2014**, *163*, 23-27.

20.   Cheng, Y.; Jiang, H.; Zhang, Y.; Yu, S. Isocyanide Insertion: De Novo Synthesis of Trifluoromethylated Phenanthridine Derivatives. *Org. Lett.* **2013**, *15*, 5520-5523.

21.   Wang, Q.; Dong, X.; Xiao, T.; Zhou, L. PhI(OAc)2-Mediated Synthesis of 6-(Trifluoromethyl)phenanthridines by Oxidative Cyclization of 2-Isocyanobiphenyls with CF3SiMe3 under Metal-Free Conditions. *Org. Lett.* **2013**, *15*, 4846-4849.

22.   Kuvychko, I. V.; Castro, K. P.; Deng, S. H. M.; Wang, X.-B.; Strauss, S. H.; Boltalina, O. V. Taming Hot CF3 Radicals: Incrementally Tuned Families of Polyarene Electron Acceptors for Air-Stable Molecular Optoelectronics. *Angew. Chem. Int. Ed.* **2013**, *52*, 4871-4874.

23.   Castro, K. P.; Clikeman, T. T.; DeWeerd, N. J.; Bukovsky, E. V.; Rippy, K. C.; Kuvychko, I. V.; Hou, G.-L.; Chen, Y.-S.; Wang, X.-B.; Strauss, S. H.; Boltalina, O. V. Incremental Tuning Up of Fluorous Phenazine Acceptors. *Chem. Eur. J.* **2016**, *22*, 3930-3936.

24.   Clikeman, T. T.; Bukovsky, E. V.; Wang, X.-B.; Chen, Y.-S.; Rumbles, G.; Strauss, S. H.; Boltalina, O. V. Core Perylene Diimide Designs via Direct Bay- and ortho-

(Poly)trifluoromethylation: Synthesis, Isolation, X-ray Structures, Optical and Electronic Properties. *Eur. J. Org. Chem.* **2015**, *2015*, 6641-6654.

25.	Orola, L.; Veidis, M. V.; Mutikainen, I.; Sarcevica, I. Neutral and Ionic Supramolecular Complexes of Phenanthridine and Some Common Dicarboxylic Acids: Hydrogen Bond and Melting Point Considerations. *Cryst. Growth Des.* **2011**, *11*, 4009-4016.

26.	Kuvychko, I. V.; Whitaker, J. B.; Larson, B. W.; Folsom, T. C.; Shustova, N. B.; Avdoshenko, S. M.; Chen, Y.-S.; Wen, H.; Wang, X.-B.; Dunsch, L.; Popov, A. A.; Boltalina, O. V.; Strauss, S. H. Substituent effects in a series of 1,7-C60(RF)2 compounds (RF = CF3, C2F5, n-C3F7, i-C3F7, n-C4F9, s-C4F9, n-C8F17): electron affinities, reduction potentials and E(LUMO) values are not always correlated. *Chem. Sci.* **2012**, *3*, 1399-1407.

Table A1.1. Temperature required to achieve a deposition rate of 0.2 Å/s for fullerene acceptors.

fullerene	temperature ºC
C_{60}	450
$C_{60}CF_2$	635
$C_{60}FHF$	385
60-2-1	360
60-4-1	280
60-8-1	200
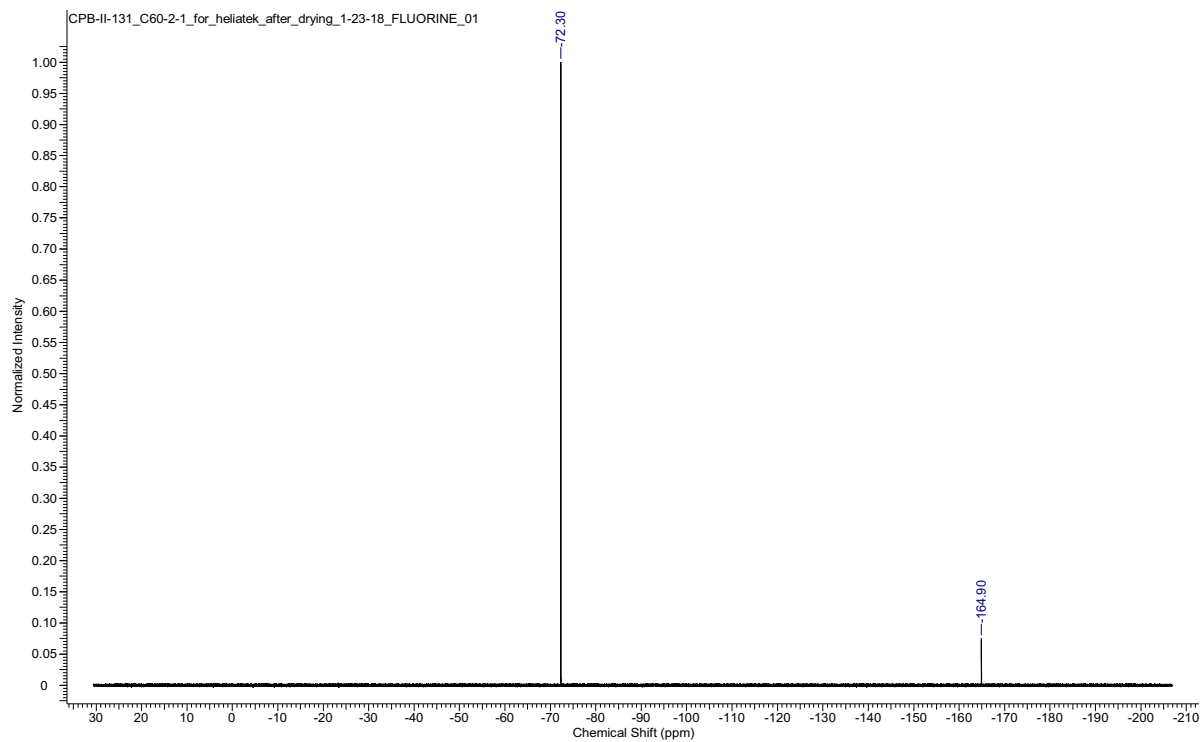
Figure A1.1. ^{19}F NMR spectrum of 60-2-1.

$C_{60}(CF_3)_2$
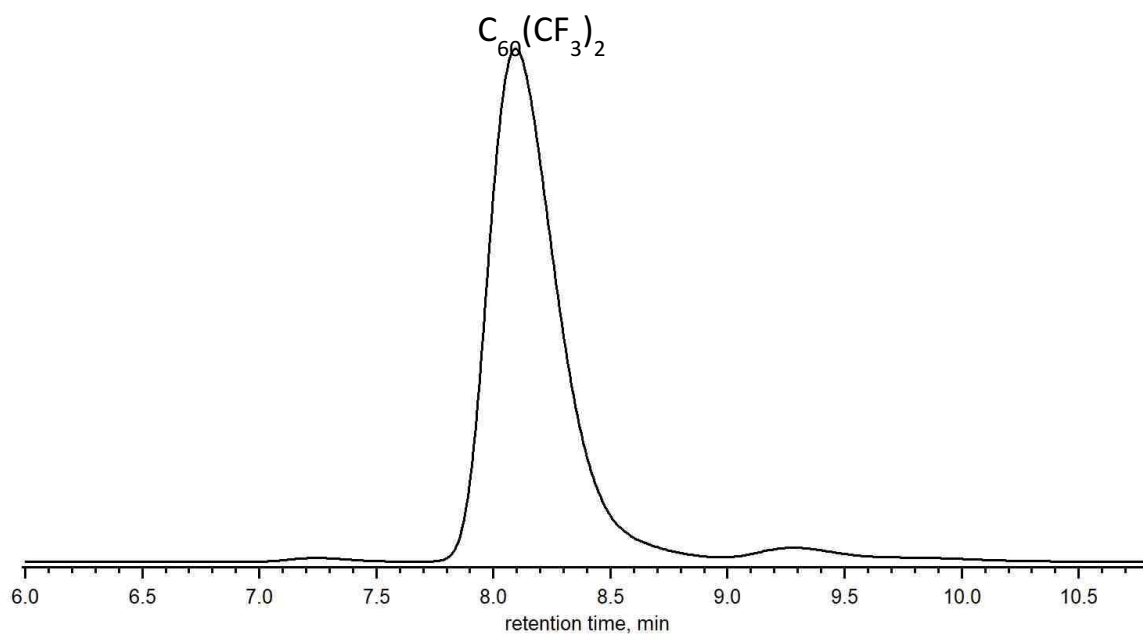
Figure A1.2. HPLC chromatogram of 60-2-1 after purification. Eluent is toluene at 5 mL/min on a Buckyprep stationary phase measured at 300 nm.
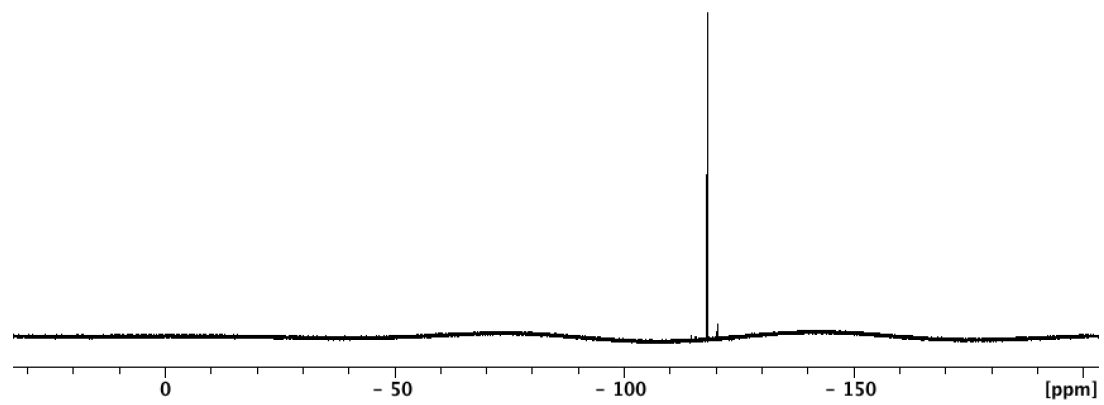
Figure A1.3. ^{19}F NMR spectrum of $C_{60}CF_2$.
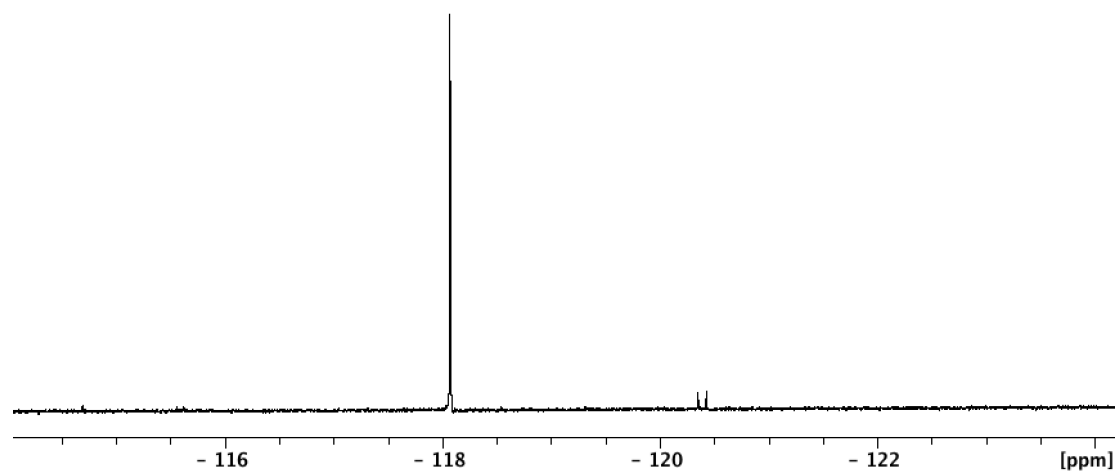
Figure A1.4. Zoomed in ^{19}F NMR spectrum of $C_{60}CF_2$. [6,6]-isomer (−118 ppm) and [5,6]-isomer (−120.4 ppm)
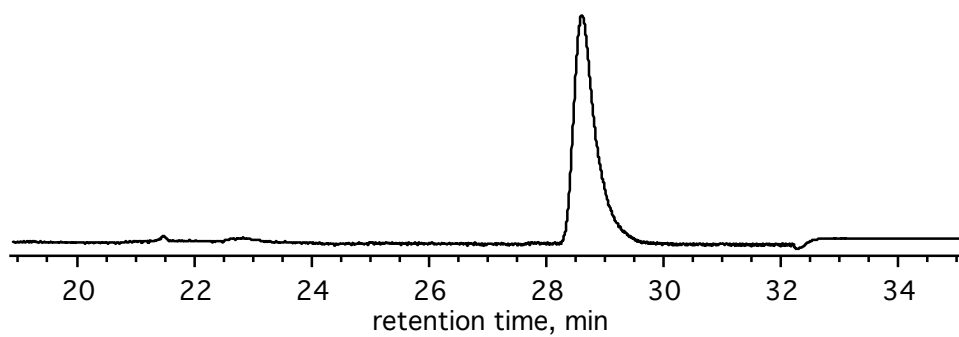
Figure A1.5. HPLC chromatogram of purified $C_{60}CF_2$. Eluent is toluene at 14 mL/min on a Buckyprep stationary phase measured at 300 nm.
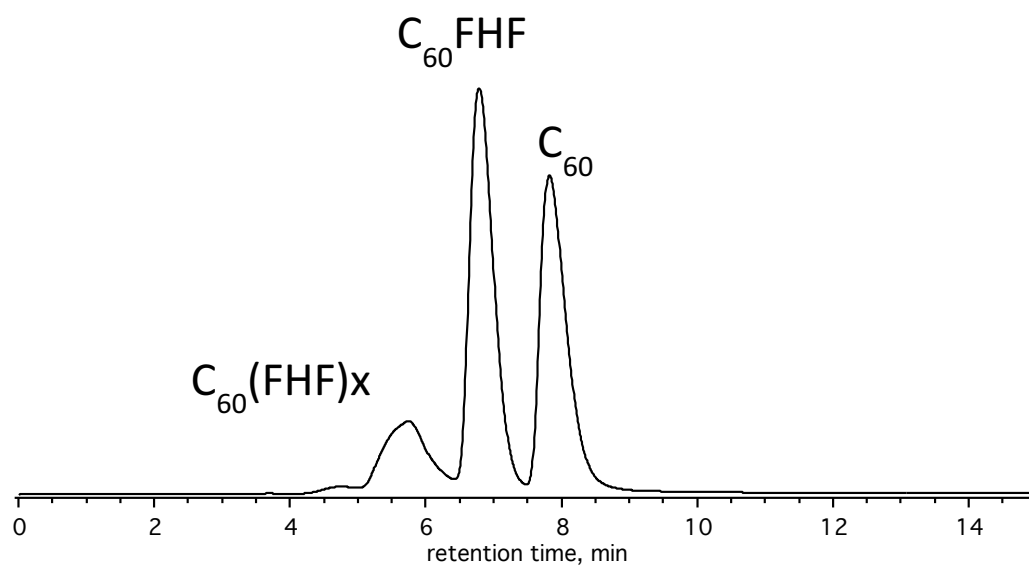
Figure A1.6. HPLC chromatogram of reaction mixture after being washed with heptanes. Eluent is toluene at 14 mL/min on a Buckyprep stationary phase measured at 300 nm.
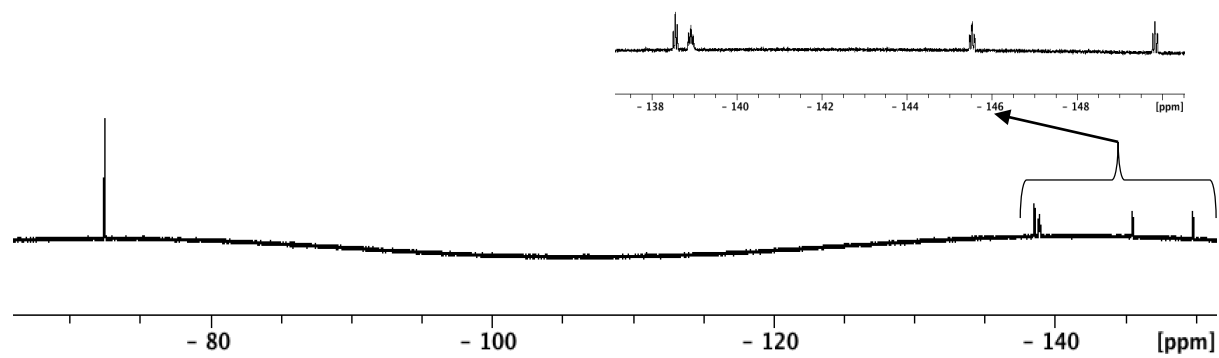
Figure A1.7. ^{19}F NMR spectrum of $C_{60}FHF$.
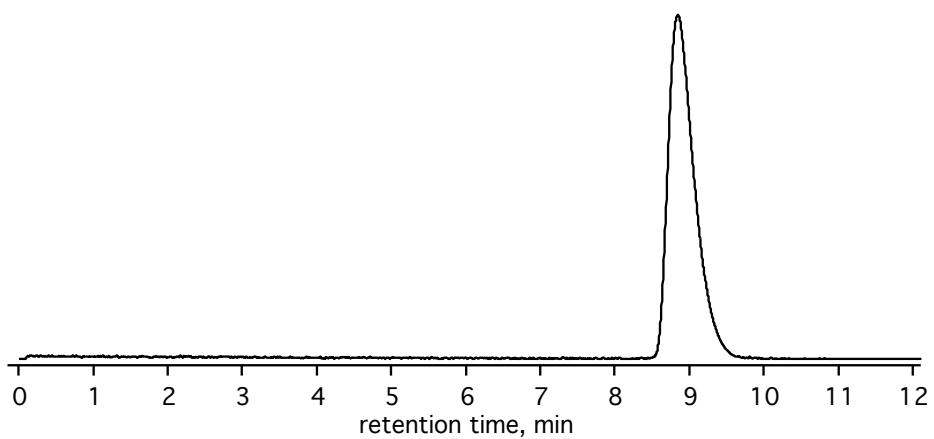
Figure A1.8. HPLC chromatogram of pure $C_{60}FHF$. Eluent is toluene at 14 mL/min on a Buckyprep stationary phase measured at 300 nm.
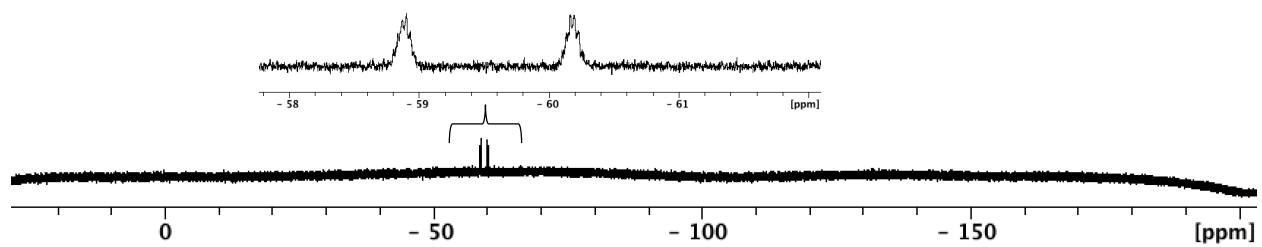
Figure A1.9. ^{19}F NMR spectrum of 60-12-1.

Table A1.2. DFT calculated HOMO/LUMO values for the donor.

Donor	HOMO (eV)	LUMO (eV)
DCV4T-Me[14]	-5.309	-4.092
DCV5T-F$_2$(3,3)-Me$_4$(2,2,4,4)	-5.139	-3.986

Table A1.3. DFT gas phase LUMO, theoretical Voc and ΔLUMO for acceptors with DCV4T-Me[14]

acceptor	DFT LUMO (eV)	Theor. V$_{OC}$ for DCV4T-Me[14]	ΔLUMO (eV)
C$_{60}$	-4.379[b]	0.93	0.287
60-2-1	-4.592[b]	0.717	0.5
60-4-1	-4.682[b]	0.627	0.59
60-8-1	-4.850[b]	0.513	0.704
60-12-1	-4.278[b]	1.03	-0.186
C$_{60}$CF$_2$	-4.5[a]	0.809	0.408
C$_{60}$FHF	-4.434[b]	(0.875)	0.342
PC$_{60}$BM	-4.215[b]		

[a] DFT LUMO (gas phase) calculated by Brotsman et al.[1]
[b] DFT LUMO (gas phase) calculated by Popov et al.[2,3]

Devices:

Table A1.4. Summary of photovoltaic figures of merit for reference devices.

Cell	fullerene	J_{SC} (mA/cm^2)	FF (%)	V_{OC} (V)	J_{SC} from EQE (mA/cm^2)	Irradiation mW/cm^2
R1	C_{60}	1.7	70.8	0.93	1.3	103
R2	$C_{60}FHF$	1	64.9	0.91	0.7	107
R3	60-2-1	1	61.4	0.72	0.8	107
R4	60-4-1	0.7	65.4	0.61	0.5	98
R5	$C_{60}CF_2$	0.7	47.9	0.6	0.5	104
R6	60-8-1	0	41.9	0.48	0	101
R7	60-12-1	0.1	36.3	0.36	0	100
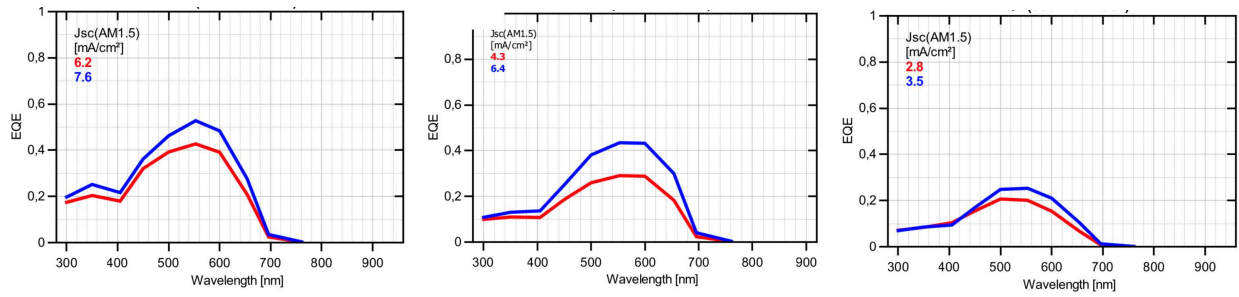
Figure A1.10. EQE spectra for BHJs with C_{60}, 60-2-1 and 60-4-1 (left to right). 10 nm BHJ layer (red line); 20 nm BHJ layer (blue line).

When comparing the EQE spectra for the BHJs with C_{60} and the TMFs, it is clear that devices with C_{60} as the acceptor exhibit a higher EQE. For 60-2-1, it is shown that an increase in thickness leads to a large increase in EQE and therefore J_{SC}.

C$_{60}$

60-2-1
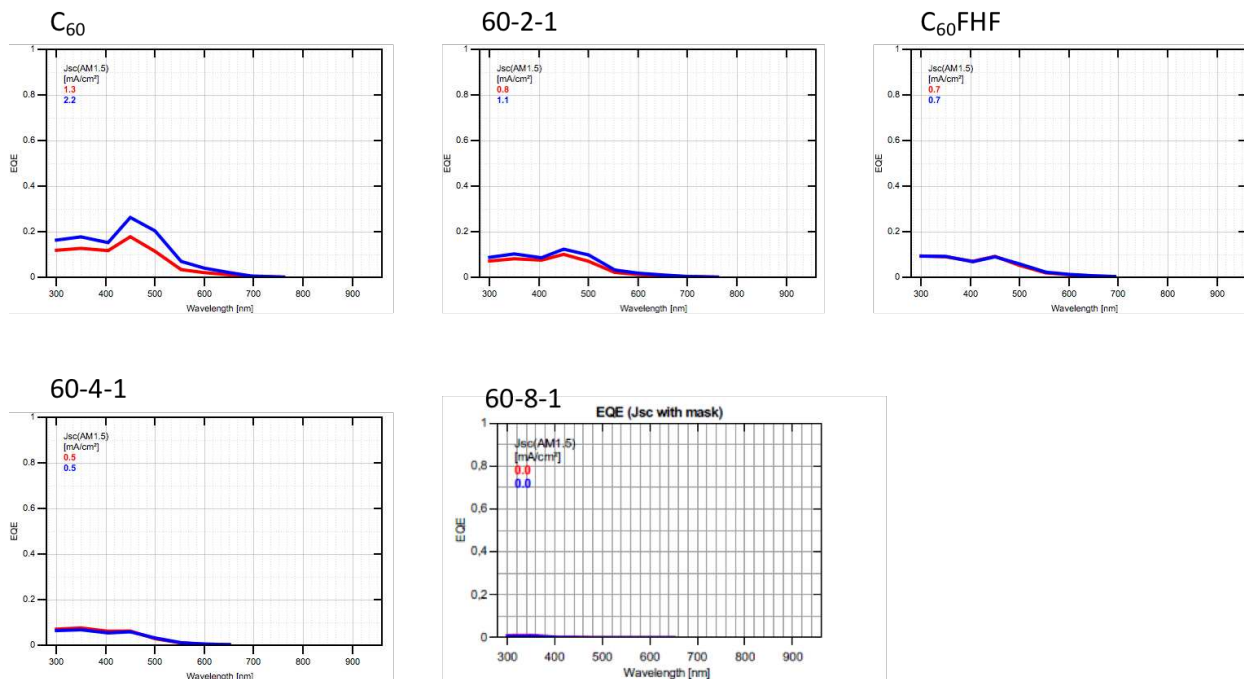
C$_{60}$FHF

60-4-1

60-8-1

Figure A1.11. EQE spectra for reference devices with C$_{60}$, 60-2-1 and 60-4-1, C$_{60}$FHF, 60-4-1, and 60-8-1. No C$_{60}$ layer on ITO (red line); 15 nm C$_{60}$ layer on ITO (blue line). It can be seen that the EQE spectra trakc with the fullerene absorption spectra (i.e. cutoff is before 600 nm in each case). EQE spectrum for 60-12-1 reference device was not collected.

Table A1.5. Summary of photovoltaic figures of merit for BHJ (1:1 donor:acceptor) devices.

Cell	fullerene on ITO	BHJ accceptor	BHJ Donor	Temp Deposited	J_{SC} (mA/cm^2)	FF (%)	V_{OC} (V)	PCE (%)	Irradiation mW/cm^2	FF % from 10-20	J_{SC} from EQE (mA/cm^2)
B9	C$_{60}$ (15 nm)	C$_{60}$ (5 nm)	DCV4T-Me[14] (5 nm)	50 °C	6.7	60.1	0.97	3.91	100		6.2
B10	C$_{60}$ (15 nm)	C$_{60}$ (10 nm)	DCV4T-Me[14] (10 nm)	50 °C	8.1	49.9	0.96	3.88	100	83	7.6
B3	C$_{60}$ (15 nm)	C$_{60}$CF$_2$ (5 nm)	DCV4T-Me[14] (5 nm)	50 °C	4.9	46.7	0.92	2.11	102		4.4
B4	C$_{60}$ (15 nm)	C$_{60}$CF$_2$ (10 nm)	DCV4T-Me[14] (10 nm)	50 °C	4.7	41.7	0.9	1.76	102	89	4.4
B5	C$_{60}$ (15 nm)	C$_{60}$CF$_2$ (5 nm)	DCV4T-Me[14] (5 nm)	70 °C	4.4	46	0.85	1.72	104		4.1
B6	C$_{60}$ (15 nm)	C$_{60}$CF$_2$ (10 nm)	DCV4T-Me[14] (10 nm)	70 °C	4.5	41.2	0.87	1.61	104	90	4.3
B7	C$_{60}$CF$_2$ (15 nm)	C$_{60}$CF$_2$ (5 nm)	DCV4T-Me[14] (5 nm)	50 °C	4.7	44.3	0.93	1.94	101		2.7
B8	C$_{60}$CF$_2$ (15 nm)	C$_{60}$CF$_2$ (10 nm)	DCV4T-Me[14] (10 nm)	50 °C	6.1	40.5	0.92	2.27	101	91	2.4
B1	C$_{60}$CF$_2$ (15 nm)	C$_{60}$CF$_2$ (5 nm)	DCV4T-Me[14] (5 nm)	RT	2.8	32.6	0.81	0.74	100		4.4

B2	$C_{60}CF_2$ (15 nm)	$C_{60}CF_2$ (10 nm)	DCV4T-Me[14] (10 nm)	RT	2.5	28.7	0.81	0.58	100	88	5.9
B11	60-2-1 (15 nm)	60-2-1 (5 nm)	DCV4T-Me[14] (5 nm)	50 °C	4.4	61	0.87	2.34	110		4.3
B12	60-2-1 (15 nm)	60-2-1 (10 nm)	DCV4T-Me[14] (10 nm)	50 °C	6.4	58.4	0.89	3.33	110	96	6.4
B13	60-4-1 (15 nm)	60-4-1 (5 nm)	DCV4T-Me[14] (5 nm)	50 °C	3	51.1	0.74	1.13	104		2.8
B14	60-4-1 (15 nm)	60-4-1 (10 nm)	DCV4T-Me[14] (10 nm)	50 °C	3.5	42.3	0.75	1.11	104	83	3.5

UV-vis of acceptors:
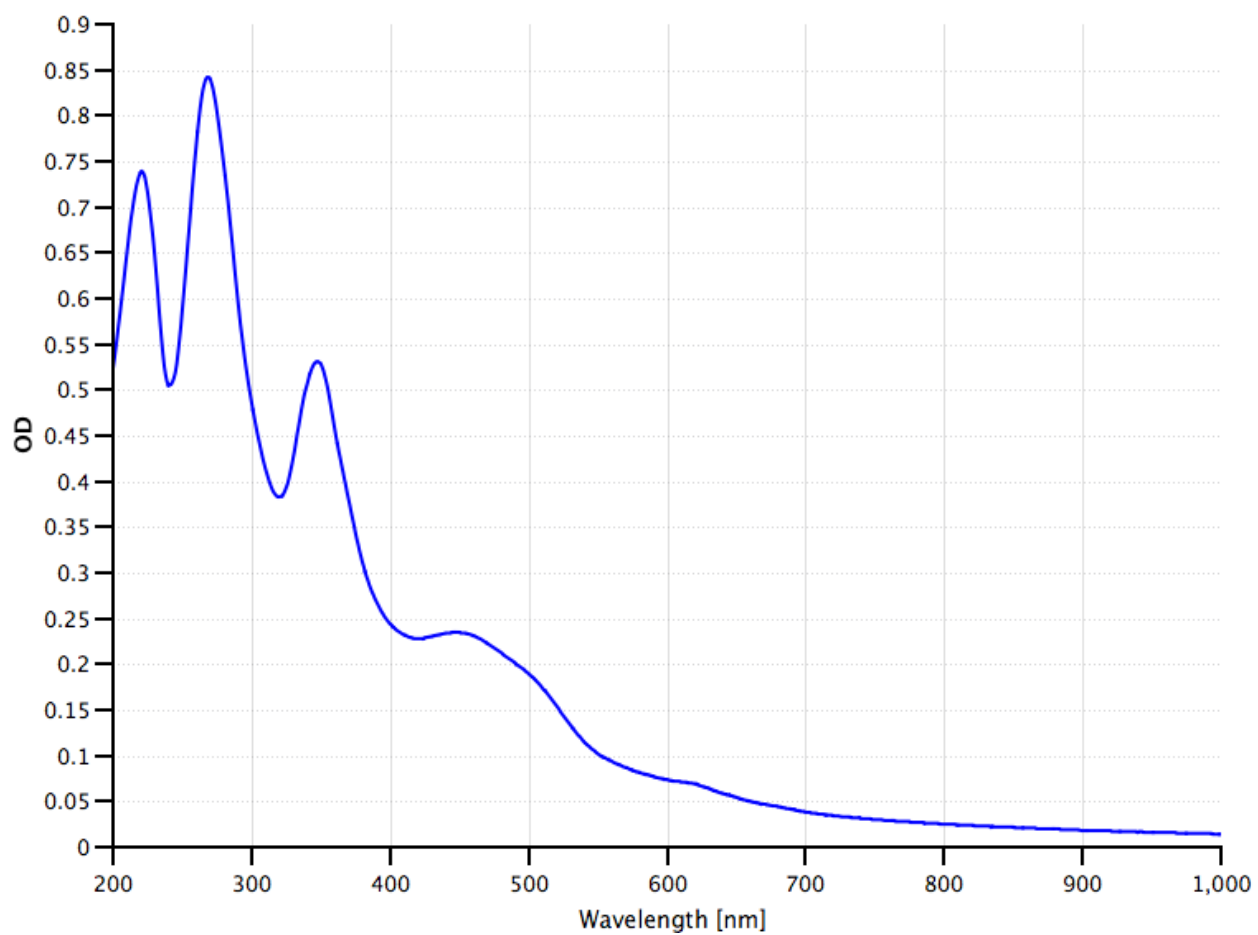
Figure A1.12. UV-vis spectrum of a 30 nm film of C_{60} deposited on ITO coated glass.
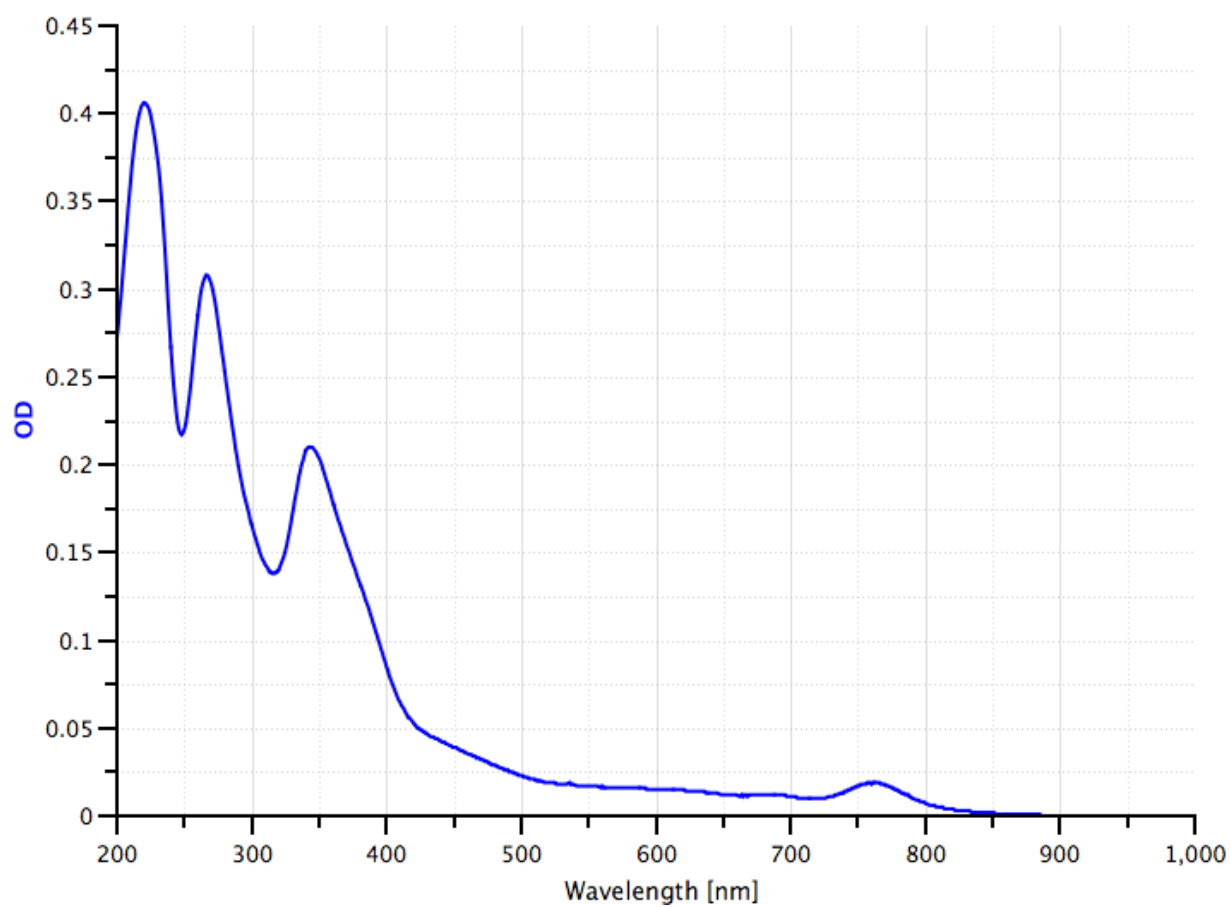
Figure A1.13. UV-vis spectrum of a 30 nm film of $C_{60}CF_2$ deposited on ITO coated glass.
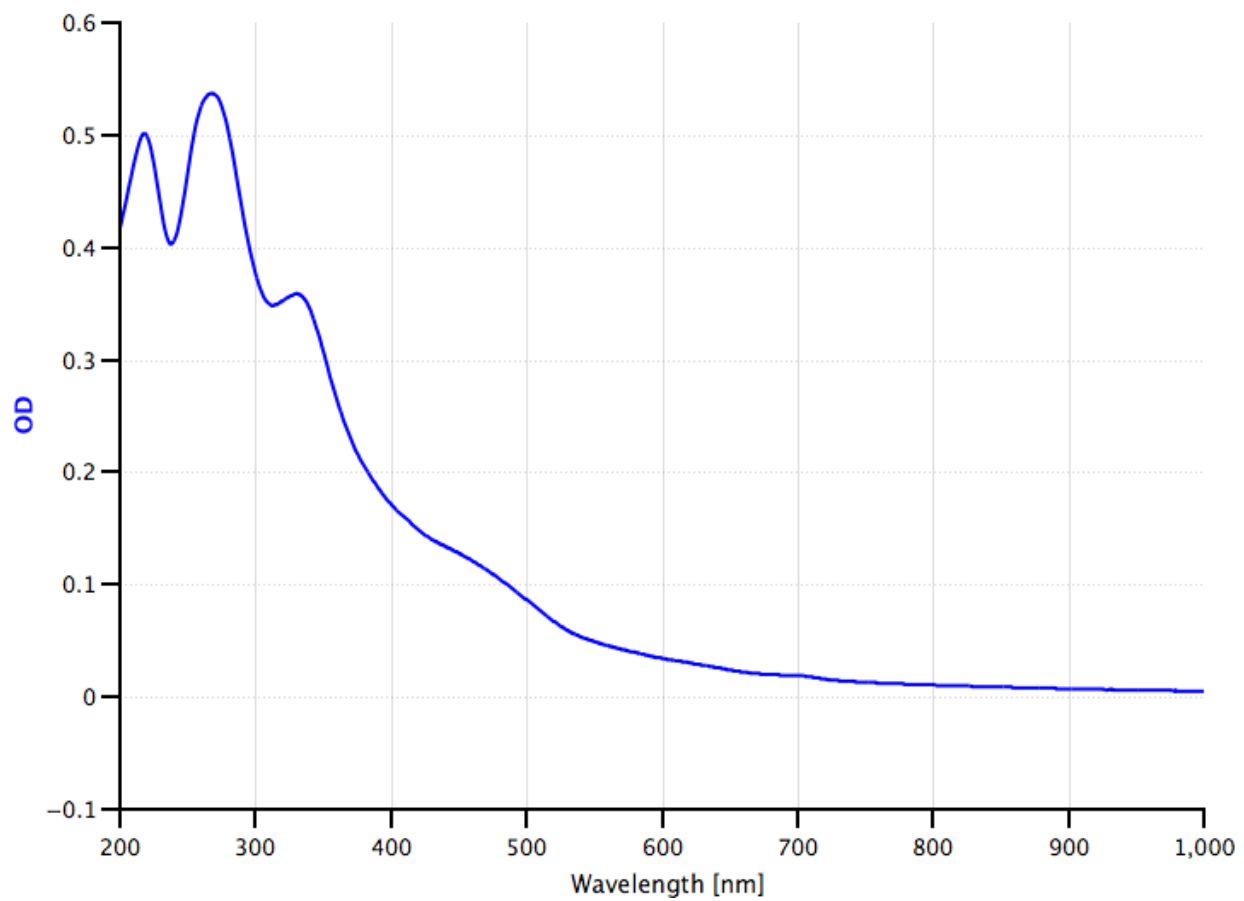
Figure A1.14. UV-vis spectrum of a 30 nm film of $C_{60}FHF$ deposited on ITO coated glass.
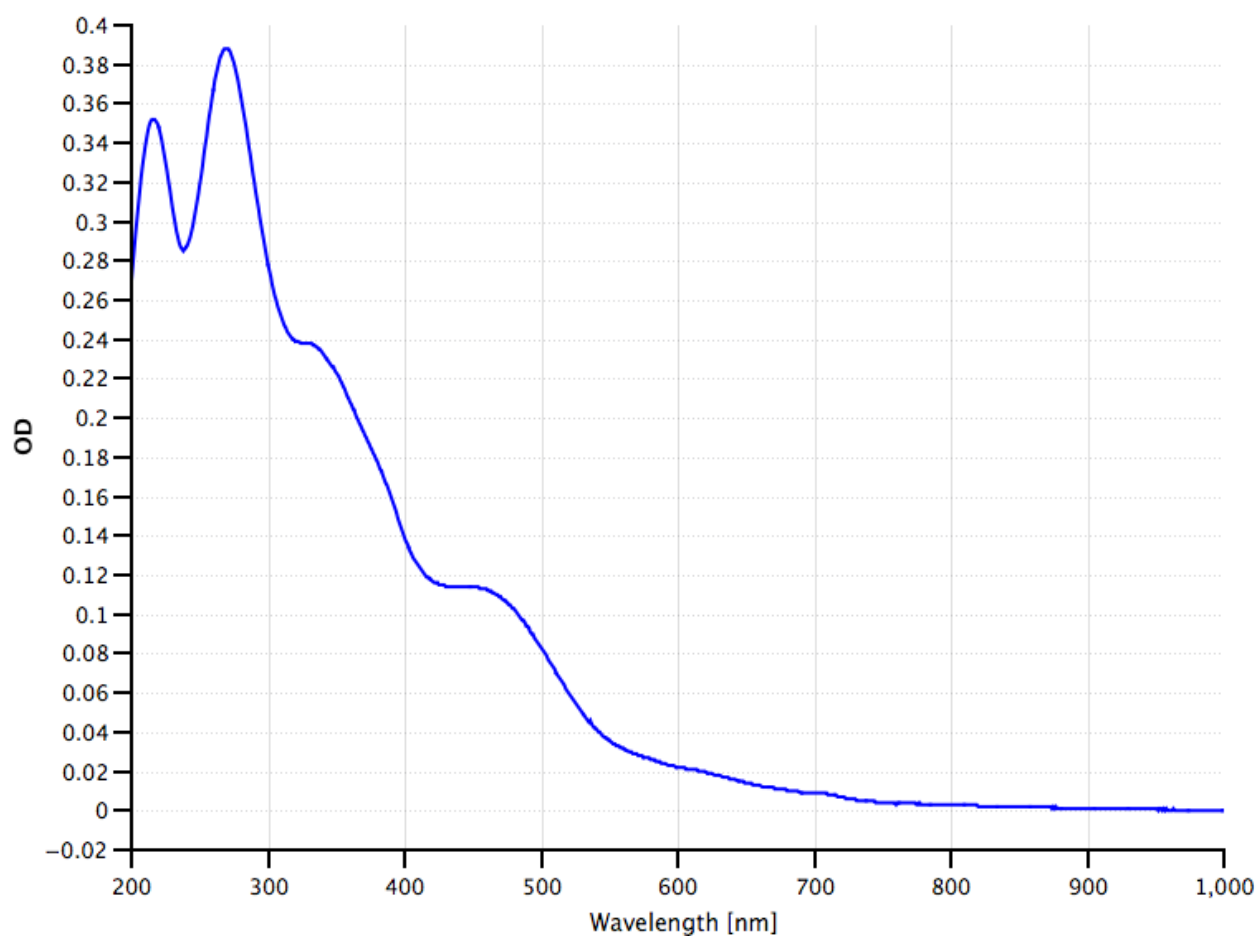
Figure A1.15. UV-vis spectrum of a 30 nm film of 60-2-1 deposited on ITO coated glass.
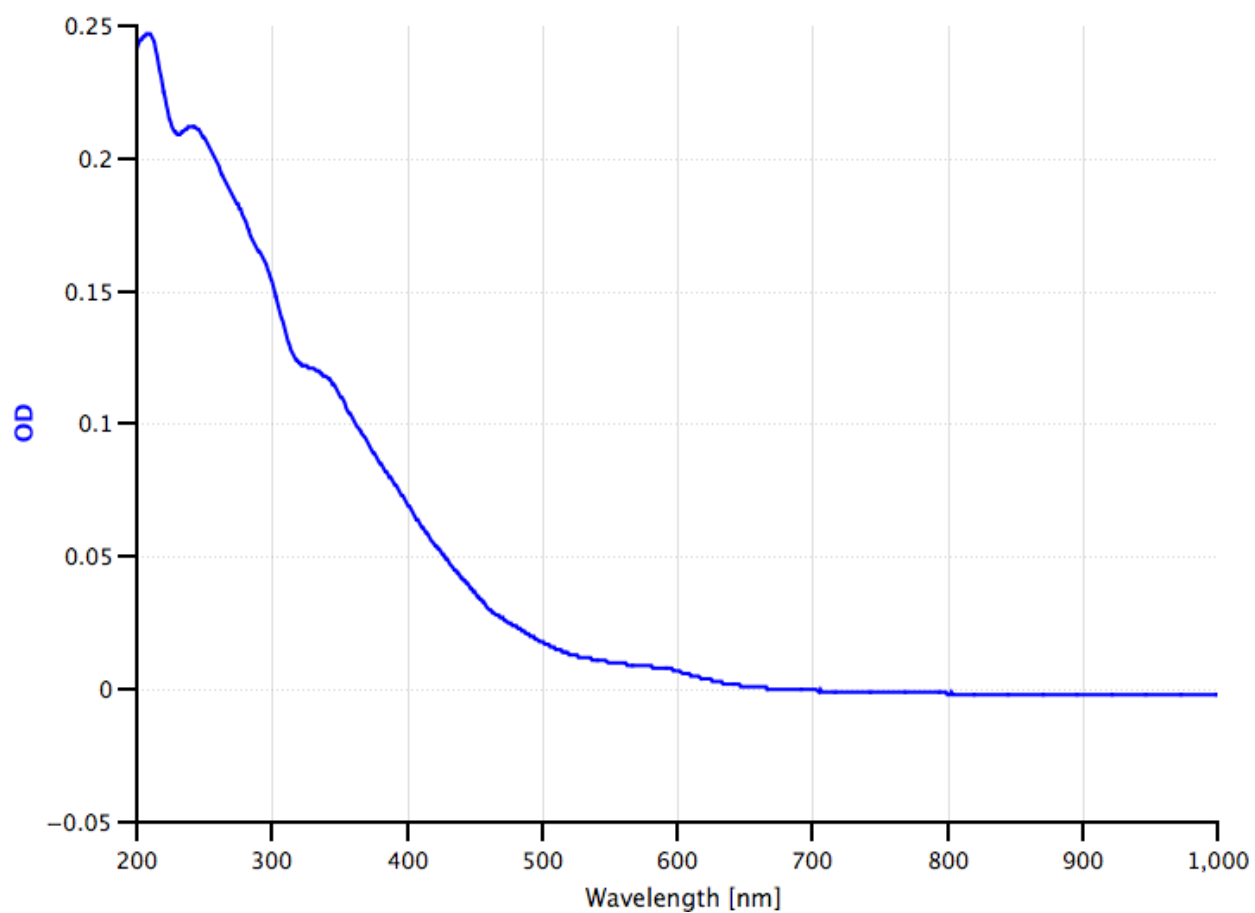
Figure A1.16. UV-vis spectrum of a 30 nm film of 60-8-1 deposited on ITO coated glass.
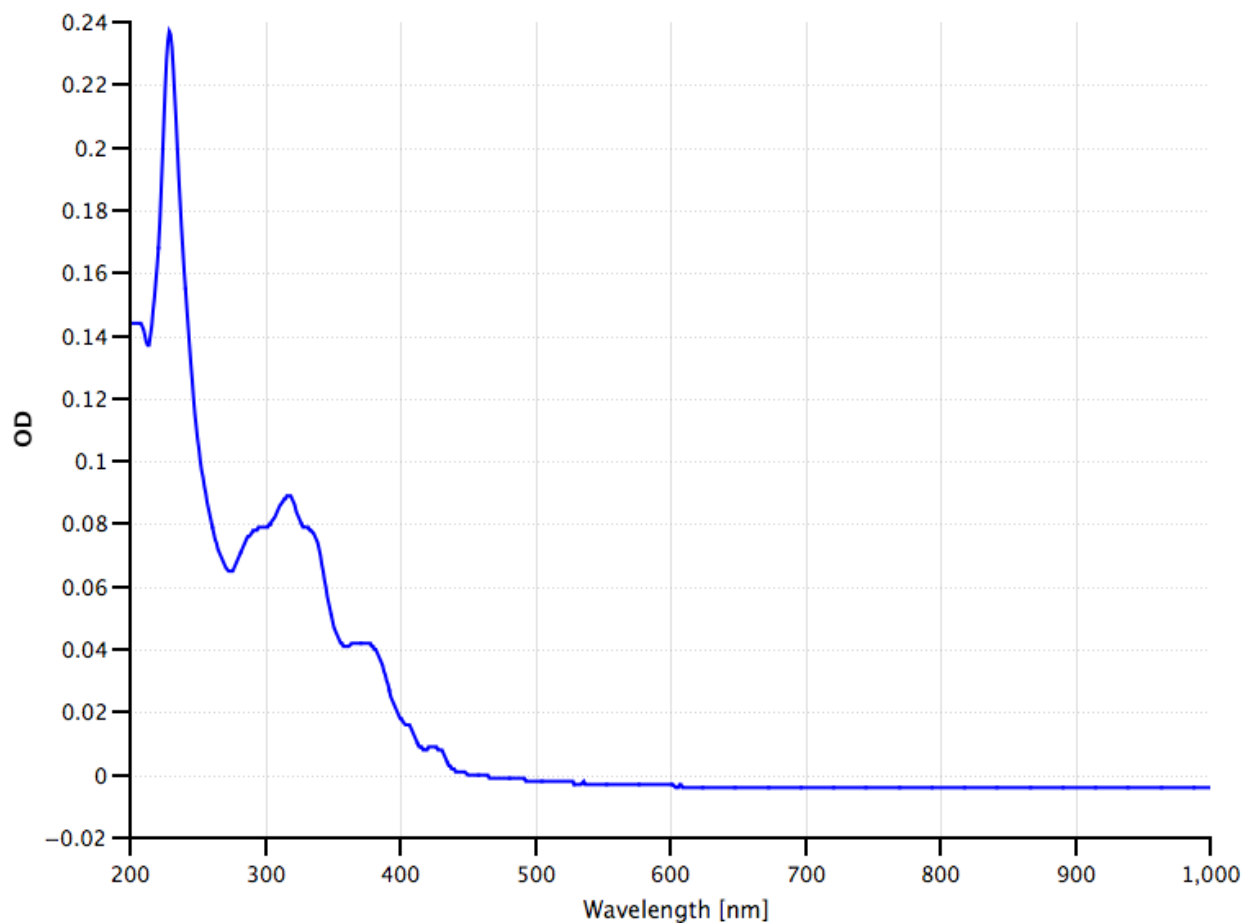
Figure A1.17. UV-vis spectrum of a 30 nm film of 60-12-1 deposited on ITO coated glass.

APPENDIX 1 REFERENCES

1.   Brotsman, V. A.; Ioutsi, V. A.; Rybalchenko, A. V.; Bogdanov, V. P.; Sokolov, S. A.; Belov, N. M.; Lukonina, N. S.; Markov, V. Y.; Ioffe, I. N.; Troyanov, S. I.; Magdesieva, T. V.; Trukhanov, V. A.; Paraschuk, D. Y.; Goryunkov, A. A. *Electrochim. Acta* **2016**, *219*, 130-142.
2.   Popov, A. A.; Kareev, I. E.; Shustova, N. B.; Stukalin, E. B.; Lebedkin, S. F.; Seppelt, K.; Strauss, S. H.; Boltalina, O. V.; Dunsch, L. *J. Am. Chem. Soc.* **2007**, *129*, 11551-11568.
3.   Popov, A. A., Private communication from Dr. A. Popov. Leibniz Institute of Solid for Solid State and Materials Research Dresden, IFW Dresden, 2018.

Crystallographic data
Table A2.1. Crystallographic data for phen(CF$_3$)$_n$ compounds.

Compound	2,4,7,9-tetrakis(trifluoromethyl)-1,10-phenanthroline	2,4,6,8-tetrakis(trifluoromethyl)-1,10-phenanthroline	2,4,5,7,9-pentakis(trifluoromethyl)-1,10-phenanthroline	2,5,9-tris(trifluoromethyl)-1,10-phenanthroline	2,4,9-tris(trifluoromethyl)-1,10-phenanthroline
Empirical formula	C$_{16}$H$_4$F$_{12}$N$_2$	C$_{16}$H$_4$F$_{12}$N$_2$	C$_{17}$H$_3$F$_{15}$N$_2$	C$_{15}$H$_5$F$_9$N$_2$	C$_{15}$H$_5$F$_9$N$_2$
Common name	phen-4-2	phen-4-3	phen-5-1	phen-3-1	phen-3-2
Formula weight	452.21	452.21	520.21	384.21	384.21
Habit, color	needle, light yellow	needle, clear colorless	needle, clear colorless	needle, clear colorless	needle, clear colorless
Crystal size, mm	0.17 × 0.04 × 0.013	0.199 × 0.05 × 0.015	0.321 × 0.063 × 0.054	0.058 × 0.066 × 0.165	0.027 × 0.032 × 0.743
Space group	C2/c	P21/c	P-1	P21/c	P21/n
a (Å)	38.472(14)	19.001(2)	12.342(5)	19.0955(17)	10.720(3)
b (Å)	18.913(7)	9.6814(11)	12.981(5)	11.6893(10)	24.449(8)
c (Å)	9.143(3)	8.5371(10)	13.192(5)	20.1529(18)	12.229(4)
α (°)	90	90	109.767(8)	90	90
β (°)	102.736(6)	92.407(3)	100.467(7)	90.692(2)	109.848(5)
γ (°)	90	90	113.697(7)	90	90
V (Å^3)	6489(4)	1569.1(3)	1693.1(12)	4498.1(7)	3014.8(16)
Z	16	4	4	12	8
T (K)	100	100	100	100	100
ρ_{calc} (g cm^{-3})	1.852	1.914	2.041	1.699	1.693
GooF [all data]	0.939	1.034	1.020	1.007	1.039
$R(F)$ ($I>2\sigma(I)$)[a]	0.0635	0.0846	0.0895	0.0636	0.0816
$wR(F^2)$ [all data][a]	0.1981	0.2177	0.2742	0.2136	0.2695
source	synchrotron	synchrotron	synchrotron	synchrotron	synchrotron

Table A2.2. Crystallographic data for copper(I) complexes.

Compound	$[Cu(phen\text{-}4\text{-}1)_2]SO_3CF_3$	$[Cu(phen\text{-}3\text{-}1)_2]SO_3CF_3$	$Cu_2(2\text{-}OH\text{-}phen\text{-}4\text{-}1)_2$
Empirical formula	$C_{33}H_8CuF_{27}N_4O_3S$	$C_{31}H_{10}CuF_{21}N_4O_3S$	$C_{32}H_6Cu_2F_{24}N_4O_2$
Formula weight	1117.03	981.03	1061.49
Habit, color	needle, orange	needle, orange	needle, dark orange
Crystal size, mm	$0.13 \times 0.021 \times 0.012$	$0.029 \times 0.059 \times 0.363$	$0.077 \times 0.014 \times 0.010$
Space group	P-1	P21/n	P21/c
a (Å)	9.5533(6)	13.5558(15)	5.2261(9)
b (Å)	11.651(2)	17.5348(19)	21.060(4)
c (Å)	17.407(3)	15.3405(17)	15.656(3)
α (°)	93.295(3)	90	90
β (°)	99.999(3)	106.109(2)	109.596(3)
γ (°)	96.846(3)	90	90
V (Å^3)	1888.4(6)	3503.2(7)	1623.3(5)
Z	2	4	2
T (K)	150	150	150
ρ_{calc} (g cm^{-3})	1.965	1.860	2.172
GooF [all data]	1.065	1.056	0.981
$R(F)$ $(I>2\sigma(I))$[a]	0.0866	0.0693	0.0519
$wR(F^2)$ [all data][a]	0.2517	0.2050	0.1188
source	synchrotron	synchrotron	synchrotron

Table A2.3. DFT calculated absorbance and the dihedral angle between ligand planes (Θ) for select ground and excited states of $[Cu(NN)_2]^+$ complexes.

	$[Cu(dmp)_2]^+$	$[Cu(phen-2-1)_2]^+$	$[Cu(phen-3-1)_2]^+$	$[Cu(phen-4-1)_2]^+$	$[Cu(phen-4-2)_2]^+$
Calculated λ_{max} (nm)	461 nm	465 nm	467 nm	480 nm	482 nm
GS Θ	89.98°	90.00°	89.84°	89.98°	89.98°
N^{th} ^{1}MLCT	90.00°	90.00°	80.00°	89.97°	78.42°
^{1}MLCT	63.92°	90.00°	78.29°	78.92°	80.27°
^{3}MLCT	62.93°	70.60°	74.92°	75.35°	74.38°

X-ray structure and NMR spectra of phen-3-1
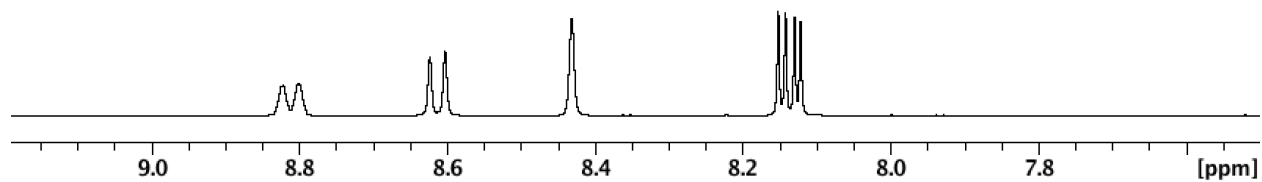
Figure A2.1. ^{1}H NMR spectrum of phen-3-1 in CDCl$_3$.
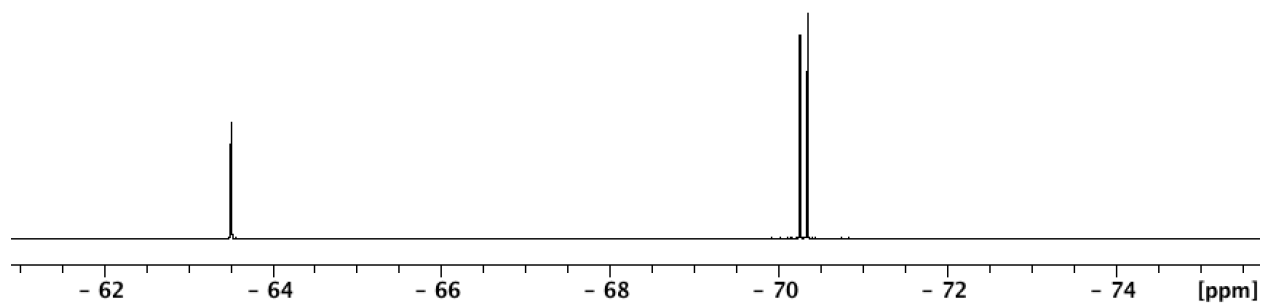
Figure A2.2. ^{19}F NMR spectrum of phen-3-1 in CDCl$_3$.
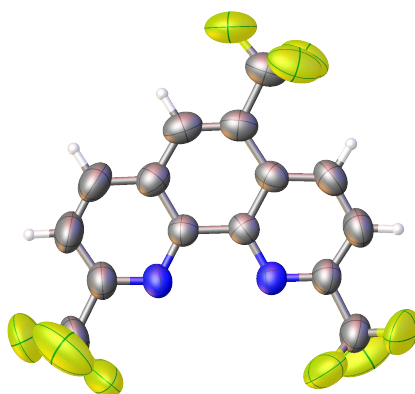
Figure A2.3. X-ray structure of phen-3-1. Thermal ellipsoids are plotted at 50% probability.

X-ray structure and NMR spectra of phen-3-2
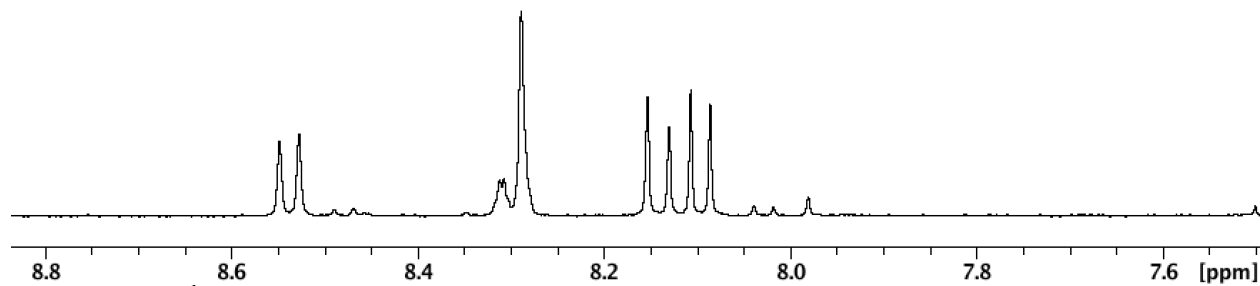
Figure A2.4. ^{1}H NMR spectrum of phen-3-2 in CDCl$_3$.
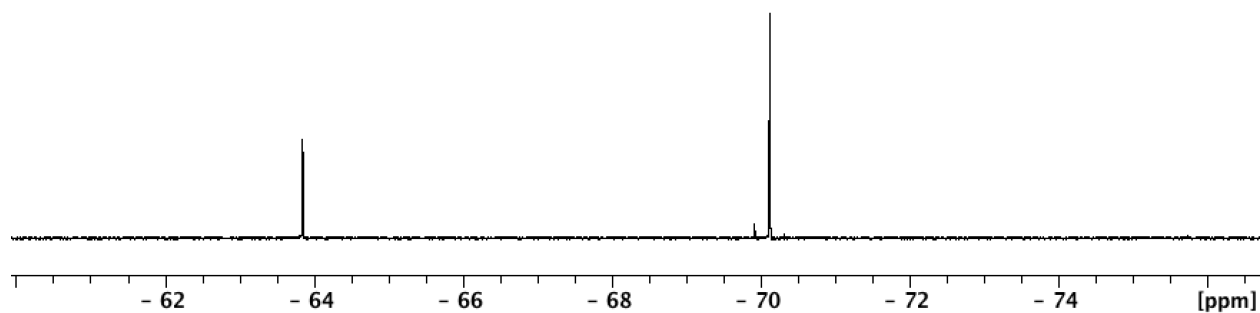
Figure A2.5. ^{19}F NMR spectrum of phen-3-2 in CDCl$_3$.
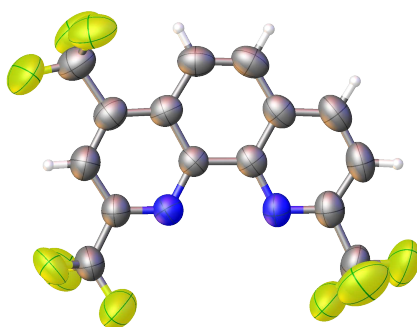
Figure A2.6. X-ray structure of phen-3-2. Thermal ellipsoids are plotted at 50% probability.

Preliminary X-ray structure and NMR spectra of phen-4-1
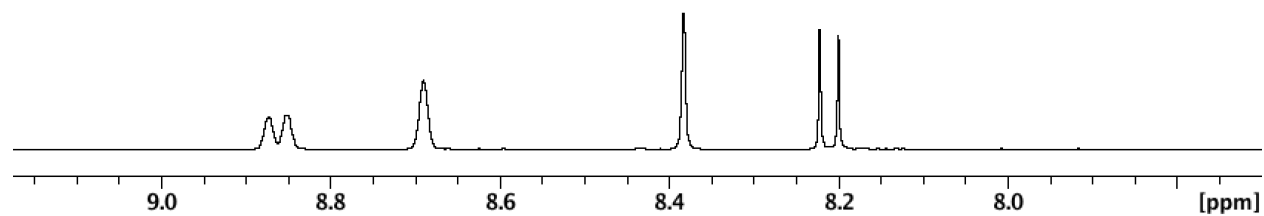
Figure A2.7. ^{1}H NMR spectrum of phen-4-1 in CDCl$_3$.
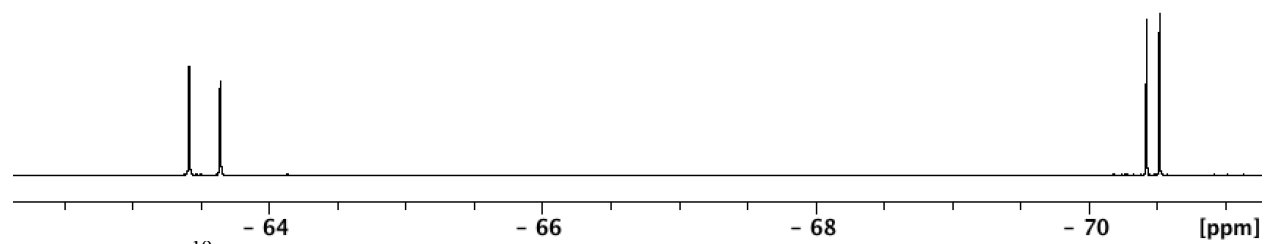
Figure A2.8. ^{19}F NMR spectrum of phen-4-1 in CDCl$_3$.
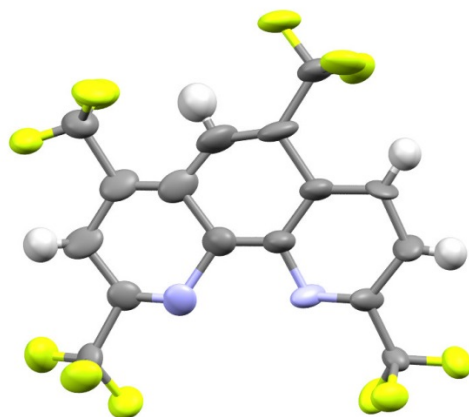
Figure A2.9. Preliminary X-ray structure of phen-4-1**.** Thermal ellipsoids are plotted at 50% probability.

X-ray structure and NMR spectra of phen-4-2
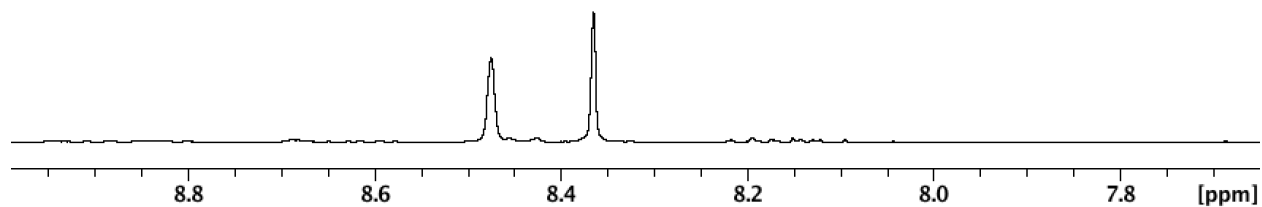
Figure A2.10. ^{1}H NMR spectrum of phen-4-2 in CDCl$_3$.
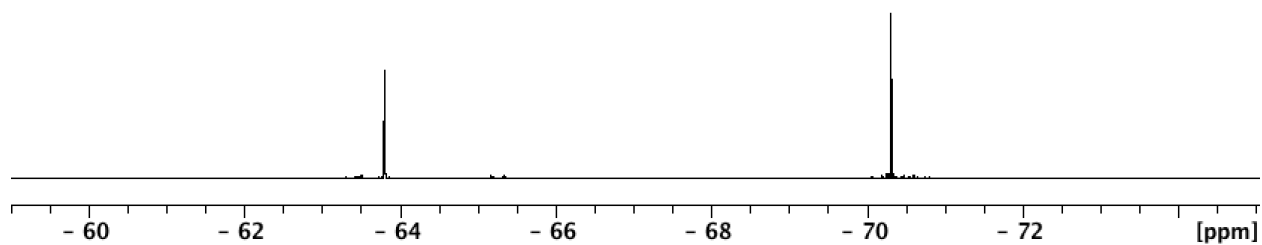
Figure A2.11. ^{19}F NMR spectrum of phen-4-2 in CDCl$_3$.
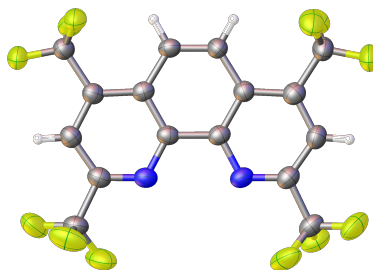
Figure A2.12. X-ray structure of phen-4-2. Thermal ellipsoids are plotted at 50% probability.

X-ray structure and NMR spectra of phen-4-3
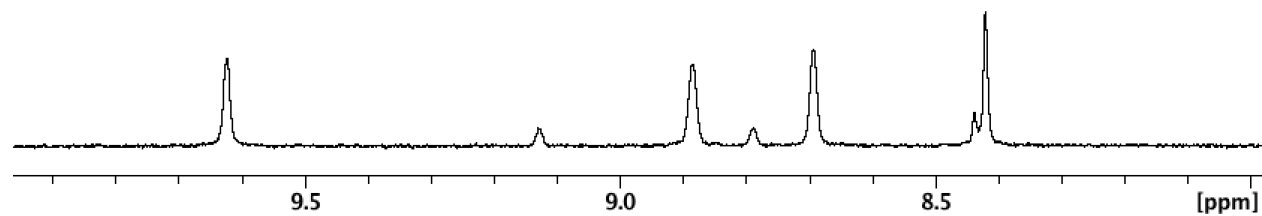
Figure A2.13. ^{1}H NMR spectrum of phen-4-3 in CDCl$_3$.
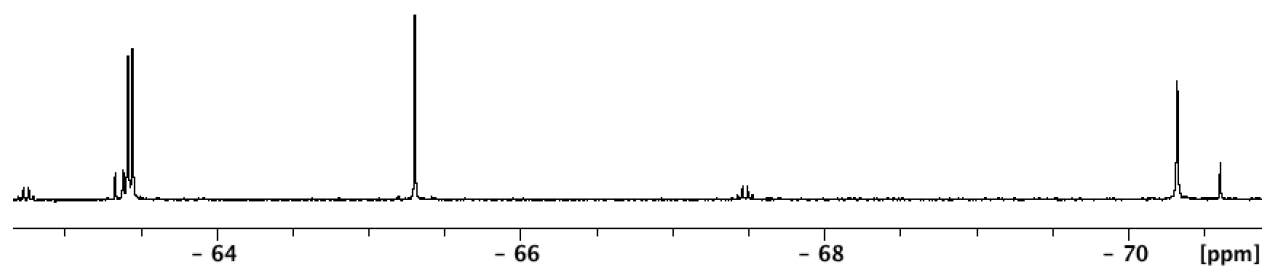
Figure A2.14. ^{19}F NMR spectrum of phen-4-3 in CDCl$_3$.
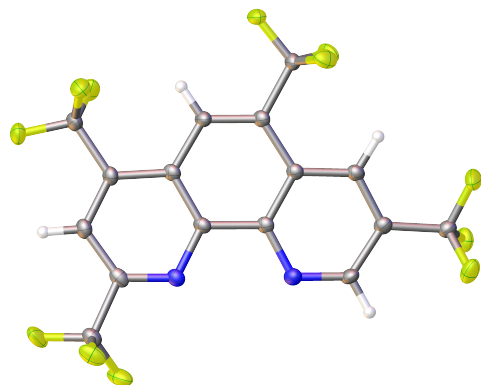
Figure A2.15. Preliminary X-ray structure of phen-4-3.

X-ray structure and NMR spectra of phen-5-1
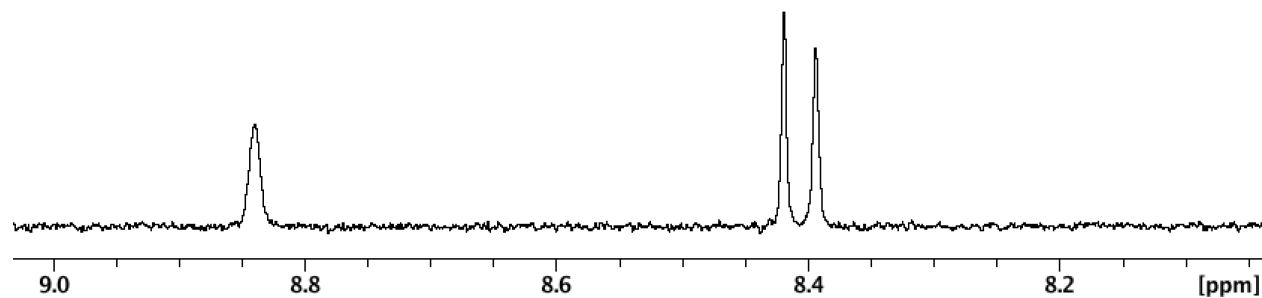
Figure A2.16. ^{1}H NMR spectrum of phen-5-1 in CDCl$_3$.
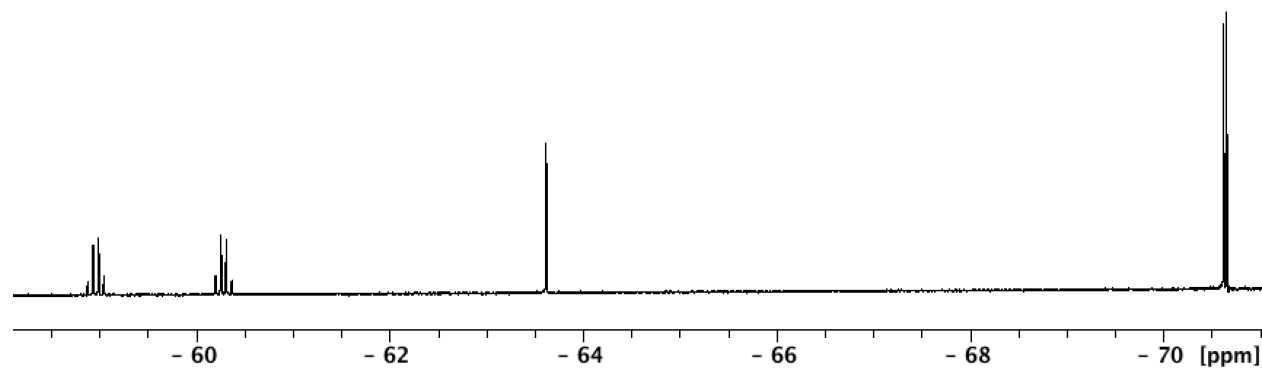
Figure A2.17. ^{19}F NMR spectrum of phen-5-1 in CDCl$_3$.
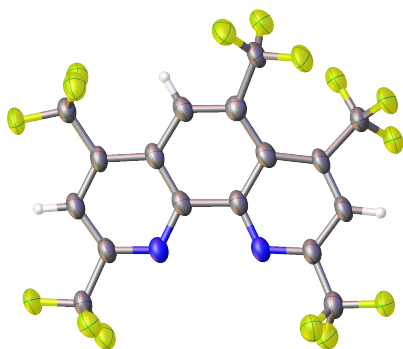
Figure A2.18. X-ray structure of phen-5-1.

NMR spectra of phen-2-1
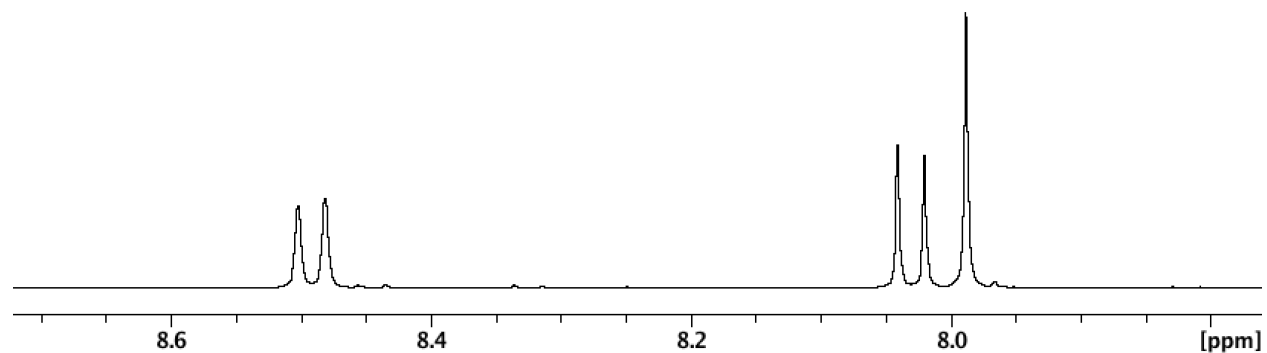
Figure A2.19. ^{1}H NMR spectrum of phen-2-1 in CDCl$_3$.
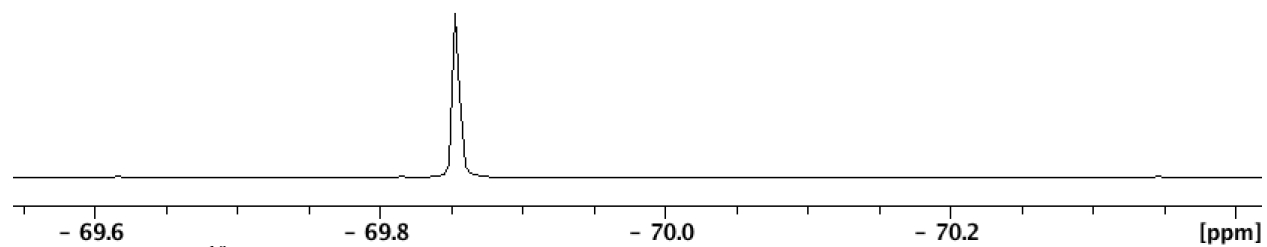
Figure A2.20. ^{19}F NMR spectrum of phen-2-1 in CDCl$_3$.
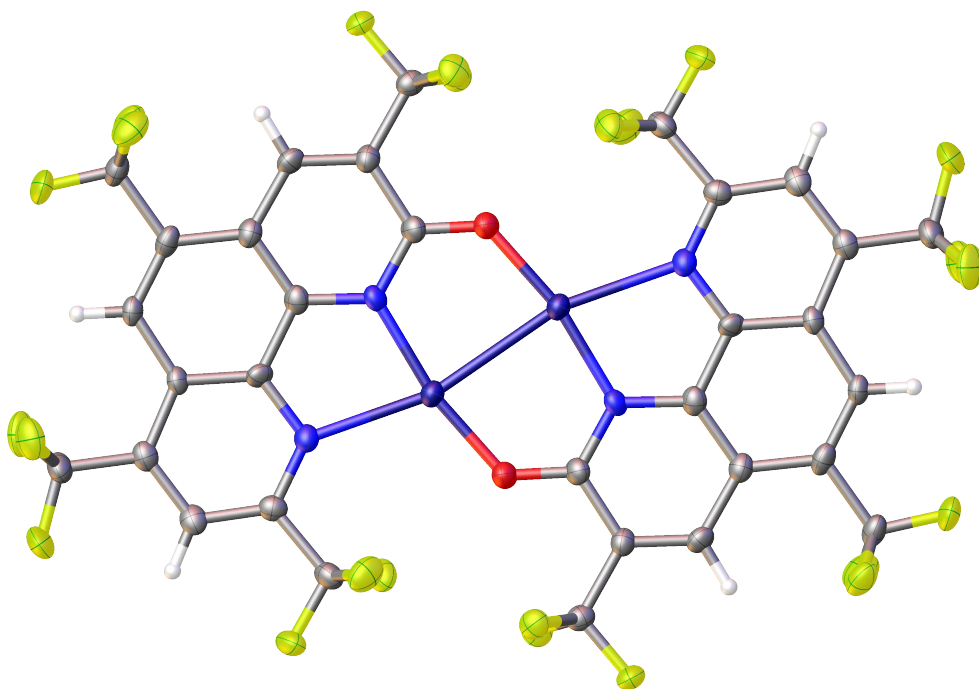
Figure A2.21. SC-XRD structure of Cu_2(2-OH-phen-4-1)$_2$. Thermal ellipsoids plotted at 50% probability.

X-ray structure, mass spectrum, and NMR spectra of [Cu(phen-4-1)$_2$]SO$_3$CF$_3$
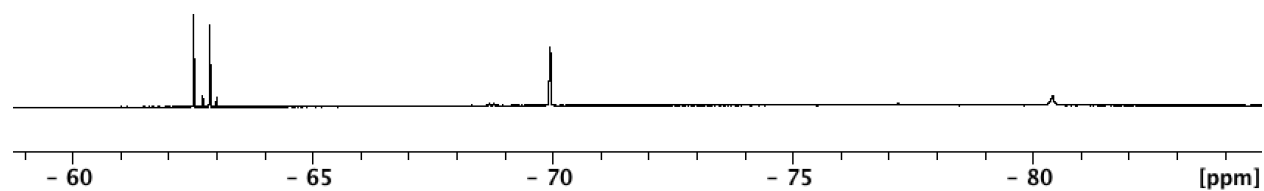
Figure A2.22. ^{19}F NMR spectrum of [Cu(phen-4-1)$_2$]SO$_3$CF$_3$ in CD$_2$Cl$_2$.
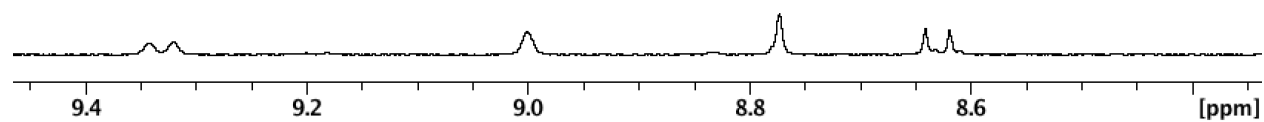
Figure A2.23. ^{1}H NMR spectrum of [Cu(phen-4-1)$_2$]SO$_3$CF$_3$ in CD$_2$Cl$_2$.
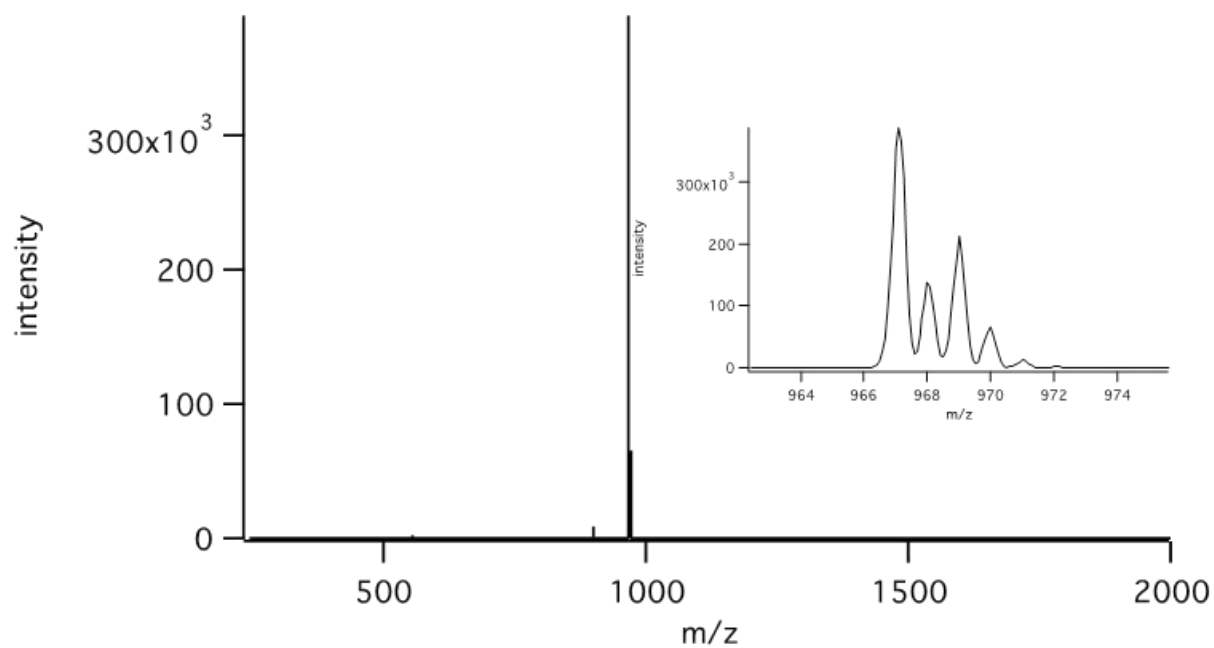
Figure A2.24. ESI+ mass spectrum of [Cu(phen-4-1)$_2$]SO$_3$CF$_3.$
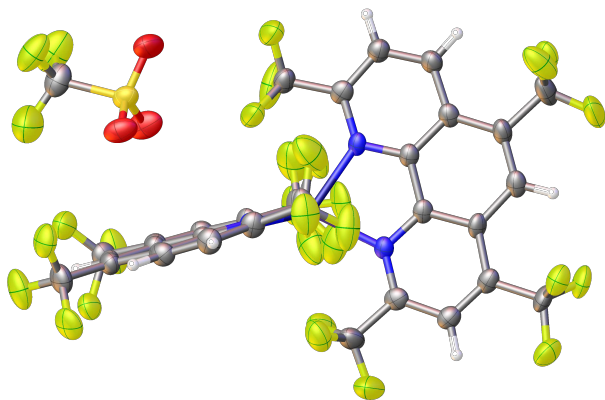
Figure A2.25. X-ray structure of [Cu(phen-4-1)$_2$]SO$_3$CF$_3$. Thermal ellipsoids are plotted at 50% probability.

X-Ray structure, mass spectrum, and NMR spectra of [Cu(phen-3-1)$_2$]SO$_3$CF$_3$
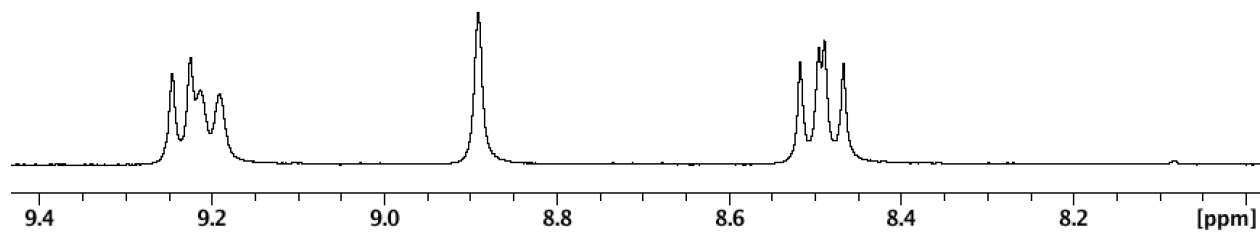
Figure A2.26. ^{1}H NMR spectrum of [Cu(phen-3-1)$_2$]SO$_3$CF$_3$ in CD$_2$Cl$_2$.
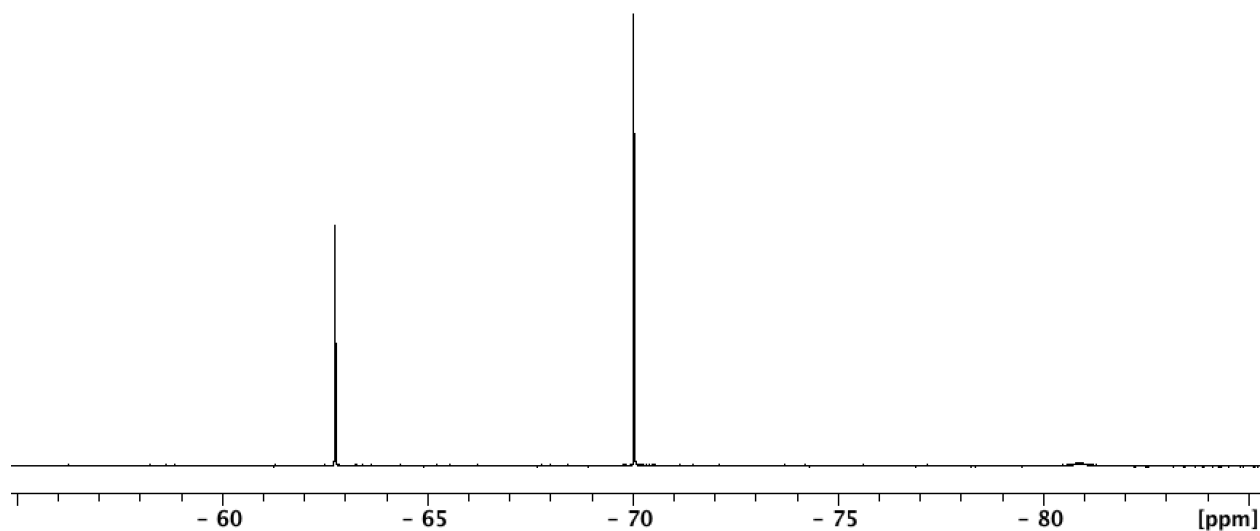
Figure A2.27. ^{19}F NMR spectrum of [Cu(phen-3-1)$_2$]SO$_3$CF$_3$ in CD$_2$Cl$_2$.
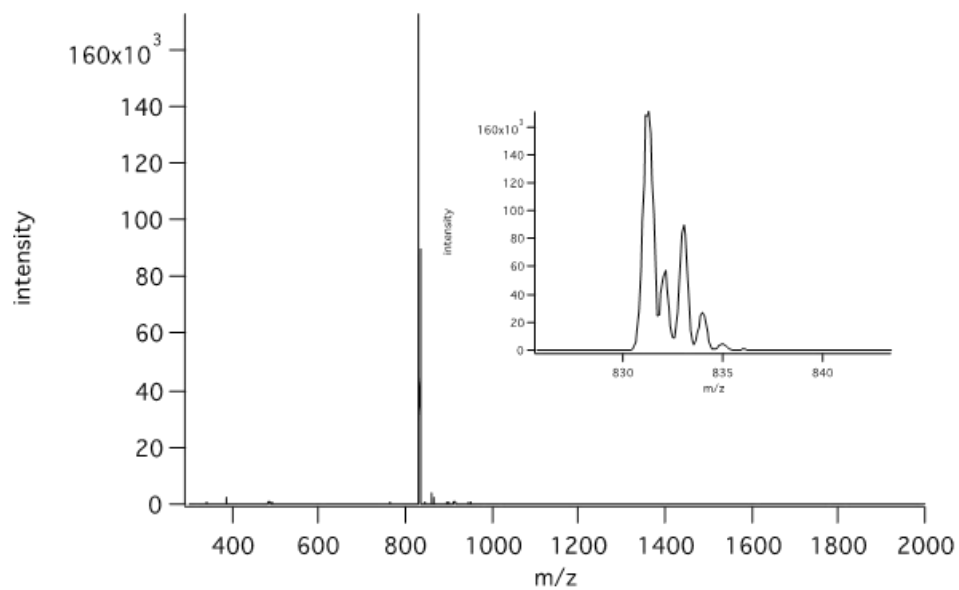
Figure A2.28. ESI+ mass spectrum of [Cu(phen-3-1)$_2$]SO$_3$CF$_3$.
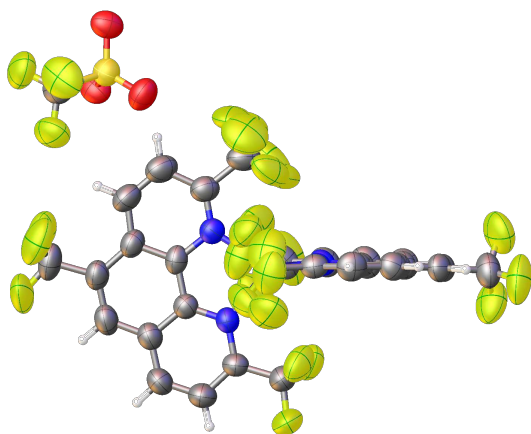
Figure A2.29. X-ray structure of [Cu(phen-3-1)$_2$]SO$_3$CF$_3$. Thermal ellipsoids are plotted at 50% probability.

Mass spectrum and NMR spectra of [Cu(phen-4-2)$_2$]SO$_3$CF$_3$
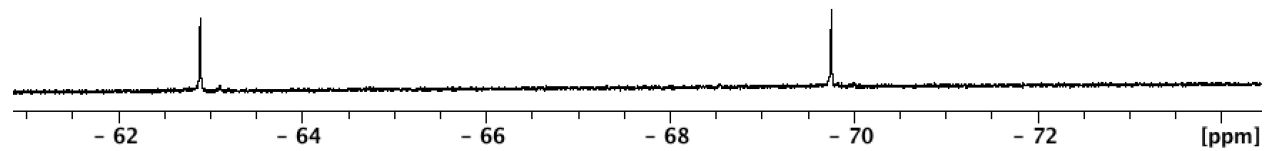
Figure A2.30. ^{19}F NMR spectrum of [Cu(phen-4-2)$_2$]SO$_3$CF$_3$ in CD$_2$Cl$_2$.
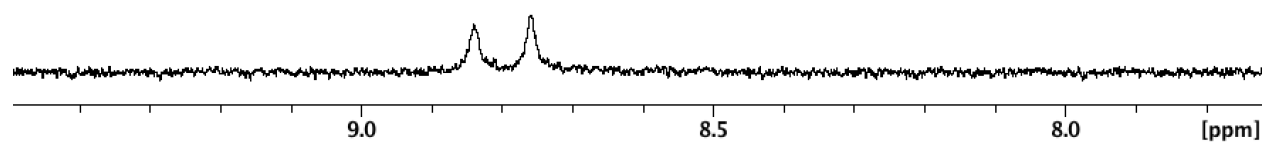
Figure A2.31. ^{1}H NMR spectrum of [Cu(phen-4-2)$_2$]SO$_3$CF$_3$ in CD$_2$Cl$_2$.
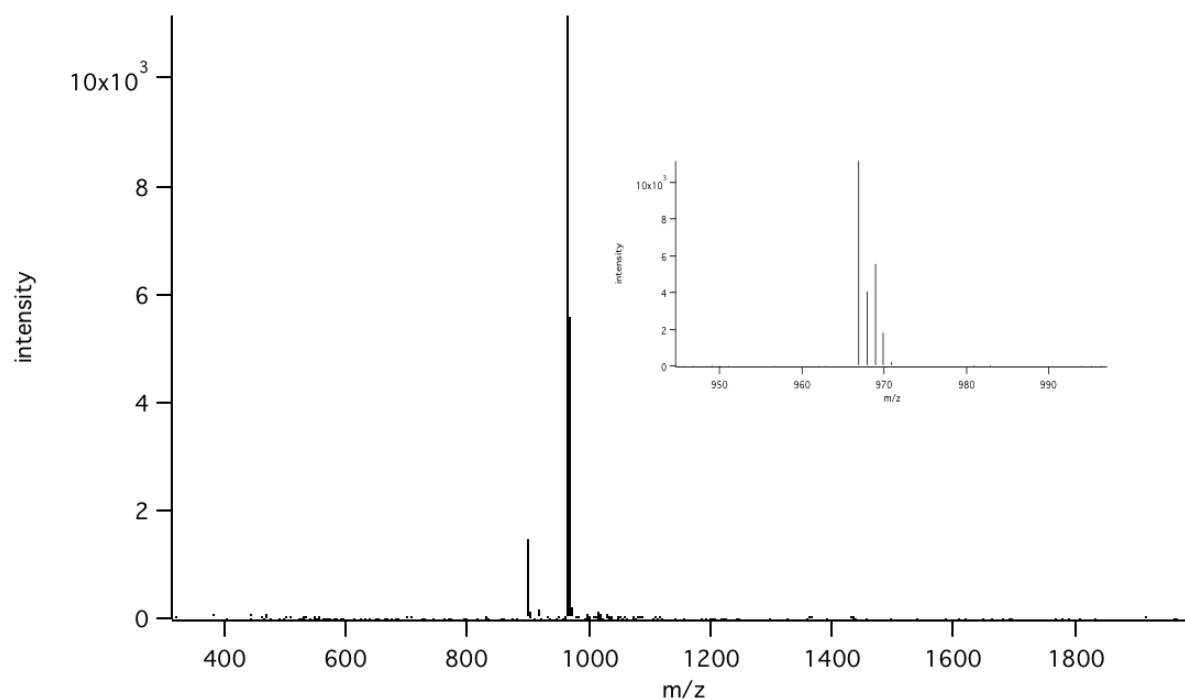
Figure A2.32. ESI+ mass spectrum of [Cu(phen-4-2)$_2$]SO$_3$CF$_3$.

Mass spectrum and NMR spectra of [Cu(phen-2-1)$_2$]SO$_3$CF$_3$
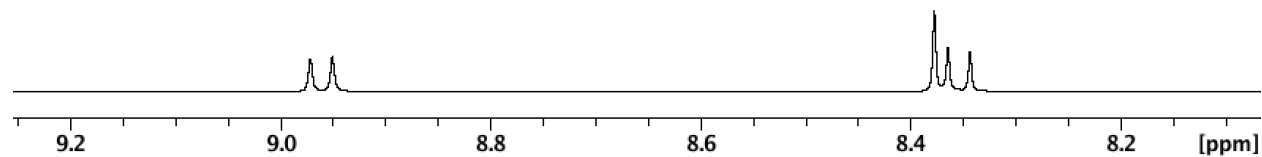
Figure A2.33. ^{1}H NMR spectrum of [Cu(phen-2-1)$_2$]SO$_3$CF$_3$ in CD$_2$Cl$_2$.
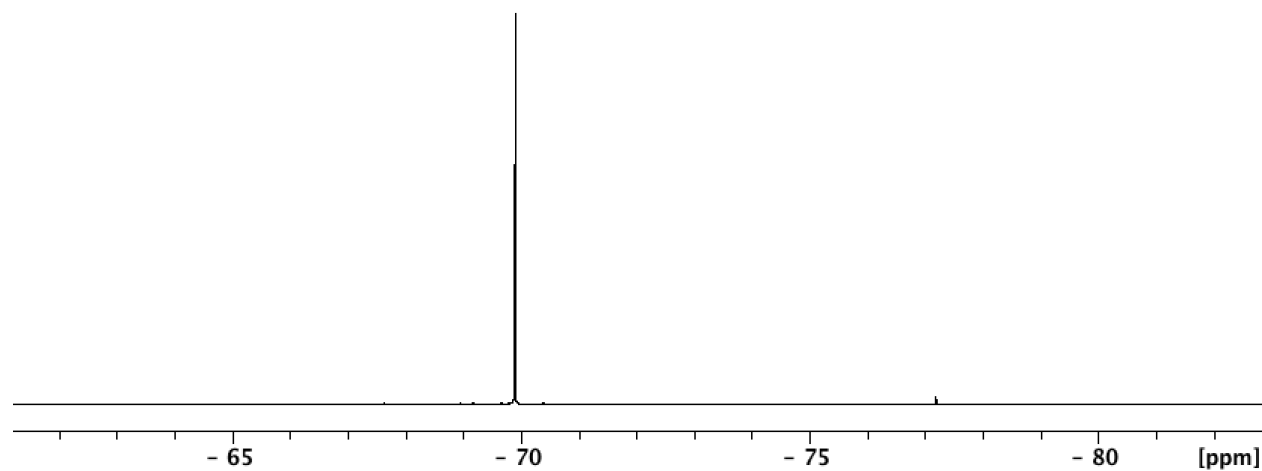
Figure A2.34. ^{19}F NMR spectrum of [Cu(phen-2-1)$_2$]SO$_3$CF$_3$ in CD$_2$Cl$_2$.
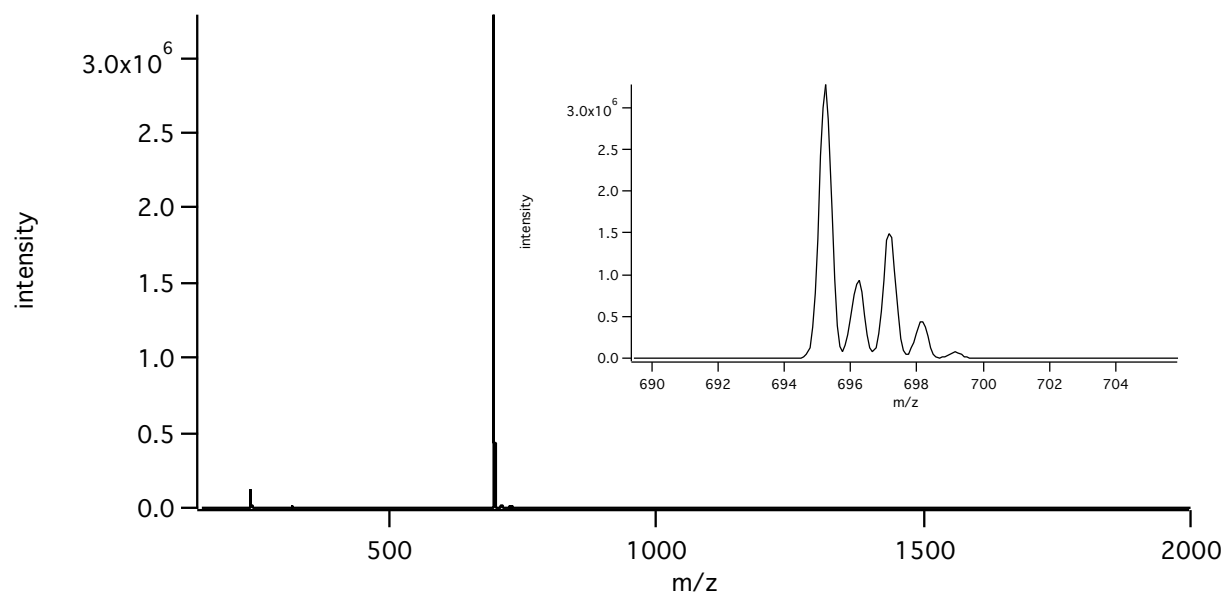
Figure A2.35. ESI+ mass spectrum of [Cu(phen-2-1)$_2$]SO$_3$CF$_3$.
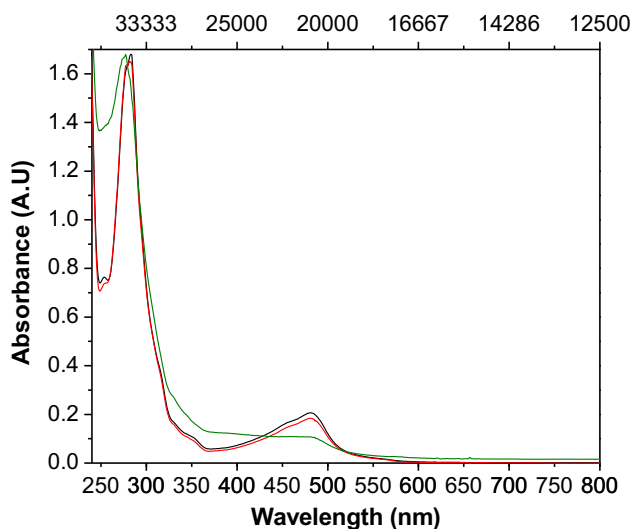
Figure A2.36. Electronic Absorption Spectra of [Cu(phen-4-2)$_2$]OTf in 1,2-dichloroethane at the start of experimentation (black), after ultrafast pump probe (red), and after nanosecond flash photolysis (green).
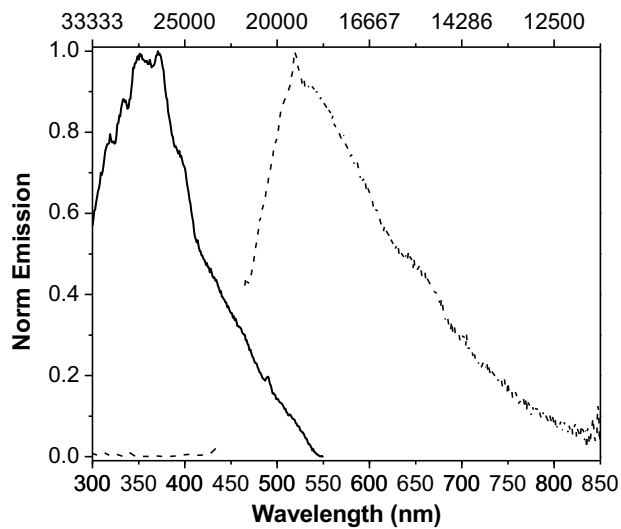
Figure A2.37. Excitation and Emission collected from a [Cu(phen-4-1)$_2$]OTf in 1,2-dichloroethane solution.
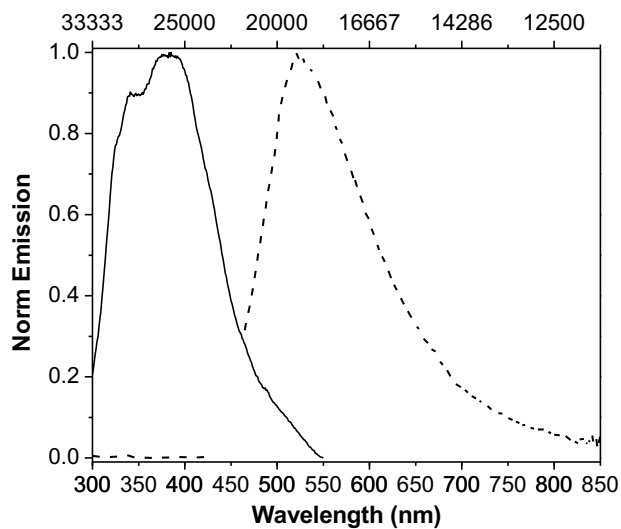
Figure A2.38. Excitation and Emission collected from a [Cu(phen-4-2)$_2$]OTf in 1,2-dichloroethane solution.
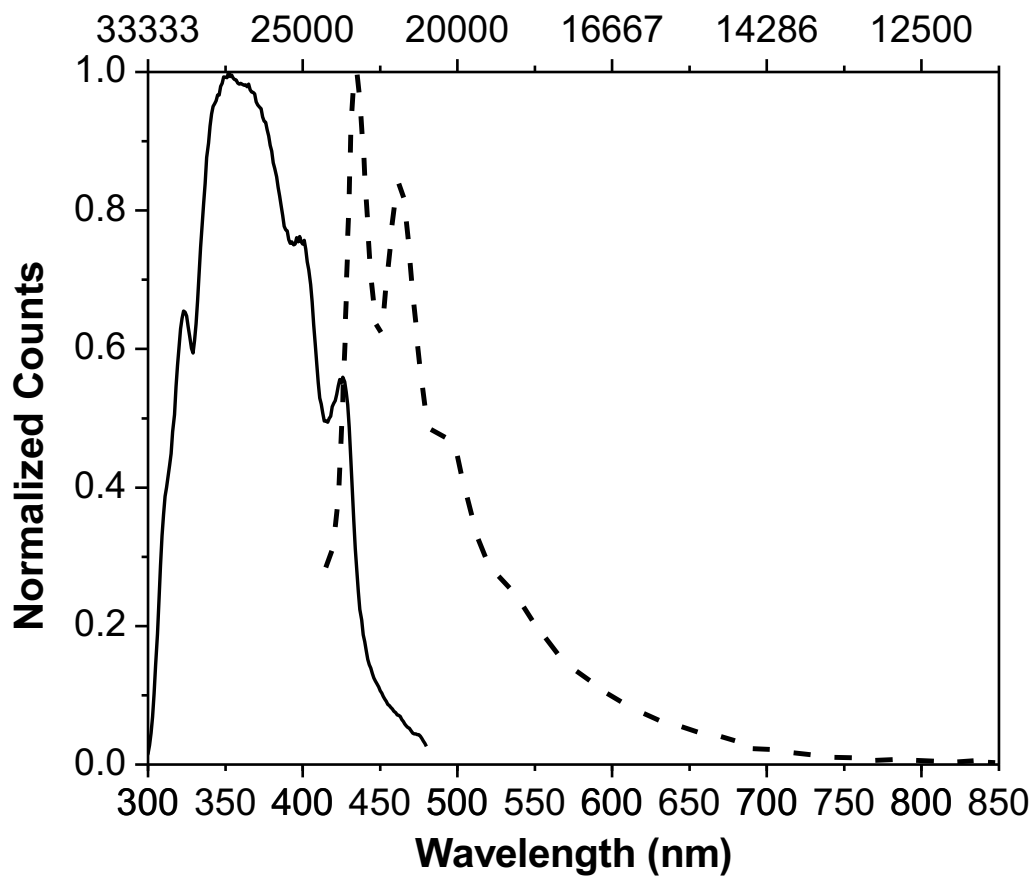
Figure A2.39. Excitation and Emission for 2,9-dimethyl-1,10-phenanthroline.

APPENDIX 3. SUPPORTING INFORMATION FOR CHAPTER 4

Crystallographic data

Table A3.1. Crystallographic Data for PHRD(CF$_3$)$_n$ compounds.

Compound	1,4,6-tris(trifluoromethyl) phenanthridine	2,4,6-tris(trifluoromethyl)phenanthridine	2,4,7-tris(trifluoromethyl)phenanthridine	3,7,9-tris(trifluoromethyl)phenanthridine	1,4,7,9-tetrakis(trifluoromethyl)phenanthridine	2,4,6,8-tetrakis(trifluoromethyl)phenanthridine
Empirical formula	C$_{16}$H$_6$F$_9$N	C$_{16}$H$_6$F$_9$N	C$_{16}$H$_6$F$_9$N	C$_{16}$H$_6$F$_9$N	C$_{17}$H$_5$F$_{12}$N	C$_{17}$H$_5$F$_{12}$N
Common name	PHRD-3-1	PHRD-3-2	PHRD-3-3	PHRD-3-4	PHRD-4-2	PHRD-4-1
Formula weight	383.22	383.22	383.22	383.22	451.22	451.22
Habit, color	prism, clear colorless	needle, clear colorless	needle, clear colorless	needle, clear colorless	needle, clear colorless	needle, clear colorless
Crystal size, mm	0.488 × 0.062 × 0.041	0.222 × 0.027 × 0.027	0.677 × 0.070 × 0.030	0.272 × 0.044 × 0.034	0.25 × 0.043 × 0.031	0.235 × 0.025 × 0.019
Space group	P2$_1$/c	Pnma	Pn	I2/m	Pbca	P2$_1$/n
a (Å)	10.0148(4)	21.920(3)	9.2853(7)	13.5867(5)	11.5001(6)	4.6817(6)
b (Å)	15.8718(7)	7.0221(9)	16.2856(13)	7.2275(2)	8.8871(4)	16.607(2)
c (Å)	9.5051(4)	9.3325(13)	19.5436(18)	16.0790(8)	31.1119(16)	20.916(3)
α (°)	90	90	90	90	90	90
β (°)	104.1440(10)	90	103.731(2)	112.9400(10)	90	92.689(3)
γ (°)	90	90	90	90	90	90
V (Å^3)	1465.06(11)	1436.5(3)	2870.9(4)	1454.05(10)	3179.7(3)	1624.4(4)
Z	4	4	8	4	8	4
T (K)	100	100	100	100	100	100
ρ_{calc} (g cm^{-3})	1.737	1.772	1.773	1.751	1.885	1.845
GooF [all data]	1.046	1.092	1.366	1.076	1.059	1.022
$R(F)$ $(I>2\sigma(I))$[a]	0.0347	0.0351	0.1735	0.0558	0.0517	0.0420
$wR(F^2)$ [all data][a]	0.0989	0.1057	0.4280	0.1956	0.1381	0.1181
source	synchrotron	synchrotron	synchrotron	synchrotron	synchrotron	synchrotron

X-Ray Structure and NMR spectra of PHRD-3-1
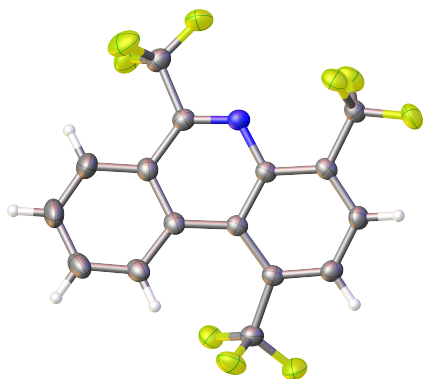
Figure A3.1. X-ray structure of PHRD-3-1.
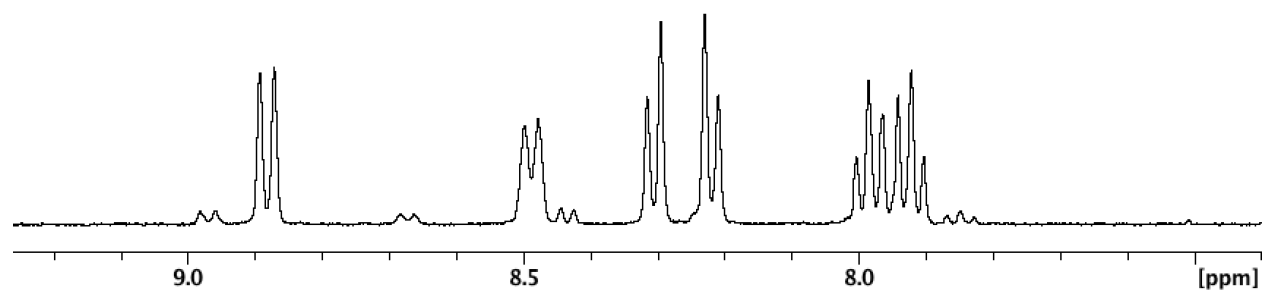
Figure A3.2. ^{1}H NMR spectrum of PHRD-3-1.
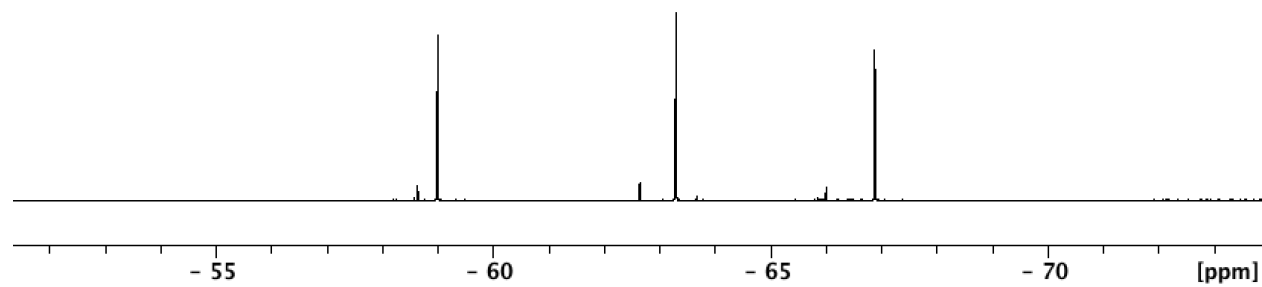
Figure A3.3. ^{19}F NMR spectrum of PHRD-3-1.

X-Ray Structure and NMR spectra of PHRD-3-2
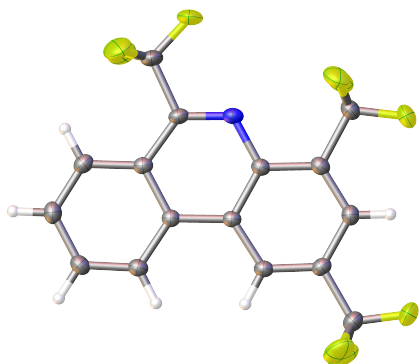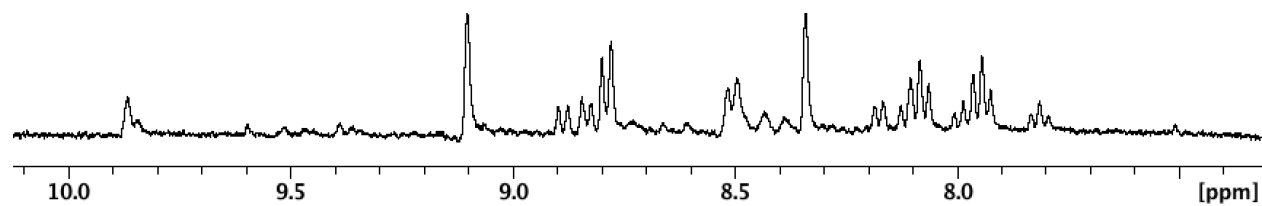

Figure A3.4. X-ray structure of PHRD-3-2.
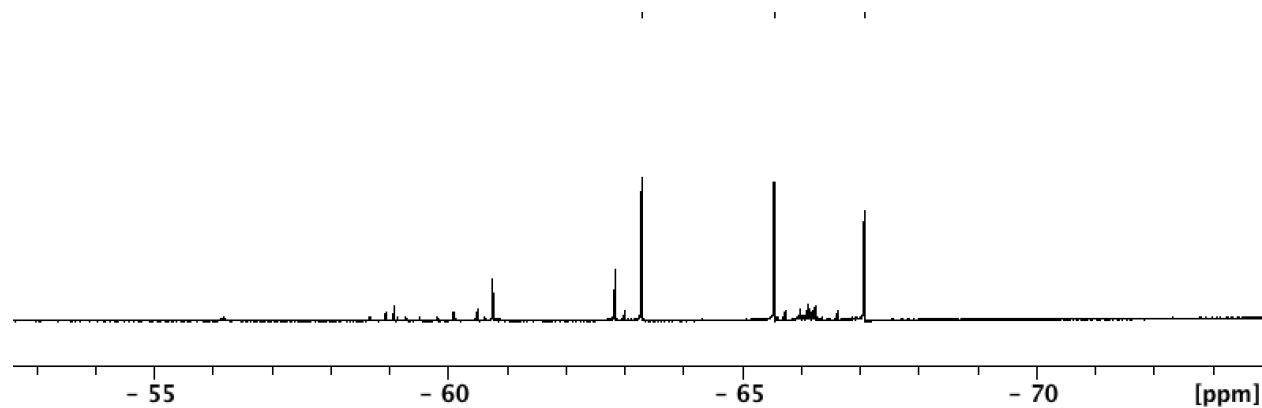

Figure A3.5. ^{1}H NMR spectrum of PHRD-3-2.

Figure A3.6. ^{19}F NMR spectrum of PHRD-3-2.

X-Ray Structure and NMR spectra of PHRD-3-3
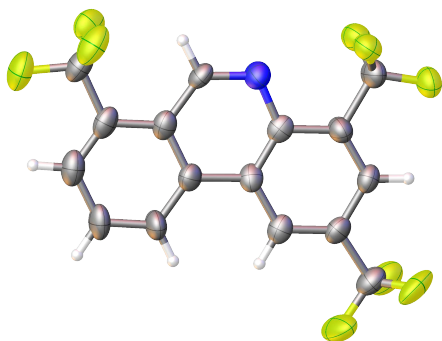
Figure A3.7. X-ray structure of PHRD-3-3.
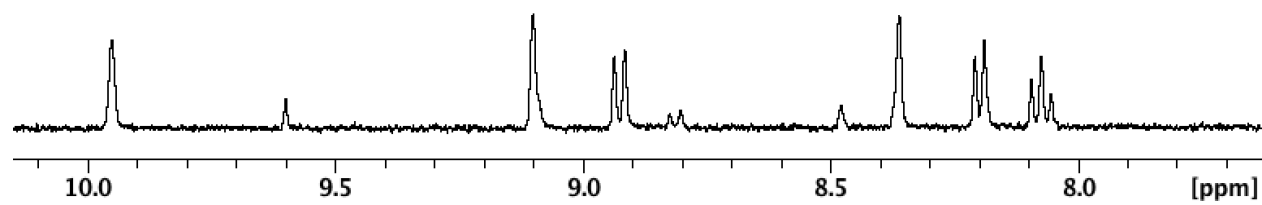
Figure A3.8. ^{1}H NMR spectrum of PHRD-3-3.
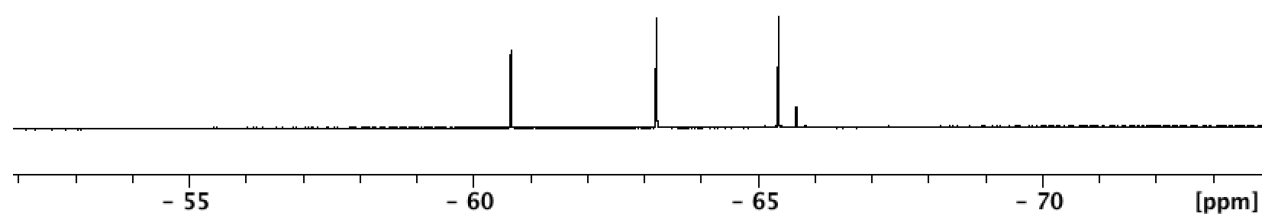
Figure A3.9. ^{19}F NMR spectrum of PHRD-3-3.

X-Ray Structure of PHRD-3-4
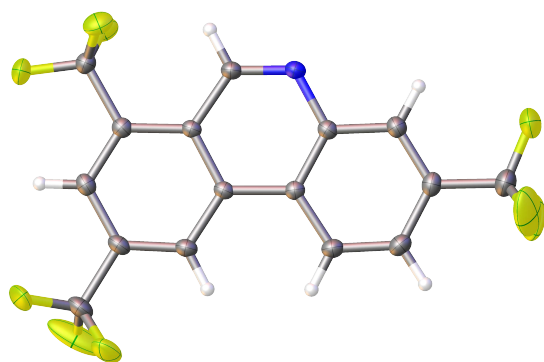
Figure A3.10. X-ray structure of PHRD-3-4.

X-Ray Structure and NMR spectra of PHRD-4-1
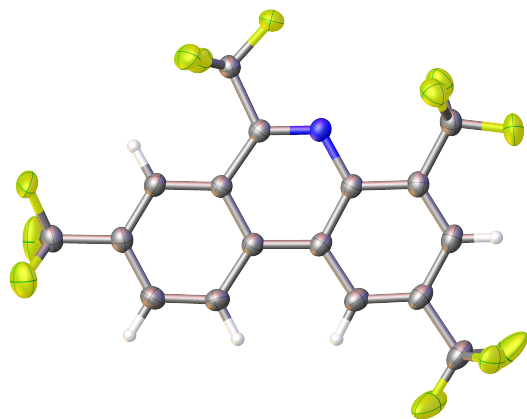
Figure A3.11. X-ray structure of PHRD-4-1
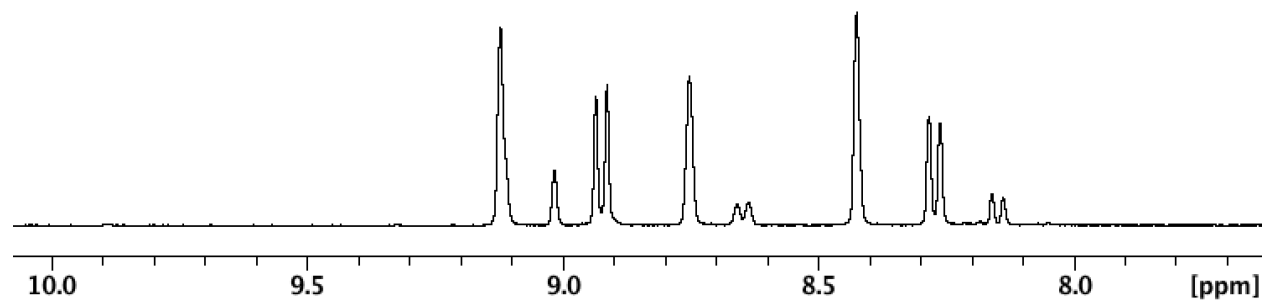
Figure A3.12. ^{1}H NMR spectrum of PHRD-4-1.
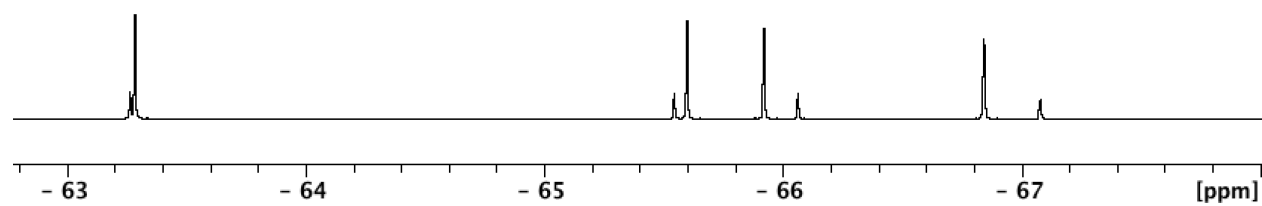
Figure A3.13. ^{19}F NMR spectrum of PHRD-4-1.

X-Ray Structure of PHRD-4-2
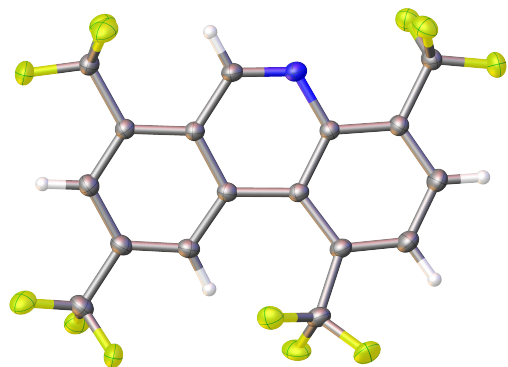
Figure A3.14. X-ray structure of PHRD-4-2.

NMR spectra of PHRD-4-3
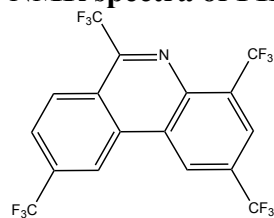
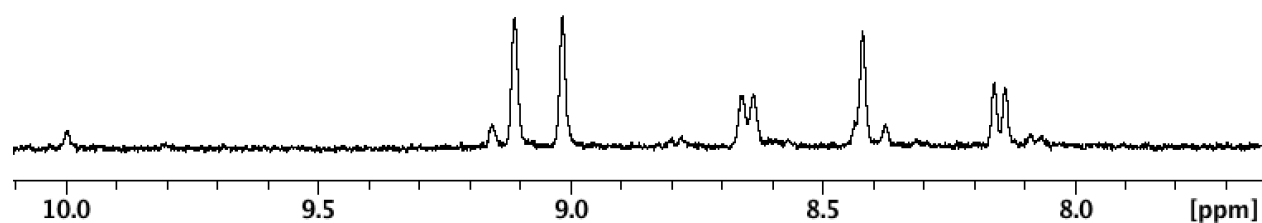**Figure A3.15.** Structure of PHRD-4-3 assigned by comparing NMR other PHRD(CF$_3$)$_n$ derivatives.
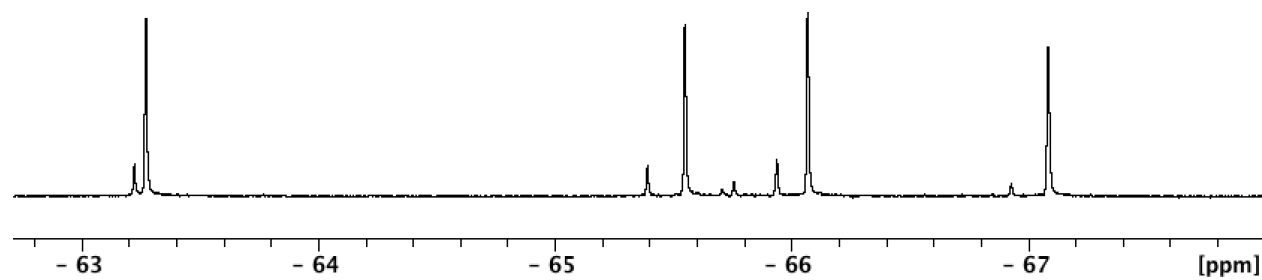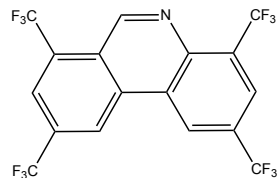

Figure A3.16. ^{1}H NMR spectrum of PHRD-4-3.

Figure A3.17. ^{19}F NMR spectrum of PHRD-4-3.

NMR spectra of PHRD-4-4

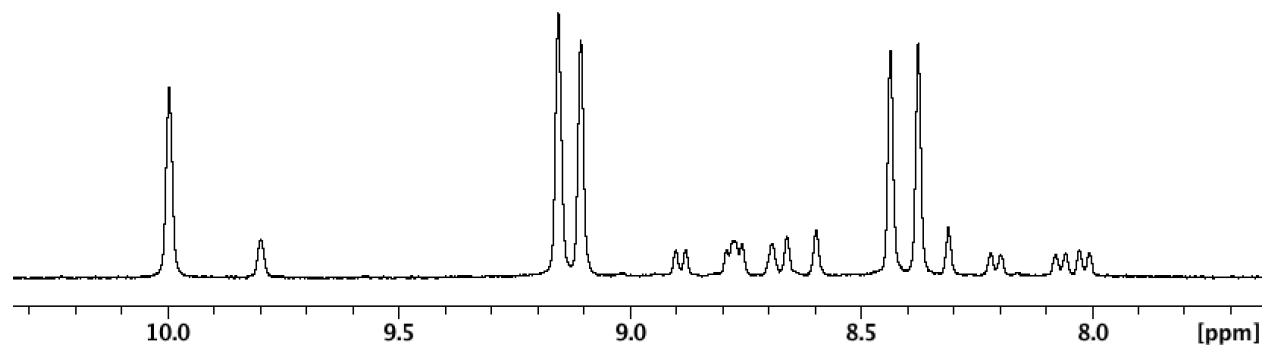**Figure A3.18.** Structure of PHRD-4-4 assigned by by comparing NMR other PHRD(CF$_3$)$_n$ derivatives.

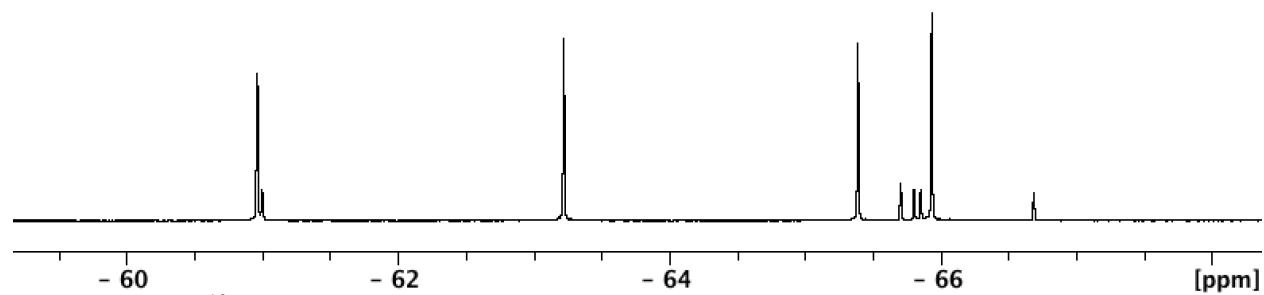**Figure A3.19.** ^{1}H NMR spectrum of PHRD-4-4.

Figure A3.20. ^{19}F NMR spectrum of PHRD-4-4.